STRUCTURE AND DYNAMICS OF THE PACIFIC UPPER MANTLE

by

RAFAEL KATZMAN

B.Sc., Tel-Aviv University, 1988
M.Sc., Tel-Aviv University, 1990

Submitted in Partial fulfillment of the Requirements for the Degree of
Doctor of Philosophy

at the

MASSACHUSETTS INSTITUTE OF TECHNOLOGY

and the

WOODS HOLE OCEANOGRAPHIC INSTITUTION

December, 1997

Signature of Author _____
Joint Program in Oceanography/Applied Ocean Science and Engineering
Department of Earth, Atmospheric, and Planetary Sciences
Massachusetts Institute of Technology, and
Department of Geology and Geophysics
Woods Hole Oceanographic Institution

Certified by _____
Thomas H. Jordan
Thesis Supervisor

Accepted by _____
Deborah K. Smith
Chair, Joint Committee for Marine Geology and Geophysics
Massachusetts Institute of Technology/
Woods Hole Oceanographic Institution

STRUCTURE AND DYNAMICS OF THE PACIFIC UPPER MANTLE

by

RAFAEL KATZMAN

Submitted to the Department of Earth, Atmospheric, and Planetary Sciences
Massachusetts Institute of Technology
and
The Department of Geology and Geophysics
Woods Hole Oceanographic Institution
December, 1997
in partial fulfillment of the requirements for the degree of Doctor of Philosophy

ABSTRACT

A new tomographic technique is employed to investigate the structure and dynamics of the Pacific upper mantle. We invert band-center travel times of *ScS* reverberations and frequency-dependent travel times of direct *S* phases, upper-mantle guided waves such as *SS* and *SSS*, and the R_1 and G_1 surface waves for the 2D composite structure in the plane of two Pacific corridors. The frequency-dependent travel times of the turning and surface waves are measured from all three components of ground motion as phase delays relative to a radially-anisotropic, spherically-symmetric oceanic mantle model, and their 2D Fréchet kernels are constructed by a coupled-mode algorithm. The travel times of the primary ScS_n and $sScS_n$ phases and their first-order reverberations from the 410 and 660 discontinuities are measured as individual phases and the 2D Fréchet kernels for these band-limited signals are calculated using the paraxial ray approximation. The model parameters include shear-speed variations throughout the mantle, perturbations to radial shear-wave anisotropy in the uppermost mantle, and the topography of the 410 and 660 discontinuities.

We construct vertical tomograms through two mantle corridors: one between the Tonga subduction zone and Oahu, Hawaii, which traverses the central Pacific Ocean; and the other between the Ryukyu subduction zone and Oahu, which samples the northern Philippine Sea, the western Pacific, and the entire Hawaiian swell. Tests demonstrate that the data sets for the two corridors resolve the lateral structure in the upper mantle with a scale length of a few hundreds kilometers and greater but that the resolving power decreases rapidly in the lower mantle. The model for the Tonga-Hawaii corridor reveals several interesting features, the most significant being a regular pattern of high and low shear velocities in the upper mantle between Tonga and Hawaii. These variations, which are well resolved by the data set, have a horizontal wavelength of 1500 km, a vertical dimension of 700 km, and an amplitude of about 3%, and they show a strong positive correlation with seafloor topography and geoid-height variations along this corridor. The geoid highs correspond to a series of northwest-trending swells associated with the major hotspots of the Society, Marquesas, and Hawaiian Islands. Where these swells cross the corridor, they are underlain by high shear velocities throughout the uppermost mantle, so it is unlikely that their topography is supported by thermal buoyancy. This result is substantiated by the model from the Ryukyu-Hawaii

corridor, which exhibits a prominent, fast region that extends beneath the entire Hawaiian swell. This anomaly, which resides in the uppermost 200-300 km of the mantle, is also positively correlated with the undulations of the Hawaiian-swell height. The other dominant features in the Ryukyu-Hawaii model include the high-velocity subducting slabs beneath the Ryukyu and Izu-Bonin seismic zones, which extend throughout the entire upper mantle; a very low-velocity in the uppermost 160 km of the mantle beneath the northern Philippine Sea, which is ascribed to the presence of extra water in this region; and a pronounced minimum in the amount of radial anisotropy near Hawaii, which is also seen along the Tonga-Hawaii corridor.

A joint inversion of the data from the two corridors reveals the same anomaly pattern and clearly demonstrates that the swells in the Central Pacific are underlain by fast velocities. It is therefore implied that the topography of the swells in the central Pacific is supported by a chemical buoyancy mechanism which is generated by basaltic volcanism and the formation of its low-density peridotitic residuum. While the basaltic depletion mechanism can produce high shear velocities in the uppermost 200 km, it cannot explain the depth extent of the fast anomalies beneath the swells which, along Tonga-Hawaii corridor, extend well into the transition zone. It is therefore hypothesized that the central Pacific is underlain by a system of convective rolls that are confined above the 660-km discontinuity. It is likely that these rolls are predominantly oriented in the direction of plate motion (like "Richter rolls") but the limited depth of the fast anomaly beneath the Hawaiian swell (200-300 km) suggests that their pattern is probably more complicated. Nevertheless, this convection pattern appears to be strongly correlated with the locations of the Tahitian, Marquesan, and Hawaiian hotspots, which raises interesting questions for Morgan's hypothesis that these hotspots are the surface manifestations of deep-mantle plumes.

Thesis Committee:

Dr. Thomas H. Jordan, Professor of Geophysics (Thesis Supervisor)
Dr. Rob van der Hilst, Professor of Geophysics
Dr. Bradford H. Hager, Professor of Geophysics
Dr. Stanley R. Hart, Senior Scientist, Woods Hole Oceanographic Institution
Dr. Jeroen Tromp, Professor of Geophysics, Harvard University

TABLE OF CONTENTS

CHAPTER 1

INTRODUCTION

The three-dimensional (3D) images of shear and compressional velocity variation provided by seismic tomography have placed strong constraints on the dynamics of the Earth's mantle [*Hager and Clayton*, 1989; *Forte et al.*, 1993; *Phipps Morgan and Shearer*, 1993; *Puster and Jordan*, 1997; *van der Hilst et al.*, 1997]. The resolution of these images has improved remarkably over the last decade, particularly for areas with high density of earthquakes and stations. On the continents, regional studies, employing large numbers of stations, have delineated lithospheric and upper-mantle structural features of dimensions less then 500 km [e.g., *VanDecar et al.*, 1995; *Zielhuis and van der Hilst*, 1996; *Saltzer and Humphreys*, 1997; *van der Lee and Nolet*, 1997]. In the oceans, numerous tomographic studies designed to image the subducted lithosphere have achieved very good resolution in the vicinity of the subduction zones, where earthquake density is high [e.g., *Zhou and Clayton*, 1990; *van der Hilst et al.*, 1991; *Hirahara and Hasemi*, 1993], and led to detailed 3D maps for the subducted slabs over the entire planet [*van der Hilst et al.*, 1997; *Grand et al.*, 1997]. Unfortunately, the resolving power of these studies decreases substantially away from the subduction zones, particularly in the upper mantle. As a result, the upper-mantle structure beneath the Pacific ocean, far from the seismic regions, has been constrained mostly by regional 1D (anisotropic and possibly age dependent) models [*Regan and Anderson*, 1984; *Nishimura and Forsyth*, 1989; *Gaherty et al.*, 1996] and by global tomographic studies [*Woodhouse and Dziewonski*, 1984; *Zhang and Tanimoto*, 1993; *Su et al.*, 1994; *Li and Romanowicz*, 1996; *Masters et al.*, 1996]. It is true that the large-scale variation in shear velocity is reasonably well resolved by these studies, but the horizontal resolving power of the global tomographic models, which is on the order of a few

thousand km, is insufficient to elucidate small-scale mantle heterogeneities that might be associated with surface tectonic features such as mid-plate hotspots and hotspot swells.

There are in fact some indications that processes of upper-mantle scale may be significant in the Pacific upper mantle. Geoid lineations of intermediate wavelength, which trend approximately in the direction of plate motion [*Wessel et al.*, 1994, 1996], have been observed in the south-central Pacific. A number of authors have suggested that these features are the expression of small-scale convection patterns [*Baudry and Kroenke*, 1991; *Maia and Diament*, 1991; *Cazenave et al.*, 1995], which are aligned into cylindrical rolls by the shearing from the overriding, fast-moving Pacific plate [*Richter and Parsons*, 1975]. However, the lack of seismic data in this region have thus far prevented seismologists from studying the correlation of these features with shear-velocity heterogeneities in the upper mantle.

The major goal of this thesis is to establish the structural and geodynamic relationship between mantle heterogeneities and surface tectonic features in the central and western Pacific, where previous knowledge of mantle heterogeneity has been limited by the lack of stations and the distance to the seismic regions. To achieve this goal, we focus on two Pacific corridors of particular interest. The first is the corridor between the Tonga-Kermadec subduction zone and the island of Oahu, Hawaii, which traverses the central Pacific Ocean nearly perpendicular to the plate motion across a series of island chains and oceanic plateaus. Despite the relatively uniform ocean depth and crustal age along this corridor, the differential travel times between an extensive set of multiply reflected ScS_n arrivals recorded on Oahu show large, systematic variation with distance and core-reflection number n [*Sipkin and Jordan*, 1980a; *Gee and Romanowicz*, 1992; *Katzman et al.*, 1997a]. This variation requires strong lateral shear-velocity gradients in the upper mantle regions sampled by their surface reflections. The global tomographic models, as well as the higher-resolution regional studies of the Pacific upper mantle [*Zhang and Tanimoto*, 1989], have thus far revealed no indications of structural variations in the upper

mantle with the magnitude and scale needed to explain these data. The second corridor extends from the Ryukyu and Izu-Bonin seismic zones to Oahu, where it is oriented almost parallel to the plate motion, as it crosses the Tonga-Hawaii corridor. This corridor traverses the northern Philippine sea, the western Pacific, and the entire Hawaiian swell. The origin of hotspot swells, and in particular the Hawaiian swell is still an open question; models which explain the uplift by reheating and thermal expansion within the lower lithosphere [*Detrick and Crough*, 1978] are at odds with the lack of heat-flow anomaly [*Von Herzen et al.*, 1989] and the normal seismic velocities obtained from dispersion of Rayleigh waves between Midway and Oahu [*Woods et al.*, 1991; *Woods and Okal*, 1996]. Other mechanisms such as dynamic support from hot plume material [*Davies*, 1988, 1992; *Sleep*, 1990], or underplating of compositionally lighter mantle residue left after the extraction of basaltic melt [*Jordan*, 1979; *Phipps Morgan et al.*, 1995], have been substantiated by seismological studies elsewhere (i.e., Yellowstone [*Saltzer and Humphreys*, 1997]), but not in the Pacific. The global and regional studies did not reveal any anomalous structure beneath the Hawaiian swell, whereas the study of Woods and his coworkers did not constrain the mantle structure away from the swell or much beneath the lithosphere. It is, therefore, not even clear whether or not the mantle structure beneath the Hawaiian swell is anomalous relative to the surrounding mantle.

In order to study these two corridors, we design a new tomographic technique which allows the construction of high-resolution vertical tomograms for single corridors, without the use of multiple crossing paths which are so essential in most other tomographies. The resulting tomograms also include lateral heterogeneity in radial anisotropy and topography of the 410 and 660 discontinuities. The new methodology introduced in this thesis directly addresses some of the current problems in mantle imaging as discussed below.

1.1 SOME CURRENT PROBLEMS IN MANTLE IMAGING

Much effort has been made in the last several years, to improve tomographic techniques [*Nolet*, 1990; *Li and Romanowicz*, 1995; *Marquering and Snieder*, 1995] and collect new data sets with enhanced spatial resolution [*Su et al.*, 1994; *Zielhuis and Nolet*, 1994; *Grand et al.*, 1997; *van der Hilst et al.*, 1997]. Attempts to resolve more of the details of the Earth's interior with better precision encounter several problems, however. The first is parameterization. Seismic wave propagation can be described to first order by a spherically symmetric Earth model $\mathbf{m}_0(r)$, such as the Preliminary Reference Earth Model (PREM) of *Dziewonski and Anderson* [1981], plus a small aspherical perturbation $\delta\mathbf{m}(r,\theta,\varphi)$. In most tomographic studies, the aspherical part is restricted to only one, or at most a few, model parameters, such as the compressional wave-speed perturbation $\delta\alpha$ or the shear wave-speed perturbation $\delta\beta$. The details of wave propagation can depend on other effects, of course, such as lateral heterogeneity of upper-mantle anisotropy [*Forsyth*, 1975; *Tanimoto and Anderson*, 1985; *Nishimura and Forsyth*, 1989; *Montagner and Tanimoto*, 1991; *Silver*, 1996] and the topography of the major transition-zone discontinuities [*Revenaugh and Jordan*, 1989, 1991b; *Shearer*, 1991, 1993; *Flanagan and Shearer*, 1997]. Therefore, attempts to improve the tomographic imaging of interior structure may require expanding the model parameterization.

A second problem concerns the way in which the measurements of seismic data are made. Seismograms, especially the broadband records from modern, high-performance instruments, encode an immense amount of information about the Earth, and seismologists have developed a diverse ensemble of techniques for extracting this information in the form of travel times, phase and group velocities, waveforms, decay rates, eigenfrequencies, splitting parameters, etc. Tomographic imaging is often sharpened if the data for a particular inversion come from measurement methods that are as uniform as possible, or at

least mutually consistent. This can be challenging for studies directed at an assortment of wave types recorded on more than one component of ground motion.

A third and related problem is how the data are connected back to the Earth. In tomography, a datum is considered to be the value of some functional of an Earth model plus an error arising from ambient and signal-generated noise. The construction of the functional relationship, which is generally nonlinear, requires a wave-propagation theory, and feasible algorithms always require some degree of theoretical approximation. Travel times of body phases like *P* and *S* are typically interpreted using geometrical optics where the influence of Earth structure is localized along the geometrical ray. This is adequate for high-frequency waves, but it begins to fail in high-resolution studies of heterogeneities having scale lengths comparable to the Fresnel scale of the waves [*Nolet et al.*, 1994; *Vasco et al.*, 1995]. In the case of intermediate-frequency body waves such as *SS* at 30 millihertz (mHz), the first Fresnel zone can have dimensions of hundreds of kilometers [*Shearer*, 1993, Figure 24], and proper interpretation requires an explicit consideration of the band-limited nature of the signals. The problem is particularly tough for body waves with *P-SV* polarizations, where the coupling among various phases is often strong and difficult to handle with ray-theoretic methods. Similarly, the classical mode-theoretic methods for the interpretation of the low-frequency, dispersed surface waves and their overtones commonly make approximations that may be inadequate for high-resolution studies (e.g., the mode group is isolated from other modes; it averages structure uniformly along its path).

1.2. A New Tomographic Technique

The measurement and interpretation techniques introduced in this thesis have been specifically designed to address these issues. The framework for the methodology is the theory of generalized seismological data functionals (GSDF) presented by *Gee and Jordan* [1992], which casts seismic information in terms of spectral parameters describing the

deviation of an observed waveform from an idealized version derived from a reference Earth model $\mathbf{m}_0$. The synthetic waveform is called an isolation filter, and the measurement procedure involves the windowing and narrow-band filtering of its cross-correlation with the data. It yields four bias-corrected GSDF parameters at each frequency, and one of these, the differential phase delay $\delta\tau(\omega)$—loosely referred to here as the "frequency-dependent travel-time residual"—is especially suitable for tomographic work. The theory specifies the linearized functional relationships, i.e., the Fréchet kernel [*Backus and Gilbert*, 1967], between $\delta\tau(\omega)$ and the model perturbation $\delta\mathbf{m}$ for arbitrary isolation filters, including complex waveforms comprising many rays or mode branches.

The power of this technique lies in its generality—the same analysis code can be applied to body waves, surface waves, and complex interference packets (e.g., oceanic G_1 groups, *Sa* and shear-coupled *PL* phases, triplicated arrivals) on all three components of ground motion—and in the precision with which it automatically characterizes the model-data functional relationship, accounting for both the band-limited nature of the signals and the interferences among the various wave constituents. Although the method is waveform driven, it does not suffer from the limitations associated with waveform inversions, where the structural dependence of the waveform is directly linearized. Waveform-inversions are particularly susceptible to problems such as cycle skipping, and require the shift between the data and the synthetic seismograms to be much smaller than the wave period. In the GSDF technique, on the other hand, large frequency-independent travel-time perturbations are easily treated (See Eq. 88 in Gee and Jordan, [1992]), without violating the linear approximation between the data functionals and the model. As a result, the inversion does not require a particularly good starting model and, as we demonstrate in this thesis, it can be successfully applied to areas with large structural diversity. Previous applications of the GSDF technique [*Gaherty and Jordan*, 1995; *Gaherty et al.*, 1996; *Kato and Jordan*, 1997] have been based on a path-averaged, 1D approximation, but here we apply for the first time an extension developed by *Zhao and Jordan* [1997] that calculates 2D Fréchet kernels for

$\delta\tau(\omega)$ by mode-coupling theory [*Woodhouse*, 1980, 1983; *Li and Tanimoto*, 1993]. The mode-coupling scheme in this implementation is made computationally efficient by taking advantage of the modal structure used in the synthesis of the isolation filter.

The GSDF technique provides a uniform methodology for measuring frequency-dependent travel times for all of the interesting wave groups in the direct-phase interval; i.e., that part of the seismogram extending from the *P* wave to the surface waves. Because we focused on the shear-velocity structure, we analyzed only the shear-dominated wavegroups beginning with the direct *S* phase and including *sS*, *SS*, *sSS*, *SSS*, *Sa*, R_1, and G_1, recovering their phase delays in the band 10-45 mHz. The waveforms in this interval represent about 79% and 95% of the data used for the Tonga-Hawaii and Ryukyu-Hawaii corridors.

We supplement the frequency-dependent travel-times for the tomographic inversions with band center travel times from a largely untapped source, the *ScS* reverberations, which arrive in a richly structured interval of the seismogram following the surface waves and preceding the long-arc arrivals. Multiply-reflected ScS_n phases have been extensively used to investigate mantle attenuation [*Jordan and Sipkin*, 1977; *Nakanishi*, 1979; *Sipkin and Jordan*, 1980b; *Lay and Wallace*, 1983] and in some reconnaissance studies of mantle heterogeneity [*Sipkin and Jordan*, 1976, 1980a], but they have not been thus far employed in mantle tomography. The primary (zeroth-order) ScS_n and $sScS_n$ phases lie in a sea of higher order reverberations generated by their interactions with mantle discontinuities, and synthetics-based migration methods have been developed to stack these data and obtain path-averaged reflectivity profiles for the entire mantle [*Revenaugh and Jordan*, 1989, 1991b]. For the Tonga-Hawaii corridor, however, some of the first-order reflections from the mid-mantle transition-zone are large and isolated enough for their travel times to be measured as individual phases [*Revenaugh and Jordan*, 1987]. We use ray-theoretical isolation filters to obtain travel-time residuals for both zeroth-order and first-order reverberations from the 410 and 660 discontinuities. These times are measured at a center

frequency of 25 mHz; hence, they sample the mantle over a broad zone transverse to their ray paths, and their interpretation cannot be based on geometrical optics. Instead, we constructed "fat ray" Fréchet kernels using a paraxial ray approximation, which we validate by comparing them with kernels computed by coupled-mode summation.

Chapters 2 and 3 summarize the procedure for measuring band-centered travel times for *ScS* reverberations and frequency-dependent travel times for surface and turning waves. We outline the procedure for calculating isolation filters for these waves and Fréchet kernels for their travel-time data. We illustrate the tomographic utilization of these travel-time data and discuss their sampling properties by showing a few distinctive examples of Fréchet kernels for a suite of isolation filters.

1.3 Pacific Corridors

Up to 45 frequency-dependent times of surface and turning waves have been extracted from single three-component seismograms along the Tonga-Hawaii and Ryukyu-Hawaii corridors. With the intense and well distributed seismicity of the Tonga, and the Ryukyu and Izu-Bonin subduction zones, the multiplicity of the wave paths was sufficient to construct high-resolution vertical tomograms in the plane of these two corridors. This type of image construction differs from most mantle tomographies, in which the horizontal resolution is obtained primarily from wave paths crossing on differing great circles. In addition to the shear-velocity perturbations, the vertical tomograms include lateral variations of upper-mantle anisotropy and the topographies of the 410 and 660 discontinuities. The topographic parameters are constrained by the first-order *ScS* reverberations and the dispersion of shear-dominated waves that turn in the transition zone. The restriction of the tomographic inversions to single corridors, precludes the recovery of the azimuthal dependence of anisotropy [*Montagner and Tanimoto*, 1991; *Silver*, 1996], but the dependence of the phase delays on polarization provided good constraints on the lateral and radial differences between the apparent *SH* and *SV* velocities, $\beta_H - \beta_V$.

In Chapter 4, we invert the Tonga-Hawaii data for an image of the vertical plane of this corridor. The data are inverted using a complete Gaussian Baysian approach [*Tarantola and Valette*, 1982], and the resulting tomogram accounts for most of the variance in the travel-time residuals. We substantiate the main features of the model by a series of data-set inversions, resolution tests (Appendix A), and resolving-power calculations which employ the posterior covariance matrix (Appendix B). Using the Baysian approach, we test the sensitivity of the results to a variety of prior assumptions, including mineralogical constraints, such as an equilibrium-olivine thermal model which involves a combination of topography and discontinuity constraints. The tomogram reveals an intriguing pattern of shear-speed highs and lows that are well resolved by the data, and are strongly and positively correlated with geoid anomalies and seafloor topography in this region. We discuss the dynamic implications of the results, which appear to reflect chemical variations associated with basaltic volcanism, and small scale convection processes in the central-Pacific upper mantle.

In Chapter 5, we obtain a model for the 2D structure in the plane of the Ryukyu-Hawaii Corridor, which is tested by a suite of resolution tests, and by a series of full and partial data-set inversions. The topography parameters along this corridor appear to be less robust owing to the lack of first-order reverberations data in the inversion. We demonstrate, however, that the linearized functional relationship between the travel-time data and the model perturbations is appropriate even for the large structural variation associated with the transition from the western Pacific to the Philippine-Sea. In this Chapter we also tie the Tonga-Hawaii and Ryukyu-Hawaii corridor by a joint inversion of the two data sets. The models reveal a fast anomaly beneath the entire Hawaiian swell which appears to agree with the Tonga-Hawaii results, requiring a compositional-buoyancy mechanism for the swell support. We also discuss the contrast between the Philippine-Sea and the Western Pacific as reflected from the tomographic inversions. We conclude by pointing out to some future research directions.

CHAPTER 2

ScS-REVERBERATION TRAVEL TIMES

2.1 INTRODUCTION

The reverberative interval—the part of the seismogram following the surface waves and proceeding the long-arc arrivals—is a rich source of seismological information. On the transverse component, this interval is populated exclusively by a series of multiply reflected *ScS* waves, which are accompanied by a sequence of higher-order reverberations generated by their interaction with internal discontinuities (Figure 2.1a). The primary *ScS* waves have been extensively used in mantle-attenuation studies [*Jordan and Sipkin*, 1977; *Nakanishi*, 1979; *Sipkin and Jordan*, 1980b; *Lay and Wallace*, 1983], and in some studies of mantle heterogeneity [*Sipkin and Jordan*, 1976, 1980a], but the higher-order reverberations are harder to utilize owing to their lower amplitudes. Although individual measurements of first-order reverberations have been used by *Revenaugh and Jordan* [1987] and by *Clarke et al.* [1995], most other studies have employed the migration techniques developed by *Revenaugh and Jordan* [1989, 1991b] to stack these data in order to obtain path-averaged reflectivity profiles for the mantle [*Revenaugh and Jordan*, 1991b-d; *Revenaugh and Sipkin*, 1994a,b]. The methodology for utilizing these data in a tomographic inversion, is described in this chapter and applied in Chapters 4 and 5 for the Tonga-Hawaii and Ryukyu-Hawaii corridors, respectively. Unfortunately, the first-order reverberations data could not be utilized for the latter corridor due to their poor signal-to-noise ratio (snr); we therefore illustrate our procedure by data from the Tonga-Hawaii corridor only.

2.2 SYNTHETIC SEISMOGRAMS, ISOLATION FILTERS, AND MEASUREMENT PROCEDURE

At the epicentral distances of our two Pacific corridors, ($0° \leq \Delta \leq 70°$), the reverberative interval contains the primary ScS_n and $sScS_n$ phases with core-reflection numbers n ranging from 1 to 4 and a series of reflections and multiple reflections from internal mantle discontinuities (Figure 2.1a). The waves that reflect only once from an internal discontinuity are called first-order reverberations [*Revenaugh and Jordan*, 1987]; in a spherically symmetric structure they occur in dynamic families [*Hron*, 1971, 1972] that arrive with the same amplitude at the same time to form discrete phases which are significantly larger (by a factor of n or n+1) than the individual reflections. We denote such an arrival by the phase symbols $ScS_n^{d\pm}$ and $sScS_n^{d\pm}$, where n is the number of core reflections of the parent ScS_n or $sScS_n$, d is the nominal discontinuity depth, and (+) or (–) indicates topside or bottomside reflections, respectively. The ray paths for the dynamic families $ScS_2^{660\pm}$ and $sScS_2^{660\pm}$ are illustrated in Figure 2.1b.

In a spherically symmetric Earth, ScS reverberations do not experience critical phenomena such as turning points and caustics, and diffractions are unimportant; hence, geometrical ray theory is usually adequate for computing synthetic seismograms [*Revenaugh and Jordan*, 1987]. This expectation can be confirmed by comparing ray-theoretic synthetics for the reverberative interval with those computed by complete mode summation (Figure 2.1a). Since the former were summed only over the zeroth- and first-order reverberations, the good agreement also demonstrates that the second- and higher-order reverberations from the transition zone can be safely ignored (see *Revenaugh and Jordan* [1987] for comparisons with ray-theoretic seismograms computed to second order).

We adopt this first-order approximation in our tomographic analysis, except that all reverberations from the crust are included for every phase via a Haskell propagator. For each data record, a complete synthetic seismogram is calculated for the appropriate reference model by summing over the zeroth-order phases and the first-order reverberations

from the G, 410 and 660 discontinuities. All rays that contribute to the reverberative interval at these epicentral distances have nearly vertical paths through the uppermost mantle, so that in our radially anisotropic (transversely isotropic) Earth model, the appropriate shear-wave speed is β_V. Prior to summation, the travel time along each ray path is corrected for ellipticity and bounce-point bathymetry; the latter is obtained by an appropriate spatial averaging of DBDB5 bathymetric model. Dynamic families are then summed, each pulse is causally attenuated assuming that the Q structure for the corridor is frequency independent, and the resulting record is convolved with the instrument response.

The measurement procedure for *ScS* reverberations involves a careful phase selection. The overlap among the phases within the reverberative interval depends strongly on source depth, which must be taken into account when constructing the isolation filters. At intermediate focal depths, for example, the topside reflections ScS_n^{660+} and $sScS_n^{410+}$ arrive at nearly the same time, as do the corresponding bottomside reflections (Figure 2.2a). In such cases, we sum the contributions from both dynamic families to obtain a single isolation filter (Figure 2.2b). This example shows that two first-order arrivals, ScS_n^{410+} and $sScS_n^{410-}$, fall within the side lobes of the primary $sScS_n$ and ScS_{n+1} phases, respectively. Since their times can not be measured without large interference corrections, we cannot utilize them. For deep-focus events, the same problem arises for ScS_n^{d+} and $sScS_n^{d-}$ (Figure 2.3), and their times are also deleted. Nevertheless, up to 6 zeroth-order and 12 first-order reverberation times can be measured from a single deep-focus record.

The concatenation of two or more reverberation phases was used to increase the snr even in cases where the individual phases were well isolated, especially for earthquakes with shallower focal depths where near-surface reverberations caused high noise levels. (Events above 70 km were always too noisy to measure first-order reverberations.) However, to retain sensitivity to discontinuity topographies, only topside or bottomside reflections were combined in this manner, e.g., groupings such as $\{ sScS_n^{410+} + ScS_n^{660+} + sScS_n^{660+} \}$ and $\{ ScS_n^{410-} + ScS_n^{660-} \}$.

To obtain the actual travel-time data, we cross-correlate a series of single-phase and concatenated isolation filters with the observed seismogram, and find the travel-time residual that maximizes the cross-correlagram (resampled at 0.1 s); we correct this time for interference with other phases by subtracting the phase delay computed for a complete synthetic seismogram. Each resulting time is then graded according to the snr and magnitude of the interference corrections, and low-scoring measurements are discarded (see also Sections 4.6.1 and 5.6.2). The final step is to remove redundant measurements from the data set. If good times are obtained for both ScS_n^{410-} and ScS_n^{660-}, for example, then the phase delay for the concatenated filter $\{ ScS_n^{410-} + ScS_n^{660-} \}$ is dropped. Table 4.2 in Chapter 4 displays a variety of isolation filters that were obtained in this manner and were used in the study of the Tonga-Hawaii corridor.

2.3 Fréchet Kernels

As noted above, the isolation filters used in the measurement of the differential phase delays $\delta\tau$ are constructed by summing only the contributions for the target wavegroup, which are either a single phase or a group of nearly coincident arrivals. In this analysis, we disregard the differential dispersion within a given arrival (which should be small for reflections from sharp discontinuities) and recover the phase delays at a single center frequency $f = \omega/2\pi \approx 25$ mHz. To first order, the relationship between $\delta\tau$ and the relative perturbation to the vertical shear velocity $\delta\beta_V/(\beta_V)_0$ in the ray plane (r, θ) can be written

$$\delta\tau(\omega) = \int_{r_c}^{R} \int_{-\pi}^{\pi} K_{\beta_V}(\omega, r, \theta) \frac{\delta\beta_V(r,\theta)}{[\beta_V(r)]_0} d\theta\, r\, dr + \sum_{i=1}^{M} \int_{-\pi}^{\pi} K_i(\omega, \theta)\, \delta r_i(\theta)\, d\theta. \quad (2.1)$$

In this expression, r_c is the core radius, R is the Earth radius, $[\beta_V(r)]_0$ is the vertical shear velocity in the reference model, $K_{\beta_V}(\omega, r, \theta)$ is the Fréchet kernel for the areal relative perturbation $\delta\beta_V(r,\theta)/[\beta_V(r)]_0$, and $K_i(\omega, \theta)$ is the kernel for the along-path topography $\delta r_i(\theta)$ of the ith discontinuity at reference radius r_{0i}. The Fréchet kernel for an isolation

filter comprising N undispersed, narrowband wavelets with model-predicted amplitudes $\{a_j\}$ and travel times $\{\tau_j\}$ is the weighted sum of the kernels for the individual wavelets; e.g.,

$$K_{\beta_V} = \sum_{j=1}^{N} c_j K_{\beta_V}^{(j)}. \tag{2.2}$$

Expressions for the coefficients $\{c_j\}$ can be derived from the general perturbation equations given by *Gee and Jordan* [1992, sect. 4.7]; the results are

$$c_j = \frac{a_j}{C} \sum_{k=1}^{N} a_k \exp[-\sigma^2(\tau_k - \tau_j)^2 / 2] \cos[\omega(\tau_k - \tau_j)], \tag{2.3}$$

where σ is the half-bandwidth and C is a normalization constant given by

$$C = \sum_{j=1}^{N} \sum_{k=1}^{N} a_j a_k \exp[-\sigma^2(\tau_k - \tau_j)^2 / 2] \cos[\omega(\tau_k - \tau_j)]. \tag{2.4}$$

The content of these equations can be elucidated by considering some special cases. For members of a dynamic ray family, a_j and τ_j are constants for all j, and c_j reduces to $1/N$. In the case of N phases with identical travel times, the kernels are just weighted by their amplitudes, $c_j = a_j / \sum_{k=1}^{N} a_k$. When the separation in travel time is large compared to σ^{-1}, the coupling terms in (2.3) are small, and the weighting is proportional to the squared amplitude, $c_j = a_j^2 / \sum_{k=1}^{N} a_k^2$. In general, the coupling can be either positive or negative, depending on the sign of $\cos[\omega(\tau_k - \tau_j)]$. For dispersed signals, such as those considered in Chapter 3, equations (2.3) and (2.4) must be generalized to include other parameters, such as the group delay and the rate of change of the logarithmic amplitude with frequency [*Gee and Jordan*, 1992].

According to the geometrical optics approximation usually employed in seismic tomography, the kernels $K_{\beta_V}^{(j)}$ are concentrated in δ-functions along the ray paths. The

propagation distances L for the ScS reverberations are very large, however, reaching 25,000 km for ScS_4, and their wavelengths λ at 25 mHz are approximately 200 km; hence, the radius of first Fresnel zone, $r_F \approx \sqrt{\lambda L}/2$, can exceed 1000 km. We therefore calculate a "fat-ray" Fréchet kernel by distributing the geometrical optics sensitivity of $-\beta_V^{-1}$ per unit path length around the ray, weighted by a cosine bell of radius $r_F/2$. To account for ray curvature, we compute the first Fresnel zone by the paraxial ray approximation [*Červený and Soares*, 1992]. Figures 2.4a and 2.4b compare the Fréchet kernel for ScS_2 derived by this ad hoc method with one calculated by the formal mode-coupling scheme of *Zhao and Jordan* [1997]. The latter is described in Chapter 3 and employed in Chapters 4 and 5 in the analysis of the surface and turning wave data, and some of the ScS arrivals on the radial and vertical components. The kernels from these two very different theories are similar, although the mode-based kernel is more diffuse near the source and receiver, where the paraxial approximation is known to fail.

One advantage of the fat-ray kernel over the mode kernel is its computational efficiency, requiring orders of magnitude less computer time than the heavy coupling calculations needed for the 2D mode summation. A second is that it can be separated into a component for each reflection in a dynamic family, which can then be individually corrected for ellipticity and seafloor topography, as discussed above. We used the fat-ray kernels to make these corrections and in all inversions.

2.4 Sampling Properties

The tomographic power of the ScS reverberations derives from their multiplicity. Because of their nearly vertical ray paths, the times of the zeroth-order reflections are essentially insensitive to radial variations other than the mantle average, but they sample heterogeneity along-path in unique ways. For example, their surface-reflection points are distributed such that the ScS_3-ScS_2 and ScS_4-ScS_3 differential times are particularly sensitive to lateral variations in the upper mantle near the center of the path having

horizontal wavelengths of about one-third of the epicentral distance (Figures 2.4c and 2.4d). This property is used in Section 4.6 to explain the systematic and large residuals of the ScS_n-ScS_m travel times from the Tonga-Hawaii corridor (Figure 4.3). If the heterogeneity responsible for these large residuals resides in the upper mantle, we expect it to contain significant power at wavelengths near $\Delta/3 \approx 15°$. As we shall see, this is indeed the case.

The first-order reverberations from transition-zone discontinuities do depend on the vertical structure; e.g., times of the topside reflections from 660 are more sensitive to upper-mantle shear speeds and the bottomside reflections are more sensitive to lower-mantle speeds, owing to the extra peg-leg reflections in these two regions, respectively. Because the travel-time observations average over the dynamic family of reflected rays, this differential sensitivity is distributed uniformly with respect to the reflection points, and we cannot take advantage of the lateral differences among members of the same family. (Such differences give rise to a splitting of the reverberation multiplet, however; assuming the 660 to be sharp, *Revenaugh and Jordan* [1989, 1991b] used frequency-dependent observations of the multiplet broadening to constrain its root-mean-square topography at the sampling wavelength, obtaining an estimate of 5-10 km for the central and western Pacific, which was consistent with their observations of interpath topography and the results presented in Chapter 4.)

As expected, the first-order reverberations are also much more sensitive to the locations of the reflecting discontinuity than the parent zeroth-order phase (Figures 2.4e and 2.4f). Since the sign of this sensitivity is opposite for the topside and bottomside reflections, their combination can be used to separate volumetric heterogeneity from discontinuity topography. For example, a topographic depression on a discontinuity will cause a time delay for the topside reverberations and a time advance for the bottomside reverberations, while a velocity perturbation situated either above or below the discontinuity will affect the travel time of only one of these phases. Because the first order reverberations were not

used in the inversion along the Ryukyu-Hawaii corridor, the resulting transition-zone topography parameters were significantly less robust.

FIGURE CAPTIONS

Figure 2.1 (a) An example of the reverberative interval for a deep-focus earthquake (h = 590 km, Δ = 46.4°). Bottom two traces are the data and the complete synthetic seismogram generated by normal-mode summation; others are synthetics computed by geometrical optics (an excellent approximation for the reverberative interval), with a Haskell propagator for crustal reverberations. Trace labeled *0th* comprises the zeroth-order ScS_n and $sScS_n$ phases (classified by their CMB reflection number n) ; those labeled 410–, 410+, 660–, 660+ are the first-order bottomside and topside reflections from the 410-km and 660-km discontinuities, respectively. Time is minutes after the origin time. (b) The ray paths for the n = 2 zeroth-order (left side) and first-order reverberations from the 660-km discontinuity. The topside and bottomside reflections in each row constitute a dynamic family of rays with the same amplitude and phase that constructively interfere to form the first-order arrivals seen on the seismograms. The families of first-order reverberations are denoted by ScS_n^{410-}, where n is the core reflection number of the parent ScS_n or $sScS_n$ phase, d is the discontinuity depth, and +/– indicates a topside/bottomside reflection.

Figure 2.2 Decomposition of a reverberative interval for an intermediate-focus Fiji earthquake recorded at KIP on Oahu (h = 246 km, Δ = 45.5°). For reference, the top panel (Figure 2.2a) shows the data and the synthetics (bottom two traces) as a summation of families of dynamic analogs corresponding to the zeroth-order reverberations and the first-order topside and bottomside reverberations from the 660 and 410 discontinuities (top five traces); traces are labeled the same as in Figure 2.1a. The bottom panel (Figure 2.2b) comprises of all the isolation filters that can be employed for this reverberative interval together with the synthetic sum and the data; the traces are numbered on the right (S - synthetics, D- data). The zeroth-order phases ScS_n and $sScS_n$ are used individually as

isolation filters (traces 1 and 2). For the first-order reverberations, the topside phases $sScS_n^{410+}$ and ScS_n^{660+}, which arrive at nearly the same time, are combined to create one isolation filter (trace 3); the bottomside reflections ScS_n^{410-} and $sScS_n^{660-}$ are also combined into one isolation filter (trace 5), for the same reason. The topside phase $sScS_n^{660+}$ and the bottomside phase ScS_n^{660-} do not interfere with any other arrival and are used individually as isolation filters if their signal-to-noise ratio is sufficiently high (traces 4 and 6, respectively). The ScS_n^{410+} and $sScS_n^{410-}$ arrivals, on the other hand, are too close to the primary $sScS_n$ and ScS_{n+1} phases, respectively, and cannot be measured separately without significant interference.

Figure 2.3 Decomposition of a reverberative interval for a deep-focus earthquake Fiji earthquake recorded at KIP (h = 590 km, Δ = 46.4°). The two panels are organized and labeled the same as in Figure 2.2. The bottom panel shows isolation filters for the zeroth-order reverberations (traces 1 and 2) and for the first-order reverberations, whose only well-isolated phases are the topside $sScS_n^{660+}$ and $sScS_n^{410+}$ (traces 3 and 4) and the bottomside ScS_n^{660-} and ScS_n^{410-} (traces 5 and 6).

Figure 2.4 Examples of Fréchet kernels for ScS reverberations. The wave type is indicated at the top of each panel. Warm colors correspond to negative sensitivity (phase-delay increase for velocity decrease), cool colors to positive sensitivity, and the green lines show the sensitivity to perturbations in the radii of 410 and 660 discontinuities; yellow circle and blue triangle show the locations of the source and receiver, respectively. All kernels except for the one in Figure 2.4b are fat-ray kernels, which were calculated using the paraxial-ray approximation (see text). (a) and (b) Comparison between a fat-ray kernel and a mode-theoretic kernel for ScS_2. The latter was calculated by the mode-coupling scheme of *Zhao and Jordan* [1996], which is employed later in the paper for calculating the kernels for the turning- and surface-wave data. Despite the very different theories, the

resulting kernels are quite similar except near the source and the receiver, where the paraxial-ray approximation breaks down. (c) and (d) Differential kernels for ScS_3-ScS_2 and for ScS_4-ScS_3, respectively. (e) and (f) First-order-reverberation kernels for ScS_2^{660+} (topside reverberation) and ScS_2^{660-} (bottomside reverberation), respectively.

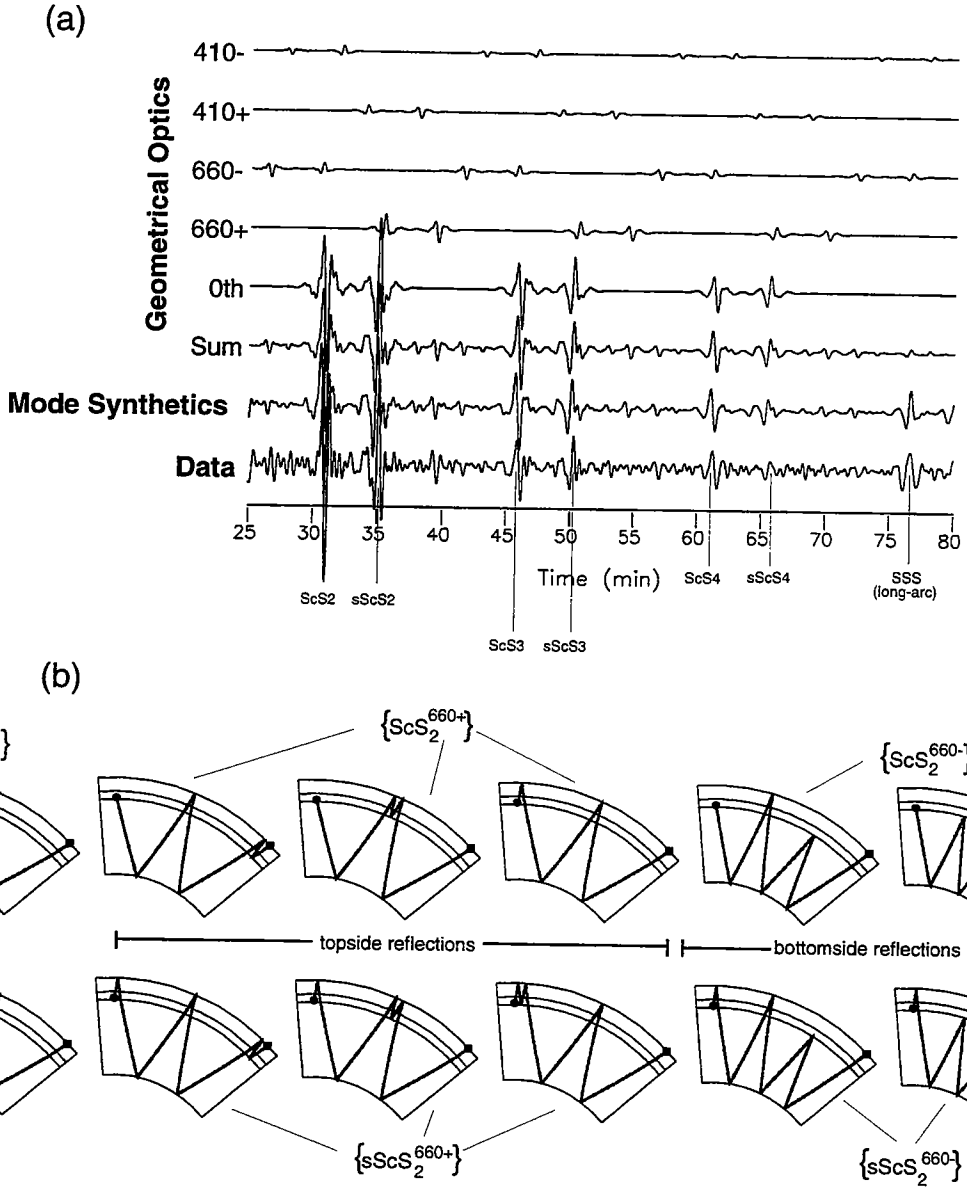
(a)
Geometrical Optics
410-
410+
660-
660+
0th
Sum
Mode Synthetics
Data
25
30
35
40
45
50
55
60
65
70
75
80
Time (min)
ScS2
sScS2
ScS3
sScS3
ScS4
sScS4
SSS
(long-arc)
(b)
{ScS2}
{ScS2 660+}
{ScS2 660-}
topside reflections
bottomside reflections
{sScS2}
{sScS2 660+}
{sScS2 660-}

Figure 2.1

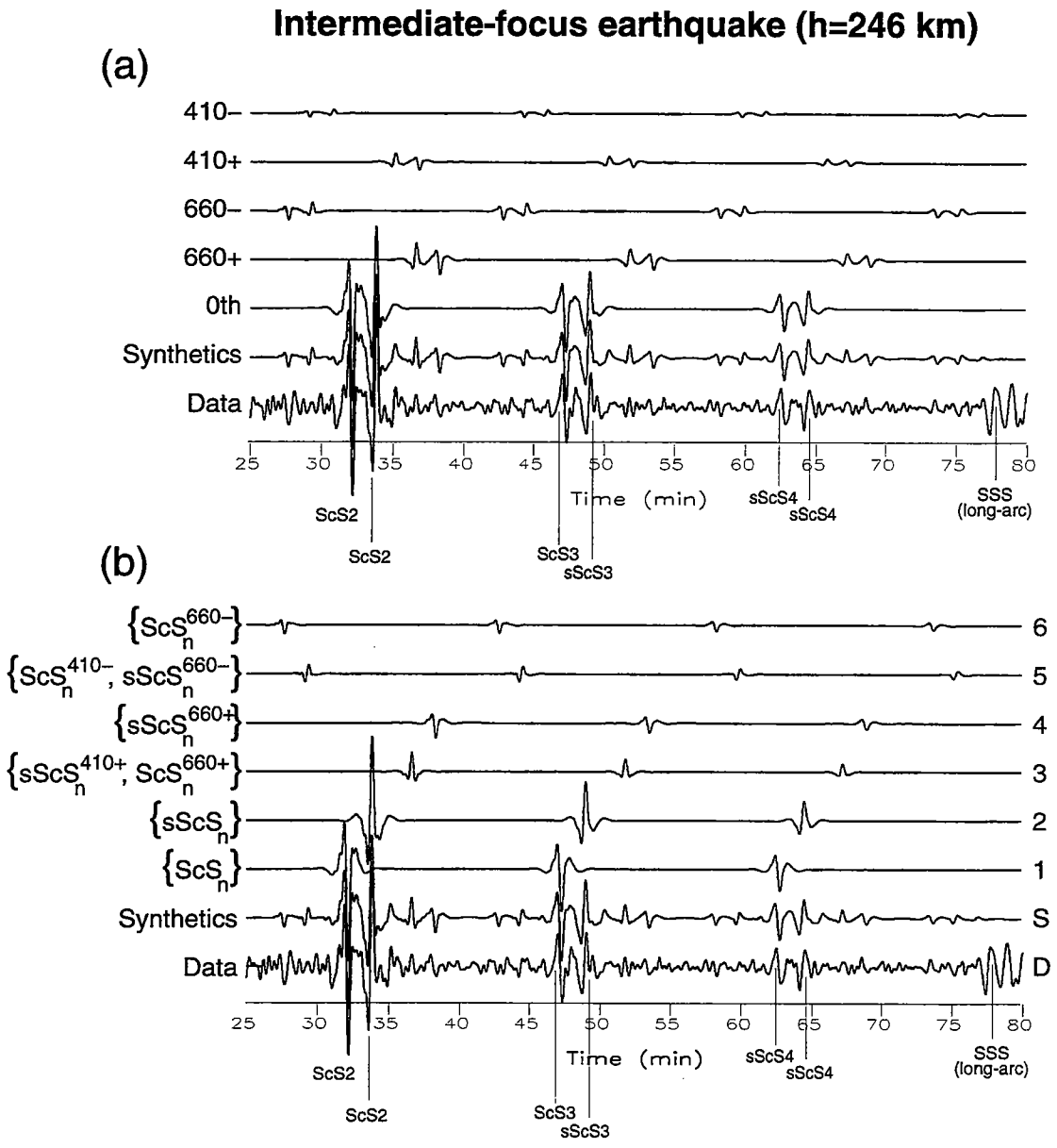
Intermediate-focus earthquake (h=246 km)
(a)
410−
410+
660−
660+
0th
Synthetics
Data
25 30 35 40 45 50 55 60 65 70 75 80
Time (min)
ScS2
ScS2
ScS3
sScS3
sScS4
sScS4
SSS
(long-arc)
(b)
{ScS_n^660−}
{ScS_n^410−, sScS_n^660−}
{sScS_n^660+}
{sScS_n^410+, ScS_n^660+}
{sScS_n}
{ScS_n}
Synthetics
Data
6
5
4
3
2
1
S
D
25 30 35 40 45 50 55 60 65 70 75 80
Time (min)
ScS2
ScS2
ScS3
sScS3
sScS4
sScS4
SSS
(long-arc)

Figure 2.2

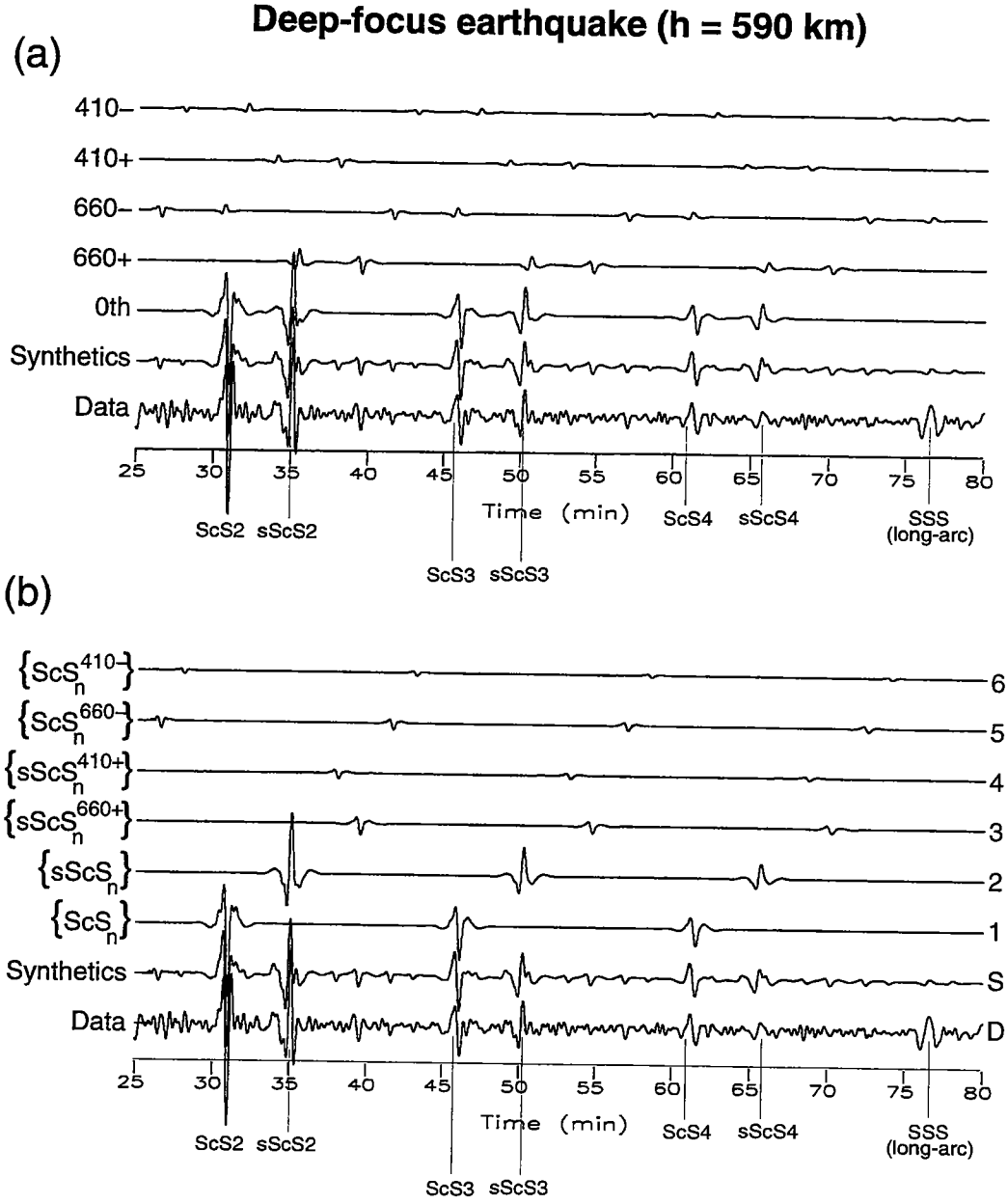
Deep-focus earthquake (h = 590 km)
(a)
410–
410+
660–
660+
0th
Synthetics
Data
25 30 35 40 45 50 55 60 65 70 75 80
Time (min)
ScS2 sScS2
ScS3 sScS3
ScS4
sScS4
SSS
(long-arc)
(b)
{ScS_n^410–}
{ScS_n^660–}
{sScS_n^410+}
{sScS_n^660+}
{sScS_n}
{ScS_n}
Synthetics
Data
6
5
4
3
2
1
S
D
25 30 35 40 45 50 55 60 65 70 75 80
Time (min)
ScS2 sScS2
ScS3 sScS3
ScS4
sScS4
SSS
(long-arc)

Figure 2.3

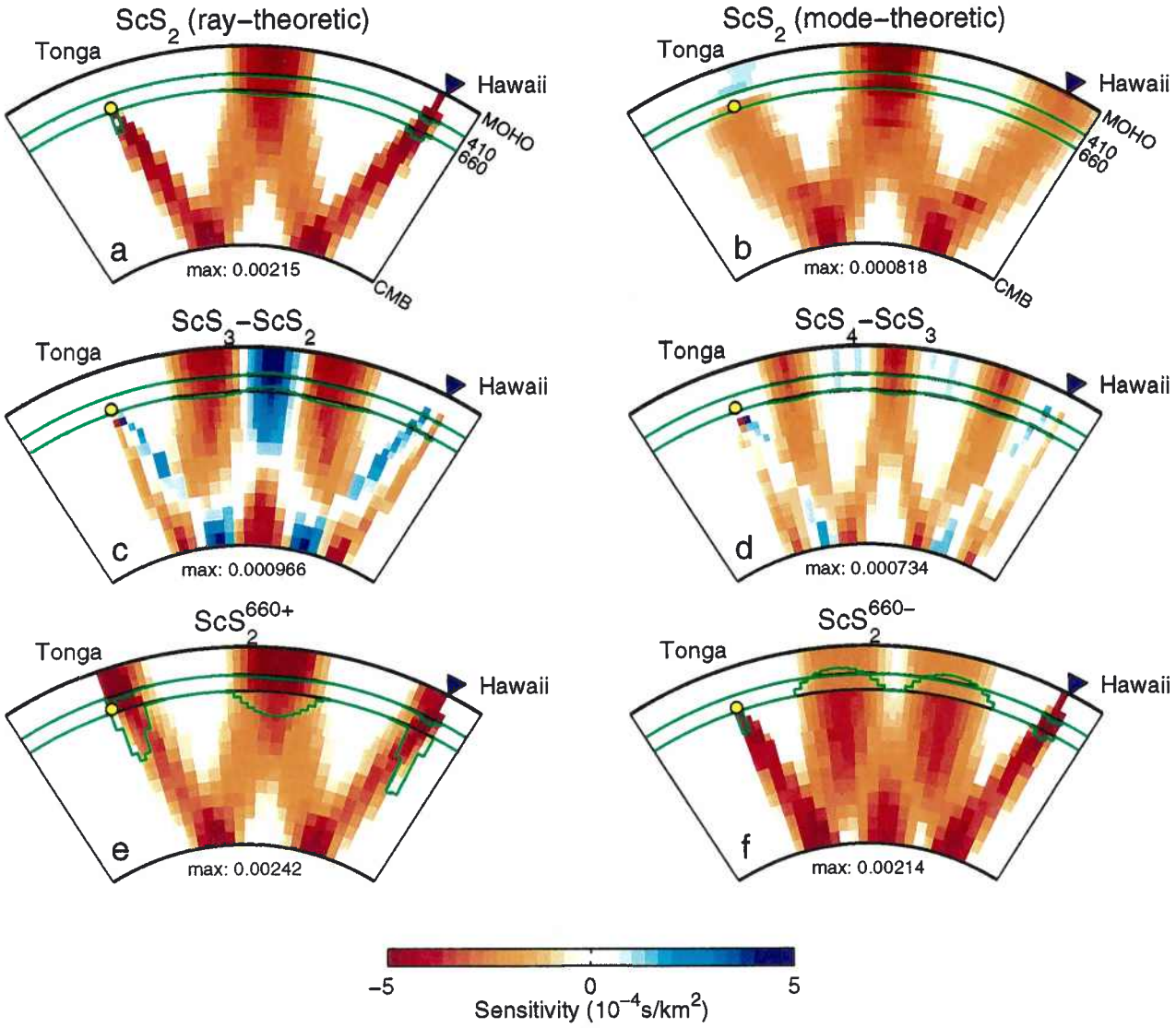
ScS2 (ray−theoretic)
Tonga
Hawaii
MOHO
410
660
CMB
a
max: 0.00215
ScS2 (mode−theoretic)
Tonga
Hawaii
MOHO
410
660
b
max: 0.000818
CMB
ScS3−ScS2
Tonga
Hawaii
c
max: 0.000966
ScS4−ScS3
Tonga
Hawaii
d
max: 0.000734
ScS2660+
Tonga
Hawaii
e
max: 0.00242
ScS2660−
Tonga
Hawaii
f
max: 0.00214
−5
0
5
Sensitivity (10−4s/km2)

Figure 2.4

CHAPTER 3

FREQUENCY-DEPENDENT TRAVEL TIMES OF TURNING AND SURFACE WAVES

3.1 INTRODUCTION

The *ScS* reverberations presented in Chapter 2 can yield valuable data regarding along-path heterogeneity and discontinuity topography, but owing to their poor vertical resolution, they alone are insufficient to resolve any corridor structure at the level needed for a robust geodynamic interpretation. Such a level of resolution, however, can be obtained by incorporating seismological data from the direct phase interval, which is the part of the seismogram extending from the *P* wave to the surface waves. The waveforms arriving within this interval were the principle data source for both the Tonga-Hawaii and Ryukyu-Hawaii inversions (Chapters 4 and 5). These waveforms have been extensively used by many previous tomographic studies on both global [e.g., *Woodhouse and Dziewonski*, 1984; *Su et al.*, 1994; *Masters et al.*, 1996; *Li and Romanowicz*, 1996] and regional scales [e.g., *Grand*, 1987, 1994; *Zielhuis and Nolet*, 1994; *Marquering and Snieder*, 1996; *Zielhuis and van der Hilst*, 1996; *van der Lee and Nolet*, 1997], and our analysis confirms the efficacy of this type of data in delineating upper-mantle structure.

The data extracted from the direct-phase interval are the frequency-dependent travel times from a diverse assemblage of shear-dominated turning and surface waves. These arrivals include the direct *S* phase and its surface reflection *sS*, the first-orbit surface waves R_1 and G_1, and several dispersed wavegroups that include the surface reflections *SS*, *sSS*, and *SSS*. While the ray-theoretic phase notation supplies convenient designations, it does not really characterize the essential nature of these waves, which are formed through a complex series of interactions with the free surface and upper-mantle discontinuities and are better described as upper-mantle guided waves. In fact, at these distances, the oceanic

Love wave G_1 is itself an interference group comprising the fundamental and several higher modes [*Thatcher and Brune*, 1969; *Gaherty et al.*, 1996].

Unlike the *ScS* reverberations, these arrivals are not very amenable to a ray-theoretic analysis, especially in two and three dimensions. Waves with *P-SV* polarizations are notorious in this respect, but the problem exists even for the waves in the simpler *SH* system. Here interconversions can usually be ignored and the number of relevant ray paths is far less, but the importance of diffraction effects dictates the use of the rather cumbersome apparatus of generalized ray theory [*Gilbert and Helmberger*, 1972; *Helmberger*, 1983]; while methods like the Cagniard-de Hoop technique have been successfully applied in 1D [e.g., *Helmberger and Wiggins*, 1971; *Grand and Helmberger*, 1984], they are difficult to extend to higher dimensions [*Hong and Helmberger*, 1978]. Much work has been done in recent years to treat this problem by devising generalized waveform-analysis and inversion methodologies based on mode summation [e.g., *Lerner-Lam and Jordan*, 1983; *Woodhouse and Dziewonski*, 1984; *Nolet*, 1990; *Li and Tanimoto*, 1993; *Marquering and Snieder*, 1995].

3.2 GSDF Measurements and 2D Fréchet Kernels

The framework for the measurement and interpretation technique summarized in this chapter is the theory of generalized seismological data functional presented by *Gee and Jordan* [1992]. The GSDF technique is particularly suitable for the type of tomography attempted in this study. It is based on observables that arise naturally in matched-filtering analysis, where synthetic waveforms (isolation filters) are cross-correlated with data seismograms. One of these observables, the phase-delay functional $\delta\tau(\omega)$, extends the concept of a differential travel time to a frequency-dependent measure of waveform dispersion (here we drop the subscript from *Gee and Jordan's* [1992] notation, $\delta\tau_p$). In GSDF analysis, the cross-correlation between the isolation filter and the data seismogram is windowed to localize in time and narrow-band filtered to localize in frequency; $\delta\tau(\omega)$ is

measured as the phase shift between this cross-correlagram, which can be approximated as a Gaussian wavelet, and the corresponding Gaussian wavelet from a complete synthetic for the reference model $\mathbf{m}_0$. This phase delay is corrected for the effects of windowing and filtering applied to the cross-correlagrams, as well as for the interference with other wavegroups, by using the procedure described by *Gee and Jordan* [1992]. Figure 3.1 shows some examples of the results obtained from two seismograms recorded on Oahu from two shallow-focus Tonga and Kermadec events. If $\mathbf{m}_0$ is a good starting model—in particular, one that properly represents the discontinuity structure of the mantle—then the isolation filter will be a reasonably good representation of the target wavegroup, and a linearized relationship between $\delta\tau(\omega)$ and the model perturbation $\delta\mathbf{m}$ will be adequate in posing the inverse problem. As emphasized by *Gee and Jordan* [1992], a principal advantage of the GSDF technique is that the linearity of this functional relationship does not require $\delta\tau(\omega)$ to be small compared to the wave period $T = 2\pi / \omega$, which is the requirement in waveform-inversion methods that linearize the relationship between the differential seismogram and $\delta\mathbf{m}$.

In this study, as in previous applications of the GSDF technique [*Gaherty and Jordan*, 1995; *Gaherty et al.*, 1996; *Kato and Jordan*, 1997], complete synthetic seismograms are calculated by summing the normal modes with frequencies less than 50 mHz for a spherically symmetric, radially anisotropic model; all toroidal modes are summed for the transverse components of displacement, and all spheroidal modes for vertical and radial components. The isolation filters are constructed by weighting each mode according to the target arrival's group and phase velocities, as well as its partitioning between compressional and shear energies. The weights obtained in this construction form a set of structure coefficients $\{0 \le \alpha_k \le 1 : k = \text{mode index}\}$ that relate the isolation filter, and hence $\delta\tau(\omega)$, to $\mathbf{m}_0$, and they specify the Fréchet kernel for $\delta\tau(\omega)$ as a sum over the kernels for individual modes [*Gee and Jordan*, 1992]. Examples of these structural factors are shown in Figure 3.2.

The GSDF theory thus yields a general procedure for constructing Fréchet kernels for essentially arbitrary isolation filters in either the *SH* or *P-SV* system, which allows the same measurement technique to be applied to a variety of waveforms on any component of ground motion. In previous applications, the phase delays have been iteratively inverted using 1D kernels to obtain corridor-averaged structures. In this thesis we utilize the 2D kernels for $\delta\tau(\omega)$ calculated by a coupled-mode algorithm that accounts for wave interactions in the vertical source-receiver plane [*Zhao and Jordan*, 1997]. The algorithm is based on first-order normal-mode perturbation theory [*Woodhouse*, 1980, 1983] and the heavy computational labor required for a full implementation of the theory is reduced in two ways. First, following *Li and Tanimoto* [1993], the angular functions are approximated by their asymptotic forms and a stationary-phase integration is performed in the direction transverse to the source-receiver plane, which reduces the kernel from 3D to 2D and decouples the toroidal and spheroidal modes. Second, the coupling matrix is summed only over modes whose structure coefficients α_k are nonzero. (To keep this set as small as possible, we employed cosine tapers in our weighting scheme rather than the Gaussian factors used by *Gee and Jordan* [1992] and *Gaherty et al.* [1996].)

Such kernels properly represent the sampling of Earth structure by the band-limited observations of $\delta\tau(\omega)$ and account for all of the interactions among the various waves that contribute to the target wavegroup. They do not, however, include the effects of perturbations to extraneous phases that interfere with the target wavegroup. In cases where *ScS* interferes with *SS*, for example, the GSDF expressions for the *SS* kernels should include *ScS* contributions, because perturbations to the latter phase by, say, velocity variations in the lowermost mantle, will affect the apparent phase delay of *SS* [*Gee and Jordan*, 1992]. Although this type of effect has been incorporated in the 1D modeling (see Figures 5 and 6 of *Gaherty et al.* [1996] for a clear example), we do not attempt to do so here. The reason is that this interference correction is computationally very intensive, as it involves the interaction with a full synthetic seismogram and therefore the coupling

between the total number of modes within the considered frequency band. Therefore, we have restricted our measurements in Chapters 4 and 5 to cases where the interference by extraneous phases is small.

3.3 SAMPLING PROPERTIES

Zhao and Jordan [1997] have given explicit expressions for 2D Fréchet derivatives of $\delta\tau(\omega)$ with respect to mass density ρ, discontinuity topography h_i, and the five elastic parameters (α_H, α_V, β_H, β_V, η) of a radially anisotropic Earth model. However, the residuals of the shear-dominant phases used here are sensitive mostly to the unknown lateral variations in h_i, β_H, and β_V, and we have thus limited the model perturbations to these quantities for both the Tonga-Hawaii and Ryukyu-Hawaii corridors. This approximation should be especially good for the Tonga-Hawaii corridor, because the residuals have been referenced to the radially anisotropic PA5 model, in which the discontinuity depths and all six volumetric parameters were derived by a nonlinear inversion of data from this particular corridor [*Gaherty et al.*, 1996].

A selection of the Fréchet kernels for the transverse-component data of Figure 3.1c are displayed in Figures 3.3a-e and for the vertical-component data of Figure 3.1d in Figure 3.3f-j. At 40 mHz, the sensitivity of the S_H travel time to β_H is highest near its turning point in the lower mantle where it travels more horizontally (Figure 3.3a), and its sensitivity to β_V is highest near the source and receiver, where it travels more vertically (Figure 3.3b). The S_V travel time is independent of β_H (Figure 3.3f), but its dependence on β_V is complicated (Figure 3.3g). In this particular example, the sP_nS phase arrives in the S window, which introduces a region of positive sensitivity (blue color) above the near-source leg of the S path; i.e., a delay in sP_nS will actually advance the S residual. To see this, consider two narrow-band phases with amplitudes $a_1 > a_2 > 0$ that arrive with a relative phase delay of magnitude

$$|\tau_1 - \tau_2| \approx (2n-1)\pi / \omega << 1/\sigma, \tag{3.1}$$

where ω is the center angular frequency of the pulses, σ is their half-bandwidth and n is an integer; equation (2.3) then shows that the Fréchet kernel of the phase delay for the combined wavegroup is

$$K \approx \frac{a_1 K_1 - a_2 K_2}{a_1 - a_2}. \tag{3.2}$$

In this example, the sP_nS phase is delayed relative to S by 25 s, which at 40 mHz satisfies criterion (3.1) for $n = 1$.

The frequency dependence of the narrow-band phase delays provides considerably more information than a single broad-band travel time. This can be illustrated by the phase delays of a Love wave at low and high frequencies. At 10 mHz, the G_1 group is dominated by the fundamental-mode surface wave with a kernel that averages β_H fairly uniformly over the crust and the top few hundred kilometers of the mantle (Figure 3.3c). At 40 mHz, however, the same group is dominated by the higher modes (Figure 3.2a; see also Figure 12 of *Gaherty et al.* [1996]), and its travel time samples β_H and β_V along a trajectory that cruises through the upper mantle, with one upper turning point at the free surface between two lower turning points at the 410 discontinuity (Figures 3.3d and e). This *SS*-like sensitivity comes from the cross-coupling between the overtone branches [*Li and Tanimoto*, 1993], and it illustrates the limitation of the path-averaging assumption for guided waves.

The along-path sampling by the SS_V wavegroup also varies substantially with its center frequency (Figures 3.3h and i), owing to frequency-dependent interactions with other arrivals such as *sSS*, *SPS*, and *SSP*. At 20 mHz, the negative regions (red colors) outline its character as an *S*-wave surface reflection bottoming at the top of the lower mantle, but the upper mantle above the turning points show a high positive sensitivity (blue colors) not expected from ray theory. Like the ScS_n-ScS_m examples in Figures 2.4c and d, this data functional is particularly sensitive to harmonic variations in upper-mantle structure, in this

case at horizontal wavelengths on the order of $\Delta/2$, rather than $\Delta/3$. The kernel at 40 mHz, on the other hand, fluctuates in a complicated pattern rich with shorter wavelengths. For example, the topography kernel for the 410 has its power concentrated at $\Delta/6$.

Figure 3.3 displays the kernels for only 8 of the 34 data obtained from the two seismograms in Figure 3.1. By combining them with similar measurements from sources at different hypocentral depths and distances, we can obtain a data set with excellent upper-mantle resolution, as documented in Appendices A and B, and in Section 5.6.4.

3.4 Special Examples

The power of the technique can be further illustrated by another example, which shows the complexity of the *P-SV* system at larger epicentral distances. Figure 3.4 shows the transverse and radial components of a seismogram recorded on Oahu from a shallow-focus Ryukyu event ($\Delta = 73°$), with the full synthetics and the isolation filters for the S_H and S_V wavegroups. While the S_H wavegroup shows a simple waveform, the S_V is followed by a large-amplitude wave train that appears both in the data and in the synthetics. This large-amplitude arrival, which is predicted by the 1D reference model, is associated with *P* to *S* and *S* to *P* conversions near the source and receiver sides, respectively, with possible contribution from shear-coupled *PL* waves (*SPL*). The latter is excited by *P-SV* guided waves near the source area that consequently leak into the mantle as S_V waves; these S_V waves propagate back towards the surface and interact with the receiver area [*Baag and Langston*, 1985]. These complex wave phenomena are naturally included in our analysis as seen by the Fréchet kernels in Figures 3.5a-c. At 35 mHz, the sensitivity of the S_H travel time to the average shear velocity β, where $\beta = (\beta_H + \beta_V)/2$, is high along the geometrical ray path for the direct *S* wave (Figure 3.5a), as expected. More complicate however, is the dependence of the S_V travel time on β, which is high along the shear-wave trajectory of the P_nS and SP_n arrivals (Figure 3.5b). In the uppermost mantle, near the source and the receiver, this travel time is mostly sensitive to the average compressional

velocity α (Figure 3.5c), where $\alpha = (\alpha_H + \alpha_V)/2$. Moreover, in order to obtain a good isolation filter for the S_V wavegroup in Figure 3.4, we were forced to center the phase-velocity window around a smaller value (Figure 3.6b) relative to that of the S_H (Figure 3.6a), which also explains the shallower turning depth in Figure 3.5b.

The GSDF technique is actually not limited to surface and turning wave, and can be used to synthesize reflected waves such as, for example, *ScS* arrivals. Figure 3.5d shows the Fréchet kernel for a broad-band ScS_1 travel time, measured on the radial component of a seismogram recorded at Taiwan from an Izu-Bonin event (Δ = 16°; seismogram is not shown). This kernel, which displays high sensitivity along the ScS_1 geometrical ray, is obtained by incorporating the appropriate group- and phase-velocity windows into the same analysis code. In this case, the contribution to the isolation filter and the kernel is primarily from the *ScS* modes (Figure 3.6c), which also include energy of multiply-reflected ScS_n. with $n > 1$. Nevertheless, the kernel for ScS_1 is not contaminated by other ScS_n arrivals, because it is calculated in a time window around the former [*Zhao and Jordan*, 1997], where the contributions from the later-arriving ScS_n are negligible. In Chapter 5, we employed the GSDF technique to analyze the *ScS* arrivals on 4 radial-component seismograms with particularly high snr, where the transverse-components were noisy.

FIGURE CAPTIONS

Figure 3.1. An example of the GSDF processing. (a) and (b) Transverse- and vertical-component seismograms recorded at HON from two shallow-focus Tonga (h = 19 km, Δ = 44°) and Kermadec (h = 54 km, Δ = 54°) events, respectively. Shown are the observed seismogram and the synthetic isolation filters for S_H and G_1 in Figure 3.1a, and for S_V, SS_V, and R_1 in Figure 3.1b. Time scale is relative to the origin time. The traces are all low-passed filter with a 45-mHz corner. (c) and (d) Frequency-dependent travel times relative to the PA5/PREM reference model, measured from the seismograms in Figures 3.1a and b, respectively, by the GSDF processing described in the text. The travel-times measurements are shown at 5-mHz intervals for S_H and S_V (circles), SS_V (squares), and G_1 and R_1 (triangles). Examples of 2D Fréchet kernel for some of these measurements are shown in Figure 3.3.

Figure 3.2. Top two panels are toroidal-mode dispersion diagrams for PA5/PREM showing the weighting factors in the partial normal-mode summation for the isolation filter of (a) the G_1 and (b) the S_H waves in Figure 3.1a. (c) Spheroidal-mode dispersion diagram for PA5/PREM showing the weighting factors in the partial normal-mode summation for the isolation filter of the S_V wave in Figure 3.1b. The sizes of the open circles are proportional to the values of the weighting factors for the corresponding modes. The four straight diagonal lines in Figures 3.2a and 3.2b correspond to the ray parameter values at which the S wave grazes, counter-clockwise from the right, the Moho, the 410 and 660 discontinuities, and the CMB, respectively. The five lines in Figure 3.2c include, also, the ray parameter at which the P wave grazes the 410 discontinuity (fourth straight diagonal line, counter-clockwise from the right). The branch numbers n = 0, 10, 20, 30 and 40 are indicated at the top of each diagram. Note that the isolation filter for the G_1 wavegroup in Figure 3.1a is dominated by the fundamental-mode brunch only at low

frequencies, while at high frequencies, it includes contributions from higher modes corresponding to S waves which graze around and above the 410 discontinuity. Note also the complicated structure of the partial normal-mode summation for the S_V wavegroup. These features are discussed in the text and are reflected in Figure 3.3.

Figure 3.3. (a)-(e) and (f)-(j) Examples of 2D Fréchet kernel computed by coupled-mode summation for some of the measurements in Figures 3.1c and 3.1d, respectively. The wave type, frequency, and velocity type (β_H for horizontal and β_V for vertical shear velocity) are indicated at the top of each panel. Warm colors correspond to negative sensitivity (phase-delay increase for velocity decrease), cool colors to positive sensitivity, and the green lines show the sensitivity to perturbations in the depths of 410 and 660 discontinuities (with twice the vertical exaggeration as that in Figure 2.4); yellow circle and blue triangle show the locations of the source and receiver, respectively. See text for discussion of these kernels.

Figure 3.4. comparison between transverse- and radial-component S waves for a seismogram recorded at HON from a shallow-focus Ryukyu event (h = 15 km, $\Delta = 73°$). The top three traces are the transverse component of the data and the synthetic seismograms, and the isolation filter for S_H. The bottom three traces are the radial component of the data and the synthetic seismograms and the isolation filter for S_V All traces are low-passed with a 45-mHz corner. ScS_1 which arrives shortly after the S_H can be observed on the transverse component; also note that the S_V. wavegroup is more complicated than the S_H and contains later arrivals. The sensitivity of these arrivals to shear and compressional velocity is shown in Figure 3.5a-c

Figure 3.5. Fréchet kernel computed by coupled-mode summation. The wave type, frequency, and velocity type (β for average shear velocity and α for average

compressional velocity) are indicated at the top of each panel. The kernels in Figure 3.5a-c are associated with the isolation filters in Figure 3.4. The ScS_1 kernel in Figure 3.5d was computes for a wider frequency band, with corners at 5 and 45 mHz. The gray colors correspond to negative sensitivity (phase-delay increase for velocity decrease; these kernels show no positive sensitivity). The perturbations to the radii of the 410 and 660 discontinuities are shown as solid line relative to the reference radii (dashed line; vertical exaggeration is the same as in Figure 3.3); white circle and black triangle show the locations of the source and receiver, respectively.

Figure 3.6. Toroidal-mode dispersion diagram (top panel) and two spheroidal-mode diagrams (bottom two panels), that are plotted in the same way as those in Figure 3.2, showing the weighting factors in the partial normal-mode summation for the isolation filter of (a) the S_H and (b) the S_V wavegroups in Figure 3.4a, and (c) an ScS_1 wavegroup. Note that the modes contributing to the S_V wavegroup are centered over a lower value of phase velocity (or higher ray parameter) relative to that of the S_H. Note also that only ScS modes are contributing to the ScS_1 isolation filter.

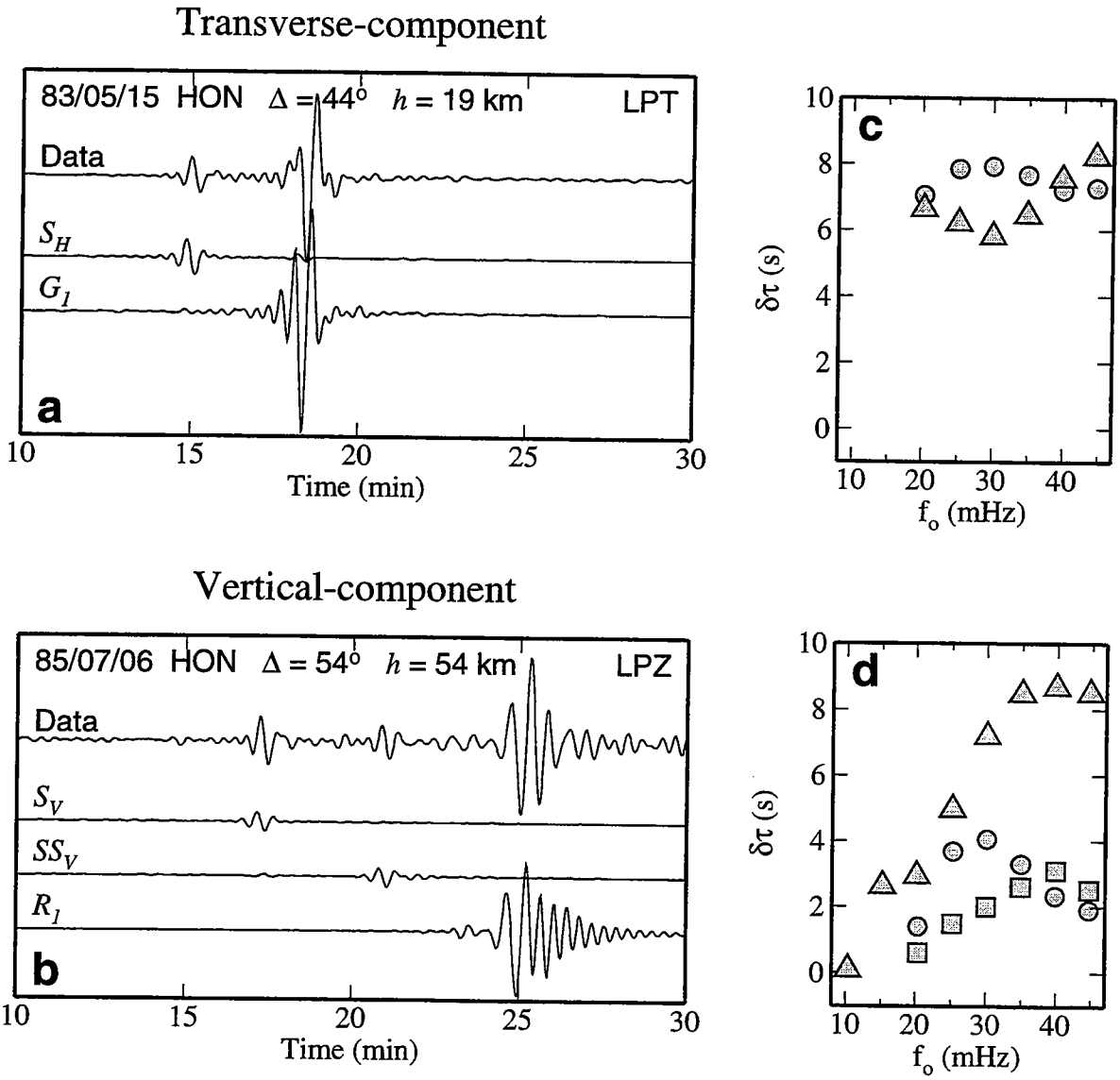
Transverse-component
83/05/15 HON Δ = 44° h = 19 km
LPT
Data
S_H
G_1
a
10
15
20
25
30
Time (min)
c
δτ (s)
f$_o$ (mHz)
Vertical-component
85/07/06 HON Δ = 54° h = 54 km
LPZ
Data
S_V
SS_V
R_1
b
Time (min)
d
δτ (s)
f$_o$ (mHz)

Figure 3.1

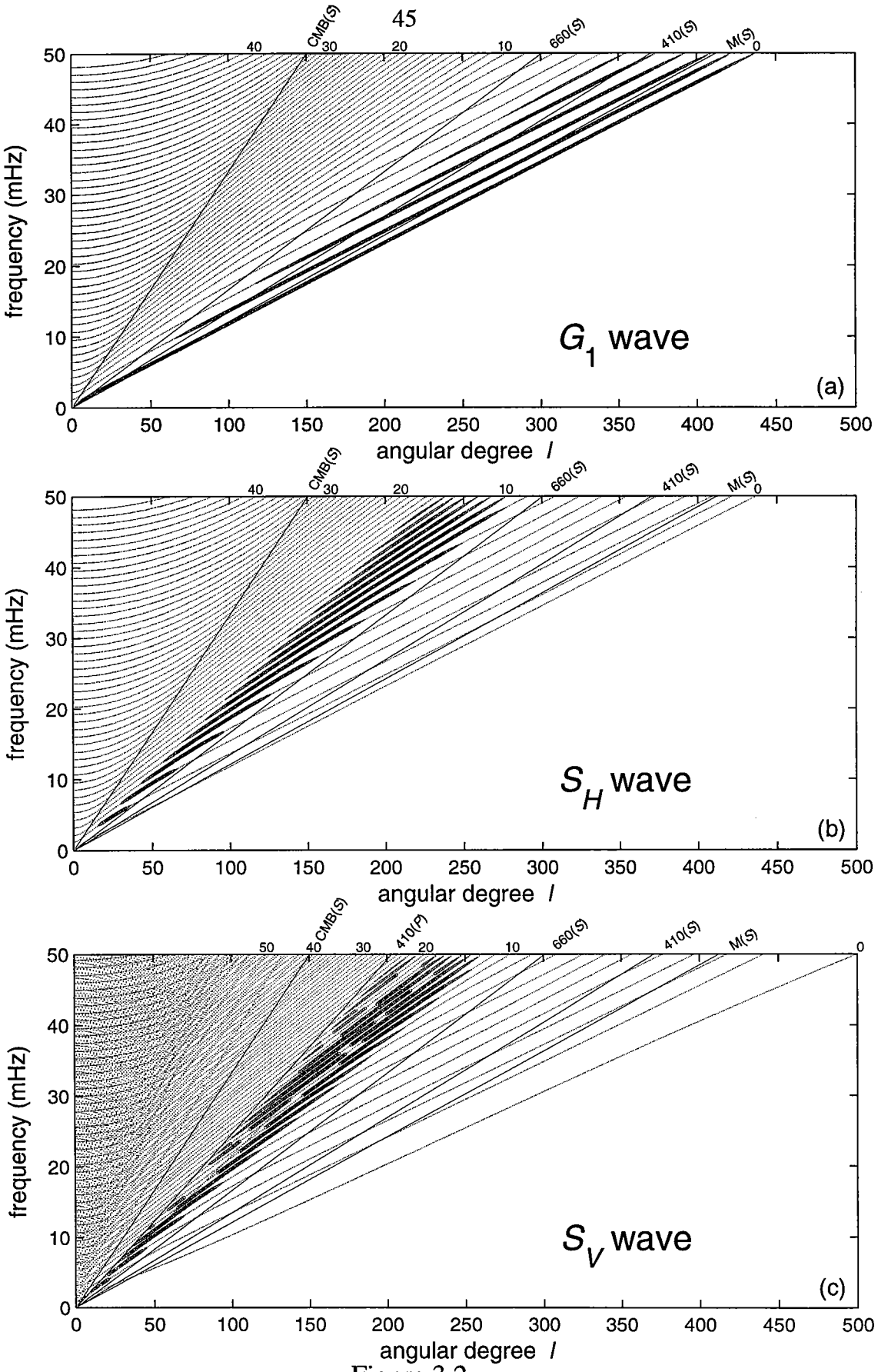
CMB(S)
660(S)
410(S)
M(S)
410(P)
frequency (mHz)
angular degree l
G_1 wave
S_H wave
S_V wave
(a)
(b)
(c)

Figure 3.2

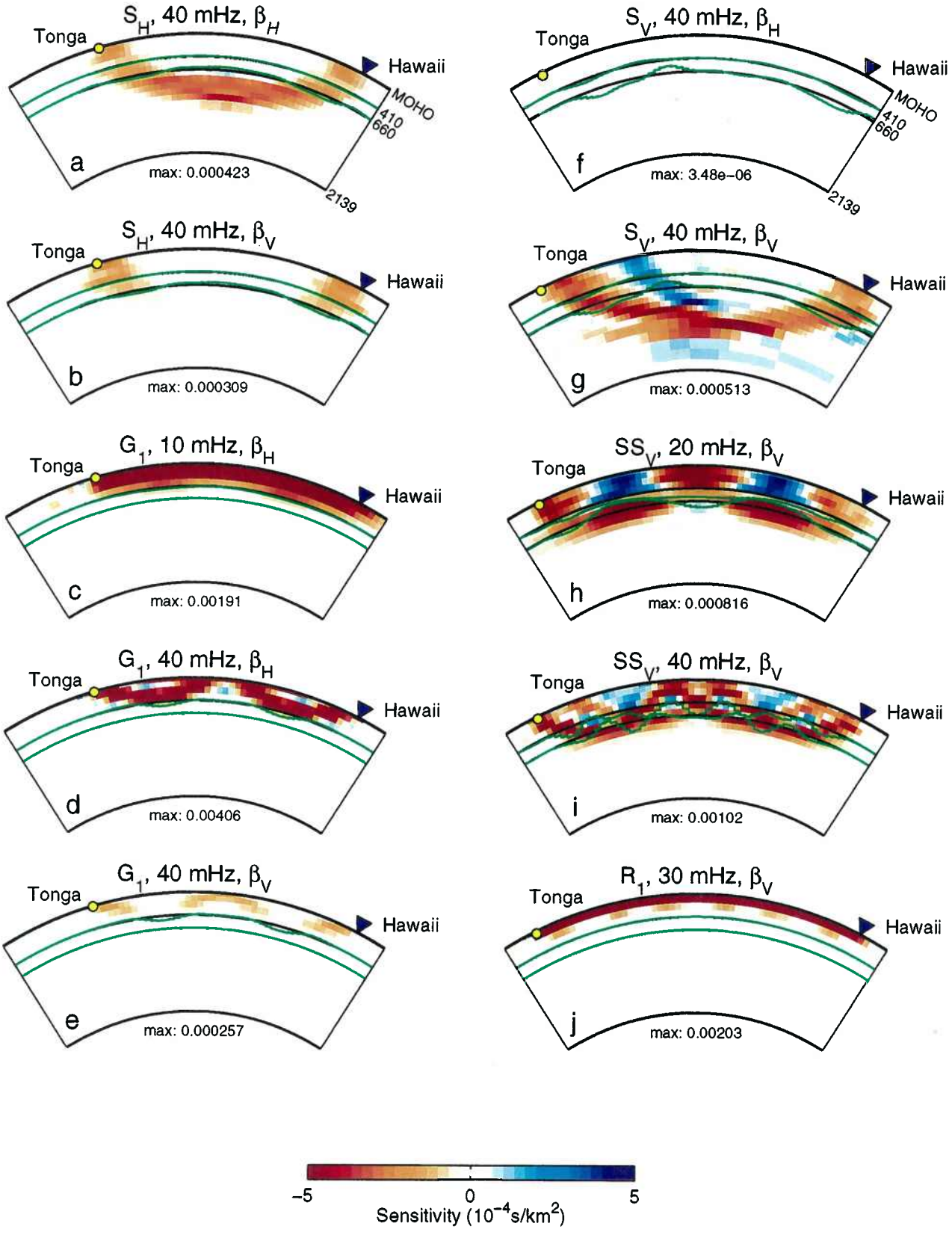
S_H, 40 mHz, β_H
Tonga
Hawaii
MOHO
410
660
2139
a
max: 0.000423
S_V, 40 mHz, β_H
f
max: 3.48e−06
S_H, 40 mHz, β_V
b
max: 0.000309
S_V, 40 mHz, β_V
g
max: 0.000513
G_1, 10 mHz, β_H
c
max: 0.00191
SS_V, 20 mHz, β_V
h
max: 0.000816
G_1, 40 mHz, β_H
d
max: 0.00406
SS_V, 40 mHz, β_V
i
max: 0.00102
G_1, 40 mHz, β_V
e
max: 0.000257
R_1, 30 mHz, β_V
j
max: 0.00203
−5
0
5
Sensitivity (10^{-4}s/km^2)

Figure 3.3

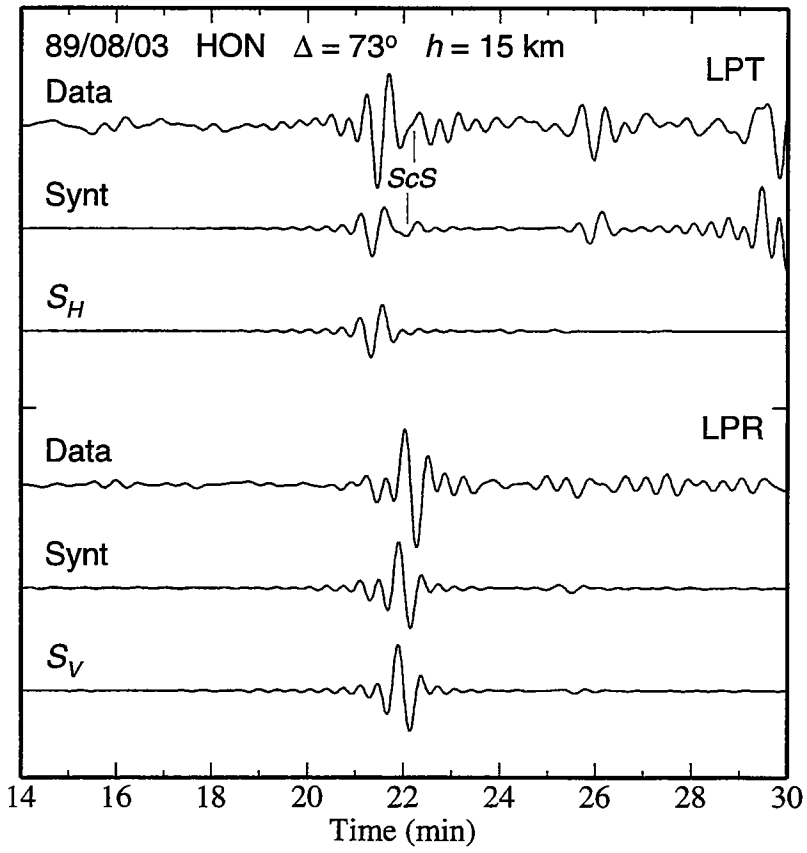
89/08/03 HON Δ = 73° h = 15 km
LPT
Data
ScS
Synt
S_H
LPR
Data
Synt
S_V
14
16
18
20
22
24
26
28
30
Time (min)

Figure 3.4

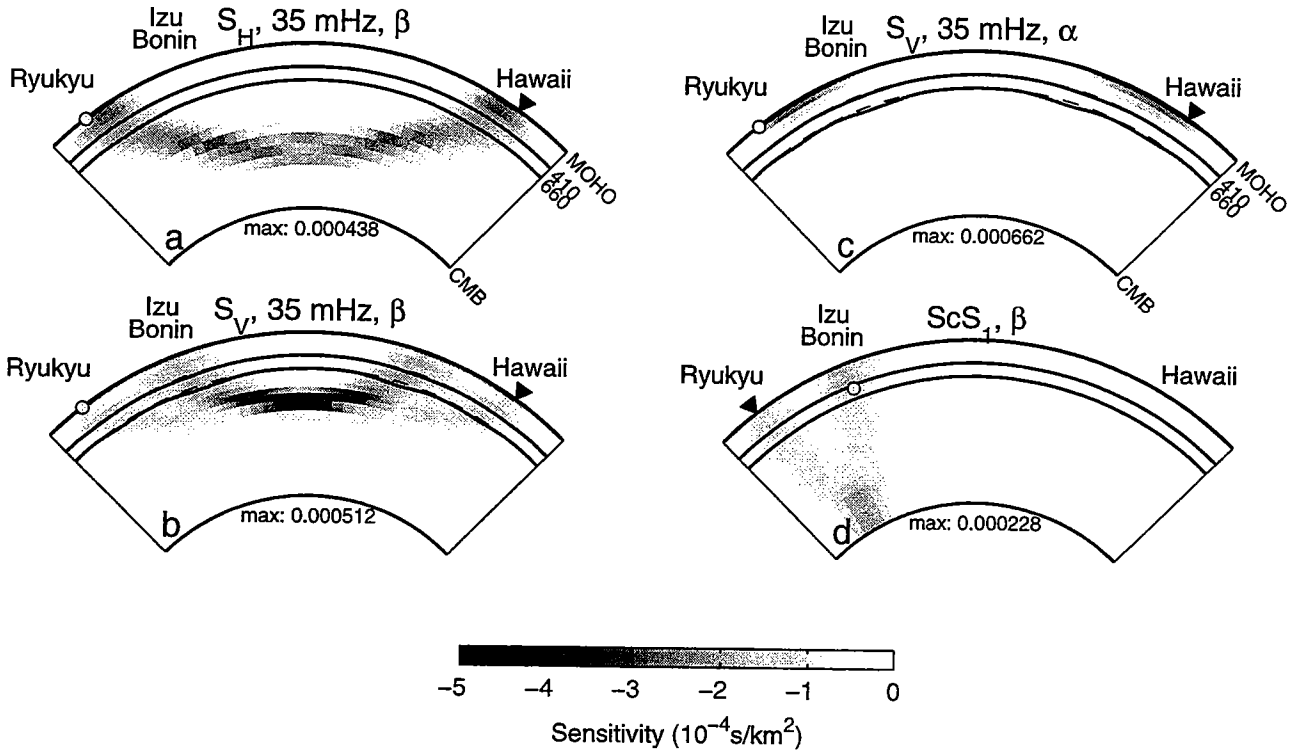
Izu
Bonin
S_H, 35 mHz, β
Ryukyu
Hawaii
MOHO
410
660
a
max: 0.000438
CMB
Izu
Bonin
S_V, 35 mHz, α
Ryukyu
Hawaii
MOHO
410
660
c
max: 0.000662
CMB
Izu
Bonin
S_V, 35 mHz, β
Ryukyu
Hawaii
b
max: 0.000512
Izu
Bonin
ScS_1, β
Ryukyu
Hawaii
d
max: 0.000228
−5
−4
−3
−2
−1
0
Sensitivity (10^{-4}s/km^2)

Figure 3.5

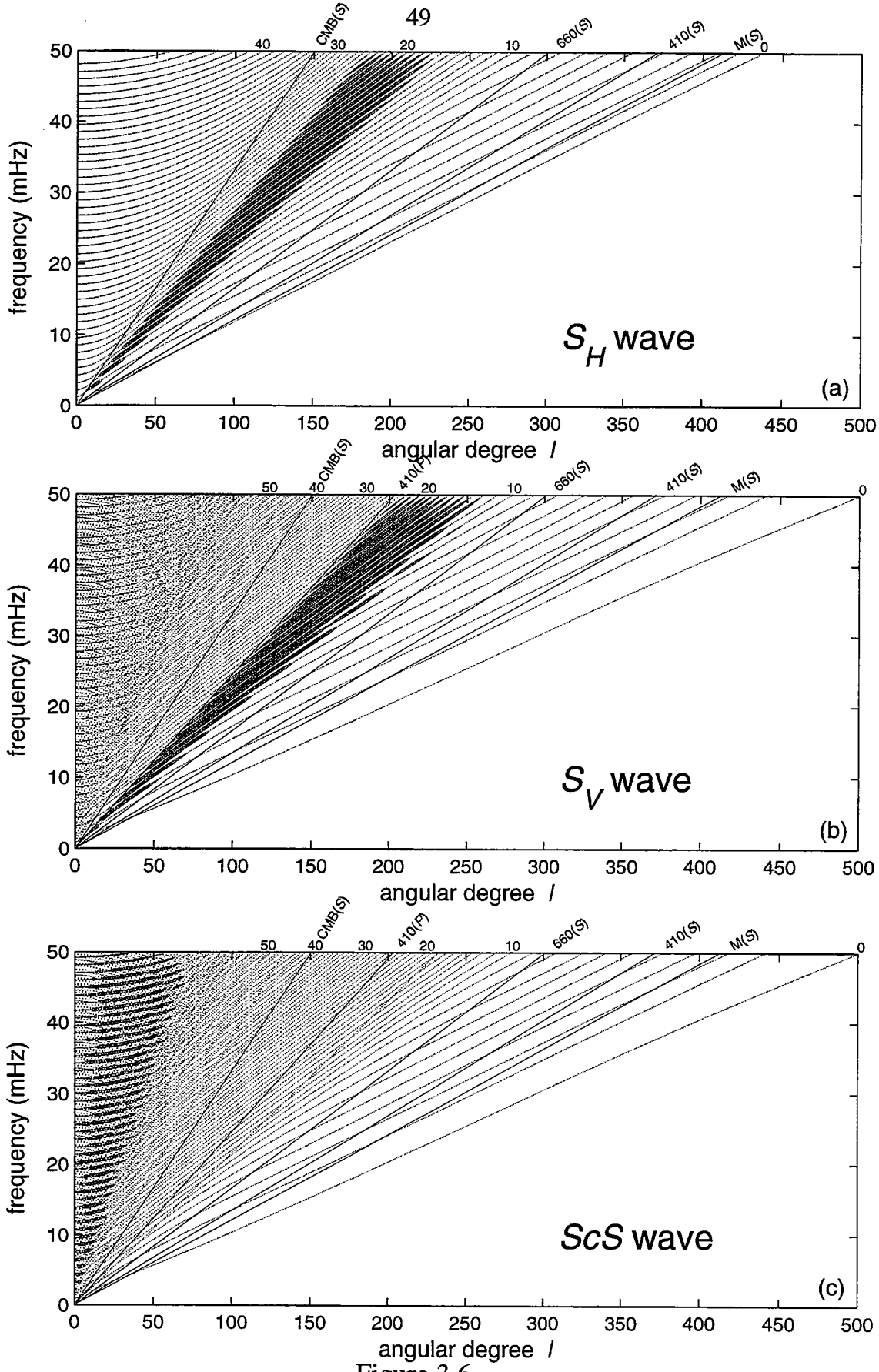
CMB(S)
660(S)
410(S)
M(S)
410(P)
frequency (mHz)
angular degree l
S_H wave
(a)
S_V wave
(b)
ScS wave
(c)

Figure 3.6

CHAPTER 4

THE TONGA-HAWAII CORRIDOR

4.1 INTRODUCTION

The corridor between the Tonga-Kermadec subduction zone and the Global Seismic Network (GSN) stations KIP and HON on the island of Oahu, Hawaii, was chosen for several reasons. It traverses the central Pacific Ocean nearly perpendicular to the plate motion across a series of island chains and ocean plateaus in a region of nearly uniform (100-125 Ma) crustal age (Figure 4.1). The intense seismicity of the Tonga arc provides a dense array of large earthquakes extending to depths exceeding 600 km that write beautiful seismograms at Oahu, with high amplitude direct phases and well excited ScS reverberations. The quality of these records has made this corridor a target for many previous studies [*Jordan and Sipkin*, 1977; *Sipkin and Jordan*, 1979; *Revenaugh and Jordan*, 1987], and much is known about its radial structure. In particular, *Gaherty et al.* [1996] have recently inverted the reflectivity results of *Revenaugh and Jordan* [1991a-c] together with a large set of frequency-dependent travel times from GSDF analysis for a radially anisotropic, 1D model, PA5 (Figure 4.2).

PA5 is notable because all of its discontinuities are confined by measurements of shear-wave reflection travel times and impedance contrasts, and the gradients between discontinuities are constrained by turning-wave data. Its features include a shallow G discontinuity (lid/low-velocity zone boundary) at 68 km; shear anisotropy of 2-3% extending to 166 km, where the average shear speed reaches its minimum value of 4.26 km/s; a steep gradient to the discontinuity at 415 km; a small discontinuity at 507 km; and a large lower-mantle discontinuity at 651 km (see *Gaherty et al.* [1997] for comparisons with other regions and a discussion of the structural implications). Because it is based on the

(nonlinear) inversion of the same types of data considered here, PA5 is the ideal upper-mantle reference model for the tomographic inversions presented here.

In this Chapter we jointly invert 1122 frequency-dependent travel times of turning and surface waves together with 304 *ScS*-reverberations travel times for the 2D structure in the vertical plan of the Tonga-Hawaii corridor. We describe the inversion procedure, which uses a complete Gaussian-Bayesian approach [*Tarantola and Valette*, 1982] and handles the model biases associated with errors in earthquake origin times and depths. We then construct a vertical tomogram through the mantle for this corridor, which is substantiated by a series of data-based inversions, resolution tests, and resolving power calculations Finally, we discuss the geodynamical implications for the central Pacific upper mantle.

4.2 Lateral Heterogeneity Between Tonga and Hawaii

The most compelling motivation for the study of this particular region is the prima facie evidence for along-path heterogeneity observed in the ScS_n-ScS_m differential travel times (Figure 4.3). Their residuals relative to the PA5/PREM reference model are very large and systematic, with a range of about 8 s, and cannot be explained by near-source or near-receiver structure. This high, along-path variability was first observed by *Sipkin and Jordan* [1980a], who speculated that it might be diagnostic of small-scale, upper-mantle convection rolls oriented by plate motion, as proposed by *Richter* [1973] and *Richter and Parsons* [1975] (Figure 4.4). *Gee and Romanowicz* [1992] collected more data that revealed the strong, nearly linear gradients of the residuals with epicentral distance evident in Figure 4.3, and they also argued that these data require significant along-path structure, presumably in the upper mantle. The magnitude of variation in two-way travel time in this part of the Pacific is almost as large as, for example, the ScS_2-ScS differences observed across the major tectonic transition from the Tertiary Arctic Ocean basin to the Precambrian Siberian craton [cf. *Sipkin and Jordan*, 1976, Figure 14]. Hence, despite its apparent tectonic uniformity, the central-Pacific mantle is strongly heterogeneous.

Because they used only vertically propagating ScS_n waves, neither of the earlier studies by *Sipkin and Jordan* [1980a] and *Gee and Romanowicz* [1992] was able to demonstrate conclusively that the locus of the heterogeneity was in the upper mantle. Global tomographic models, as well as higher-resolution regional studies of the Pacific upper mantle [*Zhang and Tanimoto*, 1989], have thus far revealed no indications of structural variations in the upper mantle with the magnitude and scale needed to explain the data in Figure 4.3. Evidence has also accumulated for significant heterogeneity in the D" layer at the base of the mantle beneath this region [*Dziewonski et al.*, 1996; *Garnero and Helmberger*, 1996; *Wysession*, 1996], raising the possibility of a deep-mantle origin. However, based on the work of *Katzman et al.* 1997a,b which is presented here, it appears that the residuals in Figure 4.3 are an expression of small-scale (~1500-km wavelength) heterogeneities several percent in amplitude located within the upper mantle and transition zone.

4.3 SCS-REVERBERATION DATA FOR THE TONGA-HAWAII CORRIDOR

We used the procedure described in section 2.2 to measure the travel times of zeroth- and first-order reverberations on transverse-component seismograms from 27 earthquakes in the Tonga-Fiji seismic zone recorded at KIP or HON during the period 1973-1993, and one shallow-focus Hawaiian earthquake (26 April 1973) recorded at KIP (Figure 4.1, Table 4.1). The Tonga-Fiji events were moderate in magnitude ($5.7 \leq M_W \leq 7.2$) with hypocentral depths ranging from 48 to 614 km and epicentral distances of 40° to 54°. For the older events (1973-1976), the focal mechanisms were taken from *Richter* [1979] and *Butler* [1982]; all the subsequent events had a well-determined CMT solutions in the Harvard catalog. The horizontal components with a 1-s sampling interval were rotated, and the transverse components were deconvolved using a damped-least-squares algorithm. This was followed by a zero-phase filtering around a center frequency of 25 mHz (Hanning taper with corner at 40 mHz and maximum frequency of passband at 60 mHz). We kept

only the records with a good signal-to-noise ratio (snr) that showed well-excited reverberation phases from the 410 and/or 660 discontinuities. Figure 4.5 shows some of these records compared with synthetic seismograms.

Table 4.2 displays the distribution of the 304 reverberation times obtained along this corridor, classified according to source depth, core-reflection number (mostly between 2 and 4 at these epicentral distances), and the concatenation scheme used in constructing the isolation filters (Section 2.2). With the exception of the Hawaiian event, this data set is identical to that used in our preliminary study [*Katzman et al.*, 1997a]. When normalized to a two-way lower-mantle path, the Tonga-Hawaii times have an average delay relative to the PA5/PREM reference model of about +4 s, which agrees with global tomographic studies that find an anomalously slow lower mantle in this part of the central Pacific [*Su et al.*, 1994; *Dziewonski et al.*, 1996; *Masters et al.*, 1996].

More interesting, however, is the steep gradient in ScS_3-ScS_2 and ScS_4-ScS_3 differential times with epicentral distance displayed in Figure 4.3. As discussed above, these times require substantial lateral heterogeneity within the mantle of the Tonga-Hawaii corridor. We also note that the mean value of ScS_n-ScS_m residual for the 1973 Hawaiian earthquake ($\Delta = 3°$) is –0.2 s relative the reference model, indicating that the average shear velocity of the sub-Hawaiian mantle is significantly higher than along the Tonga-Hawaii corridor. This is consistent with the ScS_n-ScS_m travel times observed by *Sipkin and Jordan* [1980b], who also analyzed the amplitudes ScS_n phases from the 1973 earthquake to show that the sub-Hawaiian mantle was less attenuating than the region between Tonga and Hawaii.

4.4 Surface- and Turning-Wave Data for the Tonga-Hawaii Corridor

The data set for the turning and surface waves comprised 1122 frequency-dependent phase delays from 179 waveforms on 115 long-period seismograms (49 vertical, 15 radial, and 51 transverse components). The seismograms were recorded at either KIP or HON

from 63 Tonga-Fiji earthquakes at epicentral distances ranging from 39° to 57° and focal depths from 10 to 663 km (Figure 4.1, Table 4.3). The earthquakes were of moderate size ($5.9 \leq M_W \leq 7.2$) with well-determined Harvard CMT solutions. Many of the seismograms were analyzed previously in the 1D study by *Gaherty et al.* [1996], and a number of the transverse components were the source of the data for the *ScS*-reverberations data (Table 4.1). The same measurements were used in our preliminary 2D study of this corridor [*Katzman et al.*, 1997a]

Prior to measurement, the data seismograms and their corresponding synthetics were low-passed with a zero-phase filter having a corner frequency of 45 mHz. Isolation filters were constructed for candidate wavegroups, and the data were downgraded or eliminated if the agreement was poor either because of low snr or interference by phases not included in the isolation filter (e.g. *ScS*). The isolation filters were cross-correlated with the data seismograms, and the resulting time series were windowed and filtered in 5-mHz bands between 10 and 45 mHz. The phase delays recovered by fitting Gaussian wavelets to the narrow-band cross-correlagrams were corrected for windowing and filtering effects and interference with other wavegroups using the procedures discussed by *Gee and Jordan* [1992]. Table 4.4 summarizes the data distribution by wave type, and Figures 3.1 and 4.6 displays some examples of the seismograms, isolation filters, and travel-time measurements that were obtained for this corridor.

4.5. INVERSION

The *ScS*-reverberation times and frequency-dependent phase delays have been inverted for the 2D structure in the vertical plane of the Tonga-Hawaii corridor using the model parameterization and the linear Gaussian-Bayesian inversion scheme described in this section.

4.5.1 Parameterization

The along-path structure was represented by a perturbation vector $\delta\mathbf{m}$ to the PA5/PREM reference model $\mathbf{m}_0$ of dimension M =1375. it was organized into three parts:

(1) 985 blocks representing the relative variations in isotropic shear velocity, $\delta\beta/\beta_0$, over the entire length of the corridor (65°) and depth of the mantle (2890 km). Blocks with a lateral dimension of 1° and an average vertical dimension of about 110 km were used in 4 layers above the 410 discontinuity, 2 in the transition zone, and 5 in the lower mantle from 651 to 1200 km (715 blocks total). Below 1200 km, where the data resolution was substantially lower, we coarsened the grid to 9 layers of 30 blocks each (~2.2° × 250-km) extending to the core-mantle boundary. The grid is depicted in Figure 4.7a.

(2) 260 blocks representing the relative variations in shear-velocity anisotropy, $(\delta\beta_H - \delta\beta_V)/\beta_0$, in the 4 upper-mantle layers above the 410 discontinuity; here $\delta\beta_H$ and $\delta\beta_V$ are the perturbations to the radially anisotropic shear velocities in PA5, $(\beta_H)_0$ and $(\beta_V)_0$, and β_0 is the average $[(\beta_H)_0 + (\beta_V)_0]/2$.

(3) Two sets of 65 segments representing the topographic variations, δr_{410} and δr_{660}, for the two major transition-zone discontinuities.

The perturbation was assumed to satisfy the linear system

$$\mathbf{A}\,\delta\mathbf{m} + \mathbf{B}\,\delta\mathbf{n} + \mathbf{e} = \delta\mathbf{d}, \tag{4.1}$$

where $\delta\mathbf{d}$ is the data-residual vector of dimension $D = 1426$ (1122 frequency-dependent phase delays and 304 *ScS*-reverberation times). $\mathbf{A}$ is the $D \times M$ partial-derivative matrix,

whose general element A_{ij} is the integral over the jth model cell of the Fréchet kernels for the ith datum, calculated for $\mathbf{m}_0$. The data-error vector $\mathbf{e}$ is assumed to have a zero mean, $\langle \mathbf{e} \rangle = \mathbf{0}$, and a diagonal covariance matrix, $\mathbf{C_{ee}} = \langle \mathbf{e}\mathbf{e}^{\mathbf{T}} \rangle = \mathrm{diag}[\sigma_1^2, \sigma_2^2, \ldots, \sigma_D^2]$. The vector $\delta\mathbf{n}$ comprises the "nuisance parameters"; i.e., unknown quantities not contained in the model that could possibly contaminate the data, such as source statics. In this study, $\delta\mathbf{n}$ contained only two types of source parameters: a perturbation to the centroid time for each earthquake, and an apparent shift in centroid depths for each *ScS*-reverberation seismogram.

4.5.2 Bayesian Inversion with "Exact Denuisancing" of Source Parameters

For the 2D inversions considered here, the dimension of the linear system (4.1) is sufficiently small that we could afford to invert the data and evaluate the resulting model using a complete Bayesian methodology [*Tarantola and Valette*, 1982; *Tarantola*, 1987]. The difference between the actual Earth structure and the 1D reference model $\mathbf{m}_0$ was represented as a realization of an a priori Gaussian probability density function with expectation $\delta\overline{\mathbf{m}}$ and a positive-definite covariance matrix $\overline{\mathbf{C}}_{\mathbf{mm}}$. The prior model, $\overline{\mathbf{m}} = \mathbf{m}_0 + \delta\overline{\mathbf{m}}$, was taken to be the path-averaged structure, obtained by inverting the data for a 1D, depth-dependent perturbation. The prior covariance, $\overline{\mathbf{C}}_{\mathbf{mm}}$, was specified according to the amplitude, smoothness, and correlation criteria discussed in the next section. The nuisance-parameter vector was assumed to have zero expectation and prior covariance $\overline{\mathbf{C}}_{\mathbf{nn}}$. In this Gaussian case, the Bayesian estimates minimize the quadratic form

$$\begin{aligned} \varepsilon^2 \;=\; & \left(\delta\mathbf{d} - \mathbf{A}\delta\mathbf{m} - \mathbf{B}\delta\mathbf{n}\right)^{\mathrm{T}} \mathbf{C}_{\mathbf{ee}}^{-1} \left(\delta\mathbf{d} - \mathbf{A}\delta\mathbf{m} - \mathbf{B}\delta\mathbf{n}\right) \\ & + \left(\delta\mathbf{m} - \delta\overline{\mathbf{m}}\right)^{\mathrm{T}} \overline{\mathbf{C}}_{\mathbf{mm}}^{-1} \left(\delta\mathbf{m} - \delta\overline{\mathbf{m}}\right) + \delta\mathbf{n}^{\mathrm{T}} \overline{\mathbf{C}}_{\mathbf{nn}}^{-1} \delta\mathbf{n}. \end{aligned} \tag{4.2}$$

The expressions can be simplified by normalizing the fixed quantities in (4.2) by the standard-deviation matrix for the data, $\delta\mathbf{d}' = \mathbf{C}_{\mathbf{ee}}^{-1/2}\,\delta\mathbf{d}$, $\mathbf{A}' = \mathbf{C}_{\mathbf{ee}}^{-1/2}\,\mathbf{A}$, $\mathbf{B}' = \mathbf{C}_{\mathbf{ee}}^{-1/2}\,\mathbf{B}$. In this notation, the posterior estimate of the model perturbation becomes

$$\delta\mathbf{m} = \delta\overline{\mathbf{m}} + \left(\mathbf{A'}^{\mathrm{T}}\mathbf{Q_B}\mathbf{A'} + \overline{\mathbf{C}}_{\mathbf{mm}}^{-1}\right)^{-1}\mathbf{A'}^{\mathrm{T}}\mathbf{Q_B}\left(\delta\mathbf{d'} - \mathbf{A'}\,\delta\overline{\mathbf{m}}\right), \tag{4.3}$$

where

$$\mathbf{Q_B} = \mathbf{I} - \mathbf{B'}\left(\mathbf{B'}^{\mathrm{T}}\mathbf{B'} + \overline{\mathbf{C}}_{\mathbf{nn}}^{-1}\right)^{-1}\mathbf{B'}^{\mathrm{T}}. \tag{4.4}$$

To avoid any over-interpretation of the data, we assumed total prior ignorance of the source parameters contained in $\delta\mathbf{n}$. In this limiting case ('exact denuisancing'), $\overline{\mathbf{C}}_{\mathbf{nn}} \to \infty$ and $\mathbf{Q_B} \to \mathbf{I} - \mathbf{B'}(\mathbf{B'}^{\mathrm{T}}\mathbf{B'})^{-1}\mathbf{B'}^{\mathrm{T}}$, the projection operator onto the null space of $\mathbf{B'}^{\mathrm{T}}$ (i.e., $\mathbf{Q_B}\mathbf{B'} = \mathbf{0}$ and $\mathbf{Q_B}\mathbf{Q_B} = \mathbf{Q_B}$). In terms of the transformed partial-derivative matrix $\mathbf{A''} = \mathbf{Q_B}\mathbf{A'}$ and data vector $\delta\mathbf{d''} = \mathbf{Q_B}\,\delta\mathbf{d'}$, the estimate becomes

$$\delta\mathbf{m} = \delta\overline{\mathbf{m}} + \left(\mathbf{A''}^{\mathrm{T}}\mathbf{A''} + \overline{\mathbf{C}}_{\mathbf{mm}}^{-1}\right)^{-1}\mathbf{A''}^{\mathrm{T}}\left(\delta\mathbf{d''} - \mathbf{A''}\delta\overline{\mathbf{m}}\right). \tag{4.5}$$

This projection completely removes any constraints on the Earth structure that could otherwise be explained by adjusting the source parameters [*Pavlis and Booker*, 1980; *Spencer and Gubbins*, 1980].

The posterior covariance of the model estimate can be written

$$\mathbf{C_{mm}} = \left(\mathbf{A''}^{\mathrm{T}}\mathbf{A''} + \overline{\mathbf{C}}_{\mathbf{mm}}^{-1}\right)^{-1}. \tag{4.6}$$

The diagonal elements of this matrix, $C_{mm}(i,i)$, give the posterior marginal variances of the model parameters, and the off-diagonal terms specify the posterior correlations between the ith and the jth parameters:

$$\rho(i,j) = \frac{C_{mm}(i,j)}{\sqrt{C_{mm}(i,i)C_{mm}(j,j)}}. \tag{4.7}$$

A strong posterior correlation ($\rho(i,j) \to 1$) or anticorrelation ($\tilde{\rho}(i,j) \to -1$) implies that the two parameters cannot be resolved independently by the data [*Tarantola*, 1987]. In

general, a particular parameter is well resolved by the data if its variance reduction is large. For any direction $\hat{\mathbf{m}}$ in the model space, the variance reduction is

$$R(\hat{\mathbf{m}}) = \mathbf{I} - \left(\hat{\mathbf{m}}^{\mathrm{T}}\mathbf{C}_{\mathrm{mm}}\,\hat{\mathbf{m}}\right)\Big/\left(\hat{\mathbf{m}}^{\mathrm{T}}\overline{\mathbf{C}}_{\mathrm{mm}}\,\hat{\mathbf{m}}\right) \tag{4.8}$$

$R(\hat{\mathbf{m}})$ will be larger in directions where the data information dominates over the prior information. Equations (4.6)-(4.8) were used in the error analysis discussed in Appendix B.

4.6 VERTICAL TOMOGRAMS

4.6.1 Specification of the Correlation Matrices

The standard deviations of the travel-time residuals, $\{\sigma_i\}$, varied from 1 s for high-quality observations to more than 8 s for low-quality observations. These errors were assigned according to the snr on the raw seismogram (including unmodeled interference with other phases), and the center frequency and bandwidth of the observation (low-frequency, narrow-band times being less precise, especially for the direct turning waves). They were calibrated by comparing the same types of observations from sources having nearby hypocenters. The procedures taken to insure the data quality included careful choice of the time windows, remeasurement of large outliers, and rejection of any observation judged to have substandard quality; consequently, over 50% of the 1426 times have standard deviations of less than 2 s.

The prior covariance matrix $\overline{\mathbf{C}}_{\mathrm{mm}}$ was specified in terms of the prior standard deviations $\overline{C}_{mm}^{1/2}(i,i)$ and the prior correlations $\overline{\rho}(i,j)$ among model elements. Table 4.5 summarizes the parameters adopted for the various tomographic inversions shown in Figures 4.7, 4.8, and 4.9. The prior standard deviations were assumed to be constant in the uppermost mantle above the 410 discontinuity ($\overline{C}_{mm}^{1/2}(i,i) = \overline{\sigma}_{UM}$), in the transition zone between the 410 and the 660 ($\overline{\sigma}_{TZ}$), and in the lower mantle below the 660 ($\overline{\sigma}_{LM}$).

Global and regional tomographic studies [e.g., *Grand*, 1994; *Su et al.*, 1994; *Dziewonski et al.*, 1996; *Masters et al.*, 1996; *Li and Romanowicz*, 1996] have shown that shear-velocity heterogeneities at mid-mantle depths are small, with a root-mean-square (rms) variability of about 0.5% (or less in the case of Grand's model), and their magnitude increases through the transition zone towards a maximum of about 2% in the thermal and chemical boundary layers near the surface [cf. *Li and Romanowicz*, 1996, Figure 10; *Puster and Jordan*, 1997, Figure 6]. Our preferred model (TH2) was constructed using values consistent with global tomography: $\overline{\sigma}_{UM}$ = 2%, $\overline{\sigma}_{TZ}$ = 1%, and $\overline{\sigma}_{LM}$ = 0.5%. For the anisotropic parameter $(\delta\beta_H - \delta\beta_V)/\beta_0$, we chose a standard deviation of $\overline{\sigma}_{AN}$ = 0.5% in the uppermost mantle down to 166 km, which we reduced to 0.1% below 166 km and tapered to zero below 300 where the radial anisotropy appears to be smaller [*Regan and Anderson*, 1984; *Cara and Lévêque*, 1988; *Nishmura and Forsyth*, 1989]. *Gaherty et al.* [1997] tested the depth extent of anisotropy for the Tonga-Hawaii corridor and concluded that below about 200 km the radial anisotropy is small (< 1%), and models that allow deeper anisotropy do not fit the data significantly better.

The preferred values for the discontinuity topographies were $\overline{\sigma}_{410}$ = $\overline{\sigma}_{660}$ = 10 km, which is comparable to the variability estimated on a larger scale for the central and western Pacific by *Revenaugh and Jordan* [1991b] or obtained in the global model of *Shearer* [1993] and *Flanagan and Shearer* [1997]. Recent estimates for the Clapeyron slopes of the exothermic α-to-β-olivine transition at the 410 discontinuity and the endothermic transition of γ-olivine-to-perovskite+ferropericlase at the 660 discontinuity are 3.0 MPa/K and –2.3 MPa/K, respectively [*Bina and Helffrich*, 1994], which imply $\partial r_{410}/\partial T \approx$ –0.084 km/K and $\partial r_{660}/\partial T \approx$ 0.056 km/K. When anelastic effects are taken into account, the temperature derivative of relative shear velocity in the transition zone is estimated to be $(\partial \ln\beta/\partial T)_{TZ} \approx -10^{-4}$ K^{-1} [*Karato*, 1993]. This simple "equilibrium-olivine" thermal model derived from laboratory-based mineral-physics data predicts that a temperature decrease of 100 K in the transition zone would induce a 1% velocity increase,

an 8.4-km elevation of the 410, and a 5.6-km subsidence of the 660, which are fairly consistent with the adopted values of $\overline{\sigma}_{TZ}$, $\overline{\sigma}_{410}$, and $\overline{\sigma}_{660}$. It ignores potentially important phase changes in the garnet component of mantle composition, however [*Weidner and Wang*, 1997].

A Gaussian form was chosen for the prior correlation function [e.g., *Tarantola and Nercessian*, 1984]:

$$\overline{\rho}(i,j) = s_{ij} \exp\left[-(r_i - r_j)^2 / 2l_r^2 - (\theta_i - \theta_j)^2 / 2l_\theta^2\right] \tag{4.9}$$

where r_i and θ_i are the coordinates at the center of the ith block, $s_{ij} = s_{ji}$ is a selection coefficient, and l_r and l_θ are radial and angular correlation lengths, respectively. For most of the inversion runs, we adopted l_r = 250 km and $l_\theta = 5°$. The latter yields a horizontal correlation length of about 300 km at the base of the mantle and 550 km near its top. In all but one of the inversions listed in Table 4.5, the selection coefficients s_{ij} were taken to be unity if both the ith and jth model parameters were of the same type—e.g., $\delta\beta/\beta_0$, $(\delta\beta_H - \delta\beta_V)/\beta_0$, δr_{410}, or δr_{660}—and zero otherwise; i.e., no prior correlation among parameters of different types. The exception was for an experiment in which we adopted the equilibrium-olivine thermal model of transition-zone structure (TH2.d), for which we assumed $s_{ij} = 1$ if $i \in \delta r_{410}$ and $j \in \delta\beta / \beta_0$, and $s_{ij} = -1$ if $i \in \delta r_{660}$ and $j \in \left[\delta\beta/\beta_0 \cup \delta r_{410}\right]$; this correlates the 410 and 660 topographies negatively with each other, and positively and negatively, respectively, with their nearby shear-velocity perturbations.

4.6.2 Model TH2

The preferred model for the Tonga-Hawaii corridor, TH2, is shown as a perturbation to the PA5/PREM reference model in Figure 4.7b. This inversion used a parameterization identical to our previous TH1 model [*Katzman et al.*, 1997a] (Figure 4.7a) and a data set that differed primarily by the inclusion of the near-vertical ScS_n times from the 1973

Hawaiian earthquake (13 phase-delays with low-quality Fréchet kernels were also down-weighted relative to the TH1 inversion). For both data sets, a 1D, spherically symmetric perturbation $\delta\overline{\mathbf{m}}$ to the PA5/PREM reference model $\mathbf{m}_0$ was constructed by inverting the entire data set for a path-averaged structure, which was then used as the prior model in the subsequent 2D inversions. Not surprisingly, PA5 turned out to be an excellent representation of the path-averaged structure for the Tonga-Hawaii upper mantle, and the perturbations in this region were small (only 1.5 km for the 660-km discontinuity, for example). They were also very small in the mid-mantle, so that the only region where $\delta\overline{\mathbf{m}}$ was significantly different from zero was the lowermost mantle, where the perturbation was negative, reaching about 1.5% in D". This result is consistent with previous global and regional studies that indicate the lowermost mantle beneath this corridor is slow relative to the average Earth [*Dziewonski et al.*, 1996; *Masters et al.*, 1996; *Garnero and Helmberger*, 1996; *Wysession*, 1996].

The primary feature in both models is the alternating series of highs and lows in upper-mantle shear velocity with wavelength of 1500 km and amplitude of about 3% between the northern end of the Tonga trench and the island of Oahu. Both models also exhibit a large high-velocity region in the lower mantle below the Tonga subduction zone extending to about 1200 km, anticorrelated topography on the 410 and 660 discontinuities (top two panels in Figure 4.9c), and small lateral variations in radial anisotropy. The main difference between the two models is that TH2 has higher shear velocities in the transition zone and lower mantle directly below Hawaii, dictated by the relatively fast ScS_n-ScS_m residuals from the 1973 event [*Sipkin and Jordan*, 1980b]. The distribution of the high velocities below Hawaii is uncertain, however, because the resolving power of the data set for the vertical structure of this near-receiver region is relatively low; it is possible, for example, that this high-velocity anomaly might be concentrated more towards the upper mantle (see below).

TH2 gives a good overall fit to the data, with a normalized chi-square of $\chi^2/D = 1.4$ and a total variance reduction of 97% (Table 4.4). Much of this reduction is ascribable to the source statics and the 1D perturbation to the starting model, however; the variance reduction that results from the 2D perturbation alone is only 53%. The model satisfies the general trends in the ScS_n-ScS_m differential travel times (Figure 4.10), although it tends to underpredict the steep slope in the variation of ScS_4-ScS_3 residuals with epicentral distance. The feature primarily responsible for these trends is the nearly harmonic variation of shear-velocity in the upper mantle, which has about the same horizontal wavelength (~1500 km) as the kernels for the ScS_n-ScS_m differential travel times (cf. Figures 2.4c and 2.4d). Increasing the horizontal correlation length l_θ above the 5° value used in this inversion gives a smoother structure and degrades the fit to these data.

The resolving power of the TH2 inversion has been investigated through a series of checkerboard inversions and other tests (Appendix A). In all inversion tests using synthetic data, Gaussian noise with standard deviations similar to the error estimates for the real data (up to ~ 8 s) was added to the synthetic data. Patterns with horizontal wavelengths of 1500 km are well resolved in the upper mantle, but not in the lower mantle (Figure A.1). The resolution at lower-mantle depths is decreased because the turning-point depths for most of the frequency-dependent phase delays are confined to the upper mantle or the top part of the lower mantle (e.g., Figure 3.3). The checkerboard tests indicate that the vertical resolving lengths are on the order of 200 km or less in the upper mantle, so that it is unlikely that depth extent of the upper-mantle anomalies, which persist well into the transition zone, is the result of vertical smearing of, say, lithospheric heterogeneities.

In Appendix B, we have examined the statistical significance of various features in the TH2 model using the posterior covariance matrix for the model perturbation available from the Bayesian analysis. The results for the ten regions of Figure B.3 are summarized in Table B.1. The five regions of high and low velocity in the upper mantle between the northern end of the Tonga trench and Oahu (regions 1 to 5) have high variance reductions

(>94%), and each is statistically significant from zero at the 90% confidence level. Other features have lower variance reductions and larger correlations with other model parameters, indicating that their statistical significance is lower. One example is a region of small positive topography on the 410 discontinuity near the center of the grid (region 9), where the mean amplitude (+3.6 km) is less than the posterior error (±5.3 km).

4.6.3 Other Inversion Experiments

As noted above, TH2 satisfies the steep gradients in the ScS_n-ScS_m times because the horizontal wavelength of the upper-mantle variations is closely matched to the dominant $\Delta/3$ wavelength in the sensitivity kernel for the differential times. This coincidence raises the issue of whether the modeling procedure is biased in a way that amplifies the heterogeneity at this wavelength over others that might be present in the upper mantle ("kernel-resonance bias"). To evaluate this possibility, we excluded all of the *ScS*-reverberation data from the data set and inverted only the phase delays of the surface and turning waves, obtaining a model designated TH2.a (Figure 4.8a), which depends on the *ScS* data only through the 1D prior $\delta\overline{\mathbf{m}}$ (taken to be the same in all inversions). The resulting tomogram is very similar to TH2, except beneath Hawaii, where TH2.a is poorly constrained by the reduced data set, which excludes the vertical ScS_n times from the Hawaiian earthquake. The upper-mantle variations remain well defined; in fact, the amplitude of the 1500-km variation is increased slightly (Figure 4.9a). Except for a baseline shift due to the differences in lower-mantle structure, TH2.a does almost as well as TH2 in satisfying the ScS_n-ScS_m observations, despite the fact that they were not used in the inversions (Figure 4.10). Therefore, the phase delays of the surface and turning waves independently corroborate the 1500-km variation indicated by the ScS_n data. Because the kernels for the former are distributed over a much wider range of horizontal wavelengths (Section 3.3, Figure 3.3), we conclude that the kernel-resonance bias is small.

Moreover, since the phase delays were measured from waves that turn in the upper half of the mantle and are completely insensitive to the lowermost mantle, they indicate that the contribution of the lowermost mantle to the ScS_n-ScS_m trends is relatively minor. TH2 does display some lateral structure at the base of the mantle that may be significant, however: the shear velocities in the lowermost mantle are about 0.5% lower near the middle of the corridor, which slows the ScS_3 and ScS_4 phases relative to ScS_2 and accounts for the offsets between the TH2 and TH2.a predicted times in Figure 4.10. This feature is qualitatively consistent with the study of *Garnero and Helmberger* [1996].

More consistent, however, are the variations in the upper part of the lower mantle, such as the high-velocity region at 800-1400 km depth beneath the Tonga subduction zone, which appears in both TH2 and TH2.a and is dictated mostly by the times of the direct *S* phases. This feature corresponds to a region of high velocities seen in the *P*-wave residual spheres from deep-focus Tonga earthquakes analyzed by *Fischer et al.* [1991]. These authors attribute this anomaly to the subduction of the Tonga slab, but this interpretation disagrees with the tomographic study by *van der Hilst* [1995], who puts the locus of the lower-mantle slab anomalies further to the west. We also note that such a feature is not evident in the global *P*-wave model of *van der Hilst et al.* [1997]. The structure in this complex tectonic environment is no doubt highly three dimensional, and our 2D model may be biased beneath Tonga by the inclined distribution of earthquakes transverse to the plane of the corridor. Within the source array, the perturbation to the average shear velocity in TH2, TH2.a, and all other models in Figure 4.8 varies from positive near the surface to negative in the transition zone, consistent with the notion that the rays from the shallow and intermediate-focus events sample the descending slab in the uppermost mantle and then penetrate low-velocity material underlying the slab in the transition zone. The 660 topography is elevated and the 410 topography is depressed in the region of low transition-zone velocities in the manner expected from the equilibrium-olivine thermal model, despite

the lack of any a priori correlation among these parameters imposed by the inversion. Lacking a fully 3D inversion, however, we remain cautious about this interpretation.

We performed a number of additional inversions to test the sensitivity of the TH2 model to its Bayesian prior, five of which are shown in Figures 4.8b-f. In each of these inversions, the full data set was inverted with the same 1D prior $\delta\overline{\mathbf{m}}$ as TH2, and only the parameters of the prior covariance $\overline{\mathbf{C}}_{\mathbf{mm}}$ were modified. In the TH2.b inversion, the prior standard deviation for the radial anisotropy in the uppermost mantle was increased by a factor of two ($\overline{\sigma}_{AN}$ = 1%). The resulting anisotropic variation was larger—more than 3.5% peak-to-trough compared to 1.2% for TH2 (Figure 4.9b)—but the basic features of the TH2 profile were preserved. In particular, the anisotropy perturbation peaks near the center of the corridor ($\theta = 38°$) and declines to its minimum value near Oahu. This gradient is consistent with S20A, a radially anisotropic, 3D global model complete to angular degree 20 [*Ekström and Dziewonski*, 1997], which shows a distinct minimum in $(\beta_H - \beta_V)/\beta_0$ in the center of the Pacific plate near Hawaii. The total variation in this parameter along the Tonga-Hawaii corridor in S20A is about 2.5%, larger than TH2 but smaller than TH2.b. TH2.b fits the data somewhat better than TH2 (Table 4.5), but an F-test demonstrates that the decrease in χ^2/D from 1.41 to 1.38 is not significant at the 95% confidence level; i.e., our data are consistent with the amplitude of the anisotropic heterogeneity in S20A. TH2 and TH2.b thus provide reasonable bounds on the variation of $(\beta_H - \beta_V)/\beta_0$ at horizontal wavelengths of 1000-3000 km. Moreover, the isotropic shear-velocity perturbations (Figures 4.9a) and the discontinuity topographies (Figures 4.9c) are not at all sensitive to the magnitude of this anisotropy (see also Figure B.1c, regions B and C)

In the TH2.c inversion, the topographies on the 410 and 660 discontinuities and the anisotropy perturbations in the uppermost mantle were completely suppressed by setting $\overline{\sigma}_{410}$, $\overline{\sigma}_{660}$, and $\overline{\sigma}_{AN}$ to zero. This restriction that the perturbation be isotropic and volumetric (which is typical of many previous tomographic studies) significantly increased

the misfit of the data (χ^2/D = 1.53), particularly the residuals of the first-order *ScS* reverberations that are most sensitive to the locations of the discontinuities. Again, however, this change in modeling assumptions did not substantially alter the isotropic shear-velocity perturbations, demonstrating that any coupling of the latter to the radial anisotropy and transition-zone topographies was very weak (cf. Figure B.1c).

Similar topographies were recovered from all inversions in which the locations of the 410 and 660 discontinuities were allowed to vary independently along the corridor. The main feature is a broad depression of the 660 toward the center of the profile, flanked by elevated regions beneath Tonga and Hawaii, with a peak-to-trough amplitude of just less than 40 km. The 410 perturbation is a factor of two smaller and tends to be anticorrelated with 660. As indicated by the poor performance of TH2.c in fitting the *ScS*-reverberation data, the times of the first-order reverberations dominated the determination of the transition-zone topographies. This was expected, of course, given the sensitivity of these reflection measurements to discontinuity structure (Figure 2.4). We note, however, that the run which excluded all *ScS* data, TH2.a, gave the same basic structure, albeit lower in amplitude, showing that the phase delays of the waves turning in and near the transition zone are generally compatible with the reflection times. The depression of the 660 between Tonga and Hawaii is correlated with higher shear velocities in the transition zone and uppermost part of the lower mantle, while its elevation near both ends of the corridor is correlated with lower velocities, as predicted by the equilibrium-olivine thermal model.

In the TH2.d inversion, we enforced the equilibrium-olivine thermal model of the transition zone by specifying the prior correlation matrix according to the procedure described previously (Table 4.5). The resulting 410 topography was somewhat larger in amplitude and the 660 topography somewhat smaller than in TH2, but the difference between the two—the transition-zone thickness—has a similar along-path structure: a positive perturbation near the center ($25° \lesssim \theta \lesssim 50°$) and negative perturbations near the two ends (Figure 4.9c). The two discontinuities are anticorrelated, although not exactly,

owing to their radial separation, which lowers the Gaussian factor (4.9). In particular, the 410 topography mimics the harmonic upper-mantle variation, which has a slightly larger amplitude in TH2.d than in TH2, while the 660 correlates with the smoother variation of the shear velocities in the upper part of the lower mantle. We conclude that the data along this corridor are entirely consistent with the thermal model. As noted above, however, this model ignores the garnet-to-perovskite phase change, which occurs at around 660 km depth with a positive Clapeyron slope [*Weidner and Wang*, 1997] and can potentially affect the depth and sharpness of the 660 discontinuity [*Puster et al.*, 1996]. Moreover, this correlation has not been observed in global studies of transition-zone topography [*Shearer*, 1993; *Flanagan and Shearer*, 1997]. For these reasons, we did not impose the thermal-correlation assumptions on our preferred model.

The last two experiments were designed to examine the coupling between the upper and lower mantle. In TH2.e, we reduced the prior rms variability of the lower mantle by a factor of five ($\overline{\sigma}_{LM}$ = 0.1%), suppressing almost all of the heterogeneity below 660. A good fit was maintained for most of the data by amplifying the upper-mantle heterogeneity. The average perturbation beneath Hawaii increased from 0.3% to 1.4%, for example (Figure 4.9a), as necessary to account for the data from the 1973 earthquake. The largest increase in χ^2 was for the direct *S* times, which, as we have seen, prefer a high-velocity zone in the lower mantle beneath northern Tonga. The dominance of the 1500-km harmonic pattern in $\delta\beta_{UM}$ remained, however, and the lateral variation in transition-zone thickness was again similar to TH2.

In the final experiment (TH2.f), we equalized the prior variance for all isotropic variations in the mantle ($\overline{\sigma}_{UM}$ = $\overline{\sigma}_{TZ}$ = $\overline{\sigma}_{LM}$ = 1%). The rms amplitude of the lower mantle heterogeneity increased correspondingly, reaching 0.8% at 1500 km (compared to 0.4% for TH2), but the pattern of anomalies in both the upper and lower mantle was not substantially altered. Although $\delta\beta_{UM}$ became more positive near the center of the grid and smoother overall, the upper-mantle variation remained large in amplitude and constant in

phase (Figure 4.9a). The mid-mantle heterogeneity in TH2.f is strongest at horizontal wavelengths on the order of 2000-4000 km, corresponding to spherical harmonic degrees 8-15, which should be resolvable in global tomographic studies; however, the amplitudes of comparable features in global models [*Su et al.*, 1994; *Masters et al.*, 1996; *Li and Romanowicz*, 1996] are smaller by about a factor of two. Moreover, despite its much larger lower-mantle heterogeneity, TH2.f fits the data no better than TH2. We conclude that the amplification of the lower-mantle structure in TH2.f simply reflects the poor resolving power of our data in this region, and that TH2 is more realistic.

4.7 GEODYNAMICAL IMPLICATIONS

The combination of data used in this study supplies substantially better horizontal and vertical resolution of upper-mantle structure within the Tonga-Hawaii corridor than previous studies. As demonstrated by the series of inversion employing different data subsets and a variety of prior assumptions, the pattern of upper-mantle anomalies exemplified in our preferred model TH2 is remarkably robust (Figure 4.9). The most striking and best resolved feature is an alternating series of highs and lows in $\delta\beta / \beta_0$ extending throughout the upper mantle with a horizontal wavelength of 1500 km and a peak-to-trough amplitude of about 3% (Figure 4.9a). There are only three basic mechanisms that can give rise to shear-velocity heterogeneity of this magnitude: (1) temperature anomalies associated with convection [e.g., *Hager and Clayton*, 1989], (2) compositional inhomogeneities associated with the depletion of the oceanic upper mantle by basaltic volcanism [*Green and Liebermann*, 1976; *Jordan*, 1979; *Phipps Morgan et al.*, 1995], and (3) variations in the alignment of olivine crystals by mantle flow [*Nicolas and Christensen*, 1987; *Ribe*, 1989; *Zhang and Karato*; 1995].

The latter mechanism operates only in the upper 400 km of the mantle where olivine is a stable mineral phase. A detailed investigation by *Gaherty et al.* [1996] has shown that the average radial anisotropy within this corridor is largest in the upper 100 km and decreases

to undetectable values (< 1%) below about 170 km (Figure 4.2). Our inversion experiments indicate the presence of significant lateral heterogeneity in the apparent radial anisotropy above this depth (Figure 4.9b), with a magnitude consistent with the 3D variations inferred for the Pacific by *Ekström and Dziewonski* [1997]. Moreover, they show that plausible errors in the magnitude and distribution of this radial anisotropy do not affect the estimates of the variations in isotropic upper-mantle shear velocities (cf. Figure 4.9a). The question of how the TH2 tomogram is affected by the unmodeled aspects of anisotropy, such as along-path variations in its azimuthal components, cannot be answered definitively in this 2D study, but a consideration of this problem by *Gaherty et al.* [1996], based on the seafloor-spreading history of the Pacific and some calculations by *Kawasaki and Kon'no* [1984] and *Maupin* [1985], suggests that any along-path variations in azimuthal anisotropy will tend to be absorbed into the radial anisotropy, and their effect on the isotropic velocity structure will be correspondingly small. We conclude that, at the scales resolved in this study, the anisotropic heterogeneity of the Tonga-Hawaii corridor is probably concentrated in the lithosphere and upper part of the low-velocity zone, and that anisotropic effects associated with olivine alignment cannot account for the isotropic variations in TH2 and the other successful models of Figure 4.8. We shall therefore focus our discussion on the other two possible mechanisms for shear-wave heterogeneity, thermal convection and basaltic depletion.

4.7.1 Thermal Convection

Since basaltic depletion is thought to operate only in the mantle above 100-150 km [*Ringwood*, 1975, *Liu and Chase*, 1991], it has difficulty accounting for heterogeneities much below this depth. Thermal convection thus provides the most satisfactory explanation for the upper-mantle anomaly pattern, which is organized into cell-like features with an aspect ratio near unity extending from the lithosphere to the 660 discontinuity. For typical value of the thermal coefficient of shear velocity, $\partial\beta / \partial T = -0.5$ m/s/K [e.g.,

Creager and Jordan, 1986; *Kato*, 1997], the peak-to-trough temperature difference needed to explain the shear-velocity anomalies would be ~250 K, which is about the difference between the upgoing and downgoing limbs of upper-mantle convection cells expected from simple boundary-layer theory [e.g., *Houseman and McKenzie*, 1982].

The Tonga-Hawaii corridor is oriented nearly perpendicular to the direction of motion of the Pacific plate (Figure 4.1). *Richter* [1973] and *Richter and Parsons* [1975] have suggested that, beneath the fast-moving plates, convective instabilities will align themselves as rolls in the direction of absolute plate motion (Figure 4.4). While our 2D study cannot constrain the mantle structure outside this corridor, there are some indications that the upper-mantle anomalies in TH2 are actually elongated features oriented in the direction of plate motion. For example, the large variation in ScS_n residuals observed along the Tonga-Hawaii corridor is not evident along paths parallel to the Pacific plate motion [*Sipkin and Jordan*, 1980a]. Additional evidence for this northwestward extension comes from the geoid and topography fields.

4.7.2 Correlation with Geoid Lineations and Hotspot Swells

The geoid anomalies in the central and eastern Pacific plate show lineated undulations oriented subparallel to the present-day absolute plate motion and perpendicular to our seismic corridor [*Wessel et al.*, 1994, 1996]. In the eastern Pacific, these lineations are observed over a wide spectrum of horizontal wavelengths, ranging from 200 to 1500 km [*Haxby and Weissel*, 1986; *Baudry and Kroenke*, 1991; *Maia and Diament*, 1991; *Cazenave et al.*, 1992; *Wessel et al.*, 1994, 1996; *Cazenave et al.*, 1995], and they are positively correlated with residual topography [e.g., *Cazenave et al.*, 1992]. A number of these authors have considered the possibility that these features are an expression of roll-like convection, but the paucity of seismic data in the eastern Pacific have thus far precluded a systematic study of their correlation with shear-velocity heterogeneity in the upper mantle.

We have compared our shear-velocity model with the geoid anomalies in the central Pacific derived from the new geopotential model developed to degree and order 360 by the NASA Goddard Space Flight Center (GSFC) and the U.S. Defense Mapping Agency (DMA) [*Lemoine et al.*, 1996]. Long-wavelength features associated with deep-mantle processes dominate the raw geoid and must be suppressed to exhibit structures at intermediate wavelengths. We removed the geoid components below degree and order 15 and tapered the field between degrees 15 and 20 with a Hanning function (cosine-squared taper) to avoid Gibbs oscillations at the cutoff wavelength, and we similarly tapered the short-wavelength anomalies between degrees 80 and 360. Bandpass filtering of the red geoid spectrum is notoriously sensitive to the filter parameters [e.g., *Sandwell and Renkin*, 1988], so we experimented carefully with a number of filters. The particular parameters we adopted gave a good correlation between the filtered geoid and the seafloor topography, which has a much whiter spectrum and is not sensitive to the form of the filter. Along the Tonga-Hawaii corridor, these two quantities show a high coherence with an admittance of 3.3 m/km (Figure 4.11c), which agrees with values observed previously for intermediate-scale features in this part of the Pacific [*Crough and Jarrard*, 1981; *Sandwell and Renkin*, 1988].

The resulting geoid represents the signature of upper-mantle mass anomalies with horizontal wavelengths of 500-2000 km. In this band, the dominant features are a series of ridges and troughs oriented subparallel to the absolute plate motion (Figure 4.11a). Each of the three prominent ridges extends downstream from a major hotspot: the Hawaiian swell [*Watts*, 1976; *Detrick and Crough*, 1978], the Marquesas-Line swell [*Crough and Jarrard*, 1981], and the less conspicuous extension of the Society Islands swell through the Manihiki Plateau into the Phoenix Island region. Between the Tonga trench and Hawaii, where our seismic corridor cuts across these features, we observe a strong positive correlation between geoid height, seafloor topography, and upper-mantle shear velocity

(Figure 4.11). The hotspot swells are therefore positioned above high seismic velocities; in a convection scenario, the latter correspond to low-temperature downwellings.

The superposition of swells over apparent downwellings is dynamically puzzling. As shown in Appendix C, the positive correlation between geoid highs and temperature lows can be explained by a dynamic compensation mechanism [*Hager and Clayton*, 1989], provided the viscosity profile includes an asthenospheric low-viscosity channel (LVC). These calculations account for the finite elastic thickness of the lithosphere, which has a minor effect at these wavelengths (Figure C.1), and they provide plausible viscosities for the asthenospheric LVC, approximately 3×10^{19} Pa s for a lower-mantle viscosity of 10^{22} Pa s (Figures C2 and C3). Unfortunately, this dynamic-compensation model fails regardless of the viscosity structure, because it always predicts negative dynamic topography over downwellings, whereas the observed topography for both the Hawaiian and Marquesas-Line swells is distinctly positive, as their names imply (Figure 4.11c).

An alternative is to delaminate the lithosphere at the hotspot; if η_{LVC} is low enough, the positive buoyancy of the hot replacement mantle can dominate the topographic response [*Richards et al.*, 1988], while the cold delaminated material can contribute to the deeper, high shear velocities. The high temperatures postulated by this mechanism are inconsistent with the high shear velocities found at shallow depths beneath all three swells in TH2, however (Figure 4.11b), and the depth variation expected from this primarily vertical transfer (low velocities over high) is not observed. Given the good vertical and lateral resolving power of the TH2 data set (Appendix A), we must discount this possibility.

It therefore appears that, while thermal convection can account for the seismic results, it cannot explain the positive topography of the swells, which require a shallow source of buoyancy.

4.7.3. Need for Basaltic Depletion

The most obvious way to generate a buoyant, high-velocity mantle is by basaltic differentiation. The removal of basaltic constituents lowers the Fe/Mg and Al/Mg ratios of the peridotitic source rock, creating a refractory residuum of lower density [*O'Hara*, 1975; *Green and Liebermann*, 1976]. *Jordan* [1979] quantified this effect for a range of peridotitic compositions and proposed that the buoyancy of this residuum could contribute significantly to the positive topography and geoid of hotspot swells. *Sipkin and Jordan* [1980b] invoked this chemical-differentiation mechanism to explain their observations that multiple-*ScS* waves on a Hawaii-to-Oahu path were faster (by 3 ± 1 s) and less attenuated ($Q_{ScS} = 184 \pm 48$ vs. 141 ± 16) than the average for the Tonga-Hawaii corridor. Subsequent studies have shown that the Hawaiian swell does not display the anomalies in either heat flow [*Von Herzen et al.*, 1989] or Rayleigh-wave dispersion [*Woods et al.*, 1991; *Woods and Okal*, 1996] expected if it had a strictly thermal origin [*Detrick and Crough*, 1978; *Crough*, 1983]. The weight of this evidence motivated *Phipps Morgan et al.* [1995] to examine the effects of chemical differentiation from a dynamical perspective, and they demonstrated that the accumulation and subsequent dispersal of basalt-depleted material at the base of the lithosphere could plausibly account for most of the swell topography and geoid.

While basaltic depletion increases the shear velocity of peridotites by only a small amount at ordinary temperatures [*Jordan*, 1979], this effect could be substantially amplified at temperatures close to the mantle solidus [*Sato et al.*, 1989; *Karato*, 1995] and thus easily explains the 2-3% velocity anomalies we observe at shallow depths within the Tonga-Hawaii corridor. However, it does not seem possible for this mechanism to operate much below 150-200 km. The calculations of *Phipps Morgan et al.* [1995] are instructive in this regard. The extra crustal area across the Hawaiian chain is, on average, about 12.5 km thick and 200 km wide; assuming 5% partial melting, the mantle source region would have

a cross-sectional area of ~5 × 10^4 km^2. Therefore, distributed over the 1000-km wide Hawaiian swell, the thickness of the low-density depleted root would be on the order of 50 km. Concentrating the depleted residuum in a narrower zone could increase this depth, perhaps by as much as a factor of two, but it seems highly unlikely that it could account for the depth of the high-velocity anomalies in the TH2 upper mantle, which peak near 350 km and extend down into the transition zone.

4.7.4 Relationship to Hotspots

These considerations suggest that neither thermal convection nor chemical differentiation can alone satisfactorily account for the unusual configuration of the upper mantle in this part of the Pacific, and we infer that some combination of the two is probably required [*Katzman et al.*, 1997a]. The cell-like pattern of shear-velocity anomalies in Figure 4.11b has a horizontal and vertical scale consistent with a convection system confined to the upper mantle, with its base regulated by the endothermic phase change at 660 km, as discussed by *Matchtel and Weber* [1991] and several other authors [e.g., *Honda et al.*, 1993; *Tackley et al.*, 1993; *Solheim and Peltier*, 1994], and/or a viscosity increase at the top of the lower mantle, as proposed by Hager and his colleagues [*Hager*, 1984; *Hager and Richards*, 1989; *Hager and Clayton* , 1989]. The 3D structure of this convecting system is likely to be complicated and will have to be clarified by an extension of high-resolution tomographic imaging to three dimensions, but several lines of evidence point to the existence of roll-like convection parallel or sub-parallel to the absolute plate motion, including the theoretical work of *Richter and Parsons* [1975], the multiple-*ScS* study of *Sipkin and Jordan* [1980a], and the geoid lineations evident in Figure 4.11 and other analyses of the geopotential [*Wessel et al.*, 1994; *Cazenave et al.*, 1995, 1996].

One of the most puzzling aspects of our results is the strong positive correlation of the shear-velocity variations with the geoid and topography, which implies that the hotspot swells overlie regions of mantle downwelling, at least along the Tonga-Hawaii corridor.

The association of hotspot swells with convective downwellings does not imply that the hotspots themselves are sites of downwelling. Indeed, the high rate of localized, mid-plate volcanism observed at these Pacific hotspots requires that they be the sites of active mantle upwellings; i.e., plumes. Based on our results along the Tonga-Hawaii corridor, we cannot exclude, for example, the existence of a narrow plume (~100 km radius) right beneath Hawaii (3° away from our seismic stations on Oahu). The source depth of these plumes, however, is poorly constrained. If our results are taken at face value, then it would appear that they are features whose locations are controlled by a shallow system of upper-mantle flow, rather than instabilities in the lowermost mantle as suggested by *Morgan* [1972] and others.

We can imagine, for example, a nearly steady-state situation where the cooling oceanic thermal boundary layer becomes convectively unstable [*Parsons and McKenzie*, 1978] and feeds a secondary system of plate-aligned convective rolls, with a unit aspect ratio which are confined above the 660 discontinuity. In this hypothetical picture, the major hotspots of the Hawaiian, Marquesas, and Society Islands occur upstream from the convective downwellings, perhaps above strong plumes. These plumes are generated by a counterflow in advance of the most intense areas of delamination, where the flow structures are expected to be highly three-dimensional. The high-velocity, viscous residuum of hotspot volcanism is transported downstream with the overriding plate and is rafted into the axes of the downwellings by the horizontal flow at the base of the plates, maintaining the swells over downwellings and further stabilizing the roll structures. In this model, the high-velocity anomalies beneath the swells are dictated, at the shallower depths, by the low-density residuum which also support the swell, and at the deeper depths, by the cold downwelling.

The upper-mantle convection hypothesized here is a secondary system, driven by the flux of negative buoyancy from the cooling Pacific plate, which itself participates in the primary, plate-tectonic flow balanced through deep-mantle circulation. We note that the

part of the Pacific sampled in this study corresponds to *Menard's* [1984] Darwin Rise, a region of anomalously high residual topography [*Davies and Pribac*, 1993], where this type of secondary upper-mantle flow may have been particularly active since the Cretaceous. Until further seismological investigations confirm the peculiar structural relationships in Figure 4.11, the dynamical speculations offered here must be viewed with caution. It is unlikely, however, that the location of the Hawaiian, Marquesas, and Society hotspots along the axes of features with a geometry clearly controlled by upper-mantle processes is coincidental, as would be implied from *Morgan's* [1972] hypothesis that they are the surface manifestations of deep-mantle plumes.

Finally, we wish to emphasize that the conclusions we have drawn from the discussion of these three central Pacific hotspots do not apply to hotspots in general, such as those on slow-moving younger oceanic plates.

Table 4.1. Events and stations used for *ScS*-reverberation measurements along the Tonga-Hawaii corridor

Date			Origin Time UT	Latitude °N	Longitude °E	Depth km	Station	Distance °	# of measurements 0th*	1st†
1973	04	26	20:26:27.0	19.90	-155.13	48	KIP	3.09	4	0
1973‡	07	21	04:19:13.7	-24.81	-179.22	411	KIP	50.36	6	8
1973	12	19	12:55:51.1	-20.59	-176.48	246	KIP	45.48	6	12
1973	12	28	05:31:03.8	-23.87	179.96	549	KIP	49.86	6	4
1974	03	23	14:28:33.0	-23.93	179.78	535	KIP	49.99	6	5
1974	06	04	04:14:13.8	-15.85	-175.10	276	KIP	40.65	6	9
1975	02	22	22:04:33.5	-24.89	-179.06	375	KIP	50.37	6	6
1976‡	02	03	12:27:30.1	-25.14	179.69	477	KIP	51.09	6	9
1977	01	21	06:11:11.8	-18.30	-178.40	607	KIP	44.24	5	6
1978	07	17	13:26:28.6	-14.88	-176.15	322	KIP	40.22	4	5
1986‡	06	16	10:48:35.6	-21.86	-178.87	564	HON	47.50	4	0
1986‡	10	30	01:29:05.1	-21.68	-176.45	196	HON	46.37	6	11
1989	11	29	05:49:08.7	-25.37	179.52	516	KIP	51.37	6	9
1990‡	05	28	11:28:54.7	-20.68	-178.01	494	KIP	46.18	3	0
1990‡	06	23	21:38:29.4	-21.29	-176.22	195	KIP	46.02	6	11
1990	06	26	12:08:38.5	-21.71	-179.60	614	KIP	47.76	6	6
1990‡	07	22	09:26:25.1	-23.15	-179.83	559	KIP	49.13	6	4
1991‡	06	09	07:45:10.9	-20.15	-175.90	292	KIP	44.86	6	6
1991‡	09	30	00:21:54.0	-20.67	-178.52	590	KIP	46.38	6	11
1991	11	11	16:15:55.2	-23.94	-176.97	179	KIP	48.71	5	6
1991‡	12	03	10:33:47.3	-26.11	178.69	575	KIP	52.37	5	2
1992‡	06	25	06:31:01.1	-28.17	-176.22	48	KIP	52.34	4	0
1992‡	07	11	10:44:32.7	-22.45	-177.96	394	KIP	47.74	6	6
1992‡	11	12	22:29:04.6	-22.32	-177.72	379	KIP	47.53	4	0
1993	04	16	14:08:46.7	-17.54	-178.76	592	KIP	43.73	5	3
1993	04	24	09:54:28.5	-17.51	179.97	610	KIP	44.30	3	4
1993	05	27	08:52:05.3	-29.39	-178.04	128	KIP	54.07	6	5
1993	07	09	15:38:00.8	-19.74	-177.31	418	KIP	45.05	6	8

* Number of travel-time measurements of zeroth-order ScS_n and $sScS_n$ reverberations.

† Number of travel time measurements of first-order reverberations.

‡ Source-receiver pairs that were also used for the frequency-dependent travel-time measurements (Table 4.3).

Table 4.2. Summary of the *ScS*-reverberation measurements

Depth (km)	Isolation Filter	Number of observations for reflection number, n			
		n=1	n=2	n=3	n=4
Shallow	$\{ScS_n\}$		1	1	
	$\{sScS_n\}$		1	1	
$h \leq 70$	$\{ScS_n, sScS_n\}$	1	1	1	1
	$\{ScS_n\}$		7	6	6
	$\{sScS_n\}$		7	6	7
	$\{ScS_n^{410+}, sScS_n^{410+}, ScS_n^{660+}, sScS_n^{660+}\}$				
Intermediate	$\{sScS_n^{410+}, ScS_n^{660+}, sScS_n^{660+}\}$		2	2	4
	$\{sScS_n^{410+}, ScS_n^{660+},\}$		5	5	3
$70 \leq h \leq 320$	$\{sScS_n^{660+}\}$		5	4	3
	$\{ScS_n^{410-}, sScS_n^{410-}, ScS_n^{660-}, sScS_n^{660-}\}$		1	1	
	$\{ScS_n^{410-}, ScS_n^{660-}, sScS_n^{660-}\}$	1	2		
	$\{ScS_n^{410-}, sScS_n^{660-}\}$	2	4	2	1
	$\{ScS_n^{660-}\}$		3	5	5
	$\{ScS_n\}$		9	8	8
	$\{sScS_n\}$		9	8	7
	$\{sScS_n^{410+}, ScS_n^{660+}, sScS_n^{660+}\}$		1	2	3
	$\{sScS_n^{410+}, sScS_n^{660+}\}$		2		
	$\{sScS_n^{410+}, ScS_n^{660+}\}$		1	2	
	$\{ScS_n^{660+}, sScS_n^{660+}\}$			2	3
Intermediate/Deep	$\{sScS_n^{660+}\}$		3	3	1
	$\{ScS_n^{660+}\}$		1		
$290 \leq h \leq 520$	$\{sScS_n^{410+}\}$		2	1	
	$\{ScS_n^{410-}, ScS_n^{660-}, sScS_n^{660-}\}$		3	2	1
	$\{ScS_n^{410-}, ScS_n^{660-}\}$		1		
	$\{ScS_n^{410-}, sScS_n^{660-}\}$			1	4
	$\{ScS_n^{660-}, sScS_n^{660-}\}$			2	
	$\{ScS_n^{660-}\}$		2	3	2
	$\{sScS_n^{660-}\}$		1		
	$\{ScS_n^{410-}\}$		1	2	
	$\{ScS_n\}$		10	9	9
	$\{sScS_n\}$		10	8	6
	$\{sScS_n^{410+}, sScS_n^{660+}\}$		4	4	
Deep	$\{sScS_n^{660+}\}$		3	3	4
	$\{sScS_n^{410+}\}$		3	2	
$h \geq 520$	$\{ScS_n^{410-}, ScS_n^{660-}\}$		1	3	3
	$\{ScS_n^{660-}\}$		3	4	3
	ScS_n^{410-}		2	2	2

Table 4.3. Events and stations used for frequency-dependent travel-time measurements of turning- and surface-waves for the Tonga-Hawaii corridor

Date			Origin Time	Latitude	Longitude	Depth	Station	Distance	# of measurements	
			UT	°N	°E	km		°	Surf*	Turn†
1973‡	07	21	04:19:13.7	-24.81	-179.22	411	KIP	50.36	0	6
1976‡	02	03	12:27:30.1	-25.14	179.69	477	KIP	51.09	0	11
1983	05	15	00:24:01.4	-19.09	-175.72	19	HON	43.74	8	6
1983	06	20	05:43:41.8	-23.68	179.23	561	HON	49.92	0	25
1983	09	17	12:11:43.1	-16.67	-177.24	16	HON	42.20	16	11
1984	04	18	06:49:21.9	-16.10	-174.02	158	HON	40.37	0	18
1984	04	22	03:33:07.3	-22.05	-179.24	616	HON	47.82	0	7
1984	06	15	14:22:32.8	-15.90	-174.66	269	HON	40.43	0	24
1984	11	17	13:45:56.4	-18.84	-177.96	471	HON	44.43	0	13
1984	11	17	22:43:42.5	-18.28	-175.73	10	HON	43.01	16	13
1984	11	22	17:07:44.8	-17.72	-178.05	663	HON	43.48	0	18
1985	06	03	12:06:29.7	-15.41	-173.28	46	HON	39.46	7	12
1985	07	06	03:37:25.5	-29.50	-177.64	54	HON	53.95	8	18
1985	08	28	20:50:55.5	-20.89	-179.00	640	HON	46.70	0	17
1985	11	02	19:49:31.5	-18.21	175.99	10	HON	46.82	16	12
1986	05	26	18:40:54.5	-21.57	-179.30	603	HON	47.42	0	13
1986‡	06	16	10:48:35.6	-21.86	-178.87	564	HON	47.50	0	19
1986	06	28	05:03:55.4	-19.96	-175.71	222	HON	44.53	0	18
1986‡	10	30	01:29:05.1	-21.68	-176.45	196	HON	46.37	0	6
1987	01	09	08:01:40.2	-19.28	-176.52	16	HON	44.23	8	12
1987	02	10	00:59:35.9	-19.47	-177.38	418	HON	44.75	0	23
1987	02	17	06:16:25.3	-32.73	-178.86	42	HON	57.32	7	23
1987	03	19	22:51:45.9	-20.30	-175.96	215	HON	44.93	0	13
1987	04	29	14:27:44.3	-19.06	-177.84	410	HON	44.58	0	19
1987	09	07	11:57:16.9	-31.19	-177.77	23	HON	55.55	15	30
1987	10	08	03:20:53.4	-19.72	-173.00	49	HON	43.34	15	6
1987	11	03	08:15:09.5	-17.06	-173.55	107	HON	41.07	8	17
1988	01	15	08:40:30.5	-20.68	-175.77	221	HON	45.21	0	5
1988	01	29	16:48:11.7	-15.02	-173.71	119	HON	39.26	0	5
1988	02	06	21:30:11.0	-16.10	-173.49	124	HON	40.17	0	3
1988	03	10	10:25:13.3	-21.02	-178.44	636	HON	46.57	0	21
1988	04	02	14:26:39.8	-15.08	-172.96	15	HON	39.03	15	13
1988	06	11	12:17:33.6	-15.06	-173.40	59	HON	39.18	7	0
1988	07	19	01:00:24.9	-19.71	-174.39	159	HON	43.81	0	6
1988	10	08	04:46:36.4	-18.82	-172.28	45	HON	42.27	8	13
1988	12	05	16:05:44.7	-14.76	-173.49	44	HON	38.94	7	0
1989	01	02	01:52:14.5	-18.49	-174.39	128	HON	42.69	0	24
1989	03	11	05:05:10.6	-17.78	-174.77	244	HON	42.18	0	13
1989	04	08	03:06:08.7	-15.90	-172.91	15	HON	39.77	7	7
1989	04	16	19:48:22.9	-20.79	-179.18	601	HON	46.68	0	12
1989	05	08	14:28:39.3	-23.62	-179.99	558	HON	49.53	0	13
1990‡	05	28	11:28:54.7	-20.68	-178.01	494	KIP	46.18	0	18
1990‡	06	23	21:38:29.4	-21.29	-176.22	195	KIP	46.02	0	13
1990	07	11	19:48:17.0	-25.22	178.22	596	KIP	51.79	0	10
1990‡	07	22	09:26:25.1	-23.15	-179.83	559	KIP	49.13	0	16
1990	09	08	20:32:06.5	-20.39	-173.96	21	KIP	44.38	14	11
1990	10	10	05:55:03.2	-23.08	178.93	575	KIP	49.61	0	26
1991	01	01	17:28:08.4	-21.28	-173.98	15	KIP	45.21	8	12
1991	01	08	22:04:19.0	-17.76	-173.12	15	KIP	41.65	11	13
1991	02	09	02:08:57.0	-15.00	-176.81	15	KIP	40.62	16	13
1991	03	03	15:20:32.0	-22.09	-174.58	23	KIP	46.17	7	5
1991	04	06	14:34:28.2	-14.86	-175.36	15	KIP	39.87	14	12
1991	04	19	11:25:37.3	-15.01	-174.90	15	KIP	39.81	15	13
1991‡	06	09	07:45:10.9	-20.15	-175.90	292	KIP	44.86	0	19
1991	08	05	06:05:50.3	-21.58	-173.68	15	KIP	45.39	4	11
1991‡	09	30	00:21:54.0	-20.67	-178.52	590	KIP	46.38	0	17
1991	10	17	09:05:28.4	-14.83	-173.41	62	KIP	39.06	8	4
1991	10	30	10:35:51.9	-15.11	-173.07	48	KIP	39.19	8	7
1991‡	12	03	10:33:47.3	-26.11	178.69	575	KIP	52.37	0	25
1992‡	06	25	06:31:01.1	-28.17	-176.22	48	KIP	52.34	8	16

Table 4.3. (continued)

Date			Origin Time UT	Latitude °N	Longitude °E	Depth km	Station	Distance °	# of measurements	
									Surf*	Turn†
1992‡	07	11	10:44:32.7	-22.45	-177.96	394	KIP	47.74	0	10
1992	08	30	20:09:10.9	-17.75	-178.59	574	KIP	43.84	0	20
1992‡	11	12	22:29:04.6	-22.32	-177.72	379	KIP	47.53	0	5

* Number of frequency-dependent travel-time measurements of Rayleigh and Love waves

† Number of frequency-dependent travel-time measurements of direct and multiply reflected turning waves

‡ Source-receiver pairs that were also used for the *ScS*-reverberation measurements (Table 4.1).

Table 4.4. Summary of the inversion results for model TH2

Phase	Number of Data	Data Importance	χ^2/D Reference Model	χ^2/D After Denuis.†	χ^2/D After Inversion	Variance Reduction
Rayleigh	168	4.17	12.90	2.81	2.09	0.84
Love	113	3.79	12.79	1.43	1.35	0.89
S_V	285	6.68	6.00	1.74	0.72	0.88
S_H	292	6.19	7.01	2.79	0.59	0.91
SS_V	133	7.07	4.60	1.74	0.80	0.83
SS_H	59	3.26	8.07	1.66	1.91	0.76
SSS_V	66	2.23	16.30	2.48	1.79	0.89
SSS_H	6	0.04	0.78	0.34	0.56	0.28
0th-order reverberations	148	5.70	245.11	12.50	1.41	0.99
1st-order reverberations	156	7.76	164.73	9.91	3.63	0.98
All phases	1426	46.90	50.15	4.09	1.41	0.97

† This column shows the χ^2 estimates (normalized by the number of data) after projecting the errors in source origin-time (and depth for the reverberative interval) out of the original data.

Table 4.5. Summary of the inversion tests corresponding to the models in Figures 4.7 and 4.8

model	σ_{UM} (%)	σ_{TZ} (%)	σ_{AN} (%)	σ_{AN} (%)	σ_{410} (km)	σ_{660} (km)	$\frac{\chi^2_{GSDF}}{D}$	$\frac{\chi^2_{REV}}{D}$	$\frac{\chi^2_{TOT}}{D}$	Remarks
TH1	2	1	0.5	0.5	10	10	1.11	2.58	1.42	
TH2	2	1	0.5	0.5	10	10	1.09	2.58	1.41	
TH2.a	2	1	0.5	0.5	10	10	1.00	------	1.00	ScS-reverberation data excluded
TH2.b	2	1	0.5	1	10	10	1.06	2.57	1.38	
TH2.c	2	1	0.5	0	0	0	1.14	3.01	1.53	
TH2.d	2	1	0.5	0.5	8.4	5.6	1.12	2.80	1.48	Equilibrium-olivine model enforced‡
TH2.e	2	1	0.1	0.5	10	10	1.18	2.63	1.49	
TH2.f	1	1	1	0.5	10	10	1.09	2.56	1.40	

‡ The enforcement of an equilibrium-olivine model through the prior covariance matrix is described in Section 4.6.1.

FIGURE CAPTIONS

Figure 4.1. Mercator projection of the central Pacific showing the study corridor from the Tonga-Fiji seismic zone to the stations HON and KIP on Oahu, Hawaii (inverse black triangle). The axis of the corridor (dashed line) samples a uniform old ocean basin with seafloor age ranging from 100 to 125 Ma (isochrons, marked by black contours, are taken from *Mueller et al.* [1993]), and is roughly perpendicular to the current plate motion relative to the hotspot reference frame (black arrow, from *Gripp and Gordan* [1990]). Epicenters of the 77 Tonga-Fiji events and one Hawaiian event used in this study are shown as white symbols (circles: shallow-focus; diamonds: intermediate-focus; squares: deep-focus). Gray circles are surface bounce points of ScS_n phases (core-reflection numbers n = 2-4) from 28 events. Bathymetric variations are shown by illuminated gray shading in the map.

Figure 4.2. The shear-wave structure and the Q structure of model PA5, our reference model for the upper mantle. Mean shear-wave speeds and quality factors are plotted on the right, and the anisotropic velocity perturbations relative to these mean velocities are plotted on the left. Below 800 km the model is the same as PREM [*Dziewonski and Anderson,* 1981] at a reference frequency of 35 mHz, with a quality factor of Q_{LM} = 231. PA5 is a path-average, radially anisotropic model that was obtained for the Tonga-Hawaii corridor by *Gaherty et al.* [1996]. It is based on a joint inversion of frequency-dependent travel times of surface and turning waves (such as R_1, G_1, *SSS*, *sSS*, *SS*, and *S*) together with travel times and impedance contrasts for mantle discontinuities, obtained from the *ScS*-reverberation study of *Revenaugh and Jordan* [1991a-c]. The inversion included mineralogical constrains for density and bulk sound velocity.

Figure 4.3. Plots of ScS_n–ScS_m observed travel-time residuals relative to the PA5/PREM reference model. The ScS_4–ScS_2 residuals in the middle panel have been divided by two

to normalize them to a two-way time. The positive offset of the data indicates a generally slow lower mantle in this region of the Pacific [*Su et al.*, 1994; *Masters et al.*, 1996] However, the large variation of differential times from individual events [*Sipkin and Jordan*, 1980a] and the systematic variation with distance [*Gee and Romanowicz*, 1992] cannot be explained by a different spherically-symmetric earth model or by changing the source location and/or origin time.

Figure 4.4. Top six panels are photographs taken at progressive times from the laboratory experiments of *Richter and Parsons* [1975], in which a fluid layer with a vertical temperature gradient was placed in a box with a moving upper boundary. The effect of the shear from the top was to transform the initial multimodal convection into longitudinal rolls. The implication to the Earth is shown at the bottom panel which illustrates that the large scale circulation of the plates may be accompanied by small-scale convecting rolls which are oriented parallel to the absolute plate motion and are confined above the 660 discontinuity. Figures are taken from *Richter and Parsons* [1975].

Figure 4.5. A subset of the seismograms that were used to measure *ScS*-reverberation travel times. For each record pair, the top trace is the data seismogram, the bottom trace is the synthetic, calculated for PA5/PREM. The synthetics were corrected for ellipticity, bounce-point bathymetry, and an average lower mantle of S12_WM13 (which is significantly slower then PREM in this region, as implied from Figure 4.3). All traces are band-pass filtered with corner frequencies at 15 and 40 mHz. First-order reverberations can be individually identified on each of these records.

Figure 4.6. Example of GSDF data obtained for the Tonga-Hawaii corridor. Left panels show observed seismograms (top trace) and isolation filters (other traces). Event date, station name, epicentral distance, hypocentral depth, and component (LPZ for vertical, LPT

for Transverse) are indicated in each panel. Time scale is relative to the origin time. The right panels show frequency-dependent travel times, relative to the PA5/PREM reference model, measured from the seismograms on the left by the GSDF processing described in Chapter 3. The travel-times measurements are shown at 5-mHz intervals for S_H and S_V (circles), SS_H and SS_V (squares), SSS_V (diamonds), and G_1 and R_1 (triangles). Note that 45 measurements (Figures 4.6e and f) are obtained from a single source-receiver pair using 7 isolation filters (Figures 4.6a and b).

Figure 4.7. (a) Model TH1 of *Katzman et al.*, [1997a], shown over the grid that was used for all the inversions. (b) Model TH2 of this study. The two models were obtained by the same procedure, but the dataset for the latter included the ScS_n times from a 1973 Hawaiian earthquake. The models are displayed as relative shear-velocity perturbations to the PA5/PREM reference model in a cross-section through the mantle from Tonga (left side) to Hawaii (right side). Lower figure in each panel shows the relative perturbation in isotropic velocities extending from the Moho discontinuity (M) to the core-mantle boundary (CMB); negative perturbations are in red, positive in blue. Upper figures use same color scale to show the relative perturbation in radial anisotropy, and green and red lines to represent the perturbations to 410 and 660 discontinuities, respectively (5× vertical exaggeration; the topographies are displayed more clearly in Figure 4.9c). Yellow circles are earthquakes used as sources; blue triangle marks location of the receivers.

Figure 4.8. The models obtained from the data-inversion tests summarized in Table 4.5 The models are displayed the same as in Figure 4.8 and their designated names are indicated at the top of each panel. (a) Model TH2.a, obtained from a 2D inversion of only the surface and turning waves data. This model correctly predicts the trends in the multiple-*ScS* differential travel times (see Figure 4.10), although no *ScS* data were used to constrain its lateral variations. (b)-(f) Results from full-dataset inversions where the prior

covariance matrix was modified, according to Table 4.5 and the text, by increasing the prior uncertainty for radial anisotropy in the uppermost mantle (model TH2.b); by completely suppressing the topographies on the 410 and 660 discontinuities and the anisotropic perturbations in the uppermost mantle (model TH2.c); by enforcing an equilibrium-olivine thermal model (model TH2.d); by reducing the lower-mantle prior uncertainty (model TH2.e); and by enforcing a similar prior uncertainty for the whole mantle (Figure TH2.f).

Figure 4.9. (a) Relative shear-velocity perturbation, averaged over the upper 651 km of the mantle (upper 6 grid layers); (b) relative perturbation in radial anisotropy, averaged over the upper 166 km of the mantle (upper 2 grid layers); and (c) Topographic perturbation of the 410 (dashed line) and 660 (solid line) discontinuities for the eight models in Table 4.5 and in Figures 4.8 and 4.9. The corresponding model names are indicated inside each panel. Note the robustness of the pattern for the upper-mantle isotropic anomalies and the anticorrelation between the 410 and 660 topographies.

Figure 4.10. Plots of ScS_n–ScS_m travel-time residuals relative to the PA5/PREM reference model, comparing the observations (black symbols with error bars, Figure 4.3) to those predicted by the TH2 model (gray symbols) and the TH2.a model of Figure 4.8a (resulted from inverting only the turning- and surface-wave data, white symbols). The ScS_4–ScS_2 residuals in the middle panel have been divided by two to normalize them to a two-way time. The strong trend in the data is well predicted by both models. The constant baseline shift of the data relative to the prediction from TH2.a, which is discussed in the text, reflects an inaccurate path-averaged lower-mantle which is not resolved by the turning-wave data.

Figure 4.11. Comparison of shear-velocity model with geoid and topography observations. (a) Oblique, rotated Mercator projection of the central south Pacific, showing the linear, NW-trending geoid anomalies that correlate with the variations in the upper-mantle shear velocities (Figure 4.11b). Geoid is the degree-360 NASA/DMA Joint Geopotential Model [*Lemoine et al.*, 1996], filtered to intermediate wavelengths by cosine tapering the spherical-harmonic coefficients between degrees 20 and 15 and between degrees 80 and 360. White is zero anomaly; warm colors indicate positive anomalies (red > 2 m), cool colors negative anomalies (blue < –2 m). Open black circles show approximate locations of the Society Islands (S), Marquesas (M), and Hawaii (H) hotspots; arrow indicates Pacific plate motion in the hotspot reference frame [*Gripp and Gordan*, 1990], which is subparallel to the average trend of the geoid anomalies. Thick black line is the axis of the Tonga-Hawaii corridor; earthquake and station symbols are same as in Figure 4.1. (b) Top 1200 km of TH2, shown with the same color scale as in Figure 4.7. (c) Plot of shear-velocity perturbation of TH2 averaged over the upper mantle (blue line), filtered geoid averaged over the five dashed and solid profiles in Figure 4.11a (red line), and seafloor topography band-pass filtered like the geoid and averaged over the same profiles (green line). Note the excellent positive correlation among these three profiles between the north end of the Tonga seismic zone and Hawaii. The pole of the oblique Mercator projection in Figure 4.11a is at 52°N, 84°W, and the map has been rotated clockwise by 90°.

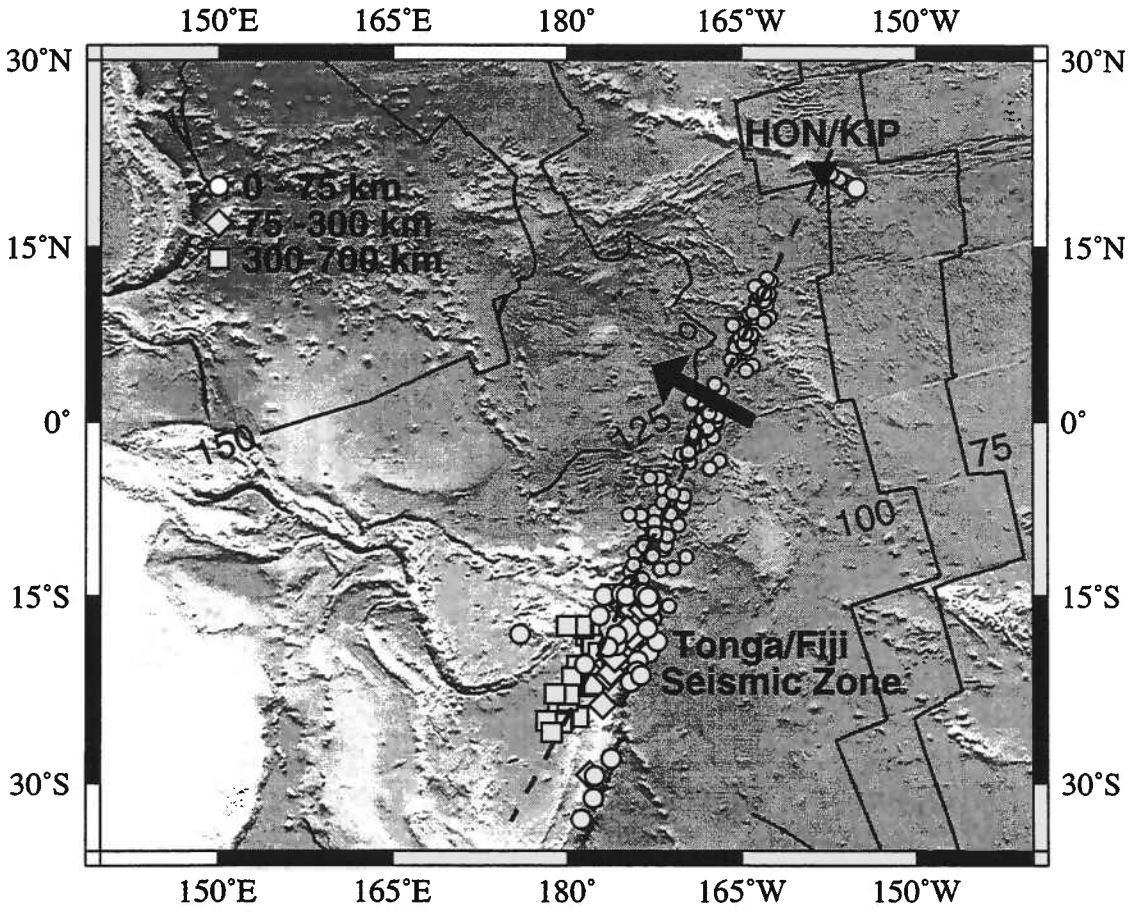
150°E
165°E
180°
165°W
150°W
30°N
15°N
0°
15°S
30°S
HON/KIP
0 - 75 km
75 - 300 km
300-700 km
150
125
100
75
Tonga/Fiji
Seismic Zone

Figure 4.1

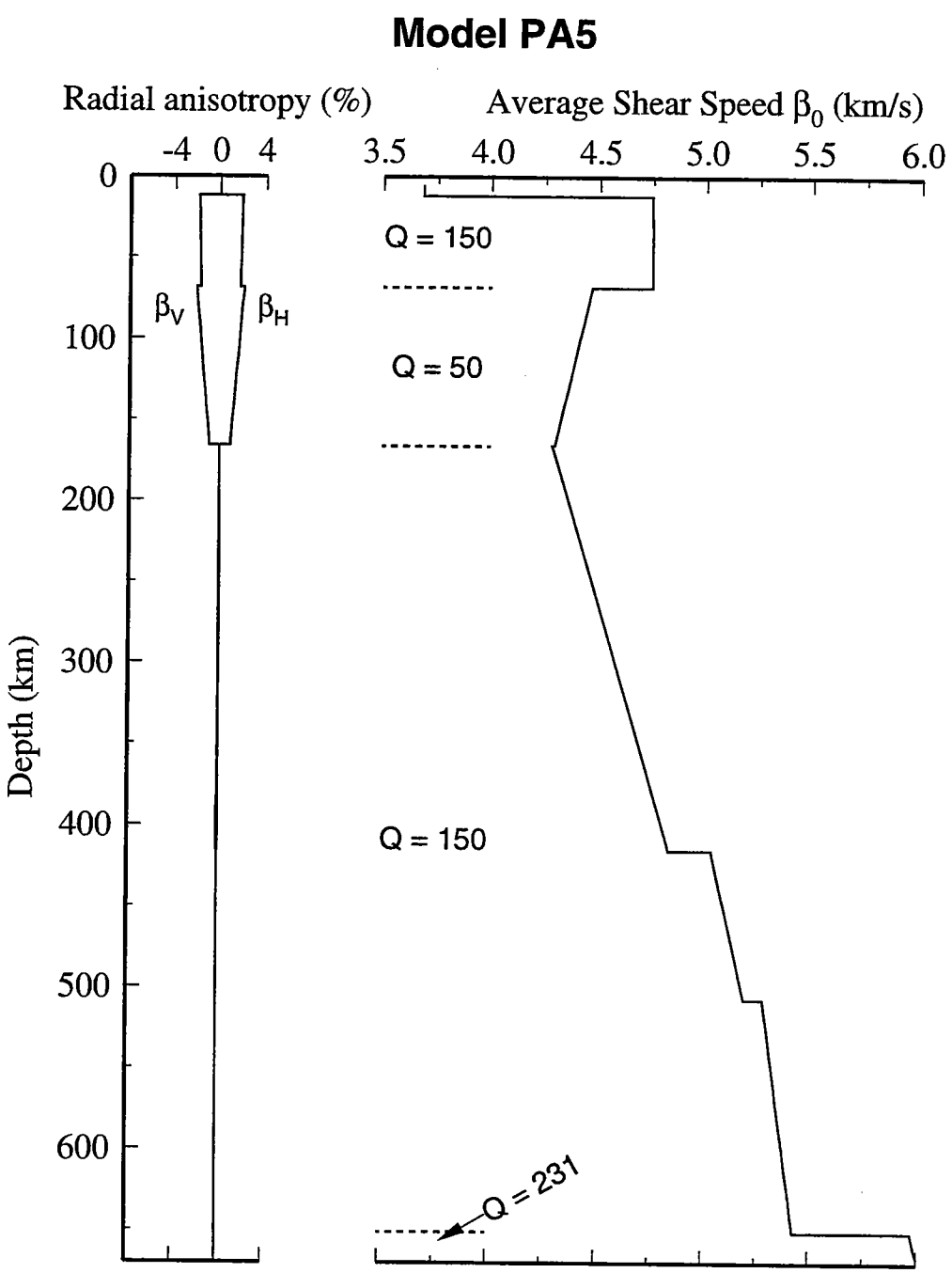
Model PA5
Radial anisotropy (%)
-4 0 4
Average Shear Speed β_0 (km/s)
3.5 4.0 4.5 5.0 5.5 6.0
0
100
200
300
400
500
600
Depth (km)
β_V
β_H
Q = 150
Q = 50
Q = 150
Q = 231

Figure 4.2

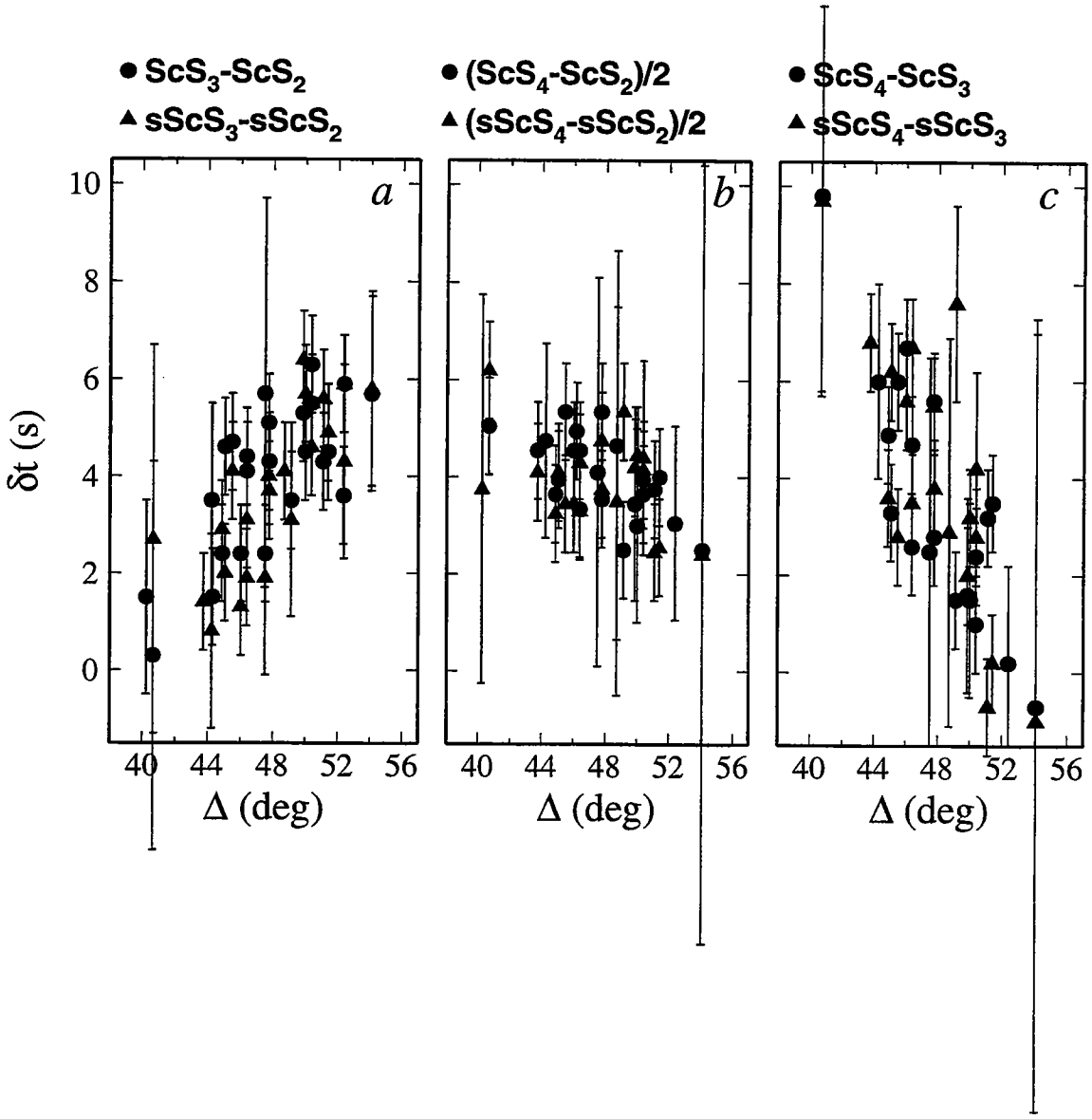
● ScS3-ScS2
▲ sScS3-sScS2
● (ScS4-ScS2)/2
▲ (sScS4-sScS2)/2
● ScS4-ScS3
▲ sScS4-sScS3
a
b
c
δt (s)
Δ (deg)
Δ (deg)
Δ (deg)

Figure 4.3

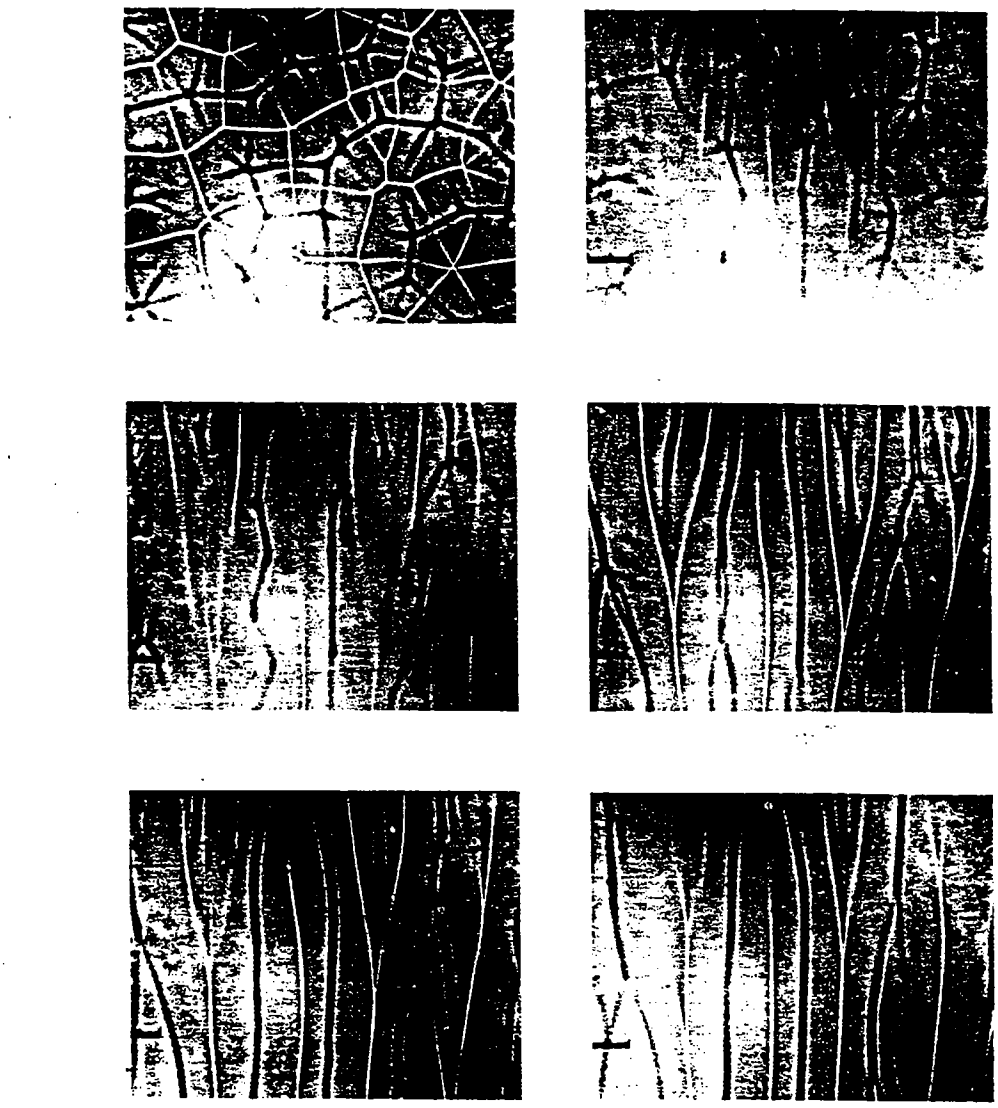

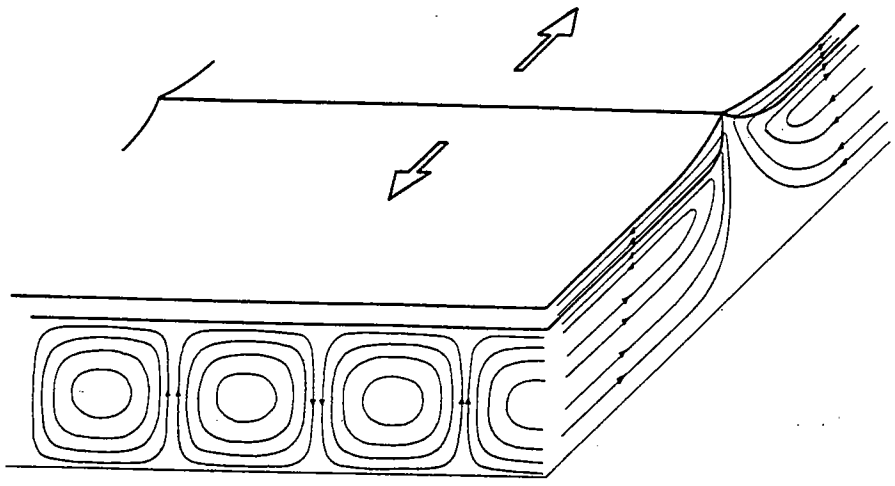

Figure 4.4

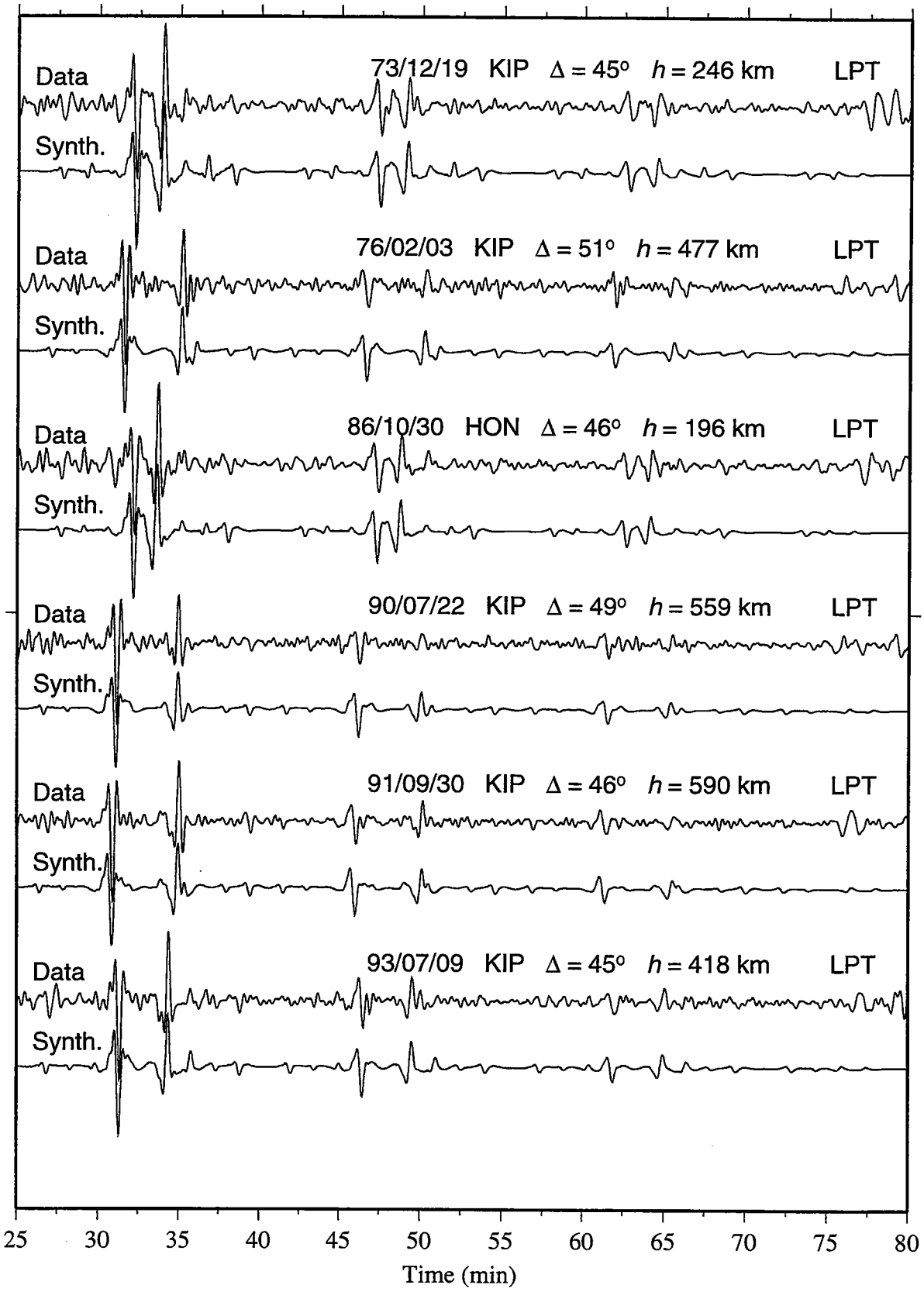
Data
Synth.
73/12/19 KIP Δ = 45° h = 246 km LPT
Data
Synth.
76/02/03 KIP Δ = 51° h = 477 km LPT
Data
Synth.
86/10/30 HON Δ = 46° h = 196 km LPT
Data
Synth.
90/07/22 KIP Δ = 49° h = 559 km LPT
Data
Synth.
91/09/30 KIP Δ = 46° h = 590 km LPT
Data
Synth.
93/07/09 KIP Δ = 45° h = 418 km LPT
25 30 35 40 45 50 55 60 65 70 75 80
Time (min)

Figure 4.5

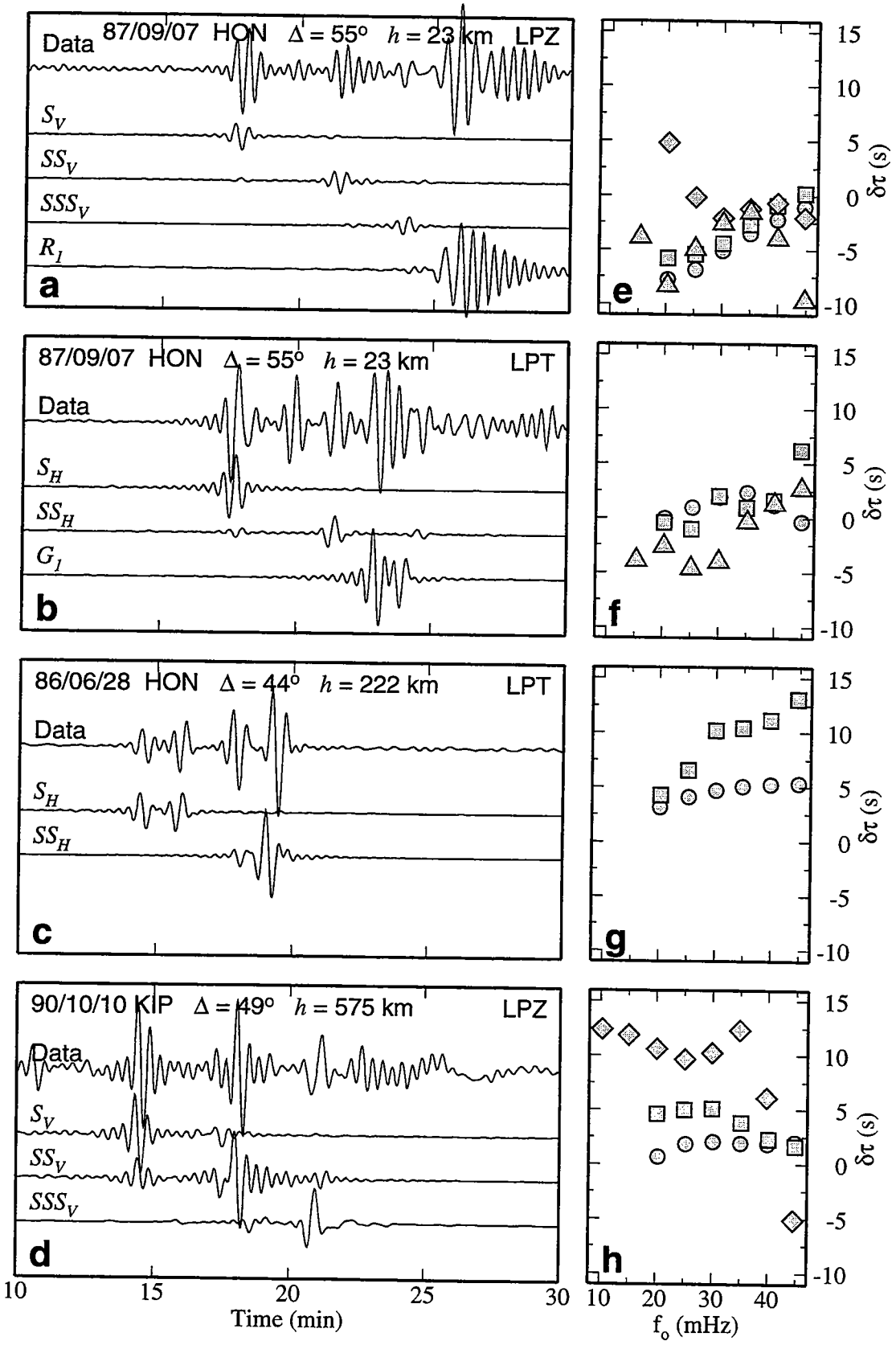
Data 87/09/07 HON Δ = 55° h = 23 km LPZ
S_V
SS_V
SSS_V
R_1
a
87/09/07 HON Δ = 55° h = 23 km LPT
Data
S_H
SS_H
G_1
b
86/06/28 HON Δ = 44° h = 222 km LPT
Data
S_H
SS_H
c
90/10/10 KIP Δ = 49° h = 575 km LPZ
Data
S_V
SS_V
SSS_V
d
e
f
g
h
15
10
5
0
-5
-10
δτ (s)
10
15
20
25
30
Time (min)
10
20
30
40
f_o (mHz)

Figure 4.6

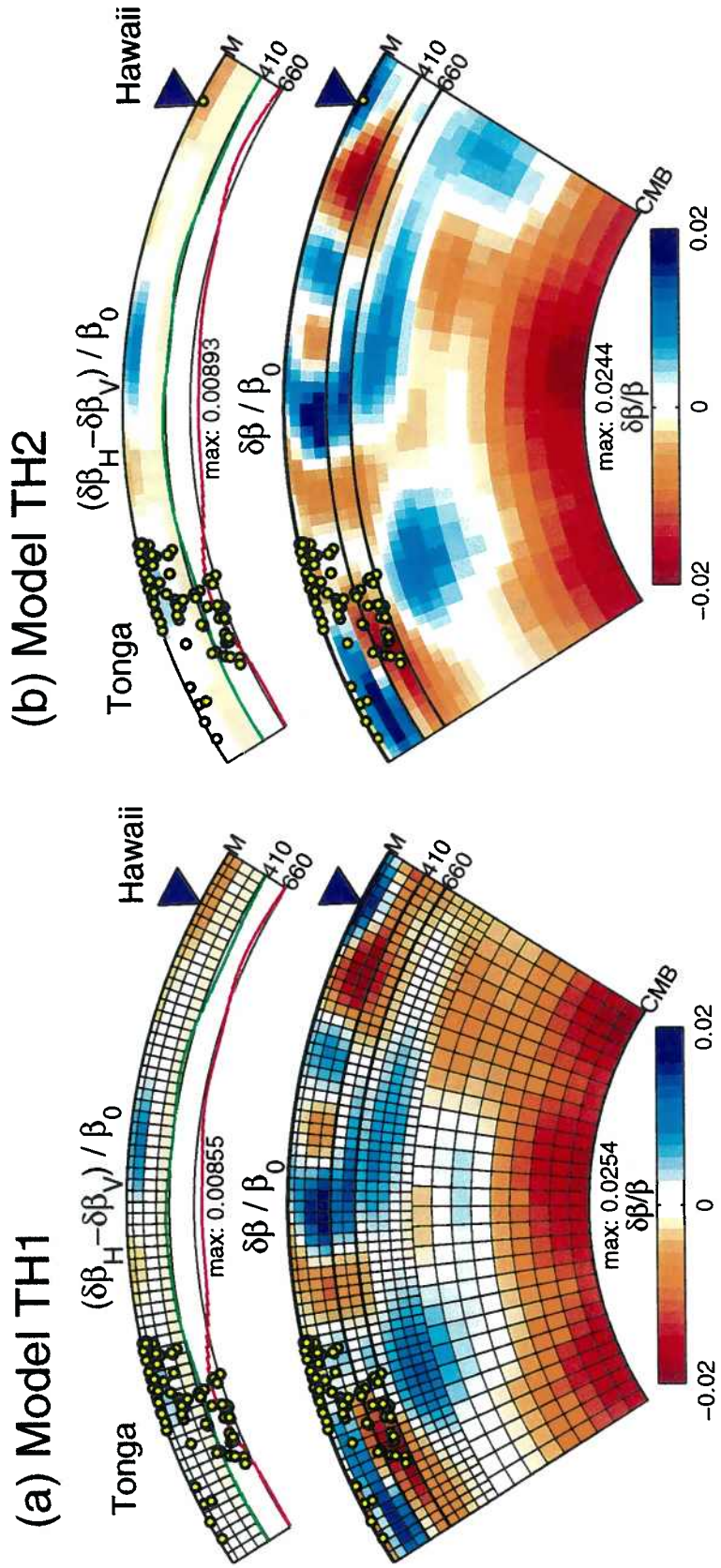
(a) Model TH1
(b) Model TH2
Tonga
Hawaii
M
410
660
CMB
$(\delta\beta_H - \delta\beta_V) / \beta_0$
max: 0.00855
max: 0.00893
$\delta\beta / \beta_0$
max: 0.0254
max: 0.0244
$\delta\beta/\beta$
0.02
0
−0.02

Figure 4.7

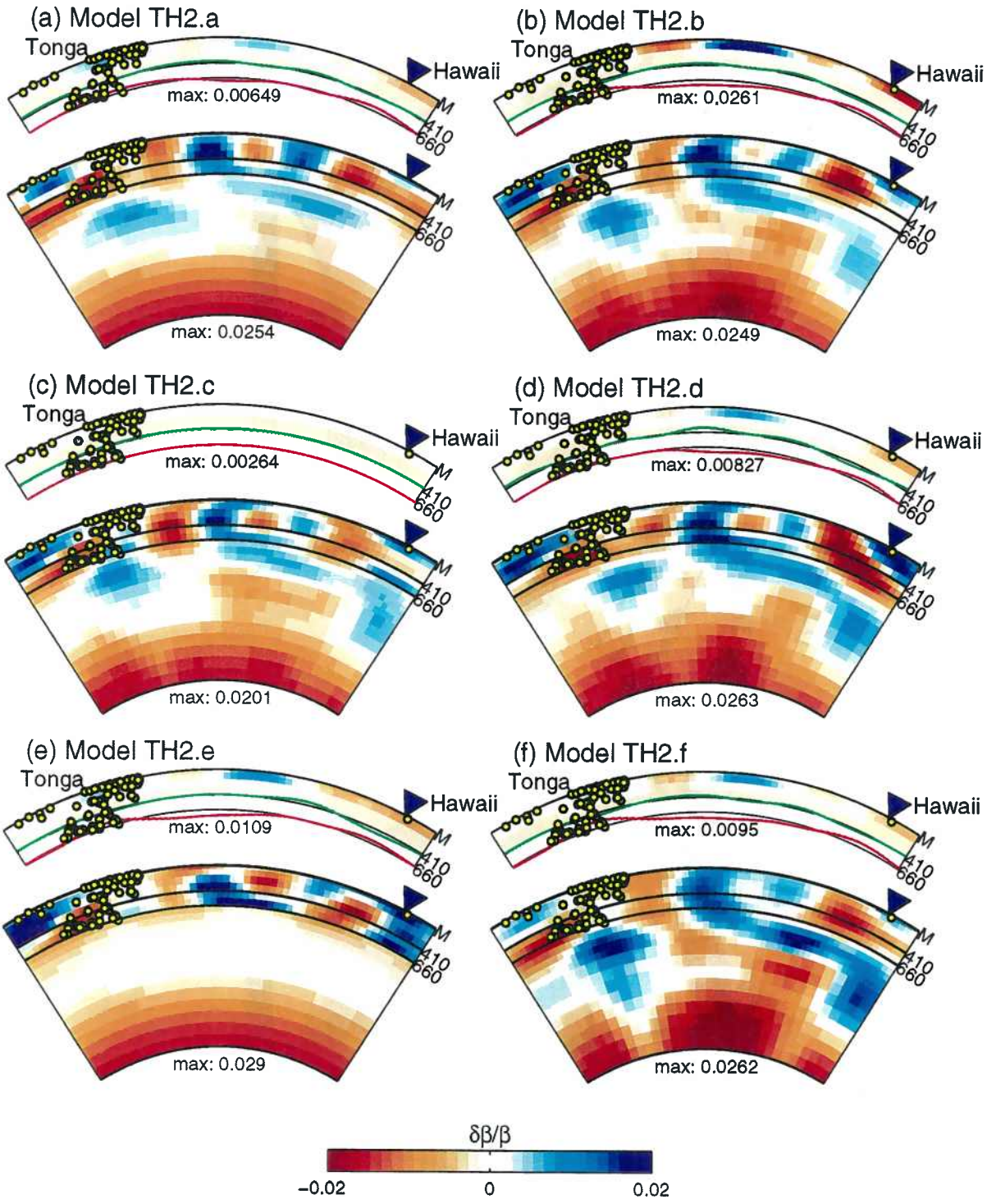
(a) Model TH2.a
Tonga
Hawaii
max: 0.00649
M
410
660
max: 0.0254
(b) Model TH2.b
max: 0.0261
max: 0.0249
(c) Model TH2.c
max: 0.00264
max: 0.0201
(d) Model TH2.d
max: 0.00827
max: 0.0263
(e) Model TH2.e
max: 0.0109
max: 0.029
(f) Model TH2.f
max: 0.0095
max: 0.0262
δβ/β
−0.02
0
0.02

Figure 4.8

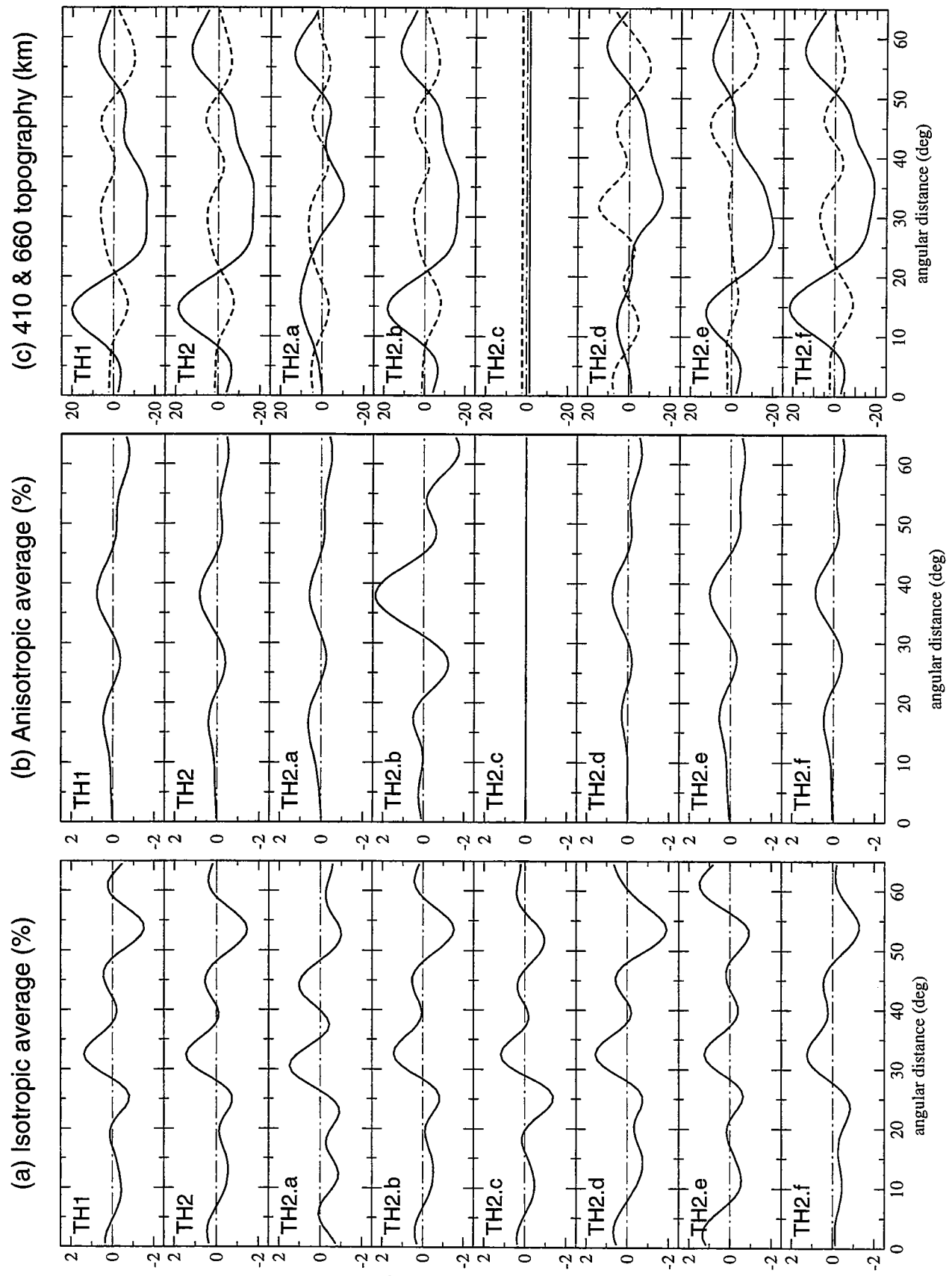
(a) Isotropic average (%)
(b) Anisotropic average (%)
(c) 410 & 660 topography (km)
TH1
TH2
TH2.a
TH2.b
TH2.c
TH2.d
TH2.e
TH2.f
angular distance (deg)

Figure 4.9

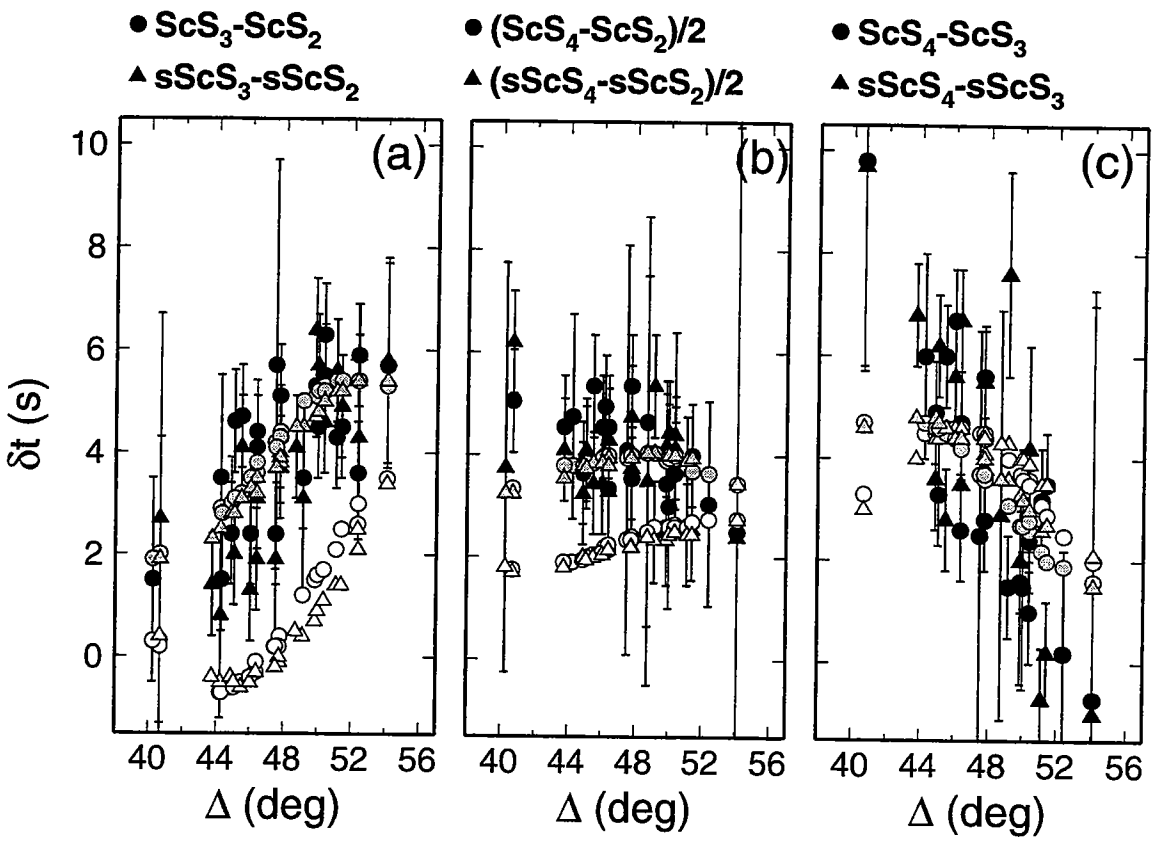
● ScS3-ScS2
▲ sScS3-sScS2
● (ScS4-ScS2)/2
▲ (sScS4-sScS2)/2
● ScS4-ScS3
▲ sScS4-sScS3
(a)
(b)
(c)
δt (s)
Δ (deg)
Δ (deg)
Δ (deg)

Figure 4.10

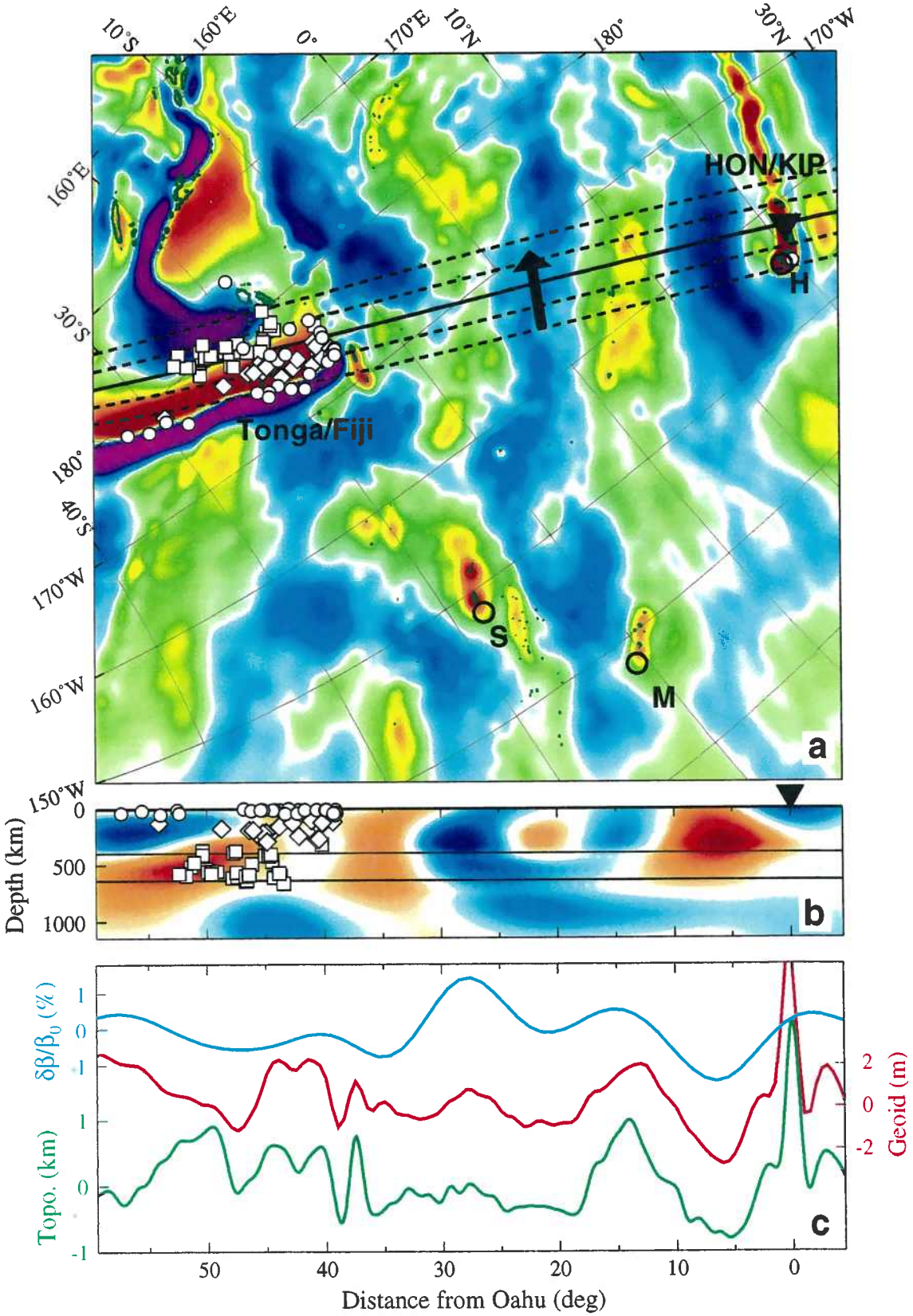
10°S
160°E
0°
170°E
10°N
180°
30°N
170°W
160°E
30°S
180°
40°S
170°W
160°W
150°W
HON/KIP
H
Tonga/Fiji
S
M
a
Depth (km)
0
500
1000
b
δβ/β0 (%)
1
0
-1
Topo. (km)
1
0
-1
2
0
-2
Geoid (m)
c
50
40
30
20
10
0
Distance from Oahu (deg)

Figure 4.11

CHAPTER 5

THE RYUKYU-HAWAII CORRIDOR

5.1 INTRODUCTION

In the previous chapter, we hypothesized that the central Pacific is underlain by a system of Richter-type convection rolls that are oriented subparallel to the absolute plate velocity, with downwelling axes that underlie high-velocity, chemically-buoyant residuum which supports the hotspot swells in the region. This hypothesis, which was generated based on a corridor that cuts across the swells, is tested in this chapter by imaging the mantle structure along the Hawaiian swell.

The paths between earthquakes in the Ryukyu and the Izu-Bonin seismic zones and the stations KIP and HON on Oahu define a corridor which sample the entire 2100 km of the Hawaiian swell from Midway to Oahu (Figure 5.1). This corridor extends several thousands of km westwards to the swell, where it samples an old part of the Pacific plate, with ocean depth of about 6 km and crustal age ranging from 120 to 160 Ma. Farther to the west the corridor cuts across the Izu-Bonin subduction zone and traverse the northern part of the Philippine-Sea plate (age $\leq$ 50 Ma) toward the Ryukyu subduction zone. Despite the intense seismicity of the Ryukyu and Izu-Bonin seismic zones, their orientations relative to the stations on Oahu forces us to select events with a rather wide range of back azimuths, in order to obtain a sufficient range of distances for the inversion (Figure 5.1). It should be noted that when a large range of azimuths is used, a potential bias can arise from averaging the 3D structure outside the corridor into the plane of the corridor. However, as we show later, this bias is small along the Hawaiian swell, where all the great-circle paths converge to the stations on Oahu.

Previous results from seismological studies of the Pacific did not reveal any anomalous structure associated with the Hawaiian swell. *Woods et al.* [1991] and *Woods and Okal* [1996] measured group and phase velocities of Rayleigh-waves between their station on Midway and the global stations on Oahu. They found that the shear velocities are consistent with a normal lithosphere of 50-110 Ma with no indication for lithospheric rejuvenation, as suggested by *Detrick and Crough* [1978]. While *Woods and Okal* [1996] did not compare the mantle beneath the swell to adjacent mantle regions, other regional [*Zhang and Tanimoto*, 1989] and global studies [*Su et al.*, 1994; *Masters et al.*, 1996; *Ekström and Dziewonski*, 1997] showed no indication for either high or low velocity anomalies associated with the swell.

Farther to the west, where the Pacific crust is older, many of the global studies show fast velocities in the uppermost mantle, which decrease sharply into rather slow velocities beneath the much younger Philippine-Sea plate. Very slow lid velocities are also observed in the regional PHB3 model of *Kato and Jordan* [1997] for the western Philippine-Sea. This 1D radially-anisotropic model exhibits a thicker lid relative to the Pacific PA5 model of *Gaherty et al.* [1996], but it is significantly slower than PA5 in the upper 160 km of the mantle and slightly faster in the transition zone [*Gaherty et al.* 1997] (Figure 5.2). Fast anomalies in the transition zone beneath the Philippine Sea are also revealed by the global tomographic studies as well as in the regional tomographies of the Izu-Bonin slab [*Zhou and Clayton*, 1990; *van der Hilst et al.*, 1991].

In this chapter we jointly invert 1681 frequency-dependent travel times of turning and surface waves together with 82 travel times of multiple *ScS* waves to obtain the 2D structure in the vertical plane of the Ryukyu-Hawaii corridor. Owing to low signal-to-noise ratio (snr) of the reverberative intervals, we do not employ first-order reverberations in this study. The inversion procedure and parameterization are similar to the one described in Chapter 4, but prior to this inversion, we add a correction to the measurements which accounts for the crustal heterogeneity along the path. We construct a vertical tomogram

through the mantle for this corridor, which is tested by a suit of resolution tests, and by a series of full and partial data-set inversions. The model is substantiated by a joint inversion of the Ryukyu- and Tonga-Hawaii corridors which ties the two tomograms beneath Oahu. All the tomograms reveal a fast anomaly beneath the entire Hawaiian swell (relative to a model for a 100 Ma old lithosphere), which is discussed in the context of the Tonga-Hawaii results from the previous chapter. We also devote a short discussion to the western part of the corridor, which exhibits a very slow anomaly in the uppermost 160 km of the mantle beneath the Philippine Sea.

5.2 Reference model and Attenuation structure

Despite the tectonic heterogeneity of the Ryukyu-Hawaii corridor, which traverses two plates and a hotspot swell and crosses two subduction zones, the combined velocity structure of PA5 for the upper mantle and PREM for the lower mantle appears to be an acceptable reference model (section 4.1, Figure 5.2). Many of the arrivals recorded on Oahu are well modeled by synthetic seismograms that are computed for the PA5/PREM model, especially for paths that sample only the western Pacific (e.g., Figure. 5.3). For these paths, the PHB3 synthetics do not fit the data nearly as well as PA5 (Figure 5.3), but even for the longer paths from Ryukyu, which traverse partly along the Philippine-Sea, the PA5 synthetics fit the data better. This is because more than 70% of the corridor length from Ryukyu to Hawaii is along a Pacific mantle, which underlies crustal ages of 90 Ma or more (Figure 5.1) that is evidently well modeled by PA5. As we show in section 5.5, however, paths that propagate through the Philippine-Sea, produce surface-wave phase delays of up to 40 s relative to PA5. These large travel-time residuals raise the issue of whether the linear functional relationship between $\delta\tau(\omega)$ and the model perturbations $\delta\mathbf{m}$, which is represented by the Fréchet kernels, is adequate.

To evaluate this linear relationship, we tested whether it can predict the large difference between the Pacific and the Philippine models by the following two steps. First, for a

selected set of wavegroups, we measured the exact frequency-dependent phase-delay differences, as predicted by full synthetics calculated for the PHB3 and the PA5 models. The epicentral distances (around 18°-20°) and the hypocentral depths were chosen according to real paths from Izu-Bonin earthquakes to TATO (in Taiwan) for which the R_1, G_1, and S wavegroups traverse mainly through the upper mantle and are thus strongly affected by the large difference between two models. The synthetics were calculated using complete normal-mode summation up to frequency of 50 mHz, and the phase delays were obtained using the same GSDF-measurment procedure that was utilized for the real data (cf. Sections 4.4 and 5.4); in this experiment, however, the data seismograms were represented by the PHB3 synthetics and the isolation filters were computed using the PA5 reference model (Figures 5.4a-d). The resulting measurements range between 0 and 30 s (open circles in Figures 5.4e-h), with large dispersions relative to PA5 for the Rayleigh and the intermediate-focus S_V waves (Figures 5.4f and g, respectively). In the second step, we expressed PHB3 as a perturbation to the PA5 model, and computed the travel-time residuals predicted by this perturbation using the appropriate Fréchet kernels. As seen by the open diamonds in Figures 5.4e-h, the phase delays predicted by this linear theory resemble the "observed" ones across the frequency band for both the surface and the turning waves, and the large relative dispersions are well reproduced. Near the lower- and higher-end of the frequency band, however, the predictions tend to deviate more from the measurements, and we therefore assigned larger errors to these measurements during the inversion procedure to reflect their inferior accuracy. On the whole, this experiment shows that the velocity structure of PA5 is sufficiently good to be used as a reference model for the entire Ryukyu-Hawaii corridor.

The attenuation structure of PA5, does not provide a good representation for the Ryukyu-Hawaii corridor. This attenuation profile, with average quality factors of $Q_{PA5}^{UM} = 113$, $Q_{PA5}^{LM} = 231$, and $Q_{PA5}^{WM} = 174$ for the upper, the lower and the whole mantle, respectively (Figure 5.5a) produces synthetic body waves whose amplitudes are

comparable to the observed. However, the synthetic surface-wave amplitudes, especially of the Rayleigh waves traversing from Izu-Bonin to Oahu, are consistently and significantly lower than the data (e.g., figure 5.5c). Using a simple forward modeling procedure, we noticed that, by increasing the Q significantly in the lid (including the crust) and in the low-velocity zone and decreasing it only slightly in the lower part of the upper mantle (Figure 5.5b), we were able to fit the amplitude of the surface waves without corrupting the amplitudes of the turning waves from either shallow-focus or deep-focus events (Figures 5.5c, d). The average quality factor of the resulting attenuation model, $Q_{RH1}^{UM} = 140$ and $Q_{RH1}^{WM} = 194$ for the upper and whole mantle, respectively, were slightly larger than those in PA5, in a rough agreement with *ScS*-attenuation studies in the western and central Pacific [*Sipkin and Jordan*, 1980b]. (The effect on our *ScS* waves however was negligible.) We note, however, that recent global studies of surface- and body-wave attenuation [e.g., *Romanowicz*, 1995; *Bhattacharyya et al.*, 1996, respectively] do not show lower attenuation in the uppermost mantle of the western Pacific relative to the south-central Pacific, as implied here.

5.3 MULTIPLE *ScS* -WAVE DATA FOR THE RYUKYU-HAWAII CORRIDOR

Using the cross correlation procedure described in Chapter 2, we measured the travel times of 82 multiple *ScS* waves on the transverse components of 13 seismograms (Table 5.1). Of these seismograms, 10 were recorded at KIP and HON, both on Oahu, from 8 Izu-Bonin ($55° \leq \Delta \leq 58°$), one Ryukyu and one Hawaiian earthquakes (the latter was also used in the study of the Tonga-Hawaii corridor). These data were complemented by additional *ScS* travel times that were measured on 3 seismograms recorded at TATO, on Taiwan, from 3 Izu-Bonin events ($16° \leq \Delta \leq 17°$). For the 1973 Hawaiian event, the focal mechanism was taken from *Butler* [1982]. For all the other events, we used the Harvard CMT solutions. The events were of moderate size ($6.0 \leq M_W \leq 7.1$), with hypocentral depths of 166 to 523 km (with the exception of two shallow-focus events). The horizontal

components of the recorded seismograms were rotated, and the transverse components were deconvolved using a damped-least-squares algorithm. This was followed by filtering with a zero-phase Hanning taper having a corner and a maximum frequency at 40 and 60 mHz, respectively. Figure 5.6 shows some examples of the reverberative intervals used along this corridor.

Unfortunately, we were unable to measure first-order *ScS* reverberations on these records because of their poor snr (Figure 5.6). As we discuss later, this limits the resolving power for the topography on the 410 and 660 discontinuities along the corridor. We measured, however, the travel times from a few well-isolated ScS_1 and $sScS_1$ arrivals outside the reverberative interval (i.e., prior to the *SSS* arrival time; see for example, event 92/01/12 in Figure 5.6). We also measured zeroth-order *ScS* travel times on some radial records from TATO which had a particularly high snr. The latter were measured using the full GSDF analysis (next section) because the ray-theoretical code used to analyze the transverse-components *ScS* waves was designed for an *SH* system only. The ScS_n-ScS_m travel times observed along this corridor do not show any consistent trend with epicentral distance, but they average to about -2 s (-3 s below the Philippine-Sea plate), 6 s faster than in the south-central Pacific (Chapter 4), implying that the lower mantle in this region is faster than beneath the Tonga-Hawaii corridor, in agreement with the global tomographies [e.g., *Dziewonski et al.*, 1996; *Masters et al.*, 1996; *Li and Romanowicz*, 1996]

5.4 Surface- and Body-Wave Data for the Ryukyu-Hawaii Corridor

The data set for the body and surface waves comprised 1681 frequency-dependent phase delays from 274 waveforms on 85 long-period seismograms (67 vertical, 36 radial, and 59 transverse components). The distribution of the events and stations are shown in Figure 5.1 and Tables 5.2 and 5.3. 54 of the 85 seismograms were recorded on Oahu from 29 Izu-Bonin and 35 Ryukyu events, 19 seismograms were recorded on Taiwan,

from 18 Izu-Bonin and one Hawaiian events, and only 2 of the seismograms were recorded on Japan (from the two Hawaiian events). We can therefore loosely classify the data into 18 Izu-Bonin to Ryukyu paths, 31 Izu-Bonin to Hawaii paths, and 36 Ryukyu to Hawaii paths; the latter traverse both the Philippine-Sea and the Pacific plates while the others traverse only one plate. All the earthquakes were of moderate size ($5.9 \leq M_W \leq 7.4$) with well-determined Harvard CMT solutions. Some of the transverse components were also used for *ScS*-reverberations measurements (Table 5.1). We also measured 10 multiple *ScS* travel times on the radial component of 4 seismograms recorded at TATO.

The Izu-Bonin and the Ryukyu subduction zones strike at large angles of about 90° and 60°, relative to great-circle paths from Oahu (Figure 5.1), which limits the epicentral-distance range to KIP and HON along any particular great-circle path. We were able to obtain a significant epicentral-distances range to Oahu of 53.7° to 74.8° only by choosing a rather large back-azimuth range of 285.3° to 297.4° (Tables 5.3). This range of epicentral distances is sufficient to obtain a good upper-mantle resolution along the entire corridor (Section 5.6.4), but the wide azimuthal range implies that the structure beneath the Philippine-Sea plate is averaged over a few hundreds km transverse to the plane of the corridor. As we show later, the result beneath the Hawaiian swell is not biased by this effect.

The measurement procedure was the same as for the Tonga-Hawaii corridor (Chapter 4). The recorded-seismograms were rotated into the tangential-radial-vertical coordinate system and were low-passed with a zero-phase filter having a corner frequency of 45 mHz. Full mode synthetic seismograms (completed to 50 mHz, and filtered like the data) were calculated for each event-station pair using the PA5 reference model with the modified Q structure (Figure 5.5b). Isolation filters were constructed for candidate wavegroups, and the data were downgraded or eliminated if the agreement was poor either because of low snr or interference by phases not included in the isolation filter (for example, when the *ScS* arrives within the time window of the *SS* arrival). The isolation

filters were cross-correlated with the data seismograms, and the resulting time series were windowed and filtered in 5-mHz bands between 10 and 45 mHz. The phase delays recovered by fitting Gaussian wavelets to the narrow-band cross-correlagrams were corrected for windowing and filtering effects and interference with other wavegroups using the procedures discussed by *Gee and Jordan* [1992]. We did not apply the narrow-band filtering in the measurements of the 10 radial-component *ScS* arrivals because these body waves are very non-dispersive. Instead, we obtained only one wide-band measurement for each of these *ScS* wavegroups, and calculated their corresponding wide-band Fréchet kernels which were comparable to the ray-theoretical kernels (cf. Figure 2.4). Table 5.4 summarizes the data distribution by wave type.

5.5 Key Features in the Data Set

Some of the key features in the data-set are illustrated in Figures 5.7, which shows examples of seismograms, isolation filters, and travel-time measurements for a few representative paths. The implications of these observations for mantle structure can be understood by observing a subset of their Fréchet kernels (Figure 5.8). The first example focuses on paths that traverse only through the Philippine-Sea plate, from Izu-Bonin to Taiwan; it shows that an *S* wave from a deep focus event is well modeled by the synthetic isolation filter (top two traces in Figure 5.7a), while a Rayleigh wave from a shallow focus event is significantly delayed relative to PA5 (bottom two traces in Figure 5.7a). This difference is quantified by the GSDF measurements (Figure 5.7b), which show nearly zero travel-time residuals at all frequencies for the *S* wavegroup, but very large phase delays for the R_1 wavegroup, which varies from 20 to more then 40 s across the frequency band. This behavior was very consistent among all the paths from Izu-Bonin to TATO, as seen by averaging the observations from the 8 surface waves and 10 *S* waves recorded along this part of the corridor (Figure 5.9a). While these *S* and R_1 waves propagate only beneath the Philippine Sea, they exhibit very distinctive sensitivity to average shear-wave speed. At

30 mHz, the *S* wave arrival time is mostly sensitive to the structure in the transition-zone and in the uppermost mantle near Taiwan (Figure 5.8a), while the R_1 arrival time is sensitive to the lid structure and to the uppermost 150 km of the mantle (Figure 5.8b). The observations in Figure 5.9a, thus, directly imply that the uppermost mantle beneath the Philippine Sea is significantly slower than PA5; the large positive slope of the surface waves residuals favor a very slow lid velocity. This interpretation agrees with the PHB3 model of *Kato and Jordan* [1997] and is confirmed in our own inversion (next section).

The next example demonstrates that paths traversing only the Pacific part of the corridor, from Izu-Bonin to Oahu, produce waveforms that are better fitted by the PA5 synthetics (Figure 5.7c). For this example, the observed R_1 waveform is advanced by a few seconds, and the *S*, and *SS*, wavegroups are delayed by 2-5 s (Figure 5.7d). The Fréchet kernels of these waves at a single frequency are shown in Figures 5.8c-e, respectively. Averaging the entire data set associated with the Pacific paths from Izu-Bonin to Hawaii reveals a similar pattern, where the surface waves are advanced by 0-4 s, whereas the turning waves are delayed relative to PA5. The phase delays of the *S* and *SS* waves are somewhat larger than those of the *SSS*, which have a smaller depth of penetration. It is interesting to compare these observations to those from the Tonga-Hawaii corridor (Chapter 4), where both the body and the surface waves average to a delay of about 4 s (Figure 5.9d), which reflects a constant station correction for KIP and HON. (This correction is taken into account in our inversions through the source statics). The surface waves from Izu-Bonin to Oahu are, therefore, about 4-8 s faster then those from Tonga to Hawaii (ignoring the 20% difference in epicentral distances); the large negative residuals at low frequencies imply that the average uppermost mantle beneath the western-Pacific (Izu-Bonin to Hawaii) is significantly faster down to a depth of at least 200 km (see Fig 5.8c). However, the lateral extent of this anomaly and even its exact vertical extent, are not clear from Figure 5.9. These summary plots represent the data rather crudely, because they do not display the variation with epicentral distances and hypocentral depths. The 30

observations in Figure 5.9b, for example, were obtained by averaging 711 surface and body-wave measurements with depth phases such as, *sS* and *sSS*, that were recorded on vertical, radial, and transverse components. It is the variation in sensitivity among these individual observations, which is partly illustrated in Figure 5.8, that provides the upper mantle resolution necessary to determine the lateral and vertical extent of the anomalies.

The data obtained from paths that traverse from Ryukyu to Hawaii share some of the general features from both the Philippine-Sea and the Hawaiian paths. Both the G_1 and the R_1 wavegroups arrive later relative to PA5 (e.g., Figure 5.7e), with large dispersion relative to this model (Figure 5.7f). The average travel time residuals obtained from all the Ryukyu-Oahu paths (Figure 5.9c), also show a positive slope of the surface-waves residuals with average phase delays of 0 to 17 s; these values are larger than for the pure Pacific paths but smaller than for the pure Philippine-Sea paths. These observations substantiate the above interpretation, that the uppermost mantle beneath the Philippine Sea is significantly slower than beneath the western Pacific. We also note that at these epicentral distance, the G_1 wavegroup is a combination of the fundamental-mode surface wave and the *SSS* arrival; the former is more dominant at lower frequencies (Figures 5.8g), while the latter dominates at higher frequencies (Figures 5.8h). These waves are therefore sensitive to lateral heterogeneity along their great-circle paths. (More discussion on this phenomena at shorter distances is given in Section 3.3.)

For the long-distance turning waves, the deeper-penetrating phases show larger delays; the average travel-time residuals for the *SSS*, *SS*, and *S* arrivals are about 0.5, 4.5, and 7 s, respectively (Figure 5.9c). This trend varies, however, for the *ScS* waves which shows a negative mean of the ScS_n-ScS_m travel-times residuals (about -2 s). The combination of fast *ScS* and slow *S* arrivals, which turn at depths of ~2000 km for these epicentral distances, imply that the lowermost mantle beneath this corridor is fast, in agreement with many recent studies [*Dziewonski et al.*, 1996; *Masters et al.*, 1996; *Li and Romanowicz*, 1996; *Wysession*, 1996; *van der Hilst et al.* 1997]. The *S* wave at these

distances are particularly interesting because they show significant splitting between the S_V and the S_H arrivals reaching an average of 5 s at 25 mHz (Figure 5.10a). This S splitting gets significantly smaller for the shorter paths, between Izu-Bonin to Oahu (Figure 5.10b) and they are negligible for the Tonga Hawaii corridor (Figure 5.10c). For large epicentral distances, upper-mantle radial anisotropy cannot generate large S splitting because both the S_V and the S_H waves travel nearly vertically in the upper mantle, with the vertical shear velocity β_V. In addition, a positive radially-anisotropic perturbation to the PA5 upper-mantle model will produce the same form of splitting in SS and SSS which is not observed. Therefore, if radial anisotropy is the cause of this splitting, it must be situated in the lower mantle, presumably close to the turning depth of the S_V and S_H waves, where they are sensitive to β_V and β_H, respectively. Lower-mantle anisotropy above D" has been previously invoked by *Montagner and Kennett* [1996] to account for some of the discrepancy between free-oscillation periods and velocity models obtained from body-wave travel times. The anisotropy at these depths can be explained, for example, by lattice preferred orientation of perovskite, through deformation by dislocation creep [*Karato et al.*, 1995]. However, lower-mantle anisotropy is clearly not required by the S wave splitting in Figures 5.10a and 5.7.f because of the fundamental difference between the propagation paths of the S_H and S_V wavegroups (Figure 5.8i and j). As discussed in Section 3.4, at epicentral distances of around 70-75°, significant portion of the S_V energy is from guided-wave propagation associated with P to S conversions near the source and receiver regions. As seen in Figure 5.8i, the S_H travel time at 30 mHz is sensitive to the shear-wave speed, β, along a theoretical ray path from the source to the receiver; in contrast, the S_V wavegroup at the same frequency, epicentral distance, and hypocentral depth, shows high structural sensitivity along multiple paths that turn about 600 km shallower than the S_H wavegroup (Figure 5.8j). The large splitting observed in Figure 5.10a can therefore be easily explained by lower-mantle heterogeneity and does not require lower-mantle anisotropy.

5.6. INVERSION FOR A VERTICAL TOMOGRAM

5.6.1. Parameterization and Inversion Procedure

1763 measurements (1681 frequency-dependent phase delays and 82 *ScS* travel times) were inverted for the 2D structure in the vertical plane of the Ryukyu-Hawaii corridor using the same linear Gaussian-Bayesian inversion scheme that was used for the Tonga-Hawaii corridor (Section 4.5), with a similar parameterization and only a few modifications. In order to account for the longer corridor, a larger dimension of M =1890 was used for the perturbation vector $\delta\mathbf{m}$, which was organized, as before, into three parts:

(1) 1350 blocks representing the relative variations in isotropic shear velocity, $\delta\beta/\beta_0$, over the entire length of the corridor (90°) and depth of the mantle (2890 km). Blocks with a lateral dimension of 1° and an average vertical dimension of 110 km were used in 4 layers above the 410 discontinuity, 2 in the transition zone, and 5 in the lower mantle from 651 to 1200 km (990 blocks total). Below 1200 km, the grid was coarser with 9 layers of 40 blocks each (~2.25° × 250-km) extending to the core-mantle boundary. The grid is depicted in Figure 5.11a.

(2) 360 blocks representing the relative variations in shear-velocity anisotropy, $(\delta\beta_H - \delta\beta_V)/\beta_0$, in the 4 upper-mantle layers above the 410 discontinuity.

(3) Two sets of 90 segments representing the topographic variations, δr_{410} and δr_{660}, for the two major transition-zone discontinuities.

The inversion procedure, like that in Chapter 4, included two steps; we first inverted the data for a 1D, path-averaged model, which was employed as the prior model in the second inversion for the final 2D model. Before the 2D inversion, a projection was applied

to both sides of the linearized perturbation equations to remove the sensitivity of the data to error in the earthquake origin times and depths (the effect of the latter was considered only for the *ScS* data; see also Eqs. 4.3-4.5). Unlike the inversion for the Tonga-Hawaii corridor, an additional crustal correction was applied to the data prior to the inversions by subtracting the *ScS* travel times and the frequency-dependent phase delays predicted from the bathymetry and crustal-thickness variation along the corridor. The bathymetry profile was obtained from the DBDB5 model, whereas the crustal structure was assumed to be that of PA5 (6.8-km thickness) and of PHB3 (11.5-km thickness) for the Pacific and the Philippine-Sea parts of the corridor, respectively. This crustal correction altered the travel-times by 6 s (for some of the surface-wave data) or less. (We have also tested a more severe correction, where, in addition to the crustal correction, the data were also corrected for the effect of a PHB3 upper-mantle beneath the Philippine-Sea section. In other words, we initiated the inversion with a 2D prior model having a PA5/PREM mantle beneath the Pacific and a PHB3/PREM mantle beneath the Philippine Sea. The final inversion result was unaffected by this modification, and we have therefore chosen not to apply the mantle correction in the inversion process. Nevertheless, this test demonstrated the ability of the inversion procedure to deal with large lateral heterogeneities in the upper mantle.)

5.6.2 Specification of the Correlation Matrices

The data were of similar quality to the observations along the Tonga-Hawaii corridor and their standard deviations varied accordingly from 1 to more than 8 s for the observations with the highest and lowest quality, respectively. The data errors were assigned according to the snr of the data seismogram, and the bandwidth of the observation; these errors were increased for wavegroups which showed significant interference with unmodeled phases; larger errors were also assigned to the narrow-band times, near the lower- and higher-end of the frequency-band (especially for the low-

frequency travel-times of the turning waves) because of their inferior accuracy. As before, more than 50% of the measurements had a standard deviation of less then 2 s.

The prior covariance matrix was specified, like for the Tonga-Hawaii corridor, by the Gaussian prior correlation of (4.9), with a horizontal half-width l_θ of 5° and a vertical half width l_r of 250 km. The prior standard deviations for the model parameters were identical to those used in obtaining the TH1 and TH2 models (Table 5.5). For shear-velocity heterogeneities, we chose values of 2% for the upper mantle, above the 410 discontinuity; 1% for the transition zone, between the 410 and 660 discontinuity; and 0.5% for the lower mantle; these values are consistent with the rms variability of the regional and global models [cf. *Li and Romanowicz*, 1996, Figure 10; *Puster and Jordan*, 1997, Figure 6]. For the radial anisotropic parameter, we chose a standard deviation of 0.5% in the uppermost mantle down to 166 km, which was reduced to 0.1% below 166 km and was tapered to zero below 300 where the radial anisotropy appears to be smaller [*Regan and Anderson*, 1984; *Cara and Lévêque*, 1988; *Nishmura and Forsyth*, 1989; *Gaherty et al.*, 1996; *Kato and Jordan*, 1997]. The prior standard deviations for the 410 and 660 discontinuities were 10 km, comparable to the variability estimated on a larger scale for the central and western Pacific by *Revenaugh and Jordan* [1991b] or obtained in the global model of *Shearer* [1993] and *Flanagan and Shearer* [1997]. No prior correlation was assigned between the two discontinuities (see Section 4.6.2 for additional discussion on the transition-zone discontinuities).

5.6.3 Model RH1

Prior to the final inversion for the 2D corridor structure, the entire data set was inverted for a 1D spherically symmetric perturbation $\delta\overline{\mathbf{m}}$ to the reference shear-velocity structure $\mathbf{m}_0$ of the PA5/PREM model. This model (Figure 5.11a) reveals a negligibly small isotropic velocity perturbation in the upper mantle, which expresses the path averaging of the slow anomalies beneath the Philippine-Sea and the faster anomalies beneath the Pacific

and the subduction zones. The model also indicates that the average topography perturbations on the 410 and 660 discontinuities are insignificant and that the path-average radial anisotropy along this corridor is ~0.2-0.5% higher then in PA5 (3.7%). In the lower mantle $\delta\overline{m}$ is more notable and the velocity perturbation ranges from negative values of -0.5±0.2% in the mid mantle, above 1850 km, to large positive values in the lowermost mantle, reaching about +1.7% in D". This result, which was dictated by the combination of the negative ScS_n-ScS_m and the positive S residuals (Figure 5.9c), is consistent with other studies that indicate a faster then average lowermost mantle in this region [*Dziewonski et al.*, 1996; *Masters et al.*, 1996; *Li and Romanowicz*, 1996; *Wysession*, 1996; *van der Hilst et al.* 1997].

Using the path average model in Figure 5.11a as a prior model, we obtained the preferred model for the Ryukyu-Hawaii corridor, RH1, which is shown in Figure 5.11b as a perturbation to the reference velocity structure of the PA5/PREM model. The model reveals considerable lateral and vertical variations in the upper mantle with velocity anomalies as high as +4.8% and as low as -7.6% (note that the scale in Figure 5.11b is significantly larger than that used for Figure 5.11a and for the Tonga-Hawaii models). Some of the largest velocity anomalies in RH1 directly reflect the data features discussed in Section 5.5. Qualitatively, the large variation simply expresses the wide distribution of the travel-time residuals measured along the Ryukyu-Hawaii corridor. For example, the normalized chi-square for the surface- and turning-wave data (after removing the data residuals due to error in the earthquakes origin time) prior to the RH1 inversion was about 4 times larger than before the TH2 inversion (compare also Figures 5.9a-c to Figure 5.9d). In the western part of the corridor, below the Ryukyu and Izu-Bonin subduction zones, the upper mantle is dominated by high velocities that mark the two slabs down to the bottom of the transition zone. The slab images in RH1 are consistent with those of *van der Hilst et al.* [1991] and *van der Hilst et al.* [1997], but they are wider and smoother in our model because of the longer period of the seismic data. The Izu-Bonin slab gets wider close to the

660 discontinuity, but the transition-zone velocity beneath the center of the Philippine-Sea section is only marginally higher then the reference velocity. This result is dictated by the *S* waves propagating from Izu-Bonin to Taiwan (Figure 5.8a), which exhibit nearly zero phase delays relative to PA5 (Figure 5.9a). The image of the Ryukyu slab is less certain because of its proximity to the model edge; it is also more biased by averaging the heterogeneity transverse to the plane of the corridor (see Section 5.6.5). The fast regions associated with the two subduction zones bound an extremely slow anomaly that covers the uppermost 160 km of the mantle beneath the entire Philippine-Sea section; the lid in this region is 6-7.5% slower than that of PA5, in agreement with the regional study of [*Kato and Jordan*, 1997] (Figure 5.2). The lower mantle beneath the Philippine-Sea region is poorly resolved (Section 5.6.4), but it appears to be faster than average due to the relatively large negative ScS_n-ScS_m residuals in this region (-3 s). In the eastern part of the corridor, near Hawaii, the primary feature is an elongated anomaly in the upper 200-300 km of the mantle, with a large positive velocity perturbation of ~2.5-4.8%, which extends laterally over 2400 km beneath the entire Hawaiian swell. Closer to Hawaii this feature overlies a slow region extending from 300 km to the bottom of transition zone but the upper mantle right beneath the stations at Oahu is faster than PA5, in accord with the results of Chapter 4 for the Tonga-Hawaii corridor and with the relatively fast ScS_n-ScS_m residuals from the 1973 Hawaiian event [*Sipkin and Jordan*, 1980b], which were used here as well. The exact depth extent of the fast anomaly beneath Hawaii is uncertain, however, because the resolving power of the data set for the vertical structure of this near-receiver region is relatively low; this structure is somewhat better elucidated in Section 5.7, where we jointly invert the data-set from the Tonga-Hawaii and Ryukyu-Hawaii corridors (which meet at Oahu). In addition to the isotropic-velocity heterogeneity, RH1 also exhibits several small positive anomalies in radial anisotropy of the uppermost mantle and one larger negative anomaly reaching -2.2% beneath Hawaii. The latter agrees with the results along the Tonga-Hawaii corridor although the anomaly here is larger; it is also consistent with the

S20A model of *Ekström and Dziewonski* [1997] which shows a distinct minimum near Hawaii. Unlike the Tonga-Hawaii models described in Section 4.6, the topography on the 410 and 660 discontinuities along this corridor, appears to be neither correlated nor anticorrelated.

RH1 gives a reasonable fit to the data, with a normalized chi-squared of 2.8 (Table 5.4), which is twice as large as the chi-squared fit obtained by the Tonga-Hawaii inversions (Table 4.4). The inferior data-fit along the Ryukyu-Hawaii corridor is caused mainly by the large surface-waves residuals (especially R_1) which are not sufficiently modeled by even the 12.5% peak-to-trough variation in the upper mantle of RH1. Similarly to the Tonga-Hawaii corridor, this model produces a total variance reduction of 93%, of which much is due the source statics and some is due to 1D structure. The 2D perturbation alone reduces the remaining variance of the data by 60%. The general data features discussed in section 5.5 are well satisfied (Figures 5.9a-c and 5.10a-b), but the large positive slope (with frequency) of the Philippine-Sea surface-wave residuals is under predicted by RH1, suggesting that the lid velocity beneath the Philippine-Sea may be slower than predicted even by this model.

5.6.4 Resolution tests

We investigated the resolving power of RH1 by inverting synthetic data sets computed for a series of input test models. In all these tests, Gaussian noise with standard deviations similar to our error estimates for the real data (up to ~8 s) was added to the synthetic data prior to the inversions, and the recovered models were compared to the input models (Figure 5.12). The procedure was identical to the one used for the Tonga-Hawaii corridor (Appendix A).

We started by inverting data sets with only Gaussian noise, in order to examine the effect of random errors on RH1. The maximum perturbations in the resulting model, which is shown in Figure 5.12a, were 4 times smaller than in RH1 for both velocity

(isotropic and anisotropic) and topography parameters. The rms heterogeneity in Figure 5.12a was also significantly smaller than in RH1 (by more than a factor of 4 for the isotropic and topographic parameters, and by about a factor of 3 for the anisotropic parameters), demonstrating that this model is not significantly biased by random errors in the data. This is particularly true for the large isotropic variation in the uppermost 160 km of the mantle (where the rms ratio between the two models was larger than 6.5).

The remaining examples in Figure 5.12 demonstrate the potential recovery of structural features within the mantle corridor. In the first test (Figure 5.12b), we inverted the data residuals that were predicted by RH1 (after adding the Gaussian noise), and obtained a model which nicely reproduced all the upper-mantle features of the original model with the right amplitude and nearly no smearing (Compare Figures 5.12b to 5.11b). The recovery of the transition-zone structure was also good, but the structural smearing was notable, especially below the Philippine Sea. The resolution for the other features in the model was significantly lower and their recovered magnitudes underestimate the originals, particularly for the anisotropic-anomalies and for some of the lower-mantle anomalies. The resolution for the discontinuity structure was reasonable, apart from an uncertainty of about 10 km associated with random data errors. Unfortunately, the transition-zone topography parameters were significantly less robust then the other model parameters, as discussed in the next section.

Despite the greater length of the Ryukyu-Hawaii corridor, owing to the larger data set and the multiple stations employed here, the resolution in the upper-mantle is comparable to that achieved along the Tonga-Hawaii corridor (Appendix A). Similar checkerboard tests (Figures 5.12c-f), indicated that patterns with horizontal wavelengths of 1500 km are well resolved horizontally as well as vertically in the upper mantle, but not in the lower mantle. An additional inversion test of an elongated fast anomaly, similar to the one beneath the Hawaiian swell in RH1 (Figures 5.12g-h), farther indicated that the vertical resolving length of such a feature is about a 100 km. The Hawaiian swell anomaly in RH1 extends

to a depth of 300-400 km along most of its length (Figure 5.11b), so it is unlikely that the maximum depth extent of the actual anomaly beneath the Hawaiian swell is much shallower than 200 km. The resolution degrades substantially in the lower mantle, which is only partly sampled by the *S* and *ScS* waves; below the 660 discontinuity, small features are not resolved anymore and patterns with horizontal wavelength of 3000 km or more are smeared along the wave paths (Figure 5.12f). The positive mid-mantle anomalies in RH1 are, therefore, most likely a result of this wave-path smearing effect. It is noteworthy that despite the poor resolution, path-average properties in the lower mantle can still be well recovered (Figure 5.12b).

The inversion experiments shown in Figure 5.12 indicate that isotropic velocity variation is not mapped into radial anisotropic heterogeneity or into topographic variations. The nearly similar topography variation in Figures 5.12 a, d, f and h, does not reflect any tradeoffs between velocity and topography parameters; it arise from Gaussian noise, with the same random-number realization, that was added to the synthetic data prior to these inversions. Other inversion experiments showed that opposite also holds, i.e., topography parameters do not map into isotropic velocities. We can conclude that in addition to the good upper-mantle resolution in RH1, the tradeoffs between parameters of different type in this model are very small.

5.6.5 Data Inversions Experiments, Testing the Model Robustness

In the resolution analysis above, as well as in the actual data inversion, we assumed that all the events and stations are distributed along a single corridor. However, some of the Ryukyu and Izu-Bonin earthquakes which were used in this study, are located as far as 500 km away from the corridor which is defined by the great-circle plane from Oahu to Taiwan (Figures 5.1 and 5.13a). The 2D structure in the RH1 model can therefore be strongly biased by lateral heterogeneity perpendicular to the plane of the corridor. We investigated this effect, which was ignored in the resolution analysis, by inverting different

portions of the data using the same procedure as for the whole data. We divided the data recorded only at KIP and HON (both on Oahu) into two halves based on the back azimuth to the earthquakes, and performed a separate inversion for each subset. We also inverted a subset of the data recorded on KIP/HON from Izu-Bonin earthquakes only. Figures 5.13b-d show the three wave paths-geometries, while Figures 5.14b-d show the resulting models obtained from inverting each of the subset individually. The elongated fast anomaly beneath the Hawaiian swell is the most stable feature in the upper mantle and appears with the same geometrical distribution in all cases; this is probably because all the wave paths converge into a narrow region along this area as they approach the stations on Oahu (Figure 5.13a). These tests demonstrate that the fast anomaly beneath the Hawaiian swell is required independently by different portions of the data and is not affected by the lateral variability perpendicular to the corridor. The western part of the corridor, on the other hand, is directly controlled by the back-azimuth range of the data which are employed in the inversion. The lateral extent of the slow region beneath the Philippine Sea, for example, appears shorter than in RH1 when we invert only those data, that correspond to the northern wave paths which sample the narrow, northern-most part of the Philippine Sea (Figures 5.13b and 5.14b); the same low-velocity feature appears longer then in RH1 when a wider section of the Philippine-Sea plate is sampled (Figures 5.13c and 5.14c). It demonstrate, therefore, that slow velocities underlie the entire northern part of the Philippine Sea, and that the western portion of RH1 represents an average over this structure.

We have also tested the robustness of the inversion results to variations in the prior parameterization by inverting the full data set with the same 1D prior as in RH1, but with a different prior covariance. (A similar analysis was employed in Section 4.6.3 for the Tonga-Hawaii corridor). The parameters adopted for three of these inversions are displayed in Table 5.5 and the resulting models are shown in Figure 5.15. The primary inference from these inversion tests is that the isotropic velocities in the upper mantle are

the most robust parameters in RH1. The high velocity anomaly beneath the Hawaiian swell and the subduction zones, and the low velocity anomaly beneath the Philippine-Sea were not altered by (1) increasing the prior standard deviation of the radial anisotropy by a factor of two (model RH1.b, Figure 5.15a); (2) suppressing the topographies on the 410 and 660 discontinuities and the anisotropic perturbations to zero (model RH1.c, Figure 5.15b); and (3) enforcing an equilibrium-olivine thermal model (cf. Section 4.6.1) by specifying the appropriate correlation between the topographies on the 410 and 660 discontinuities and the velocity parameters (model RH1.d, Figure 5.15d). The first model fits the data somewhat better than RH1 and the other two slightly decrease the overall data fit (Table 5.5), but an F test demonstrates that the differences in χ^2/D among the model are not significant at the 95% confidence level.

The topography on the 660 discontinuity in RH1 is depressed beneath the Philippine Sea, and the Ryukyu and Izu-Bonin subduction zones, in agreement with the global study of *Flanagan and Shearer* [1997], it is also uncorrelated with the topography on the 410 discontinuity (in contrast to the result along the Tonga-Hawaii corridor). However, the results in Table 5.5 indicate that the data can be fit nearly as well by an equilibrium-olivine thermal model, where the two discontinuities are anticorrelated (Figure 5.15c) or by a model with no topographic variation at all (Figure 5.15b). While these three models, RH1, RH1.c, and RH1.d, display nearly the same isotropic velocity structure, their transition-zone topographies are significantly different. This imply that the robustness of the topography parameter in RH1 is rather poor, which probably reflects the absence of first-order *ScS* reverberations—the data most sensitive to the discontinuity structure—in the Ryukyu-Hawaii inversions.

The basic features of the anisotropic perturbation, having a minimum negative value near Oahu and few smaller positive anomalies to the west ($\theta < 80$), were not altered by varying the prior parameterization. The minimum in $(\beta_H - \beta_V)/\beta_0$ near Hawaii is consistent with the global model of *Ekström and Dziewonski* [1997] and with our own

inversion results along the Tonga-Hawaii corridor (Figure 4.7), but the variations in RH1 are larger (3.5% peak-to-trough, Figure 5.11b). Despite the stability and large amplitude of these variations, however, their lower bound is close to zero because models with no variations in anisotropy, like RH1.c (Figure 5.15b), fit the data nearly as well as RH1 (χ^2/D = 3.00 and 2.84, respectively; Table 5.5). The anisotropic variation along the Ryukyu-Hawaii corridor should therefore be interpreted with caution.

5.7 Joint Inversion of the Tonga-Hawaii-Ryukyu Corridors

An obvious extension of the inversion methodology presented in this thesis is the incorporation of multiple crossing paths into a full 3D inversion. The potential resolving power, particularly for the isotropic and transition-zone discontinuity parameters, should dramatically increase in such a study. A full 3D study, however, requires an extensive data set of frequency-dependent and *ScS*-reverberation travel times, a measurement effort which has not yet been undertaken. Nevertheless, we can still make the first step toward a full 3D inversion without collecting any more data; this is done here by jointly inverting the data sets from the Ryukyu- and Tonga-Hawaii corridors for a composite structure, which ties the two corridors near Oahu, where they meet.

5.7.1 Parameterization and Inversion Procedure

We parameterized the double corridor, simply by combining the model perturbation vectors from the individual corridors into one larger vector of size 3265, which comprises 2335 isotropic velocity parameters, 620 radial anisotropy parameters, and 310 transition-zone topography parameters. The grid, which is shown in Figure 5.16, is the same as described in Sections 4.5.1 and 5.6.1. The data sets from the two corridors were also combined into a single data set of 3189 travel-time residuals. The size of this problem still permitted the use of a complete Bayesian approach [*Tarantola and Valette*, 1982; *Tarantola*, 1987], and we have, therefore, followed the same inversion procedure described before. The prior correlation between parameters of the same or of different corridors were both

computed using the Gaussian form (4.9), with the same correlation lengths; for this inversion, however, the geographical position of each parameter (as opposed to the relative location along a single corridor) was used to compute the angular distances between blocks. As a prior model for the final 2D inversion, we employed a smooth 2D model, rather than a path-average 1D model, in order to account for the long-wavelength variations in the lowermost mantle, along the two corridors. This 2D model (Figure 5.16), was obtained by inverting the data set using a large lateral correlation length of 300°. We emphasize, however, that the choice of the prior model did not affect the structure of the uppermost 1500 km in the final model resulted from the second inversion.

5.7.2 Model THR1

The preferred composite model for the Tonga-Hawaii-Ryukyu corridors, THR1, is shown as a perturbation to the PA5/PREM reference model in Figure 5.17. This inversion used a parameterization identical to our previous TH2 and RH1 models. The primary features in this model are nearly identical to those obtained by the individual corridor inversions, and we therefore review them only briefly. The alternating series of highs and lows in upper-mantle shear velocity along the Tonga-Hawaii corridor (see Figure 4.7) is clear in THR1; this model also shows nicely that the fast anomaly beneath Hawaii, extends westward beneath the entire Hawaiian swell, down to depths of 200-400 km. The distribution of the fast upper-mantle anomaly beneath the stations in Oahu is probably more reliable in THR1 than in both TH2 and RH1, because in the former it is constrained by data from both corridors. The distribution of the deeper anomalies near Hawaii, however, is still uncertain because it is dictated mostly by the negative ScS_n-ScS_m residuals from the Hawaiian event, which provide no vertical resolution.

THR1 also exhibits the same velocity structure as RH1 beneath the Philippine-Sea, with very slow uppermost mantle bounded by fast anomalies beneath the Izu-Bonin and Ryukyu subduction zones. The topography on the 410 and 660 discontinuities and the

variation in radial anisotropy are also the same as before. In particular, the strongest anisotropic feature revealed by THR1 is a distinct minimum near Hawaii, which also appears in the model of *Ekström and Dziewonski* [1997] as the strongest negative anomaly in radial anisotropy over the entire Pacific. The long-wavelength variation in shear velocity of the lowermost mantle agrees with recent models [*Dziewonski et al.*, 1996; *Masters et al.*, 1996; *Li and Romanowicz*, 1996; *Wysession*, 1996], showing high anomaly beneath the western Pacific and Philippine Sea and low anomaly beneath the Tonga-Hawaii corridor.

Because we used a complete Bayesian approach with an exact matrix inversion, the calculation of this relatively small inverse problem was rather heavy (more the 24 hours on an Ultra-Sparc station). We therefore did not perform the resolution analysis or the other inversion tests, as we have done for the single-corridor inversions. Nevertheless, the resolution of THR1 must be very similar to the resolution of TH2 and RH1 because the same data and Fréchet kernels were used to constrain the structure in the individual corridor inversions. Relative to the latter two models, THR1 is probably more robust near Oahu, where it is better constrained.

5.8 Discussion

We have demonstrated above, by a series of inversion tests, using real and synthetic data-sets, that the upper mantle structure along the Ryukyu-Hawaii corridor is well resolved, both vertically and horizontally. The two most dominant features in the upper mantle are a fast elongated anomaly beneath the entire Hawaiian swell, which is particularly robust and unbiased by 3D structural averaging (Figure 5.14), and a very slow anomaly beneath the Philippine-Sea which is bounded by fast subducting slabs.

5.8.1 The Philippine Sea Region

The shear velocity in the uppermost 160 km of the mantle, beneath the Philippine Sea is 3% to 7.5% slower then the reference model, and the average lid velocity in this region is 6% slower than PA5 (Figure 5.11b). These variations are too large to be explained by

difference in plate age [*Nishimura and Forsyth*, 1989] . The Philippine-sea area that is sampled by the corridor, includes mostly the Northern part of the Western Philippine Basin (35-60 Ma) [*Hilde and Lee*, 1984], and the Shikoku basin (15-25 Ma) [*Chamot-Rooke et al.*, 1987; *Park et al.*, 1990]. If we assume an average lithospheric ages of ~ 30 Ma for this region and ~110 Ma for PA5, then the plate-cooling model of *Stein and Stein* [1992] predicts an average temperature difference of ~240°C, which can amount to an average velocity difference of about 120 m/s [*Kato*, 1997]. This is about 2-3 times less than the velocity difference revealed by RH1, and both estimates underpredict the large delays of the surface waves from Izu-Bonin to Taiwan (Figure 5.9a).

The same dramatic variation, 5.8%, is observed between the lid velocities of PA5 (4.75 km/s) and PHB3 (4.48 km/s)—the 1D upper-mantle model for the western Philippine Sea [*Kato and Jordan*, 1997]. *Gaherty et al.* [1997] argued that this contrast is not due to temperature alone because the lid appears to be thin in the old, central Pacific and thicker in the younger Philippine-Sea (Figure 5.2). Instead they proposed that the G discontinuity, which marks the lid bottom, represents the depth of melting in the ridge environment; this depth was supposedly larger in the Philippine-Sea due to the presence of extra water [*Hirth and Kohlstedt*, 1996] which was provided by the long history of subduction around the area. This mechanism, which accounts for the thicker crust in the Philippine Sea [*Revenaugh and Jordan*, 1991a], does not actually explain the slow velocities in the lid, which is expected to dry out subsequent to the MORB melting [*Hirth and Kohlstedt*, 1996]. However, we note that the velocity contrast across the G discontinuity in PHB3 is less than half of that in PA5, suggesting that the Philippine-Sea lid may still contain some amount of water which decreases its melting temperature and its seismic velocity [*Sato et al.*, 1989; *Karato*, 1995; *Kato and Jordan*, 1997] relative to PA5. Compositional variation of this kind can also explain the large velocity heterogeneity observed by [*Lebedev et al.*, 1997] across the Central Basin Ridge which is hard to reconcile with thermal variation alone.

The slow lid in the Philippine Sea is bounded by high-velocity anomalies beneath both the Ryukyu and Izu-Bonin trenches (Figure 5.12b) These anomalies are about 3-4% faster than PA5, indicating a 300-400 °C temperature decrease within the two subducted slabs (assuming $\partial v/\partial T \approx -0.5$ m/s/°C [*Creager and Jordan*, 1986]). We assume that the anomaly beneath Ryukyu is poorly resolved because of lateral variability perpendicular to the corridor (Figures 5.14), and because of its proximity to the model edge. Several previous regional tomographic studies indicated that the transition zone beneath the Philippine-sea is faster than average, suggesting that the Izu-Bonin slab deflects above the lower mantle [*Zhou and Clayton*, 1990; *van der Hilst et al.*, 1991; *Fukao et al.*, 1992]. In RH1, the Izu-Bonin slab widen near the 660 discontinuity and the average transition-zone velocity beneath the Philippine Sea is somewhat faster than in PA5. The 660 discontinuity is depressed in this region, in agreement with *Kato and Jordan*, [1997] and *Flanagan and Shearer* [1997], and as expected from the negative Clapeyron slope of the transition of γ-spinel to perovskite and magnesiowustite. The model may indicate, therefore, that the Izu-Bonin slab deflects above the 660 discontinuity, as suggested by the previous studies. We remain careful about this interpretation, however, because significant part of the transition zone beneath the Philippine Sea is only marginally faster than average. This is supposedly due to the nearly zero travel-time residuals of the *S* waves propagating from Izu-Bonin to Taiwan (Figure 5.9a), which are strongly sensitive to this region (Figure 5.8a). Also, the lower-mantle velocity in this region is higher than average, but our resolving power is nearly lost beneath the 660 discontinuity (Figure 5.12) and we therefore cannot reveal the fate of the Izu-Bonin slab below this boundary.

5.8.2 The Hawaiian swell

The velocity structure beneath the Hawaiian swell in RH1, is not consistent with the actual 90-110 Ma age of its lithosphere, as suggested by *Woods and Okal* [1996]; it is, in fact, significantly faster. This region exhibits the highest shear velocities in the Pacific

upper mantle beneath both the Tonga- and Ryukyu-Hawaii corridors (Figure 5.17), which sample lithospheric ages of 85-120 and 85-160 Ma, respectively. The fast anomaly extends over a horizontal distance of 2400 km from Oahu to Midway and is remarkably correlated with the positive topography of the swell (Figure 5.18). This correlation, which was even more notable along the Tonga-Hawaii corridor (Figure 4.11), can not be explained by only thermal anomalies within the lithosphere and the uppermost mantle. The lower attenuation within the uppermost-mantle, which is manifested by the surface waves propagating from Izu-Bonin to Hawaii (Section 5.2), is also at odds with an elevated temperature beneath the Hawaiian swell. The problem of associating the Hawaiian swell with a strictly thermal origin, such as lithospheric rejuvenation [*Detrick and Crough*, 1978; *Crough*, 1983] has already been raised by others. Heat flow measurements taken along a profile transverse to the swell found anomaly which does not correlate with the swell location [*Von Herzen et al.*, 1989], surface-wave tomography does not reveal any low-velocity anomaly below the swell [*Zhang and Tanimoto*, 1989; 1991], and two-station measurements of Rayleigh-wave dispersion found no evidence for lithospheric thinning between Midway and Oahu [*Woods et al.*, 1991; *Woods and Okal*, 1996].

The effect of anisotropy, however, was ignored in the previous studies of Woods and his coworkers. It might be argued, for example, that the low velocity beneath the swell can be masked by the effect of azimuthal anisotropy, in particular if the direction of propagation is parallel to the fast axis, in which case the typical Love-Rayleigh wave discrepancy can even change its sign [*Maupin*, 1985]. Such biases in isotropic velocities due to anisotropic structure are significantly reduced in our study, where both Rayleigh and Love waves from three-component seismograms are used, and variation in radial anisotropy is considered. Our inversion experiments indicated that the variations in isotropic upper-mantle shear velocities are not effected by errors in the distribution of radial anisotropy (Figures 5.14a and b), and that we can fit the data nearly as well with or without anisotropic variations, using the same isotropic structure. Moreover, near Oahu the anisotropic perturbation

declines to its minimum value along both the Tonga-Hawaii and the Ryukyu-Hawaii corridors (Figures, 4.7 and 5.11b, respectively), which are perpendicularly oriented. This observation is hard to reconcile with azimuthal anisotropy [*Maupin*, 1985]; instead, it indicates that the amount of radial anisotropy is, indeed, smaller near Hawaii. This anomaly can originate from lattice-preferred orientation of olivine due to vertical flow beneath Oahu, or from a large disturbance in the predominantly horizontal alignment due to vigorous convection near the hotspot.

Another source of bias to the velocity structure can arise from lateral heterogeneity, where the phase-delay measurements for waves traversing along the swell will be influenced by the unperturbed structure outside the swell [*Maupin*, 1992]. In particular, the presence of a low-velocity channel beneath the swell can potentially causes the propagation paths of the surface waves to deviate from the ideal source-receiver great circles. However, nearly all the radial components, do not show any transverse energy (see for example Figure 5.5), which argues for great-circle propagation and against lateral refraction. Also, inversions of data subsets with different range of back azimuths produce the same fast anomaly beneath the swell (Figure 5.14), implying that this anomaly is fairly unbiased by the lateral heterogeneity transverse to the corridor.

The robust, high seismic velocities underneath the Hawaiian swell confirm our previous result for the uppermost mantle along the Tonga-Hawaii corridor. As discussed in Section 4.7.3, the required buoyant, high-velocity mantle can be generated by a basaltic-differentiation mechanism which depletes the source region from its incompatible elements (Fe, Al) and strip it from its volatiles (H_2O, CO_2). Depletion of Fe and Al causes a significant reduction in the density [*O'Hara*, 1975; *Green and Liebermann*, 1976; *Oxburgh and Parmentier*, 1977; *Jordan*, 1979] and a slight increase in the seismic velocity [*Jordan*, 1979], whereas the extraction of volatiles elevates the solidus temperature [*Hirth and Kohlstedt*, 1996] which consequently causes a significant increase in the seismic velocity [*Sato et al.*, 1989; *Karato*, 1995]. This chemical-differentiation mechanism was invoked

by *Sipkin and Jordan* [1980b] to explain their multiple-*ScS* data beneath Hawaii, and its dynamical implications was investigated by *Phipps Morgan et al.* [1995]. The latter study showed that the amount of basalt-depletion that is expected from the extra crustal area across the Hawaiian chain can also account for most of the swell relief. However, in Chapter 4 we demonstrated that along the Tonga-Hawaii corridor, the volume of this residuum could not explain the depth extent of the fast anomalies beneath the swells. This inconsistency led us to suggest that the dynamic configuration of the upper mantle in that region, consists of small-scale convection, in the form of Richter-rolls, with high-velocity cold downwellings underneath the high-velocity chemically-buoyant residuum. The results along the Ryukyu Hawaii corridor are less definitive in this respect. The high velocities beneath the Hawaiian swell extends only down to depth of 200-400 km, and we probably cannot rule out a model where much of this anomaly resides in the uppermost 100-250 km of the mantle. In such a model, it may be possible to account for the high seismic velocities by chemical differentiation alone, provided that either some of the hotspot melting occurs deeper then 200 km, or that the depleted root is advected downward by convective currents in the upper mantle. The initial depth of melting and the plume temperature beneath Hawaii are poorly known, but, if we assume a source material with the garnet-peridotite solidus of *McKenzie and Bickele* [1988], than a melting depth of 200 km or more, will require a potential temperature of at least 1600°C which is 300°C higher than the estimate for an average mantle adiabat.

A substantial amount of partial melting is required to fully account for the 2.5-4.8% increase in shear velocity beneath the Hawaiian swell by chemical differentiation alone. While the tomographic results are somewhat limited in their spatial resolution, they give an accurate measure for the integrated effect of the anomaly. Therefore, squeezing the fast anomaly into say the uppermost 200 km of the mantle, will still require, overall, the same amount of melt extraction to fully account for the higher velocities of this modified

anomaly. Some support for the high degree of melting, comes from volcanic glasses with 15% MgO which are found in Kilauea [*Clague et al.*, 1991].

As shown in Figure 5.18a, which was reproduced from *Wessel* [1993], the size of the swell does not decrease monotonically along the chain, as predicted by the rejuvenation model of *Detrick and Crough* [1978], but rather shows undulations which correlate with the depth and magnitude of the velocity anomaly in RH1 (Figure 5.18b). *Davies* [1992] suggested that these along-axis undulations reflect variation in the buoyancy flux of the Hawaiian plume which may be related to changes in plate motion associated with the Emperor-Hawaiian bend. *Wessel* [1993] noted that the swell area maximizes near its intersection with the Molokai and Murray fracture zones (Figure 5.18) and suggested that the undulations may be due to hotspot-lithosphere interaction. Both authors, however, used the assumption that the swell is dynamically supported by the hot, buoyant asthenosphere provided by the plume [*Davies*, 1988; *Sleep*, 1990], which clearly contradicts our observation that the high velocities underneath the swell maxima extends to 300-400 km. We prefer, therefore, the mechanism of *Phipps Morgan et al.* [1995] who explained the variation in swell magnitude by contrasts in hotspot melting and swell-root creation associated with variation in lithospheric-thickness. They argued that the melting beneath older and thicker lithosphere is reduced due to the smaller depth interval between the initiation of melting and the base of the (thicker) lithosphere. This mechanism also predicts the enhancement in volcanism and swell relief near fracture zones (Figure 5.18a).

The hypothesis that chemical differentiation alone accounts for the velocity structure beneath the Hawaiian swell raises a few issues. As mentioned before, *Gaherty et al.* [1997] argued that the G discontinuity, (the lid to low-velocity-zone boundary) marks a compositional boundary from dry harzburgite to wet peridotite, which reflects the fossil depth of melting in the ridge environment. If melt and volatile extraction occurs beneath G, as proposed here, than this boundary should appear at a much greater depth or effectively disappear beneath the Hawaiian swell. However, *Bock* [1991] found a shear-wave

velocity decrease of 15% across a strong G discontinuity at depth of 75 km, directly beneath Hawaii, which he interpreted as an indication for partial melt in the asthenosphere. This result contradicts our observations along the swell and suggests that the dynamic configuration near the active hotspot may be more complicated. Another issue concerns the geoid/topography ratio, $\delta N/\delta h$, along the Hawaiian swell which is about 6 m/km [*Crough*, 1978] . For long-wavelength features, simple local compensation directly relates this ratio to the depth of compensation D by $\delta N/\delta h\,(\mathrm{m/km})\,\Delta\rho_{wm} \approx 0.1D$ (km) ($\Delta\rho_{wm}$ is the difference between mantle density and water density), which implies that $D = 60$ km for the Hawaiian swell [*Crough*, 1978]. According to this, the geoid/topography ratio expected from a buoyant, depleted root which extends down to depth of 200 km, will be about 20 m/km. This ratio can be reduced by 30%, if we assume that 1/3 of swell support comes from shallow crustal emplacement associated with the hotspot volcanism [*Phipps Morgan et al.*, 1995], but it still overestimates the observations. (We note, however, that $\delta N/\delta h$ varies significantly with viscosity when a dynamic compensation mechanism is invoked [*Robinson et al.*, 1987; *Hager and Clayton*, 1989]; see also Appendix C). Finally, as mentioned above, significant amount of melting is required at depths that are somewhat larger than expected [*Liu and Chase*, 1991], especially beneath the swell maxima.

It seems that some of the above issues can be better addressed by incorporating a thermal-convection component into the dynamic picture envisaged above. One speculation is that the hypothetical picture proposed in Chapter 4 and in *Katzman et al.* [1997a,b] to explain the results across other swells in the Pacific also holds along the Hawaiian swell. In this scenario, vigorous upper mantle convection accompanied by intense volcanism initiates near the location of the hotspots, where the cooling oceanic thermal boundary layer becomes convectively unstable and starts to delaminate. The swell relief is still supported by the basalt-depleted, higher-velocity residuum of volcanism, which is transported with the overriding plate, but the residuum is now maintained, at least partly, above the downwellings axes by the horizontal flow at the base of the plates. The deeper part of the

fast anomaly beneath the swell, can be therefore associated with cold downwellings and does not require melt extraction at great depth. It is plausible that the orientation of the Ryukyu-Hawaii corridor does not quite sample the full extent of these downwellings which can reach the bottom of the transition zone (Section 4.7.4), or that the geometry of the flow is even more complicated. Clearly, these aspects are highly questionable and will need to be clarified in the future. Nevertheless, compositional inhomogeneity must play a major rule in the dynamics of the Pacific upper-mantle in this region

5.9 FUTURE DIRECTION

The results presented here and in Chapter 4 are the first 2D applications of a new tomographic technique which have been developed in this thesis. We believe that its resolving power, especially for the variation in radial anisotropy and in the topography on the 410 and 660 discontinuities, will be dramatically improved by incorporating multiple crossing paths into a 3D inversion. A 3D study would better address the hypotheses posed above by elucidating the structure outside these corridors; in the Pacific, it may confirm (or disprove) the relationship between mid-plate hotspots and upper-mantle circulation; in the Philippine Sea, it may unveil the importance of water in the dynamics of the upper mantle.

The richness of the seismological information that is employed by our methodology provides the means to study the mantle structure beneath the entire western Pacific, Australia, and Eastern Asia. This is an area of extreme tectonic diversity which contains collision zones that account for nearly 50% of the plate consumption including the most rapid ocean-plate subduction (Mariana), and the most violent continent-continent collision (Himalayan-Tibetan orogen). It includes several active marginal basins (e.g., Mariana, Woodlark [*Tamaki and Honza*, 1991]), the oldest oceanic plate (western Pacific, [*Mueller et al.*, 1993]), one of the oldest continental craton (western Australia [*Rutland*, 1981]), and an active region of shearing and extension (China, [*Burchfiel and Royden*, 1991]). The construction of a 3D tomographic model for this entire region, which includes lateral

heterogeneity in radial anisotropy and topography of the 410- and 660- discontinuities, can contribute significantly to the understanding of mantle dynamic processes beneath these different environments.

Table 5.1. Events and stations used for *ScS* travel-time measurements along the Ryukyu-Hawaii corridor

Date			Origin Time UT	Latitude °N	Longitude °E	Depth km	Station	Distance °	# of measurements 0th*
1973	04	26	20:26:27.0	19.90	-155.13	48	KIP	3.09	4
1978‡	03	07	02:48:55.3	31.90	137.44	434	KIP	57.88	7
1978‡	03	15	22:04:46.1	26.22	140.65	270	KIP	55.87	6
1978‡	05	23	07:50:39.6	31.00	130.45	176	KIP	63.92	6
1986‡	02	03	20:47:40.1	27.84	139.34	516	TATO	16.24	6
1987	12	12	04:51:54.7	29.69	139.95	166	TATO	17.06	8
1988‡	09	07	11:53:30.9	30.14	137.21	491	HON	58.35	6
1990‡	08	05	01:35:02.0	29.48	137.50	520	KIP	58.14	7
1992‡	01	20	13:37:10.7	28.02	139.38	523	KIP	56.72	8
1992‡	05	30	12:42:06.6	30.75	141.84	15	KIP	54.26	1
1992‡	10	30	02:49:51.6	29.92	139.20	408	KIP	56.62	8
1992‡	10	30	02:49:51.6	29.92	139.20	408	TATO	16.47	8
1996‡	03	16	22:04:11.9	29.12	139.12	478	KIP	56.79	7

* Number of travel-time measurements of zeroth-order ScS_n and $sScS_n$ reverberations. There have been no measurements of first-order reverberations along this corridor

‡ Source-receiver pairs that were also used for the frequency-dependent travel-time measurements (Table 5.2).

Table 5.2. Events and stations used for frequency-dependent travel-time measurements of body- and surface-waves for the Ryukyu-Hawaii corridor

Date			Origin Time UT	Latitude °N	Longitude °E	Depth km	Station	Distance °	# of measurements Surf*	Turn†	*ScS*§
1973	04	26	20:26:27.0	19.90	-155.13	48	MAT	59.94	0	13	0
1977	02	18	20:51:34.6	32.69	140.96	53	KIP	54.84	13	18	0
1977	05	13	11:13:36.7	28.12	139.73	440	KIP	56.40	0	19	0
1977	12	21	01:00:34.3	25.48	143.26	27	KIP	53.66	8	12	0
1977	12	22	04:45:20.1	29.00	127.45	15	KIP	66.87	8	4	0
1978	02	08	00:15:41.8	24.37	122.77	15	KIP	72.06	0	6	0
1978‡	03	07	02:48:55.3	31.90	137.44	434	KIP	57.88	5	15	0
1978‡	03	15	22:04:46.1	26.22	140.65	270	KIP	55.87	8	16	0
1978‡	05	23	07:50:39.6	31.00	130.45	176	KIP	63.92	15	17	0
1978	05	26	23:58:25.2	23.71	143.20	22	TATO	19.82	13	0	0
1978	05	27	10:17:21.5	23.82	143.35	16	TATO	19.94	6	0	0
1978	09	02	01:57:42.1	24.61	121.73	89	KIP	72.90	4	11	0
1978	09	11	07:40:56.0	24.41	124.77	15	KIP	70.29	15	10	0
1979	05	18	20:18:07.9	23.94	142.66	581	TATO	19.30	0	6	0
1979	12	11	17:26:24.8	28.81	140.83	125	TATO	17.66	0	6	0
1982	01	01	18:51:07.4	26.84	142.70	37	TATO	19.17	6	0	0
1983	06	21	14:48:11.3	23.77	122.26	23	HON	72.71	7	9	0
1983	06	24	09:06:51.3	23.74	122.50	38	HON	72.51	14	16	0
1983	08	02	02:17:44.3	20.50	122.05	166	HON	73.82	8	17	0
1983	08	25	20:23:38.4	33.42	131.31	128	HON	62.86	8	22	0
1983	09	21	19:20:48.2	23.65	122.11	25	HON	72.87	6	7	0
1983	11	16	16:13:05.9	19.40	-155.59	11	MAJO	59.83	8	12	0
1983	11	16	16:13:05.9	19.40	-155.59	11	TATO	75.86	7	6	0
1984	01	01	09:03:46.8	33.38	136.81	384	HON	58.30	0	29	0
1984	03	06	02:17:30.6	29.60	139.11	446	TATO	16.32	0	0	2
1984	04	24	04:11:35.2	30.81	138.46	395	HON	57.19	0	19	0
1984	08	06	19:06:43.7	32.34	131.94	29	HON	62.50	7	18	0
1984	09	18	17:02:46.5	34.11	141.37	35	HON	54.45	7	20	0
1985	04	03	20:21:41.2	28.40	139.61	455	HON	56.50	0	25	0
1985	04	10	16:26:22.1	29.92	138.86	398	HON	56.96	0	19	0
1985	04	10	16:26:22.1	29.92	138.86	398	TATO	16.18	0	6	3
1985	09	10	06:39:06.3	27.14	139.91	497	HON	56.42	0	26	0
1985	09	10	06:39:06.3	27.14	139.91	497	TATO	16.69	0	6	3
1985	10	04	08:41:41.2	27.56	139.82	468	HON	56.44	0	10	0
1985	11	08	18:40:26.6	27.87	140.18	10	HON	56.08	8	12	0

Table 5.2. (continued)

Date			Origin Time UT	Latitude °N	Longitude °E	Depth km	Station	Distance °	# of measurements Surf*	Turn†	*ScS*§
1985	11	08	18:40:26.6	27.87	140.18	10	TATO	16.99	5	0	0
1986	02	03	20:47:40.1	27.84	139.34	516	HON	56.82	0	25	0
1986‡	02	03	20:47:40.1	27.84	139.34	516	TATO	16.24	0	6	0
1986	03	24	02:01:35.2	28.36	129.86	15	HON	64.97	15	6	0
1986	05	11	01:24:32.7	26.37	125.21	204	HON	69.45	0	30	0
1986	07	25	23:41:11.1	26.29	125.73	15	HON	69.02	16	5	0
1986	11	14	21:20:17.8	23.97	121.85	33	HON	73.01	0	13	0
1987	03	18	03:36:34.1	31.94	131.77	38	HON	62.70	8	18	0
1987	06	07	05:49:47.6	20.38	120.95	37	HON	74.85	7	20	0
1987	12	12	04:51:54.7	29.69	139.95	166	HON	56.04	16	18	0
1988‡	09	07	11:53:30.9	30.14	137.21	491	HON	58.35	7	25	0
1989	04	27	02:20:07.4	30.48	140.41	78	HON	55.56	8	11	0
1989	04	27	02:20:07.4	30.48	140.41	78	TATO	17.62	5	0	0
1989	06	16	23:42:40.2	31.76	138.11	366	HON	57.38	6	14	0
1989	08	03	11:31:22.5	22.86	121.80	15	HON	73.37	16	18	0
1989	08	21	23:12:43.1	23.85	122.27	24	HON	72.68	12	6	0
1990	02	17	02:28:05.0	29.28	130.45	44	KIP	64.24	14	28	0
1990‡	08	05	01:35:02.0	29.48	137.50	520	KIP	58.14	0	26	0
1990	09	23	21:13:15.3	33.19	138.34	17	KIP	56.99	15	11	0
1990	09	30	19:05:04.9	24.15	125.02	21	KIP	70.14	15	16	0
1990	12	13	03:01:52.5	23.90	121.47	15	KIP	73.33	7	6	0
1990	12	13	19:50:29.0	23.89	121.84	18	KIP	73.01	6	6	0
1991	05	03	02:14:23.2	28.14	139.65	453	KIP	56.46	0	33	0
1991	09	03	08:44:51.6	34.09	138.48	15	KIP	56.80	14	16	0
1992‡	01	20	13:37:10.7	28.02	139.38	523	KIP	56.72	0	19	0
1992	04	19	18:32:23.0	23.78	121.59	31	KIP	73.26	6	19	0
1992	05	29	21:52:31.2	31.14	141.82	17	KIP	54.24	14	18	0
1992	05	29	21:52:31.2	31.14	141.82	17	TATO	18.95	6	0	0
1992‡	05	30	12:42:06.6	30.75	141.84	15	KIP	54.26	8	12	0
1992	05	30	12:42:06.6	30.75	141.84	15	TATO	18.88	6	0	0
1992	06	04	04:04:09.2	28.07	128.05	21	KIP	66.55	8	5	0
1992	08	11	15:15:01.6	32.69	141.89	15	KIP	54.06	16	14	0
1992	08	29	19:19:11.4	33.40	138.09	309	KIP	57.18	0	25	0
1992	09	28	14:06:11.9	24.37	122.60	38	KIP	72.21	0	12	0
1992‡	10	30	02:49:51.6	29.92	139.20	408	KIP	56.62	0	18	0
1992‡	10	30	02:49:51.6	29.92	139.20	408	TATO	16.47	8	0	0
1993	05	18	10:19:42.3	19.97	122.65	188	KIP	73.41	5	12	0
1993	08	07	00:00:42.2	26.68	125.84	165	KIP	68.78	0	18	0
1994	06	05	01:09:34.5	24.55	121.77	21	KIP	72.88	8	10	0
1994	09	13	04:28:06.9	29.18	130.11	41	KIP	64.55	15	18	0
1995	02	23	05:19:03.9	24.06	121.51	28	KIP	73.25	16	11	0
1995	04	08	17:45:19.5	21.93	142.68	281	TATO	19.67	8	0	0
1995	06	25	06:59:07.0	24.48	121.50	40	KIP	73.14	8	6	0
1995	10	01	17:06:08.7	29.30	139.02	448	TATO	16.18	0	12	0
1995	10	18	10:37:38.7	28.06	130.18	19	KIP	64.72	16	22	0
1995	10	18	23:26:03.6	28.18	130.14	27	KIP	64.73	14	13	0
1995	10	19	02:41:46.7	28.21	130.16	17	KIP	64.70	16	16	0
1996‡	03	16	22:04:11.9	29.12	139.12	478	KIP	56.79	0	33	0
1996	03	16	22:04:11.9	29.12	139.12	478	TATO	16.24	0	6	2
1996	06	26	03:22:09.0	27.82	139.85	479	TATO	16.69	0	12	0

* Number of frequency-dependent travel-time measurements of Rayleigh and Love waves

† Number of frequency-dependent travel-time measurements of direct and multiply reflected turning waves

§ Number of GSDF measurements of *ScS* wavegroups. These were measured around a single frequency only on radial components with particularly high snr.

‡ Source-receiver pairs that were also used for the *ScS*-reverberation measurements (Table 5.1).

Table 5.3. Distribution of events and stations used for the frequency-dependent travel-time measurements along the Ryukyu-Hawaii corridor

Source region*	Station	Number of paths	Hypocentral depths (km)		Epicentral distances (°)		Back azimuths	
			Min	Max	Min	Max	Min	Max
Hawaii (2)	MAT/MAJO	2	11	48	59.8	60.0	301.3‡	301.5‡
	TATO	1	11	11	75.9	75.9	291.8‡	291.8‡
Izu-Bonin (38)	KIP/HON	29	10	523	53.7	58.3	286.5	297.4
	TATO	18	10	581	16.2	19.9	66.5	94.5
Ryukyu (35)	KIP/HON	35	15	204	62.5	74.8	285.3	297.5

* The number of events is indicated in parentheses below each region name.

‡ These are azimuths from the Hawaiian events to the corresponding stations.

Table 5.4. Summary of the inversion results for model RH1

Phase	Number of Data	Data Importance	χ^2/D Reference Model	χ^2/D After Denuis.†	χ^2/D After Inversion	Variance Reduction
Rayleigh	291	4.54	66.40	33.79	7.30	0.89
Love	237	7.44	46.52	5.54	3.26	0.93
S_V	329	7.93	106.93*	3.15	1.76	0.98
S_H	239	4.17	17.23	2.30	1.26	0.93
SS_V	167	4.95	5.47	3.22	1.82	0.67
SS_H	105	1.72	13.12	1.96	1.26	0.90
SSS_V	164	8.70	2.36	3.53	1.55	0.34
SSS_H	116	5.08	7.93	2.87	1.59	0.80
Other guided waves	23	0.92	3.91	5.11	11.74	-1.99
ScS on R component (GSDF)	10	0.54	1.95	1.49	1.53	0.21
ScS on T component (ray)	82	6.26	14.51	5.78	0.89	0.94
All phases	1763	52.25	42.29	8.50	2.84	0.93

* The exceptionally large χ^2 of the S_V arrivals is due to 6 high-quality observation from an event with an extremely large origin-time error of more then a 100 s. Correcting this origin time reduced the χ^2 estimate for the 329 S_V measurements by ~85% (see next column). Other measurements from this event were given larger error (due to their lower snr) and did not effect the χ^2 estimate by as much. The summary plots in Figures 5.9 and 5.10 do not include the data from this event.

† This column shows the χ^2 estimates (normalized by the number of data) after projecting the errors in source origin-time (and depth for the reverberative interval) out of the original data.

Table 5.5. Summary of the inversion tests corresponding to the models in Figures 5.15*

model	σ_{UM} (%)	σ_{TZ} (%)	σ_{AN} (%)	σ_{AN} (%)	σ_{410} (km)	σ_{660} (km)	$\frac{\chi^2_{GSDF}}{D}$	$\frac{\chi^2_{REV}}{D}$ †	$\frac{\chi^2_{TOT}}{D}$	Remarks
RH1	2	1	0.5	0.5	10	10	2.94	0.89	2.84	
TH2.b	2	1	0.5	1	10	10	2.85	0.89	2.76	
TH2.c	2	1	0.5	0	0	0	3.20	0.88	3.00	
TH2.d	2	1	0.5	0.5	8.4	5.6	3.00	0.86	2.90	Equilibrium-olivine model enforced‡

* See section 4.6.1 for definition of the parameters.

† Only zeroth-order *ScS* travel-times are used.

‡ The enforcement of an equilibrium-olivine model through the prior covariance matrix is described in Section 4.6.1.

FIGURE CAPTIONS

Figure 5.1. Mercator projection of the western Pacific showing the study corridor from the Ryukyu and Izu-Bonin seismic zones to Oahu, Hawaii. Inverse black triangles show the stations used in this study (only two records from MAT/MAJO were used). The area sampled by the corridor (dashed line) includes the entire Hawaiian swell, from Oahu to Midway, the older part of the Pacific basin, with seafloor age ranging from 100 to 165 Ma (isochrons, marked by black contours, are taken from *Mueller et al.* [1993]), and the northern Philippine Sea. The corridor also cuts across the Izu-Bonin and the Ryukyu subduction zones. Black arrows are the current plate motion relative to the hotspot reference frame [*Gripp and Gordan*, 1990]. Epicenters of the events used in this study are shown as white symbols (circles: shallow-focus; diamonds: intermediate-focus; squares: deep-focus). Bathymetric variations are shown by illuminated gray shading in the map.

Figure 5.2. Comparison between two regional oceanic models: Solid line is model PA5, which was obtain for the central Pacific [*Gaherty et al.*, 1996]; dashed line is model PHB3, which was obtained for the western Philippine Sea [*Kato and Jordan*, 1997]. The mean shear-wave speeds $\beta = [\beta_H + \beta_V]/2$ are plotted in the right panel, and the anisotropic deviations about these means $[\beta_V - \beta]/\beta$ and $[\beta_H - \beta]/\beta$ (in percent) are plotted in the left panel. In both models, β_V is the slower velocity and β_H is the faster velocity. Note the thick and very slow lid in PHB3. The inset map keys the models to the appropriate seismic corridors, including the stations (triangles) and earthquakes (dots) used in the data processing.

Figure 5.3. Comparison of observed and synthetic seismograms computed from the regional models PA5, and PHB3 (Figure 5.2; the Q structure for the PA5 model was modified according to Figure 5.5b). The data seismograms were recorded on Oahu from a

shallow-focus Izu-Bonin event; transverse, radial, and vertical components are shown on top, middle, and bottom, respectively; all seismograms have been band-pass filtered with corners at 5 mHz and 45 mHz. The western Pacific corridor which is sampled by this source-receiver path, is much better modeled by the upper-mantle structure of PA5.

Figure 5.4. Examples of the ability of the Fréchet kernels for the frequency-dependent phase-delays to predict large mantle heterogeneities associated with the transition from the Pacific to the Philippine Sea. Four representative examples from shallow-, intermediate- and deep-focus events are shown. (a)-(d) (top) Complete synthetics for PHB3; (middle) complete synthetics for PA5 (with the modified Q structure of Figure 5.5b); (bottom) isolation filter. Epicentral distance, hypocentral depth, and component (LPZ for vertical, LPT for transverse), are indicated in each panel. time scale is relative to the origin time. (e)-(f) (circles) "Observed" frequency-dependent travel times, $\delta\tau$, of the PHB3/PREM synthetics relative to the PA5/PREM reference model, measured from the seismograms on the left by the GSDF processing described in Chapter 3; (diamonds) frequency-dependent travel times predicted by the Fréchet kernels due to the known structural difference between PHB3 and PA5.

Figure 5.5. (a) The original shear Q structure of PA5 which was used in Chapter 4 for the Tonga-Hawaii corridor. (b) The preferred shear Q structure that was used for the Ryukyu-Hawaii corridor. (c) and (d) Examples of seismograms recorded at HON from shallow- and deep-focus Izu-Bonin events, respectively. Top triplet in each panel is vertical-component records; bottom triplet is transverse components. In each triplet, top trace is data, and bottom two traces are synthetics calculated with the PA5/PREM velocity structure, using the Q structure in Figure 5.5b (middle trace), and the Q structure of PA5 (bottom trace). Note that the modified Q structure effects only the synthetic amplitude of

the surface waves (R_1 and G_1) which underestimate the observations. This Q structure was used in all the PA5 synthetics throughout this chapter.

Figure 5.6. A subset of the seismograms that were used to measure *ScS*-travel times. For each record pair, the top trace is the data seismogram, the bottom trace is the synthetic, calculated for PA5/PREM. The synthetics were corrected for ellipticity and bounce-point bathymetry. All traces are band-pass filtered with corner frequencies at 15 and 40 mHz. The low snr of these records prevented us from measuring first-order reverberations

Figure 5.7. Example of GSDF data obtained for the Ryukyu-Hawaii corridor, classified according to the tectonic region they sample: Philippine-Sea only (top panels), western Pacific only (middle panels), and both (bottom panels). The left panels show observed seismograms (labeled Data) and isolation filters. Source region and station location are indicated above each panel. Event date, station name, epicentral distance, hypocentral depth, and component (LPZ for vertical, LPR for radial, and LPT for transverse) are indicated within each panel. Time scale is relative to the origin time. The right panels show frequency-dependent travel times, relative to the PA5/PREM, measured from the seismograms on the left by the GSDF processing described in Chapter 3. The travel-times measurements are shown at 5-mHz intervals for S_V and S_H (white and gray circles, respectively), SS_V (white squares), and R_1 and G_1 (white and gray triangles, respectively). The Fréchet kernels for some of these measurements are shown in Figure 5.8.

Figure 5.8. Examples of 2D Fréchet kernel for average shear velocity, computed by coupled-mode summation for some of the measurements in Figure 5.7. The wave type and frequency are indicated at the top of each panel. dark colors correspond to negative sensitivity (phase-delay increase for velocity decrease), bright colors to positive sensitivity, and the solid lines show the sensitivity to perturbations in the depths of the 410 and 660

discontinuities; white circle and black triangle show the locations of the source and receiver, respectively.

Figure 5.9. Summary of the frequency-dependent travel-time data obtained from waves which traverse (a) only along the Philippine Sea, from Izu-Bonin to Taiwan; (b) only along the western Pacific, from Izu-Bonin to Oahu; (c) along both the Philippine Sea and the western Pacific, from Ryukyu to Oahu; and (d) along the Tonga-Hawaii corridor (Chapter 4). Each summary time is the mean over all distances and depths (within a subset) of all the residuals classified into four nominal wave categories: Surface waves, *SSS* , *SS*, and *S*. The symbols represent the residuals relative to PA5, while the lines represent the predicted fit of models RH1 and TH2 to the data in Figures 5.9a-c and 5.9d, respectively. Definitions of symbols and line types are given in the upper-right corner. Dispersion relative to PA5 is indicated by a frequency-dependent trend. The total number of phase-delays measurements summarized are: Izu-Bonin to Taiwan, 107; Izu-Bonin to Oahu, 711; Ryukyu to Oahu, 768; Tonga to Oahu 1122. Error bars are determined by a weighted average of estimated prior errors.

Figure 5.10. Summary of the frequency-dependent travel-time data obtained for the S_H and S_V waves which traverse (a) from Ryukyu to Oahu ($62° \leq \Delta \leq 75°$); (b) from Izu-Bonin to Oahu ($54° \leq \Delta \leq 59°$); and (c) from Tonga to Oahu ($39° \leq \Delta \leq 57°$). Each summary time is the mean over all distances and depths of the *S* residuals classified into S_H , from the transverse components, and S_V, which are obtained by averaging over residuals from both the vertical and radial components. The symbols represent the residuals relative to PA5, while the lines represent the predicted fit of models RH1 and TH2 to the data in Figures 5.10a-b and 5.10c, respectively. Definitions of symbols and line types are given in Figure 5.10a. Error bars are determined by a weighted average of estimated prior errors. The

separation of the *SH* and *SV* observations shown here does not require the presence of anisotropy (see text)

Figure 5.11. (a) The 1D path average model obtained from inverting the Ryukyu-Hawaii data set, shown over the grid that was used for all the inversions. This model was used as a prior for the 2D inversions. (b) Model RH1, the final model obtained from the 2D inversion. The models are displayed as relative shear-velocity perturbations to the PA5/PREM reference model in a cross-section through the mantle from Ryukyu (left side) to Hawaii (right side). Lower figure in each panel shows the relative perturbation in isotropic velocities extending from the Moho discontinuity (M) to the core-mantle boundary (CMB); negative perturbations are in red, positive in blue. Upper figure in each panel uses same color scale to show the relative perturbation in radial anisotropy, and green and red lines to represent the perturbations to 410 and 660 discontinuities, respectively (5× vertical exaggeration). Note that the two models are displayed with different color scales, which are shown at the bottom of each panel. Yellow circles are earthquakes used as sources; blue triangle marks location of the stations.

Figure 5.12. Examples of resolution tests. Each of the models is displayed in the same way as the RH1 model in Figure 5.11b, but an additional panel is used for displaying the topography on the 410 (green line) and 660 (red line) discontinuities. Output models were obtained by an inversion, identical to TH2. In all the examples, synthetic data were generated by adding (the same) realistic Gaussian noise to phase delays computed from the input models. (a) Output model obtained by inverting Gaussian noise only. (b) Output model from an inversion of the data residuals predicted by TH2 (Figure 5.11b). (c) and (e) Input models with harmonic variation in isotropic shear velocities, having a horizontal and vertical wavelengths of (c) 15° and 1500 km, and (e) 30° and 2000 km. The perturbation in both models has a peak-to-trough amplitude of 10% in the uppermost

mantle, which decays to 5% below 410 km, but no perturbation in radial anisotropy or to discontinuity depths. (g) Input model with an elongated anomaly of 5%, which mimics the fast anomaly beneath the Hawaiian swell in RH1. (d), (f), and (h) Output models resulted from inverting the data residuals predicted by the input models in Figures 5.12c, e, and g, respectively.

Figure 5.13. The earthquake and station distribution (white circles and black triangles) and the source-receiver paths used in (a) the inversion for RH1, and (b-d) the other three inversion tests shown in Figure 5.14. (ϕ and Δ are the back azimuth, and the epicentral distance from the stations on Oahu, respectively)

Figure 5.14. Effect of back-azimuth ϕ and epicentral-distance Δ from Oahu on the inversion results. The models were obtained from inverting data subsets corresponding to the source-receiver paths in Figure 5.13. (a) model RH1 (shown for reference), (b-d) Results from inversion of data subsets recorded only on Oahu from earthquakes which correspond to (b) only the northern paths, $291.8° < \Phi < 298°$ (Figure 5.13b); (c) only the southern paths, $285° < \Phi < 291.8°$ (Figure 5.13c); (d) only the Izu-Bonin earthquakes, $\Delta < 60°$ (Figure 5.13d). All the models are displayed the same as in Figure 5.11b.

Figure 5.15. Results from full-dataset inversions where the prior covariance matrix was modified, according to Table 4.5 and the text, by (a) increasing the prior uncertainty for radial anisotropy in the uppermost mantle (model TH2.b); (b) completely suppressing the topographies on the 410 and 660 discontinuities and the anisotropic perturbations in the uppermost mantle (model TH2.c); and (c) enforcing an equilibrium-olivine thermal model (model TH2.d). The models are displayed the same as in Figure 5.11b and their designated names are indicated at the top of each panel.

Figure 5.16. The prior model for the Tonga-Hawaii-Ryukyu inversion, shown over the grid used for the inversions. This model was obtained from jointly inverting the Ryukyu-Hawaii and the Tonga-Hawaii data sets for a smooth 2D perturbation along the two corridors. The model is displayed as relative shear-velocity perturbations to the PA5/PREM reference model in a cross-section through the mantle from Tonga (right) to Hawaii (middle), where the two corridors meet, and from Hawaii to Ryukyu (left). Lower figure shows the relative perturbation in isotropic velocities, where positive perturbations are in dark shading; upper figure uses same color scale to show the relative perturbation in radial anisotropy, and green and red lines to represent the perturbations to the 410 and 660 discontinuities, respectively. Lines of longitude and latitude indicate the position of the surface; illuminated green sphere, marks the core-mantle boundary.

Figure 5.17. Model THR1 for the Tonga-Hawaii-Ryukyu corridors. This model is displayed the same as in Figure 5.16, but with a larger red-blue color scale.

Figure 5.18. (a) Comparison of the shear-velocity model with the height of the Hawaiian swell. Dashed line estimates the swell height by subtracting swell topography (along its flank) and regional topography; Circles are estimates for the swell height obtained by approximating the swell shape with "super Gaussians" [*Wessel*, 1993]; heavy, solid line is shear-velocity perturbation of RH1 average over the uppermost 290 km. Figure is modified from *Wessel* [1993]. (b) Top 1200 km of RH1.

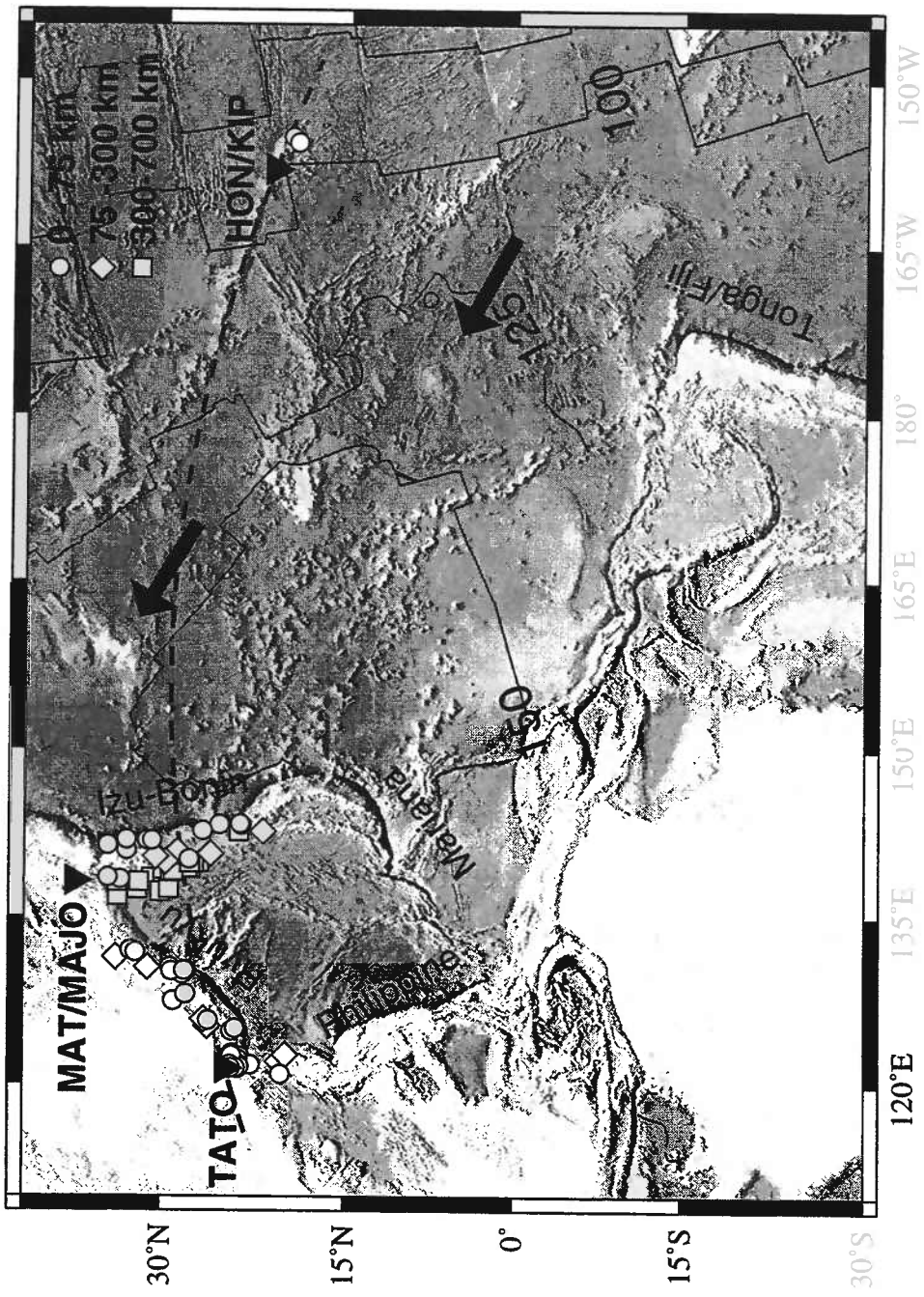
0 - 75 km
75 - 300 km
300 - 700 km
HON/KIP
100
125
150
Tonga/Fiji
Izu-Bonin
Mariana
Philippine
MAT/MAJO
TATO
120°E
135°E
150°E
165°E
180°
165°W
150°W
30°N
15°N
0°
15°S
30°S

Figure 5.1

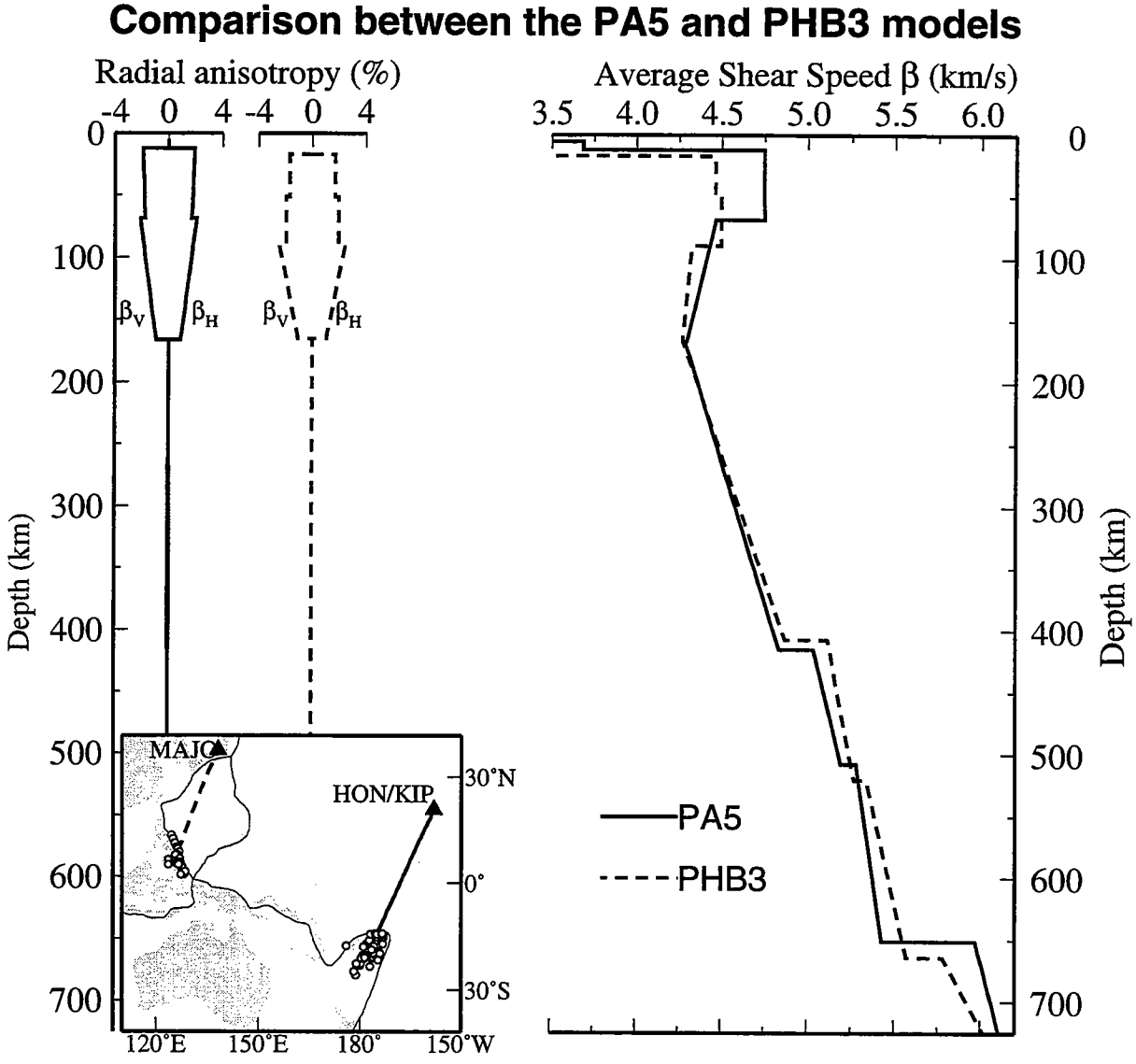
Comparison between the PA5 and PHB3 models
Radial anisotropy (%)
-4 0 4 -4 0 4
Average Shear Speed β (km/s)
3.5 4.0 4.5 5.0 5.5 6.0
Depth (km)
0
100
200
300
400
500
600
700
β_V
β_H
β_V
β_H
MAJO
HON/KIP
30°N
0°
30°S
120°E
150°E
180°
150°W
PA5
PHB3

Figure 5.2

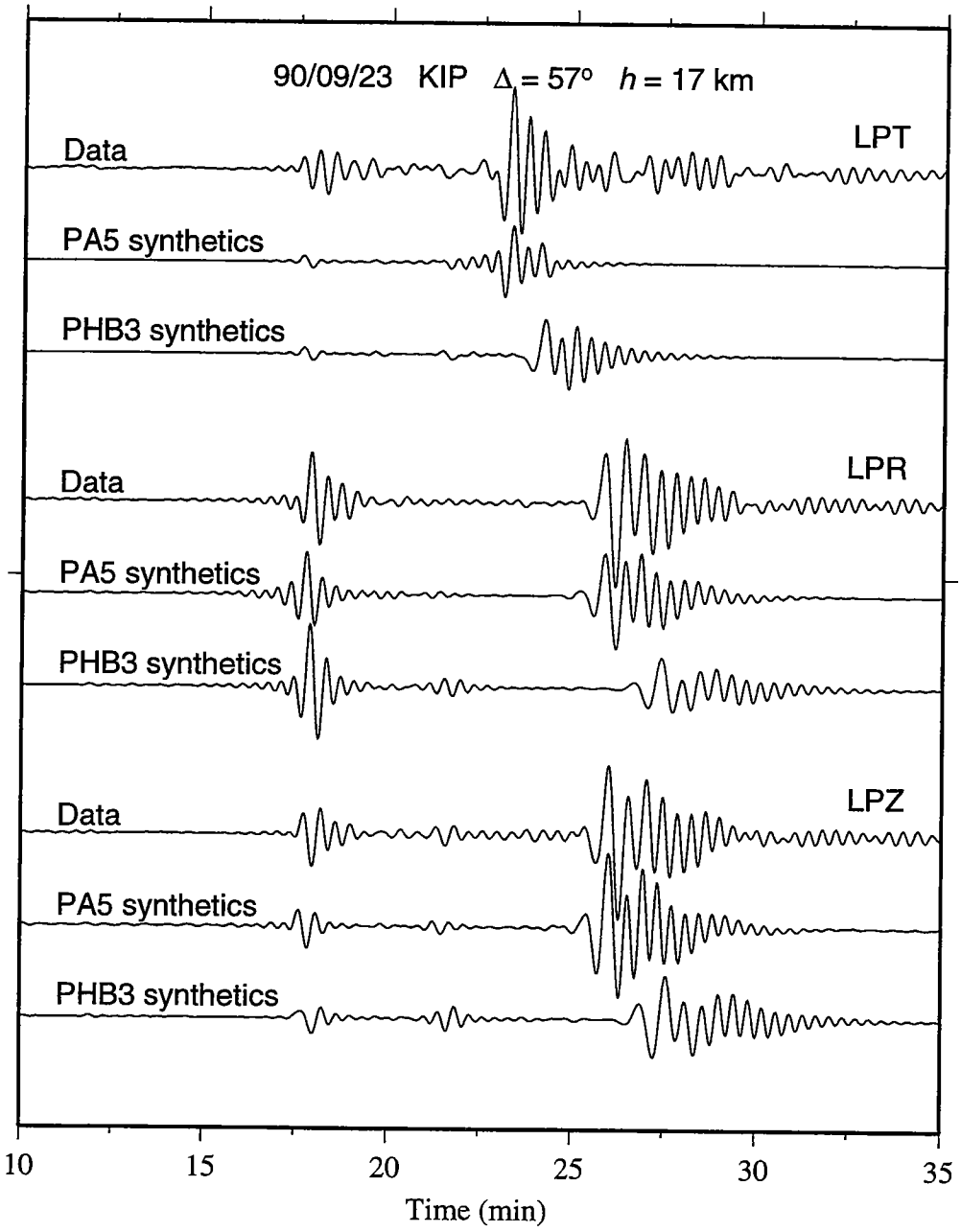
90/09/23 KIP Δ = 57° h = 17 km
Data
LPT
PA5 synthetics
PHB3 synthetics
Data
LPR
PA5 synthetics
PHB3 synthetics
Data
LPZ
PA5 synthetics
PHB3 synthetics
10
15
20
25
30
35
Time (min)

Figure 5.3

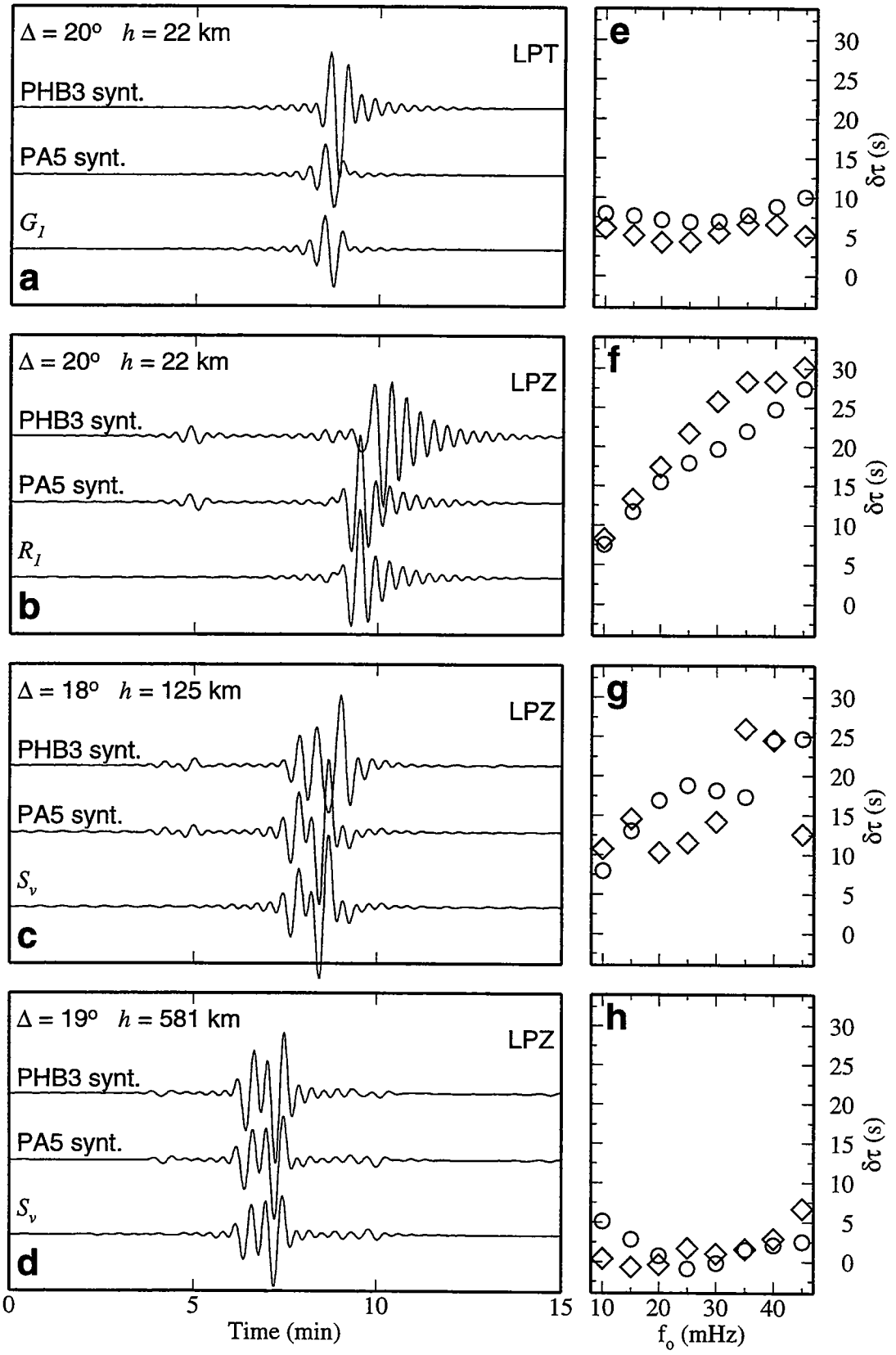
Δ = 20° h = 22 km
LPT
PHB3 synt.
PA5 synt.
G_1
a
e
Δ = 20° h = 22 km
LPZ
PHB3 synt.
PA5 synt.
R_1
b
f
Δ = 18° h = 125 km
LPZ
PHB3 synt.
PA5 synt.
S_v
c
g
Δ = 19° h = 581 km
LPZ
PHB3 synt.
PA5 synt.
S_v
d
h
0 5 10 15
Time (min)
10 20 30 40
f_o (mHz)
0 5 10 15 20 25 30
δτ (s)

Figure 5.4

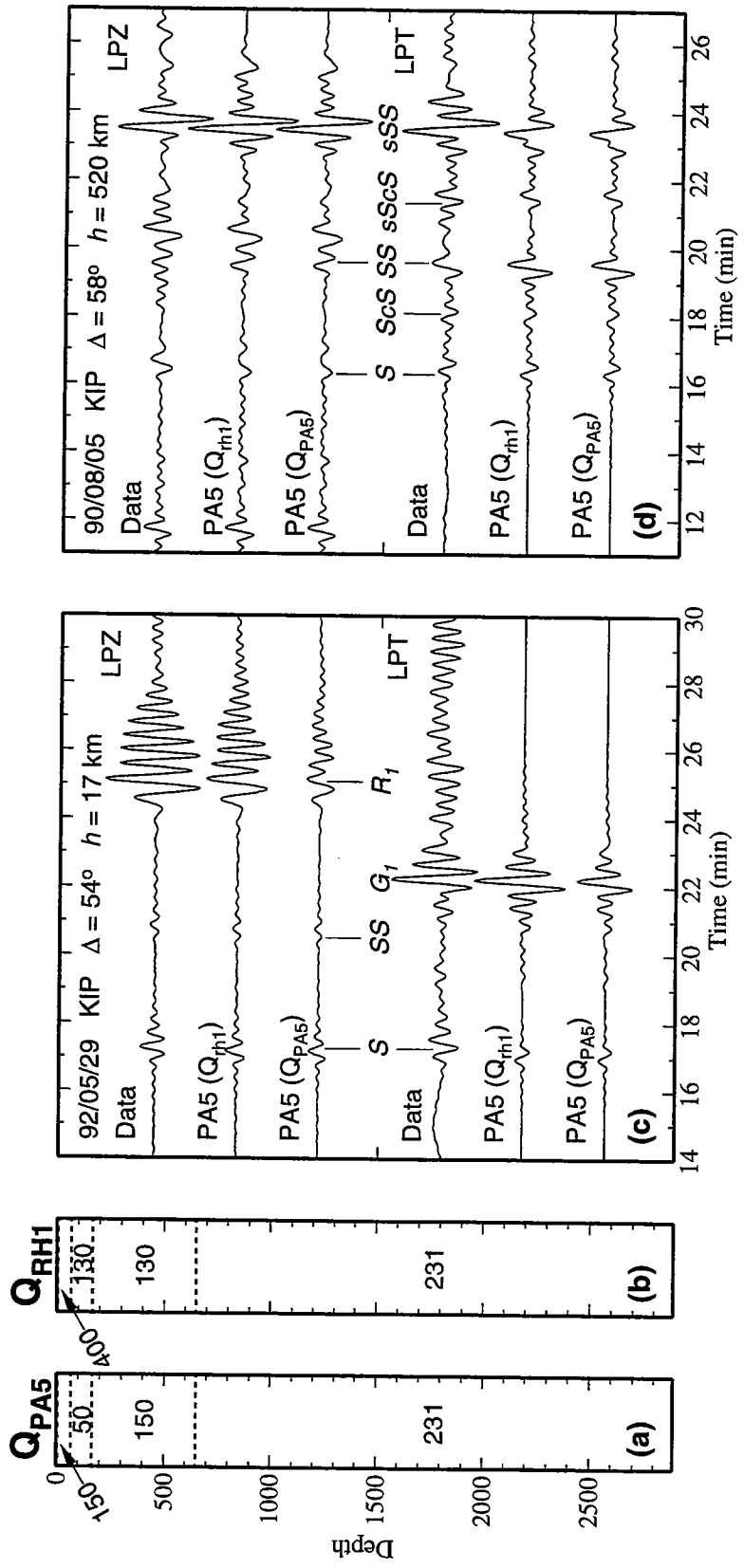
Q_{PA5}
Q_{RH1}
Depth
0
150
500
1000
1500
2000
2500
50
150
130
231
400
(a)
(b)
92/05/29 KIP Δ = 54° h = 17 km LPZ
Data
PA5 (Q_{rh1})
PA5 (Q_{PA5})
S
SS
G_1
R_1
LPT
(c)
90/08/05 KIP Δ = 58° h = 520 km LPZ
ScS SS sScS sSS
(d)
Time (min)

Figure 5.5

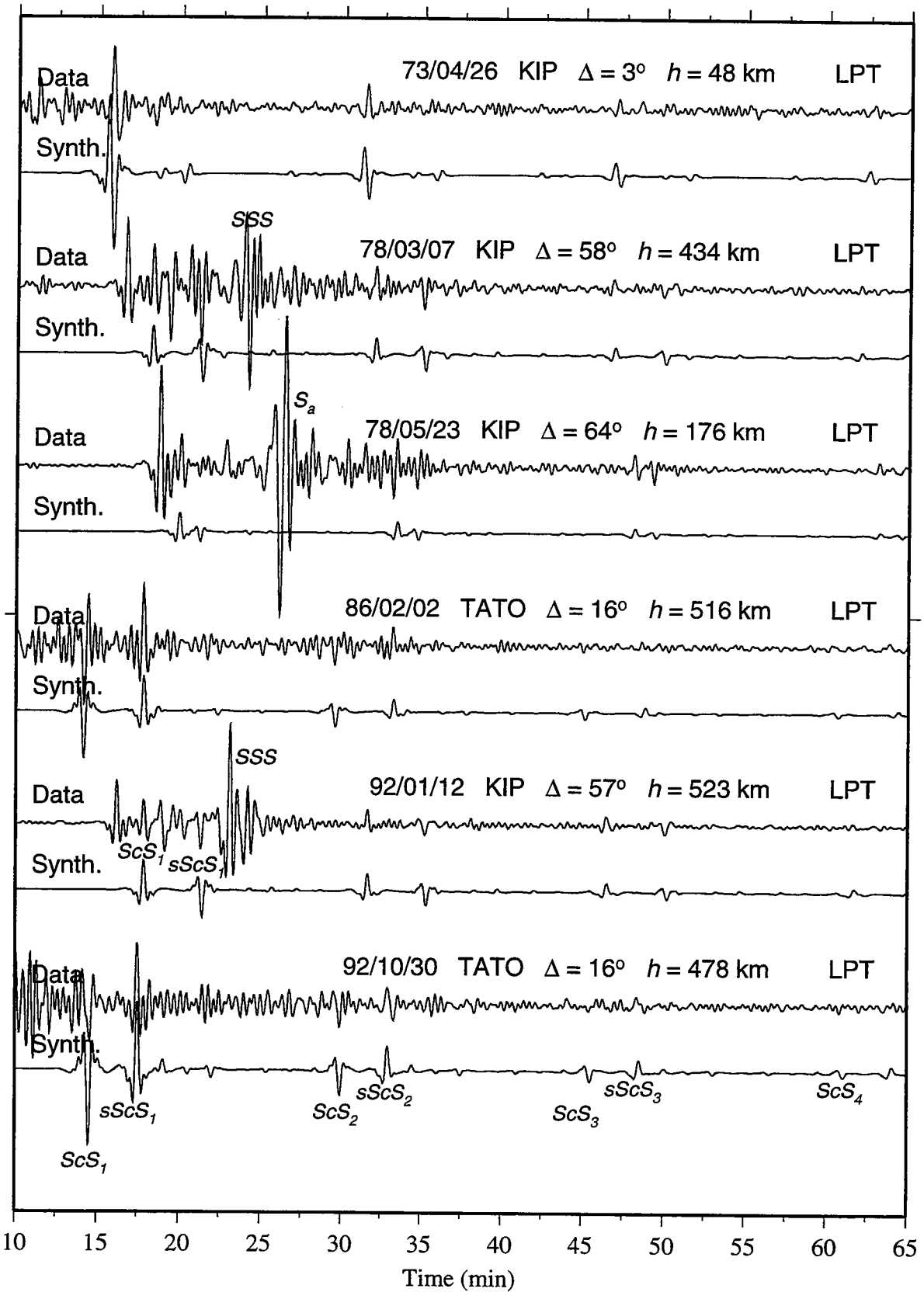
Data
Synth.
73/04/26 KIP Δ = 3° h = 48 km LPT
SSS
78/03/07 KIP Δ = 58° h = 434 km LPT
S_a
78/05/23 KIP Δ = 64° h = 176 km LPT
86/02/02 TATO Δ = 16° h = 516 km LPT
SSS
92/01/12 KIP Δ = 57° h = 523 km LPT
ScS_1
$sScS_1$
92/10/30 TATO Δ = 16° h = 478 km LPT
$sScS_1$
ScS_1
ScS_2
$sScS_2$
ScS_3
$sScS_3$
ScS_4
10 15 20 25 30 35 40 45 50 55 60 65
Time (min)

Figure 5.6

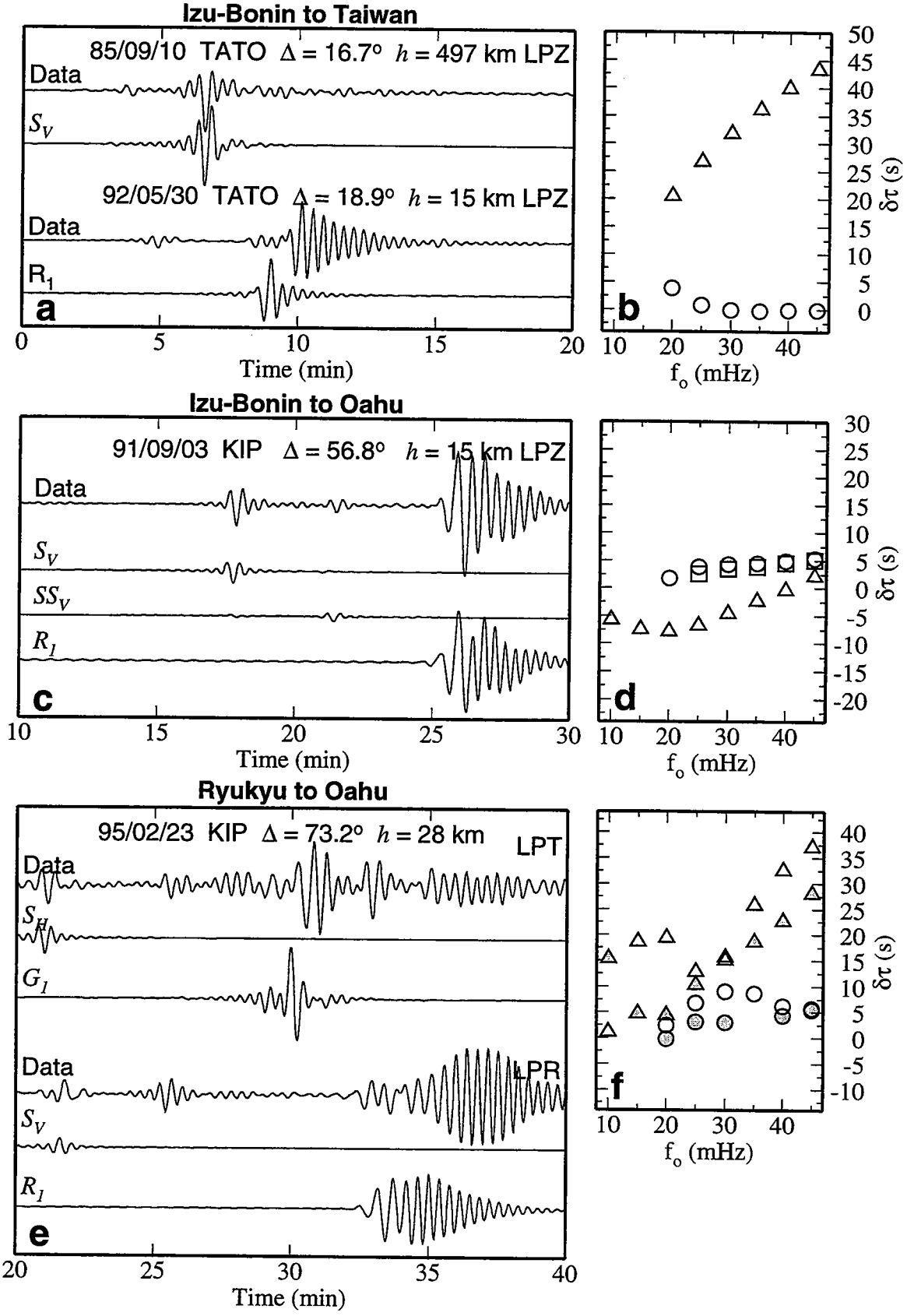
Izu-Bonin to Taiwan
85/09/10 TATO Δ = 16.7° h = 497 km LPZ
Data
S_V
92/05/30 TATO Δ = 18.9° h = 15 km LPZ
Data
R_1
a
Time (min)
b
f_o (mHz)
δτ (s)
Izu-Bonin to Oahu
91/09/03 KIP Δ = 56.8° h = 15 km LPZ
Data
S_V
SS_V
R_1
c
Time (min)
d
f_o (mHz)
δτ (s)
Ryukyu to Oahu
95/02/23 KIP Δ = 73.2° h = 28 km
LPT
Data
S_H
G_1
Data
LPR
S_V
R_1
e
Time (min)
f
f_o (mHz)
δτ (s)

Figure 5.7

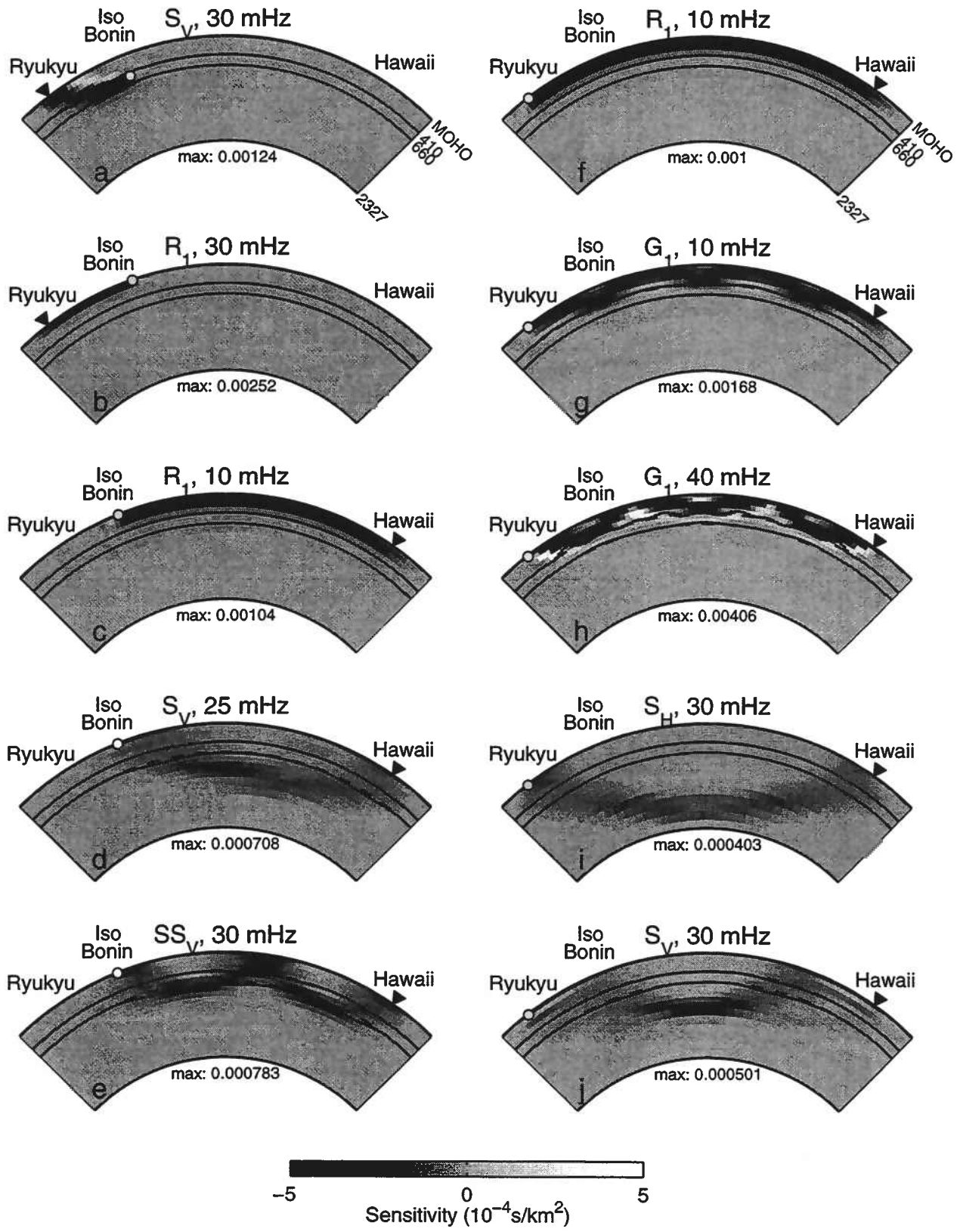
Iso
Bonin
Ryukyu
Hawaii
S_V, 30 mHz
max: 0.00124
a
MOHO
410
660
2327
R_1, 10 mHz
max: 0.001
f
R_1, 30 mHz
max: 0.00252
b
G_1, 10 mHz
max: 0.00168
g
R_1, 10 mHz
max: 0.00104
c
G_1, 40 mHz
max: 0.00406
h
S_V, 25 mHz
max: 0.000708
d
S_H, 30 mHz
max: 0.000403
i
SS_V, 30 mHz
max: 0.000783
e
S_V, 30 mHz
max: 0.000501
j
−5
0
5
Sensitivity (10^{-4}s/km^2)

Figure 5.8

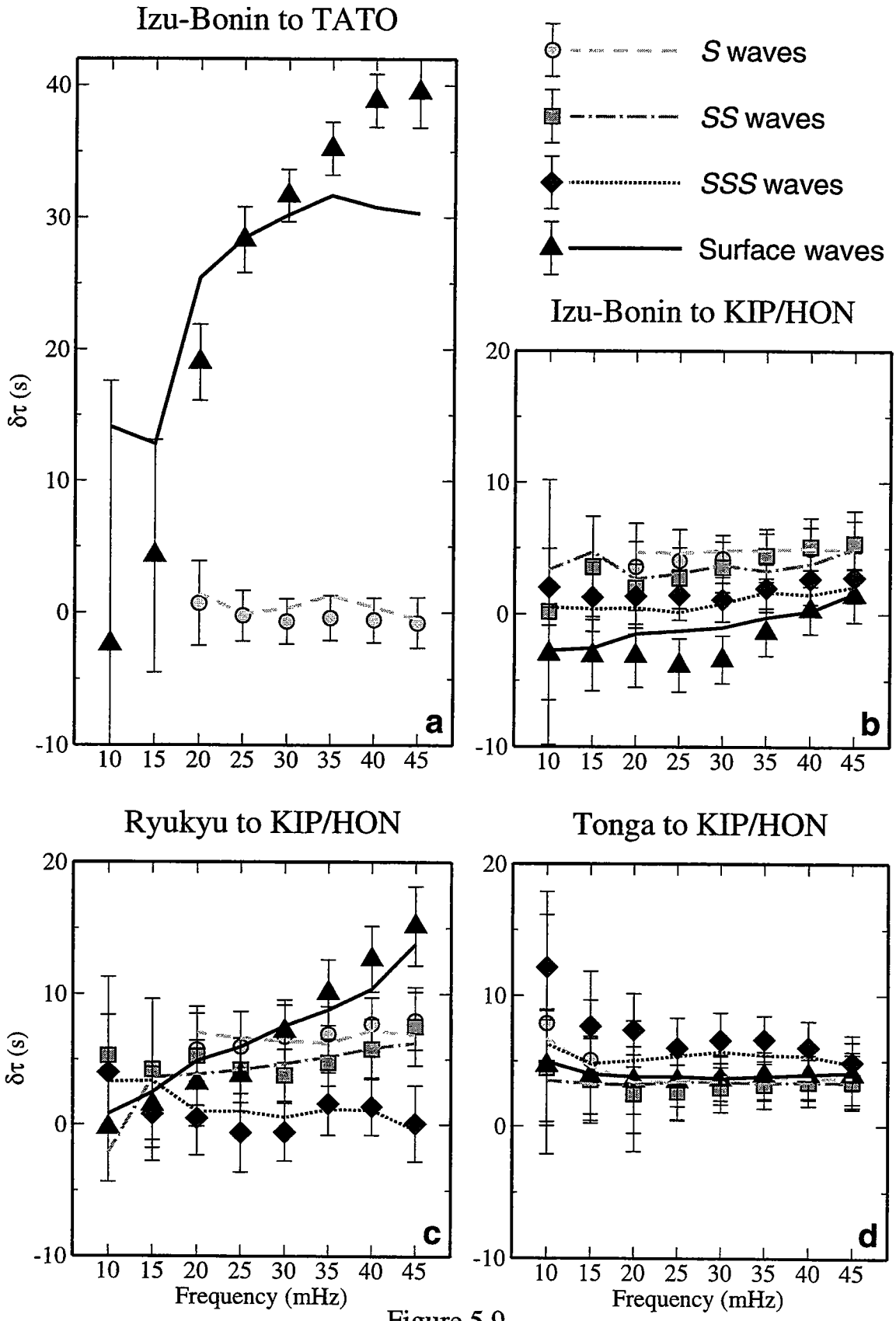
Izu-Bonin to TATO
S waves
SS waves
SSS waves
Surface waves
Izu-Bonin to KIP/HON
Ryukyu to KIP/HON
Tonga to KIP/HON
δτ (s)
Frequency (mHz)
a
b
c
d

Figure 5.9

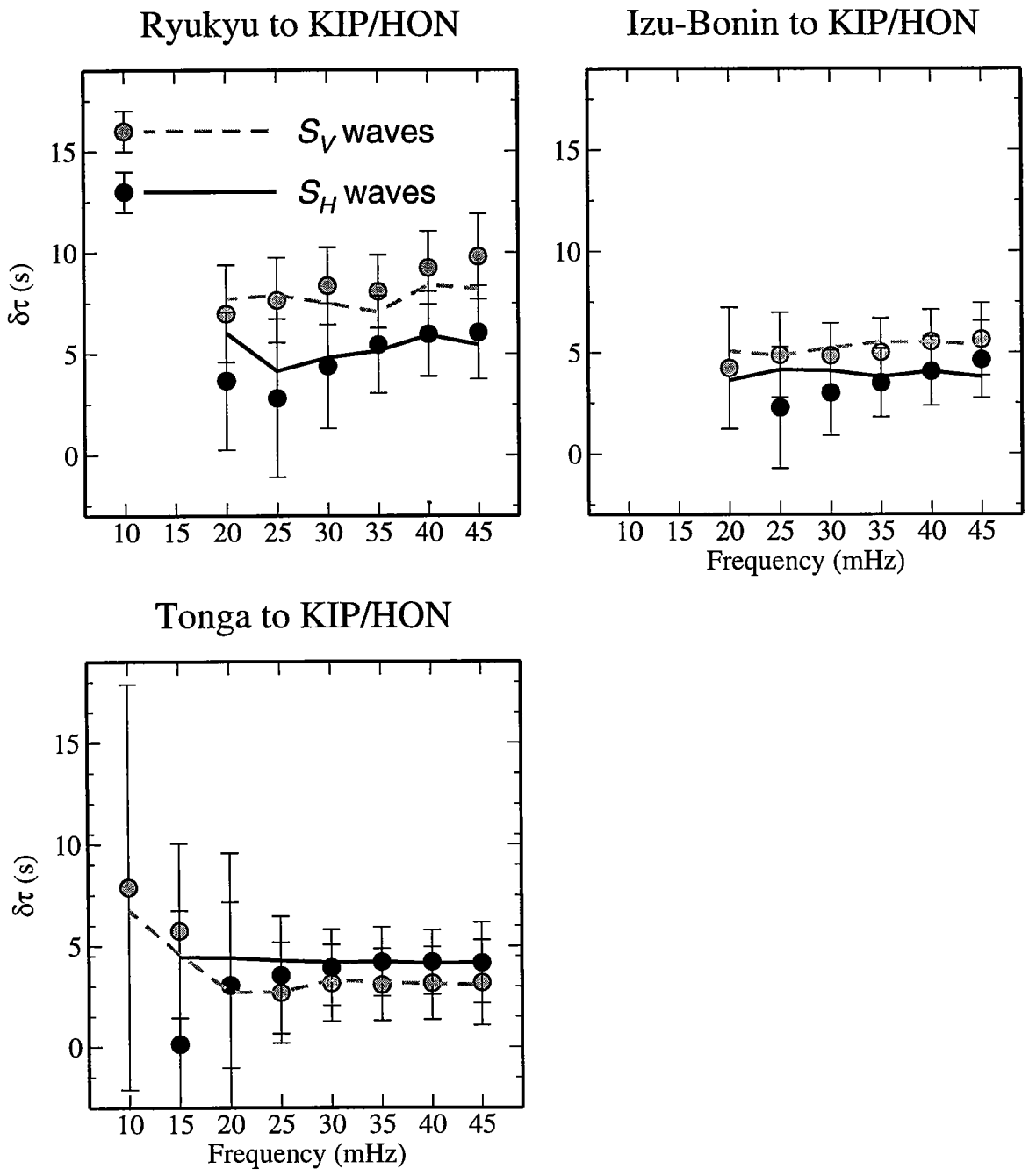
Ryukyu to KIP/HON
Izu-Bonin to KIP/HON
Tonga to KIP/HON
S_V waves
S_H waves
δτ (s)
Frequency (mHz)
0
5
10
15
10 15 20 25 30 35 40 45

Figure 5.10

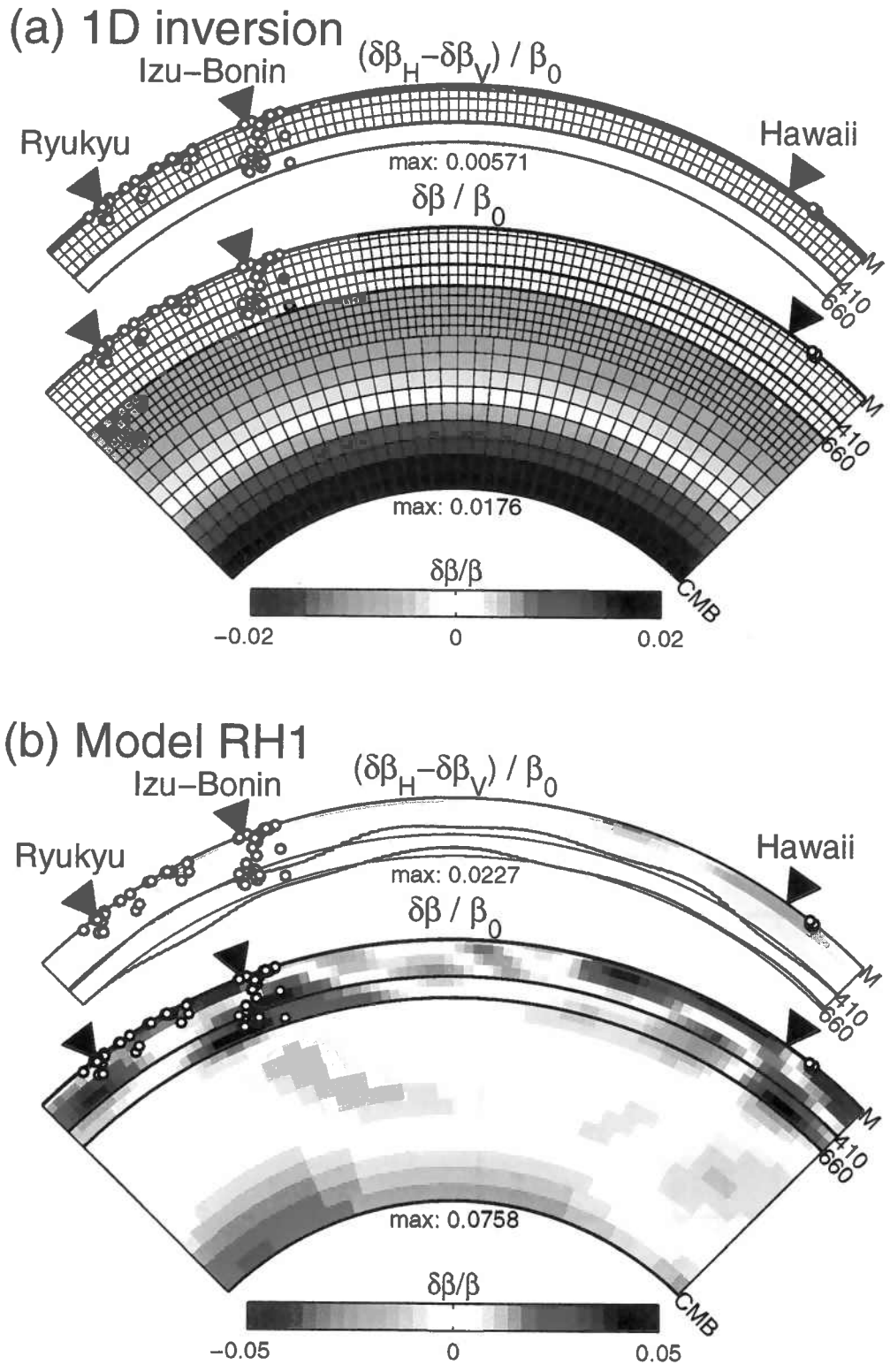
(a) 1D inversion
Izu–Bonin
$(\delta\beta_H - \delta\beta_V) / \beta_0$
Ryukyu
Hawaii
max: 0.00571
$\delta\beta / \beta_0$
M
410
660
M
410
660
max: 0.0176
$\delta\beta/\beta$
CMB
−0.02
0
0.02
(b) Model RH1
Izu–Bonin
$(\delta\beta_H - \delta\beta_V) / \beta_0$
Ryukyu
Hawaii
max: 0.0227
$\delta\beta / \beta_0$
M
410
660
M
410
660
max: 0.0758
$\delta\beta/\beta$
CMB
−0.05
0
0.05

Figure 5.11

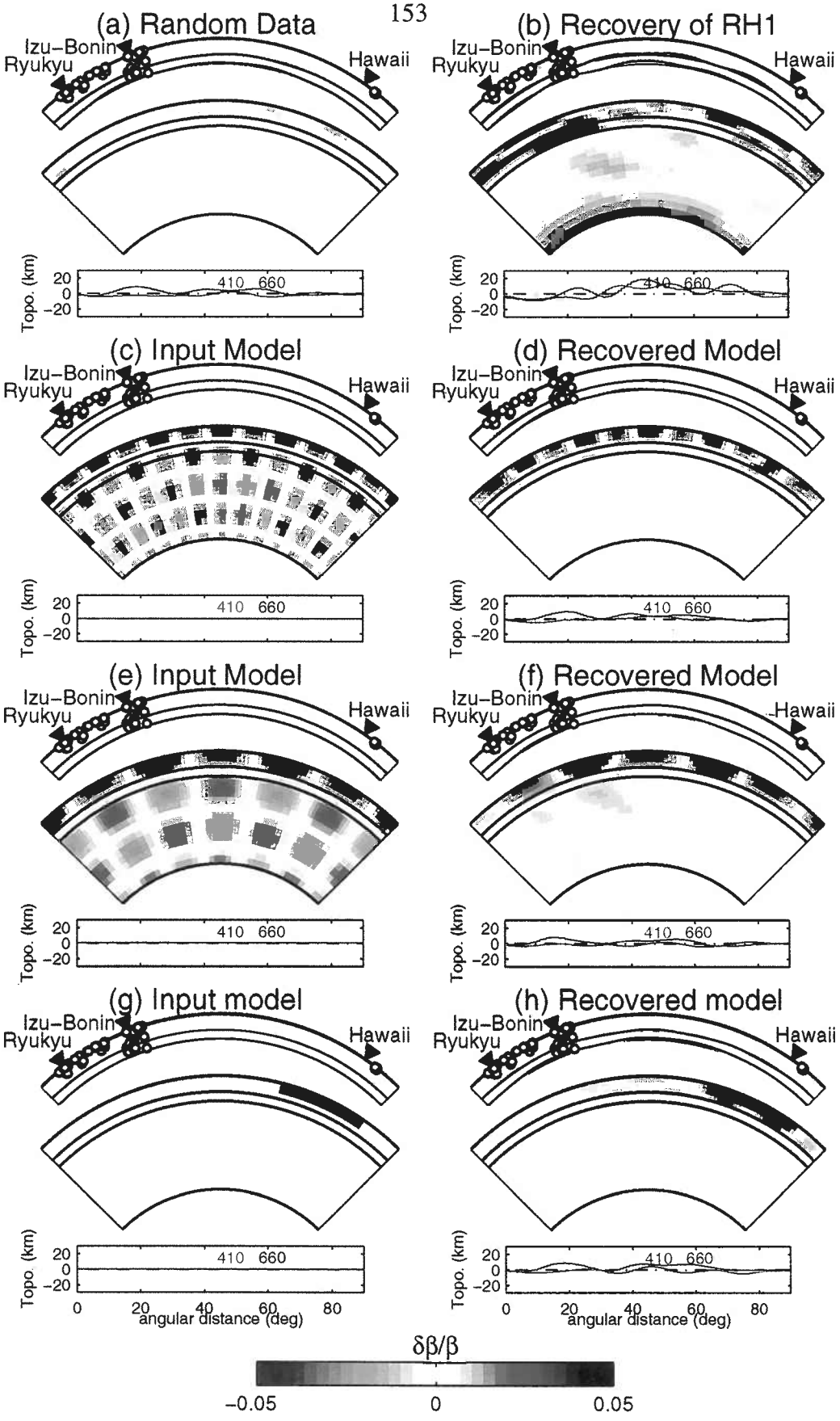
(a) Random Data
(b) Recovery of RH1
(c) Input Model
(d) Recovered Model
(e) Input Model
(f) Recovered Model
(g) Input model
(h) Recovered model
Izu–Bonin
Ryukyu
Hawaii
Topo. (km)
20
0
-20
410
660
0
20
40
60
80
angular distance (deg)
δβ/β
-0.05
0
0.05

Figure 5.12

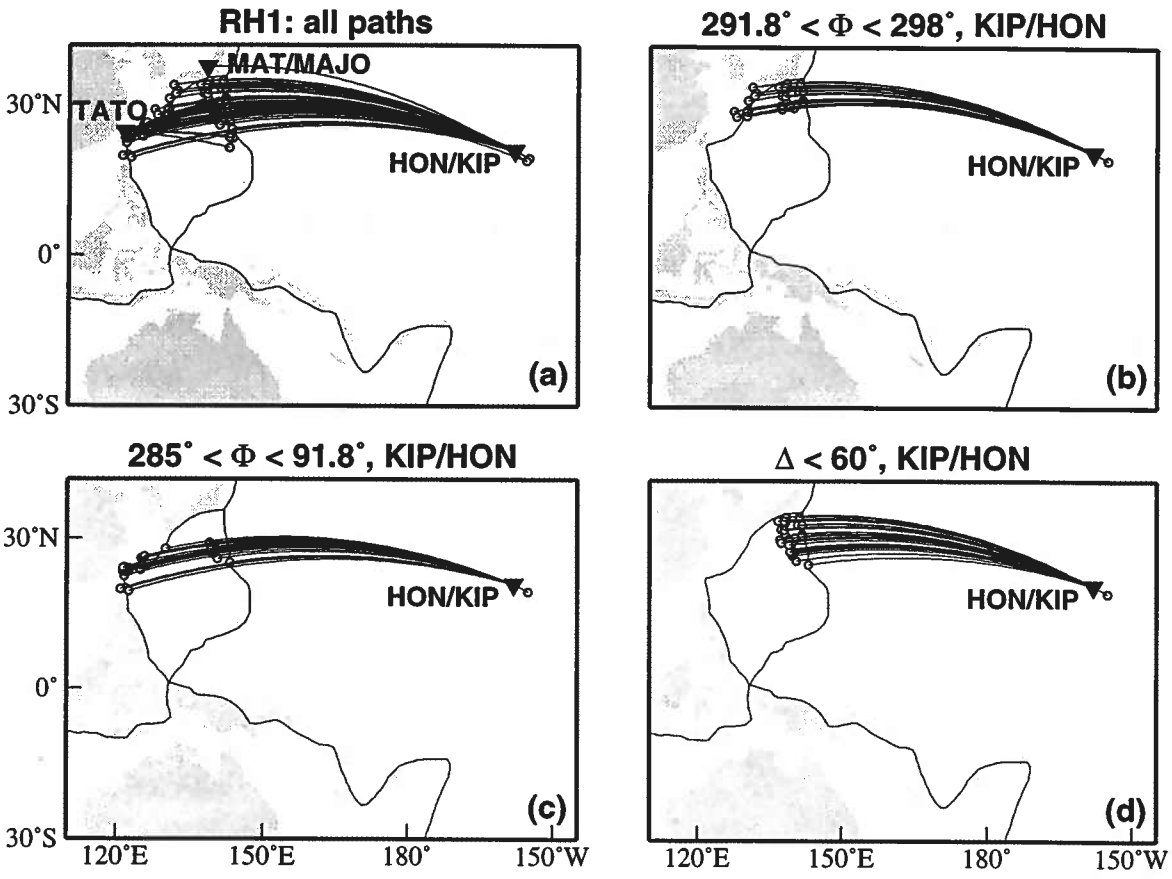
RH1: all paths
MAT/MAJO
TATO
HON/KIP
30°N
0°
30°S
(a)
291.8° < Φ < 298°, KIP/HON
HON/KIP
(b)
285° < Φ < 91.8°, KIP/HON
HON/KIP
30°N
0°
30°S
(c)
120°E
150°E
180°
150°W
Δ < 60°, KIP/HON
HON/KIP
(d)
120°E
150°E
180°
150°W

Figure 5.13

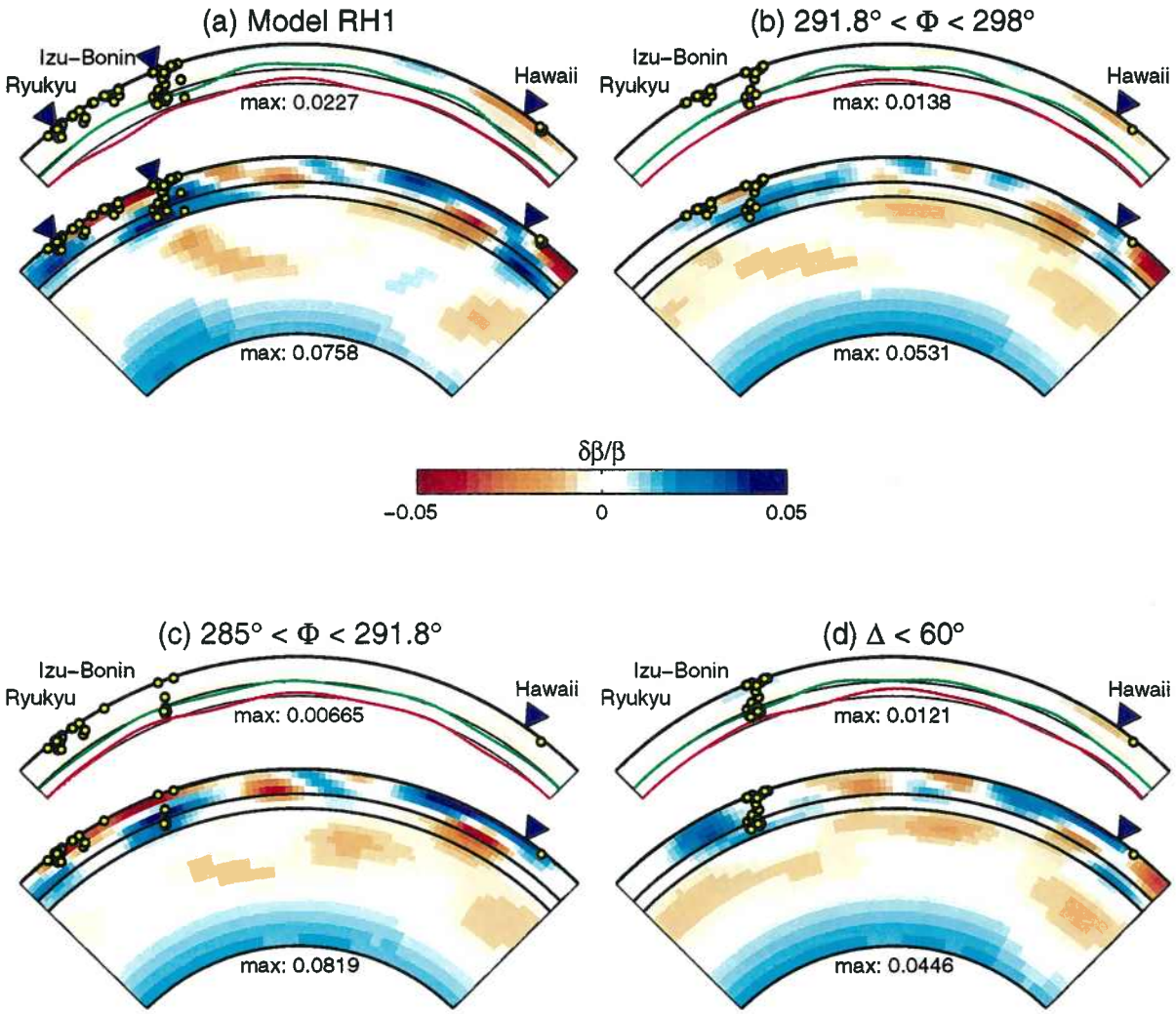
(a) Model RH1
Izu–Bonin
Ryukyu
Hawaii
max: 0.0227
max: 0.0758
(b) 291.8° < Φ < 298°
Izu–Bonin
Ryukyu
Hawaii
max: 0.0138
max: 0.0531
δβ/β
−0.05
0
0.05
(c) 285° < Φ < 291.8°
Izu–Bonin
Ryukyu
Hawaii
max: 0.00665
max: 0.0819
(d) Δ < 60°
Izu–Bonin
Ryukyu
Hawaii
max: 0.0121
max: 0.0446

Figure 5.14

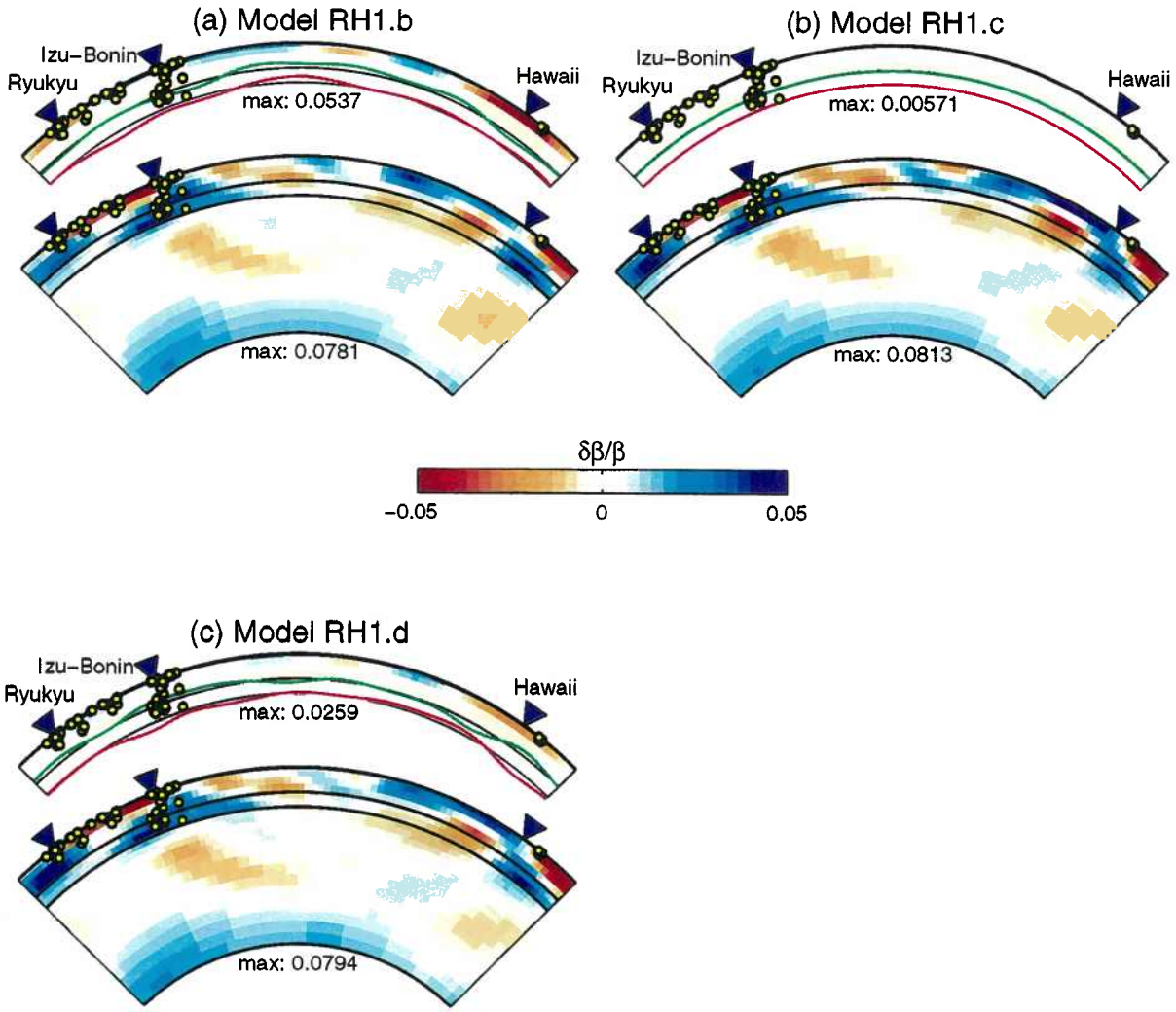
(a) Model RH1.b
Izu–Bonin
Ryukyu
Hawaii
max: 0.0537
max: 0.0781
(b) Model RH1.c
Izu–Bonin
Ryukyu
Hawaii
max: 0.00571
max: 0.0813
δβ/β
−0.05
0
0.05
(c) Model RH1.d
Izu–Bonin
Ryukyu
Hawaii
max: 0.0259
max: 0.0794

Figure 5.15

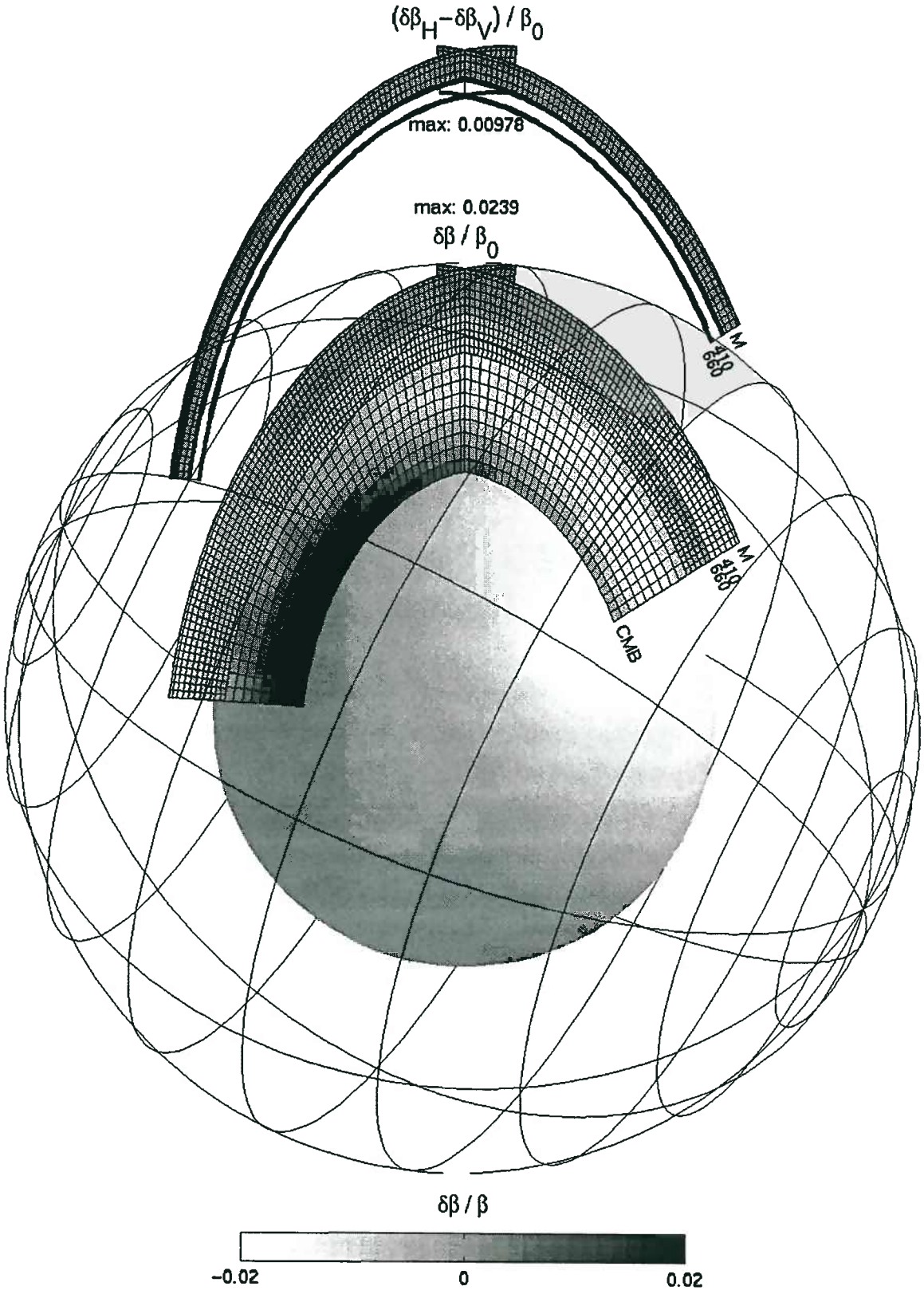
Prior model for THR1
(δβH−δβV) / β0
max: 0.00978
max: 0.0239
δβ / β0
M
410
660
M
410
260
CMB
δβ / β
−0.02
0
0.02

Figure 5.16

Model THR1

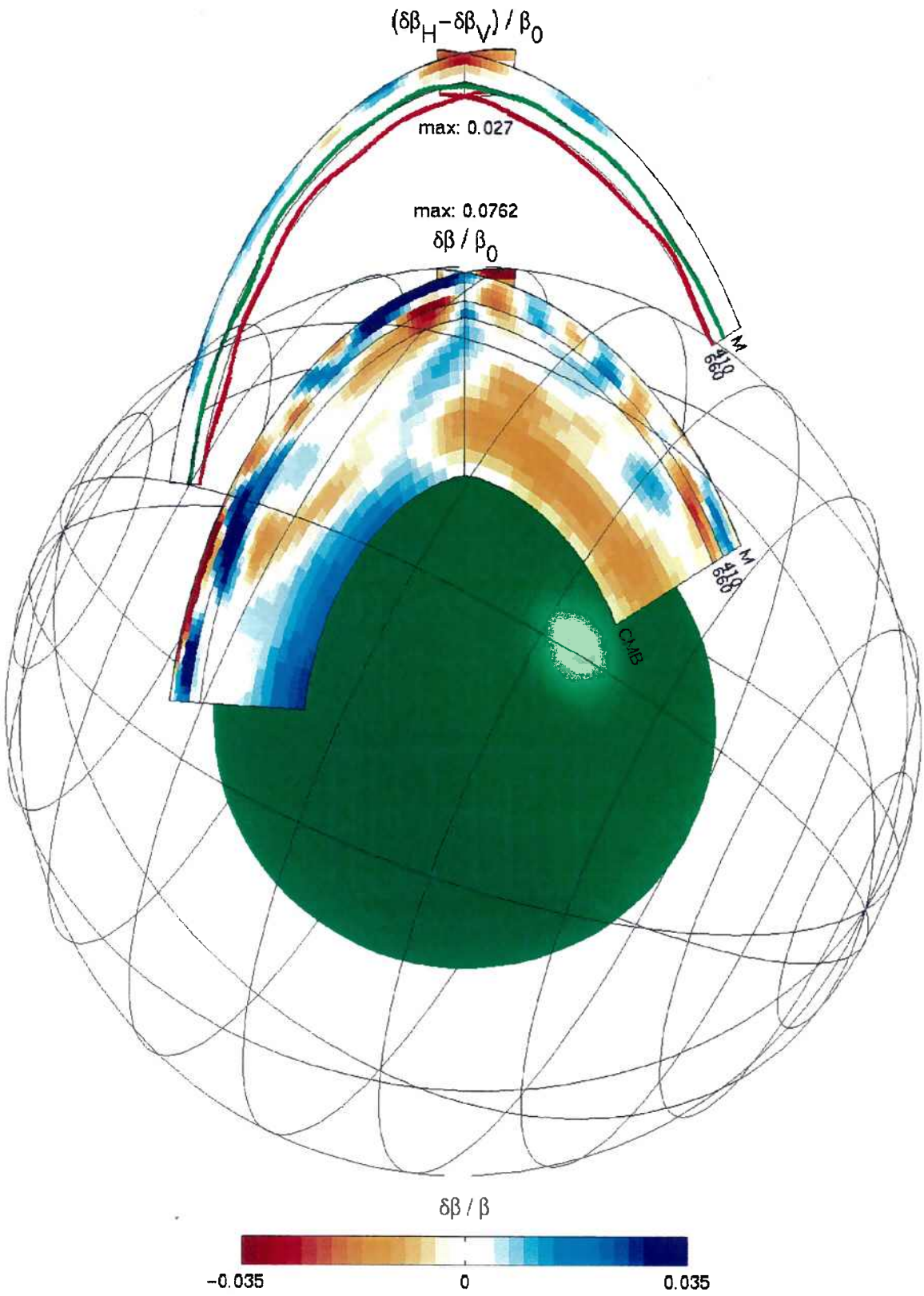

Figure 5.17

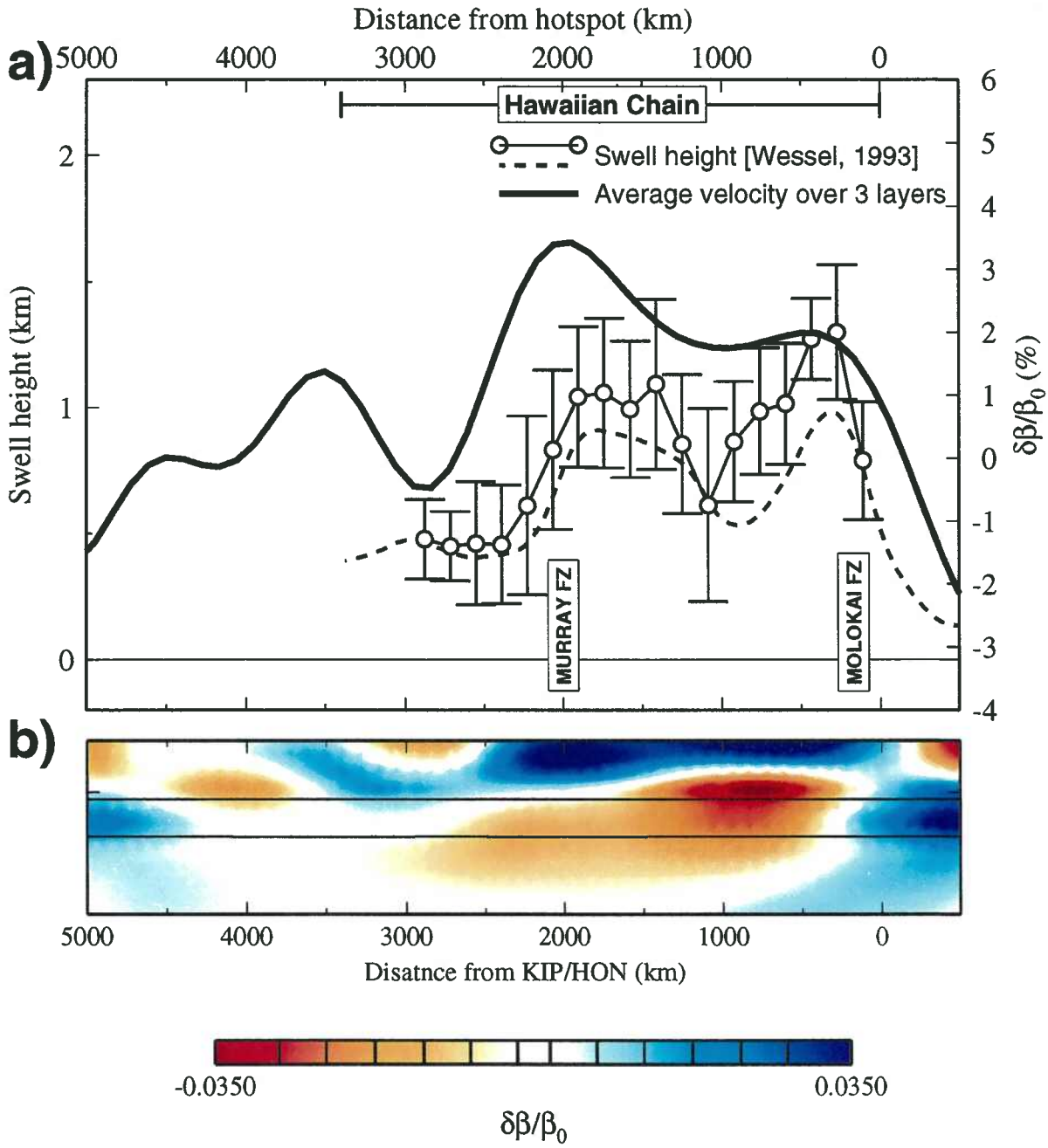
a)
Distance from hotspot (km)
5000
4000
3000
2000
1000
0
Hawaiian Chain
Swell height [Wessel, 1993]
Average velocity over 3 layers
Swell height (km)
δβ/β0 (%)
MURRAY FZ
MOLOKAI FZ
b)
Disatnce from KIP/HON (km)
-0.0350
0.0350
δβ/β0

Figure 5.18

APPENDIX A

RESOLUTION TESTS FOR THE TONGA-HAWAII CORRIDOR

In this appendix, we perform a simple sensitivity analysis to the results along the Tonga-Hawaii corridor by employing a series of resolution tests; we invert synthetic data calculated for various of test models, using the same procedure and parameterization as in the inversion of the real data, and observe how well these models are reproduced. Gaussian noise with standard deviations similar to our estimates for the real data (up to ~8 s) is added to the synthetic data prior to all the inversions. This procedure does not provide a complete resolution analysis, but it does give some useful basis for interpreting the final model by revealing areas of higher and lower sensitivity and primary model tradeoffs. We emphasize, however, that this type of resolution analysis, commonly used in tomographic studies, does not test inaccuracies in the forward theory, such as non linear wave-propagation effects; it assumes that the errors in the data are not correlated; and it depends on the prior model parameterization. Figure A.1 shows some examples of the input and recovered models, plotted with the same color scale as TH2 and the other models in Figures 4.7 and 4.8.

To estimate the effect of random errors on the final model, we invert a series of data sets with random travel-time residuals and compare the magnitudes of the anomalies in the resulting models with those in the TH2 model. The models resulted from inversions of several random number realizations showed maximum perturbation of about 0.9%, 0.3%, and 10 km for isotropic velocities, anisotropic velocities, and transition-zone topographies, respectively (e.g., Figure A.1a). The maximum isotropic velocity perturbations at each depth in Figure A.1a are smaller than in TH2 by at least a factor of 3 and the rms variation in the upper mantle is 4 times smaller, implying that isotropic velocities in TH2 are not

strongly biased by random errors in the data. The same conclusion holds for radial anisotropic heterogeneity in the uppermost mantle. The transition-zone topographies, on the other hand, are more affected by random errors; while the rms variation of the 660's topography in Figure A.1a is about 3 times smaller than in TH2, the variation on the 410 is nearly the same. The transition-zone topographies in TH2 should therefore be interpreted with caution.

The recovery of actual mantle heterogeneities is assessed through a series of synthetic data inversions. In order to test the potential recovery of different features in TH2 we inverted the data residuals that are predicted by this model (after adding the Gaussian noise). The recovered model is shown in Figure A.1b and should be directly compared with Figure 4.7b. Most of the structural features in TH2 remain in this second inversion. The high and low velocity anomalies in the upper mantle between the northern end of Tonga and Hawaii are reconstructed with similar magnitudes and almost no smearing. The other features, however, are not as well reproduced and their magnitudes are underestimated by up to a factor of three, as, for example, the radial anisotropic anomalies or some of the lower-mantle velocity anomalies.

The same behavior is observed in a series of checkerboard inversions. Figures A.1c and A.1e show examples of input models with harmonic variation in isotropic shear velocities at two different wavelengths, and no perturbation in radial anisotropy or transition-zone topographies. The velocity perturbation has peak-to-trough amplitude of 4% in the uppermost mantle which decays to 2% below the 410 discontinuity. The recovered models for both the short- and the long-wavelength examples (Figures A.1d and A.1f, respectively) show an excellent resolving power for upper-mantle isotropic velocities; in particular, the inversion recovers the reversal in the sign of the anomalies at about 350 km in Figure A.1d and at about 500 km in Figure A.1f, demonstrating a good vertical resolution. However, the resolution degrades in the upper part of the lower mantle, below the 660 discontinuity; at this depth, only large features can be partially recovered, as seen

in Figure A.1b. At depths that are below 1200 km or below the turning point of the *S* waves, most of the lateral resolution is lost because the turning-wave data do not sample this region and the *ScS*-reverberations data alone cannot provide sufficient lateral resolution.

The two inversion experiments in Figures A.1c-f also demonstrate that isotropic velocity variation is not mapped into radial anisotropic heterogeneity or into topographic variations. The unwanted topography variation in Figures A.1d and A.1f, is entirely due to the large uncertainties in the data that control the discontinuities (simulated by the large random errors for the first-order reverberations) and does not reflect any tradeoffs between velocity and topography parameters. This can be seen from the nearly identical topography variation in Figure A.1a, which was obtained by inverting pure Gaussian noise, with the same random-number realization. This conclusion is substantiated in the next example, where we invert the synthetic data computed from a model containing only topography variation, with no perturbation in velocity (Figure A.1g). The anticorrelated topography pattern in the input model is well observed in the recovered model (Figure A.1h) despite the small magnitude of the input topographies (maximum perturbation of 10 km). The velocity anomalies are small and are mostly due to the random noise that was added to the synthetic data.

We conclude that the upper-mantle isotropic velocities are the best resolved parameters in TH2, with horizontal and vertical resolving lengths of about 500 and 200 km or less, respectively. Radial anisotropy in the uppermost mantle is resolvable but may be underestimated by a factor of 2-3. The resolution in the upper part of the lower mantle is quite limited and only structures with dimensions of 1000 km or more and perturbation larger than 1% can be partially recovered. The transition-zone topographies are biased by errors in the data but long-wavelength patterns are resolvable. Tradeoffs between parameters of different type are very small.

FIGURE CAPTIONS

Figure A.1. Examples of resolution tests. Each of the models is displayed in the same way as the TH2 model in Figure 4.7, but an additional panel is used for displaying the topography on the 410 (green line) and 660 (red line) discontinuities. Output models were obtained by a joint inversion, identical to TH2. In all the examples, synthetic data were generated by adding (the same) realistic Gaussian noise to phase delays computed from the input models. (a) Output model obtained by inverting Gaussian noise only. (b) Output model from an inversion of the data residuals predicted by TH2 (Figure 4.7b). (c) and (e) Input models with harmonic variation in isotropic shear velocities, having a horizontal and vertical wavelengths of (c) 15° and 1500 km, and (e) 30° and 2000 km. The perturbation in both models has a peak-to-trough amplitude of 4% in the uppermost mantle, which decays to 2% below 410 km, but no perturbation in radial anisotropy or to discontinuity depths. (d) and (f) Output model resulted from inverting the data residuals predicted by the input models in Figures A.1c and A.1e, respectively. (g) Input model with topographic variation on the 410- and 660-km discontinuities, The perturbation has a horizontal wavelength of 30° and a peak-to-trough amplitude of 10 km, but no perturbation in shear velocities. (h) The model recovered by inverting the data residuals predicted by the input model in Figure A.1g.

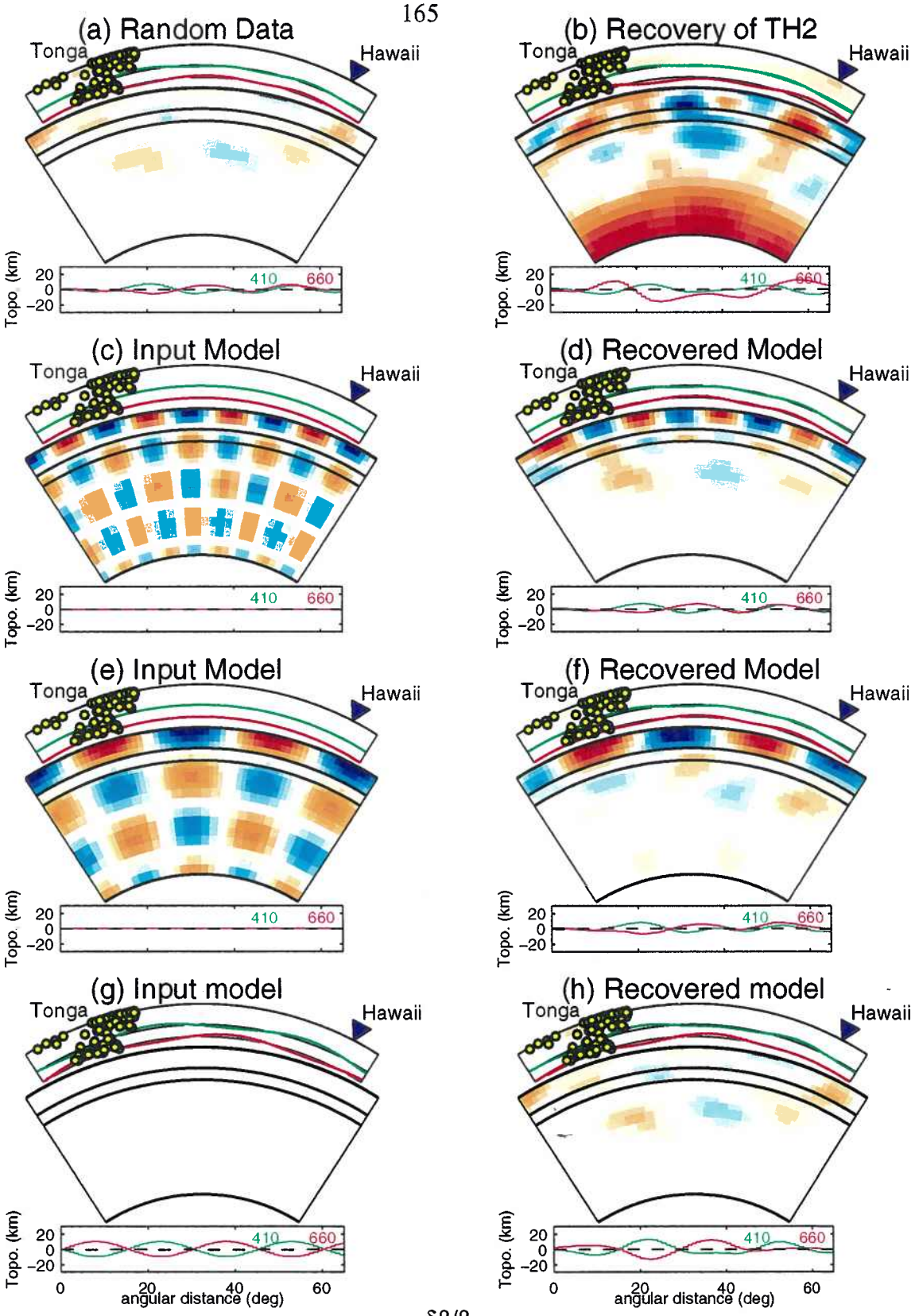
(a) Random Data
(b) Recovery of TH2
(c) Input Model
(d) Recovered Model
(e) Input Model
(f) Recovered Model
(g) Input model
(h) Recovered model
Tonga
Hawaii
Topo (km)
Topo. (km)
20
0
-20
410
660
0
20
40
60
angular distance (deg)
δβ/β
-0.02
-0.01
0
0.01
0.02

Figure A.1

APPENDIX B

APPENDIX B: RESOLVING-POWER CALCULATIONS FOR THE TONGA-HAWAII CORRIDOR, USING THE PRIOR AND POSTERIOR COVARIANCE MATRICES

The prior correlation matrix, $\overline{\rho}$, is a normalized version of the prior covariance matrix $\overline{\mathbf{C}}_{\mathbf{mm}}$ and its elements

$$\overline{\rho}(i,j) = \frac{\overline{C}_{mm}(i,j)}{\sqrt{\overline{C}_{mm}(i,i)\overline{C}_{mm}(j,j)}} \tag{B.1}$$

specify the correlations between the prior uncertainties of the *i*th and the *j*th parameters (4.9), loosely referred to here as the "smoothness constraint" (for $i \neq j$). Figure B.1a shows a color image of $\overline{\rho}$ for the 1375 model parameters of TH2. When interpreting the images in Figure B.1, it is important to remember that the serial number of the model parameters increases fastest horizontally; as a result, the distance between the *i*th and the *j*th parameter wraps around every $i - j = N_d$ blocks, where N_d is the number of blocks at each depth layer. The deviation of $\overline{\rho}$ from a unit matrix is entirely due to the smoothness constraint. The width of each individual diagonal features in Figure B.1a is proportional to the horizontal correlation length l_Δ in (4.9), whereas the width of the global pattern is proportional to the vertical correlation length l_r. The correlation lengths are the same for the entire mantle but the pattern become narrower for the lower mantle below 1200 km, because the blocks (parameters with serial numbers 716 to 985) are larger. The zero correlations outside the three squares in Figure B.1a imply that no prior correlation was imposed between isotropic and anisotropic velocity parameters or between velocity and topography parameters. The figure also shows that no prior correlation was imposed between the two discontinuities.

Parameters that are well resolved in TH2 will show small posterior uncertainties relative to their prior uncertainties, i.e., large variance reduction. We define the matrix $\tilde{\rho}$ as the posterior covariance matrix (4.6) normalized by the diagonal terms of the prior covariance matrix, i.e.,

$$\tilde{\rho}(i,j) = \frac{C_{mm}(i,j)}{\sqrt{\overline{C}_{mm}(i,i)\overline{C}_{mm}(j,j)}} \tag{B.2}$$

(Figure B.1b). The diagonal terms of this matrix, $1-\tilde{\rho}(i,i)$, are the ratios between the posterior and prior variances of the model parameters. The variance reduction for the ith model parameter is therefore $1-\tilde{\rho}(i,i)$ (Figure B.2). Figures B.1b and B.2 indicate that the best resolved parameters are the isotropic velocities in the upper-mantle and the transition zone ($i \leq 390$) which show $\sigma^2(i)/\overline{\sigma}^2(i)$ of about 0.1 or variance reduction of 0.9. The variances for the upper part of the lower mantle ($391 \leq i \leq 585$) are also significantly reduced to about 30 to 45% of their prior values. The smallest variance reduction, $1-\sigma^2(i)/\overline{\sigma}^2(i) = 0.1$, is observed for the lower mantle below 1200 km ($716 \leq i, j \leq 985$). The anisotropic parameters (middle square in Figure B.1b), and the 410's and 660's topography (upper-right square) show better variance reductions of about 0.35, 0.5, and 0.6 respectively (Figure B.2).

Figure B.1c shows the posterior correlation matrix ρ (4.7), which indicates how well two given model parameters are independently resolved by the inversion. A parameter that is independently resolvable will have off-diagonal terms with magnitude close to zero. The posterior correlation matrix, due to the normalization in (4.7), is +1 along the diagonal, and gradually decreases to negative values greater than –1, away from this axis of symmetry. The global pattern associated with the smoothing constraint in Figure B.1a is still dominant in Figure B.1c, indicating that velocity perturbations on neighboring blocks are strongly affected by the prior smoothing and are not independently resolved by the data. Farther examination, however, reveals small posterior correlations (and anti-correlations) between:

(1) upper-mantle and mid-mantle isotropic velocities (region A), (2) anisotropic and isotropic velocities in the upper mantle (region B), and (3) isotropic velocities and transition-zone topographies (region C). In all of these cases, the correlations are of order 0.2 or less, much smaller than the posterior correlations associated with the prior smoothing constraint. Finally, region D indicates that the posterior uncertainties for the 410 and the 660 discontinuities are neither correlated nor anti-correlated, implying that both discontinuities can be independently resolved by the inversion.

We examine the statistical significance of ten specific features in TH2 (Figure B.3) by calculating their posterior mean, their prior and posterior uncertainties, and their variance reductions using (4.8). Table B.1 summarizes the results for the ten regions of Figure B.3. As an example, consider the area of high upper-mantle shear velocity near the center of the model grid (region 2), which has an integrated amplitude of 1.6%. The uncertainty for this integral computed from the prior distribution is about 1.8%, whereas its posterior uncertainty is less than 0.4%. In other words, the inversion sharpens the estimate from a prior value of $0\% \pm 1.8\%$ to a posterior value of $1.6\% \pm 0.4\%$. An examination of the off-diagonal terms of the posterior correlation matrix (Figure B.1c) shows that the cross-correlation between this error and those for other regions is small, so that this particular feature is statistically significant at a very high confidence level. A similar conclusion can be drawn for the other four regions of high and low velocity in the upper mantle (regions 1 to 5); each of these regions is significantly different from zero at the 90% confidence level and they all have a variance reduction exceeding 94%. The other features in Figure B.1 have lower variance reductions. For example, the area of increased anisotropy in the uppermost mantle near the center of the grid (region 8) shows variance reduction of less than 50%. However, the posterior estimate of this specific feature ($0.68\% \pm 0.32\%$) indicates that it is statistically significant at the 90% confidence level; the small variance reduction in this case, simply reflects the small prior uncertainty imposed on the anisotropic parameters. In contrast, the region of small positive topography on the 410 discontinuity

near the center of the grid (region 9) is not statistically significant at this high confidence level, as indicated by its large posterior uncertainty (5.6 km), which is larger than its mean amplitude (3.6 km).

On the whole, Figure B.1 and table B.1 substantiate the conclusions from Appendix A that the best resolved model parameters in TH2 are the isotropic velocities above the 660 discontinuity. Lower mantle velocities below 1200 km are essentially unresolved and only average quantities can be obtained. Large-scale anomalies in all the other parameters are at least partially resolvable, and coupling between model parameters of different type is weak.

Table B.1. Standard error analysis for the regions shown in Figure B.3

Region	posterior mean	standard deviation		variance reduction
		posterior	prior	
1	-0.69 %	0.41 %	1.87 %	0.953
2	+1.64%	0.36 %	1.84 %	0.962
3	-0.45 %	0.29 %	1.87%	0.976
4	+0.58 %	0.38 %	1.87%	0.958
5	-1.82%	0.43 %	1.84 %	0.945
6	+0.49%	0.19 %	0.32 %	0.635
7	+1.01 %	0.31 %	0.46 %	0.546
8	+0.68%	0.32 %	0.44 %	0.482
9	+3.63 km	5.26 km	8.37 km	0.604
10	-16.10 km	4.45 km	8.37 km	0.717

FIGURE CAPTIONS

Figure B.1. Color image of the elements of (a) the prior correlation matrix $\overline{\rho}(i,j)$, (b) the posterior, normalized covariance matrix $\tilde{\rho}(i,j)$, and (c) the posterior correlation matrix $\rho(i,j)$. The horizontal and vertical axes represent the serial number of the model parameters. The numbering starts from the top-left cell and increases fastest horizontally; as a result, the distance between the *i*th and the *j*th model parameter wrap around every $i-j=N_d$ cells, where N_d is the number of cells at each depth layer. The global pattern becomes narrower for $716 \le i, j \le 985$ because in this interval each mantle layer is sampled by only 30 instead of 65 cells (cf. Figure 4.7a and section 4.5.1). The large, bold, lower-left square bounds the 985 isotropic velocity parameters. The other two bold squares bound the anisotropy parameters ($i,j \in [986,1245]$), and the topography parameters ($i,j \in [1246,1375]$). Note the small values of the posterior, normalized covariance in Figure B.1b for the isotropic velocities of the upper mantle and the transition zone ($i, j \le$ 390). The general morphology of these three matrices as well as specific features, like those marked by A, B, C, and D in the posterior correlation matrix, are discussed in the text.

Figure B.2. Variance reduction, $1-\tilde{\rho}(i,i)$, for the TH2 model parameters. Gray scale in the top two panels marks the variance reduction of the isotropic and anisotropic velocity parameters; darker regions correspond to areas with high variance reduction. Bottom panel display the variance reduction for the topography of the 410 (dashed line) and 660 (solid line) discontinuities.

Figure B.3. White areas are specific features whose individual prior and posterior standard are shown in Table B.1. In TH2 (Figure 4.7b) regions 1, 3, and 5 represent low-velocity anomalies while regions 2 and 4 represent high velocity anomalies within the upper mantle.

Regions 6 and 7 (gray area within region 6) represent the high lower-mantle velocity anomaly below Tonga; region 8 represents the positive anisotropic anomaly in the middle of the corridor; and regions 9 and 10 represent the topographic high on the 410- and the topographic low on the 660 km discontinuities between angular distances of 24° and 35°.

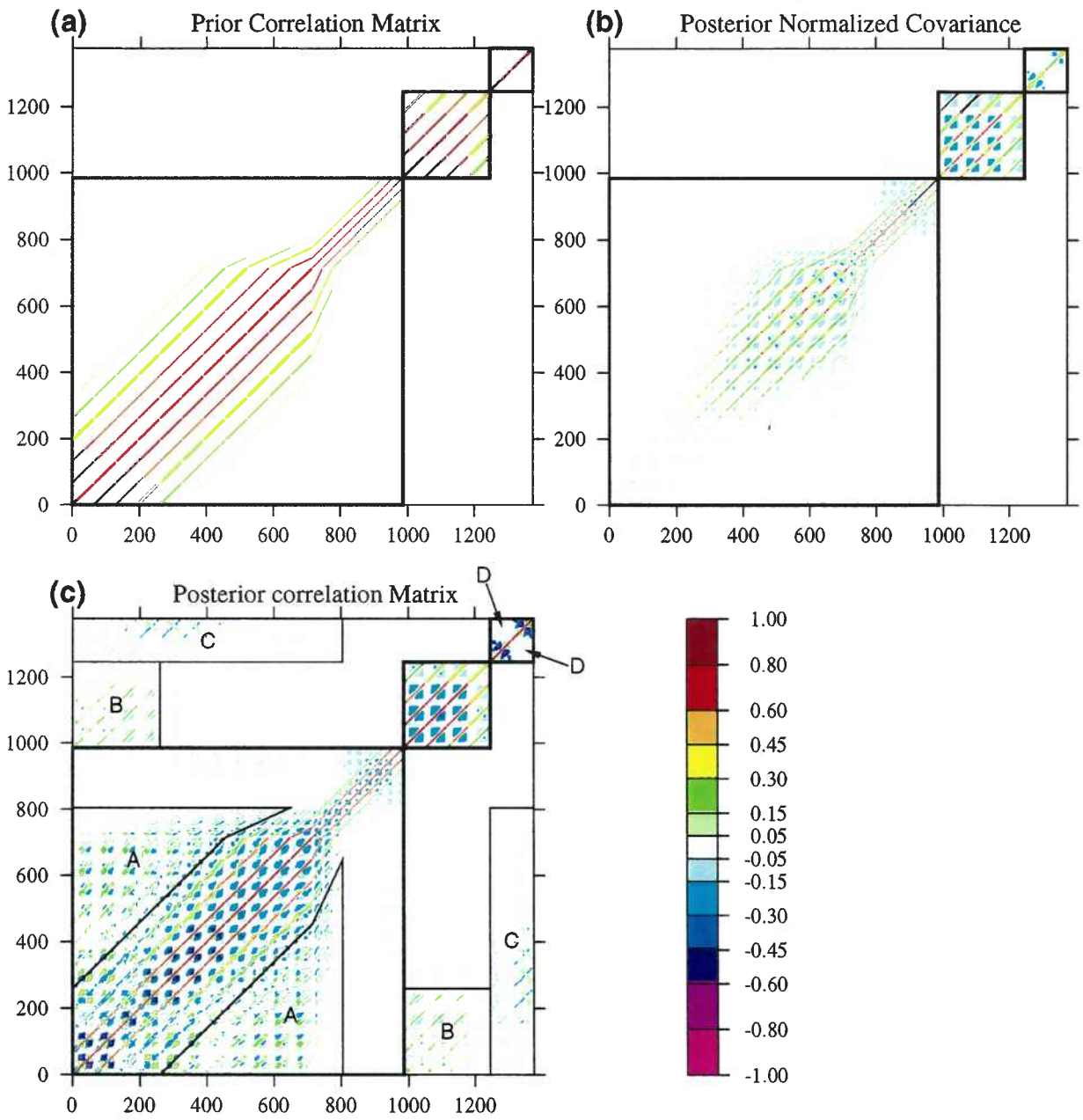
(a)
Prior Correlation Matrix
(b)
Posterior Normalized Covariance
(c)
Posterior correlation Matrix
A
B
C
D
1.00
0.80
0.60
0.45
0.30
0.15
0.05
-0.05
-0.15
-0.30
-0.45
-0.60
-0.80
-1.00
0
200
400
600
800
1000
1200

Figure B.1

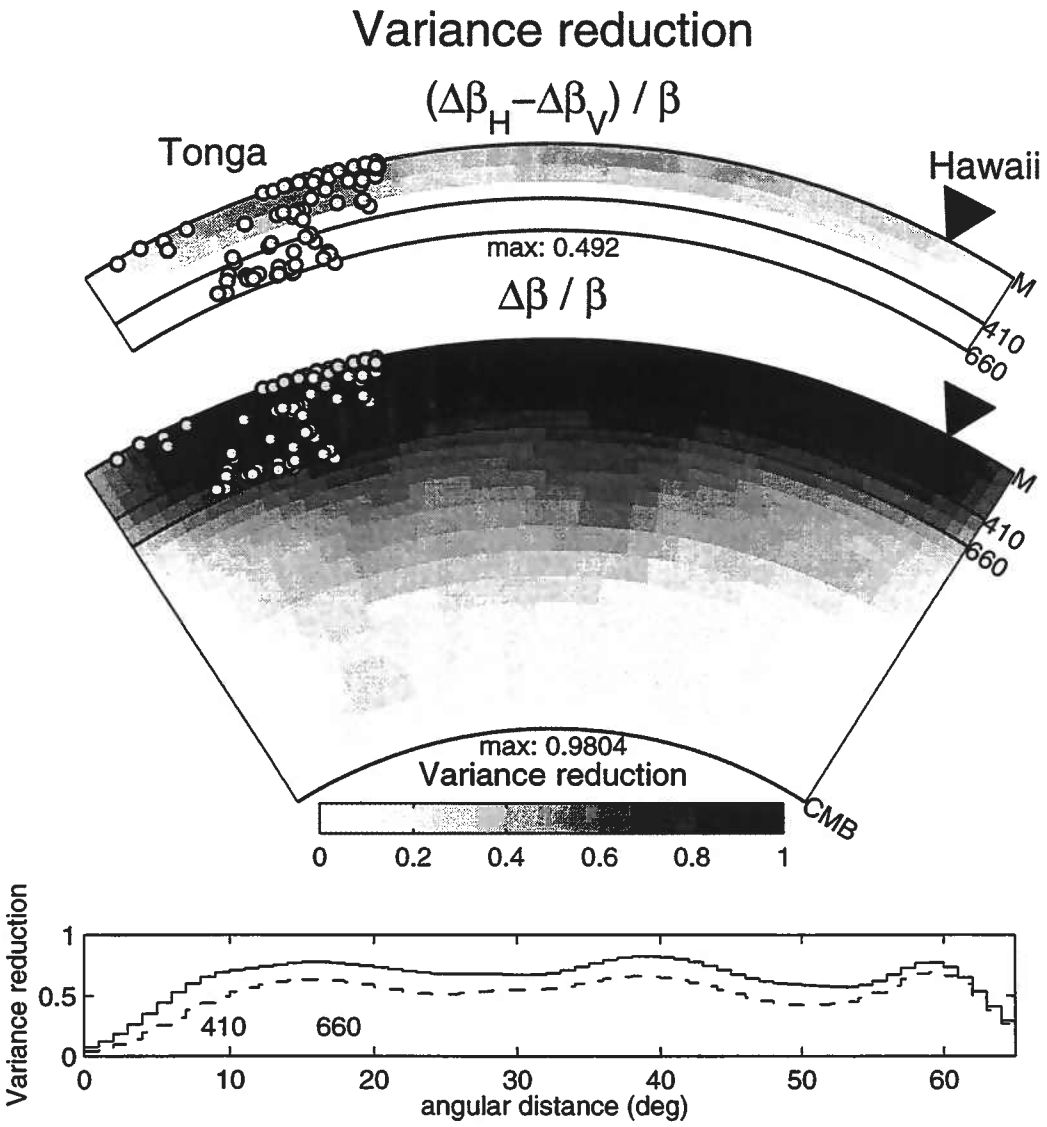
Variance reduction
$(\Delta\beta_H - \Delta\beta_V) / \beta$
Tonga
Hawaii
max: 0.492
$\Delta\beta / \beta$
M
410
660
M
410
660
max: 0.9804
Variance reduction
CMB
0
0.2
0.4
0.6
0.8
1
Variance reduction
1
0.5
0
410
660
0
10
20
30
40
50
60
angular distance (deg)

Figure B.2

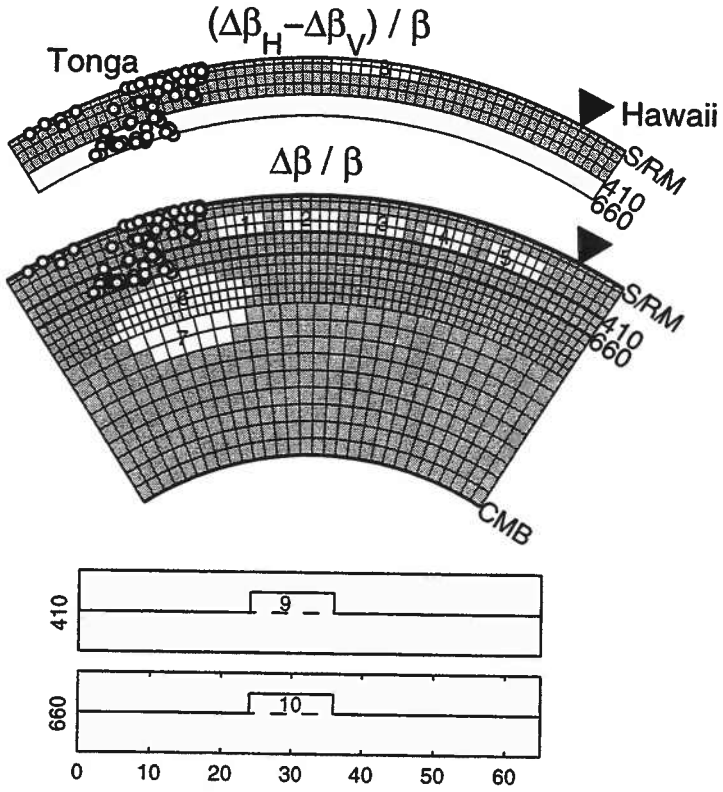
$(\Delta\beta_H - \Delta\beta_V) / \beta$
Tonga
Hawaii
S/RM
410
660
$\Delta\beta / \beta$
1
2
3
4
5
6
7
S/RM
410
660
CMB
410
9
660
10
0
10
20
30
40
50
60

Figure B.3

APPENDIX C

APPENDIX C: DYNAMIC COMPENSATION MODELS FOR THE TONGA-HAWAII CORRIDOR

We demonstrate here that the positive correlation between geoid highs of the swells and temperature lows (which are represented by the high upper-mantle seismic velocities in TH2) along the Tonga-Hawaii corridor, can be explained by a dynamic compensation mechanism with a viscosity profile that includes a low viscosity channel (LVC). It is important to emphasize, however, that the thermal convection models invoked in this appendix cannot explain the positive topography of the swells.

C.1 HARMONIC ANALYSIS OF GEOID AND VELOCITY ANOMALIES

In order to obtain a dynamic model for the mantle which satisfies both the seismological and the gravitational-potential data, we analyze the correlation between the seismic velocities and the geoid anomalies around the dominant wavelength of the former. We start by finding the harmonic degree and the phase that best fit the upper-mantle velocity structure of TH2 in the interval $[\theta_1, \theta_2]$, by solving the following least-square problem

$$\bar{\gamma}(\theta) = A_1 \cos\left[(l+1/2)\theta + \varphi\right] + A_2\theta + A_3; \qquad \theta_1 \le \theta \le \theta_2, \tag{C.1}$$

where θ is the distance along the corridor measured from the station, $\bar{\gamma}(\theta) = \text{avg}\left(\delta\beta/\beta_0\right)$ is the relative velocity perturbation averaged over the upper mantle and the transition zone (blue line in Figure 4.11c), l is the harmonic degree, A_1 and φ are amplitude and phase factors respectively, and A_2 and A_3 are variables to account for a linear trend and a constant deviation of $\bar{\gamma}$. An harmonic degree of $l = 26$ seems to provide the best fit to $\bar{\gamma}$. Using l and φ obtained from (C.1) we compute the harmonic coefficients $\bar{N}^l$, $\bar{\gamma}^l$, and

$\gamma^l(z)$ for the average profile of the filtered geoid along the corridor, and for the depth-averaged and original velocity perturbations of TH2, respectively:

$$\begin{aligned} \overline{N}^l &= \int_{\theta_1}^{\theta_2} \overline{N}(\theta) b(\theta) d\theta, \\ \overline{\gamma}^l &= \int_{\theta_1}^{\theta_2} \overline{\gamma}(\theta) b(\theta) d\theta, \\ \gamma^l(r) &= \int_{\theta_1}^{\theta_2} \gamma(\theta, r) b(\theta) d\theta, \end{aligned} \tag{C.2}$$

where $\overline{N}(\theta)$ is the average profile of the filtered geoid along the corridor (red line in Figure 4.11c), $\gamma(\theta,r) = \delta\beta/\beta_0$ is the velocity perturbation of TH2 at a distance θ from the station and radius r, and $b(\theta)$ is the basis function:

$$b(\theta) = \frac{\cos\left[(l+1/2)\theta + \varphi\right]}{\left[\int_{\theta_1}^{\theta_2} \cos^2\left[(l+1/2)\theta + \varphi\right] d\theta\right]^{1/2}}. \tag{C.3}$$

The phase term φ both here and in (C.1) depends on the fitting interval $[\theta_1, \theta_2]$, which was chosen to be [5°, 32°] measured southwesterly from Hawaii. Using this interval, which avoids the Hawaiian islands and the Tonga subduction zone, we obtain $\overline{N}^l = 0.71$, and $\overline{\gamma}^l = 0.0042$. The correlation between the geoid and the upper-mantle velocity perturbation, or the ratio $\overline{N}^l/\overline{\gamma}^l$, is therefore 170 ± 70 m (or 1.7 ± 0.7 m for each 1% of velocity perturbation, see Figure 4.11c). The uncertainty term was obtained from several tests, where we computed the correlation coefficient assuming different geoid-filter parameters and/or different fitting interval. We emphasize that this correlation was always positive and was unaffected by the parameterization to within an uncertainty of less then 50%.

C.2 Dynamic Calculations of the Geoid and Constraints on Viscosity Structure

The surface dynamic topography and geoid anomaly can be calculated for a given wavelength using the corresponding kernels and the harmonic coefficients for the velocity perturbations as a function of depth, after assuming a distribution of viscosity with depth and a scaling relation between the relative density and velocity perturbations [*Hager and Clayton*, 1989]. The calculations below are performed using the geoid and dynamic-topography kernels of *Panasyuk et al.*, [1996], which include the effects of mantle compressibility and an overlying ocean layer (both effects, however, decrease with wavelength and are negligible at $l = 26$). We also include the effect of an elastic lithosphere on the geoid kernels [see, *Hager* , 1991] by specifying a lithospheric viscosity that is high enough to prohibit tangential flow close to the surface and by modifying the dynamic topography. The former condition was satisfied by choosing a viscosity factor $\geq 3\times10^3$ between the lithosphere and the asthenosphere, whereas the latter condition was incorporated into the non-dimensional geoid kernel as follows:

$$G_e^l = G^l + H^l\left[\frac{1}{1+Dk^4/\Delta\rho g} - 1\right], \tag{C.4}$$

where G^l and H^l are the original non-dimensional geoid and surface-topography kernels respectively [*Hager and Clayton*, 1989; *Panasyuk et al.*, 1996], $k = (l+1/2)/R$ is the wave number, R is the Earth radius, $\Delta\rho$ is the density difference across the surface, g is the gravitational acceleration at the surface and $D = ET_e^3/\left[12\left(1-\nu^2\right)\right]$ is the flexure rigidity of an elastic plate of thickness T_e, Young's modulus E, and Poison's ratio ν [*Turcotte and Schubert*, 1982]. Equation (C.4) states that the geoid at the surface is affected by the dynamic topography of an elastic lithosphere and not by the dynamic topography of a viscous upper layer with no flexural rigidity.

The harmonic coefficients of the geoid anomaly predicted at the surface from a density perturbations $\delta\rho^l(r)$ situated within the upper 660 km of the mantle are

$$\tilde{N}^l = \frac{4\pi\Gamma R}{(2l+1)g}\int_{r_{660}}^{R} G_e^l(r)\delta\rho^l(r)dr, \qquad \text{(C.5)}$$

where Γ is the gravity constant, r_{660} is the radius of the 660-km discontinuity, and $l=26$ is the harmonic degree of our analysis. The density perturbations are obtained from the relative velocity perturbation in TH2 using a constant scaling $\delta\rho/\rho = C_{\rho\beta}\,\delta\beta/\beta$. The conversion parameter, $C_{\rho\beta}=0.2$, was obtained by assuming a thermal expansion coefficient of 3×10^{-5} /K and a thermal coefficient of shear velocity, $\partial\beta/\partial T$ = –0.5 m/s/K [*Creager and Jordan*, 1986; *Kato*, 1997].

The observed geoid anomaly was compared to the geoid predicted from a series of viscosity models. The viscosity profiles were prescribed relative to the viscosity in the transition zone, because the gravitational potential depends only on the viscosity contrasts but not on the absolute viscosities [*Hager and Clayton*, 1989]. As a starting model, we employ a modified version of the *Hager and Clayton* [1989] preferred viscosity structure (Figure C.1a). The 3.5 order of magnitude viscosity jump from the lid to the asthenosphere implies that the lid viscosity in this model is effectively infinite. The high-viscosity lid is assumed to be bounded at its bottom by the sharp G discontinuity of PA5, at 68 km depth [*Gaherty et al.*, 1996]. This viscosity profile also includes a low-viscosity asthenospheric channel with sub-asthenosphere viscosity, low enough to allow flow, and a high-viscosity lower mantle, which are all required in order to fit the global geoid observations [*Hager*, 1991]. Placing these viscosity jumps near the phase transitions at 400 and 670 km seems to be geophysically plausible [*Sammis et al.*, 1977].

In a thermal convection model where $C_{\rho\beta}>0$, the robust observation that the geoid anomaly, $\overline{N}_l$, is positively correlated with the upper-mantle velocity perturbations, around the dominant wavelength of ~1500 km ($l=26$), implies that the geoid kernel at this

wavelength should be mostly positive. However, the geoid kernel for our starting viscosity model (solid line in Figure C.1b) is, on average, strongly negative because the gravitational effect from the surface boundary deformation (Figure C.1c) overwhelms the effect from the driving density contrast. This geoid kernel predicts a negative geoid anomaly over the cold downwellings, i.e., $\tilde{N}_l < 0$, which does not match the observed value of $\overline{N}_l = 0.71$. One way to flip the sign of $\tilde{N}_l$ is by adding the gravitational effect from the flexural rigidity of the lithosphere, which tends to decrease the surface dynamic topography and to make the overall geoid kernel more positive (C.4). However, at wavelength of 1500 km, a 100-Ma lithosphere with an elastic plate thickness, T_e, of 30-40 km [*Watts et al.*, 1980; *Watts and ten Brink*, 1989] reduces the dynamic topography by less then 1% (dashed line with dots in Figure C.1c) so that the change in the geoid kernel is negligible (Figure C.1b). Figure C.1d shows that we can flip the sign of $\tilde{N}_l$ and fit the observed value only by choosing T_e of 90 and 130 km respectively. Since these elastic thicknesses are 3 to 5 times larger than those expected for the Tonga-Hawaii corridor [*Calmant*, 1987], these particular models are ruled out.

An alternative way to fit the positive correlation between the geoid anomalies and the density distribution is by modifying the viscosity structure of the upper mantle (e.g., Figures C.2a and C.3a). It is easy to see, that in order to obtain a geoid kernel which is mostly positive, one needs to invoke an LVC beneath the high-viscosity lid. The geoid kernels for a constant viscosity structure are always negative for all wavelengths because the gravitational effect from the boundary deformation overwhelms the effect from the driving density contrasts; adding a high-viscosity lid, which can support a larger surface deformation, will only make these kernels more negative [*Hager and Clayton*, 1989]. An LVC below the lid, on the other hand, decreases the coupling of the flow to the surface and increases the coupling to the CMB. The gravitational effect from the driving density contrast, in this case, becomes more dominant, and the resulting geoid kernel is less negative and can change sign (e.g., Figures C.2b, and C.3b). The geoid-anomaly sign at a

given wavelength (which is strongly influenced by the depth at which the kernel change its sign) is controlled by the viscosity, η_{LVC}, of the LVC and by its thickness, h_{LVC} (Figures C.2d and C.3d). If h_{LVC} is smaller than the thickness of the thermal boundary layer of the convecting cell, then the geoid kernel will be negative and not much affected by the channel [*Robinson et al.*, 1987]; on the other hand, if h_{LVC} is too large, the kernel shape would tend to that of a conducting lid over a constant viscosity mantle and would become mostly negative again.

Following this rationale, the positive correlation between the geoid and density anomalies can be achieved, with the same viscosities as in the initial model, by decreasing LVC thickness to the range of 170 km < h_{LVC} < 280 km (bold line in Figure C.2d; these calculations and the ones below included the negligibly-small contribution from a 40-km thick elastic lithosphere). In this model η_{LVC} is 2.5 orders of magnitudes smaller than the viscosity of the lower mantle implying a reasonable asthenospheric viscosity of $\eta_{LVC} \approx 3.2 \times 10^{19}$ for a lower-mantle viscosity of 10^{22} Pa s. When η_{LVC} is allowed to vary, a range of allowable viscosities and thicknesses are obtained (Figure C.2d). An alternative viscosity model, which fits the observation but does not include the sharp viscosity jump in the middle of the upper mantle, can be obtained by decreasing the viscosity of the asthenosphere by less than a factor of two and by placing a gradational viscosity increase from the LVC to the reference viscosity at 400 km depth (Figure C.3a). This viscosity structure, which mimics the seismic structure of PA5 (Figure 4.2), is more plausible for a mantle viscosity that is pressure and temperature dependent. Figure C.3d provides some plausible bounds for h_{LVC} and η_{LVC} for models of these type.

Although these thermal-convection models can explain the seismic results and the geoid anomalies observed along the Tonga-Hawaii corridor, they fail to predict the positive topography of the swells above the high-velocity, 'cold' regions. These models will always predict negative dynamic topography over the cold downwelling (note that the surface-topography kernels are negative at all depths, e.g., Figures C.1c, C.2c, and C.3c).

Therefore, we are forced to incorporate a shallow source of buoyancy with high seismic velocities beneath the swells to explain the observations. Compositional inhomogeneities associated with basaltic volcanism seems to provide the necessary mechanism.

FIGURE CAPTIONS

Figure C.1. Effect of elastic thickness on the geoid. (a) Our initial viscosity model is modified from the preferred model of *Hager and Clayton* [1989]. It includes a 60-km-thick lid with viscosity a factor of 100 larger than the reference viscosity, an asthenospheric layer with viscosity a factor of 30 smaller than the reference viscosity, between depths of 60 and 400 km, and a lower mantle viscosity a factor of 10 larger than the reference viscosity. (b) and (c) Three geoid kernels and three dynamic-topography kernels, respectively, which are calculated for $l = 26$, using the viscosity model in Figure C.1a, with a lithospheric elastic thickness of 0 km (solid line), 40 km (dashed line with dotes), and 130 km (dotted line). At this wavelength (~1500 km) the original kernel, which is strongly negative in the upper mantle, is not effected by adding an elastic plate thickness of 40 km. (d) Solid line is the harmonic coefficient of the calculated geoid, $\tilde{N}^l$ for $l = 26$, as a function of the elastic plate thickness; dashed line is the observed value, $\overline{N}^l$, derived from the harmonic analysis described in the text; shaded zone represents the 50% uncertainty of the observed value. Note that a minimum elastic thickness of 90 km is needed in order to flip the sign of $\tilde{N}^l$ and a thickness of ~130 km (heavy dot) is required to fit the observed value.

Figure C.2. Effect of a low-viscosity channel (LVC) on the geoid. (a) A profile with viscosities similar to those in Figure C.1a, but with an asthenospheric LVC thickness of 210 km (instead of 340 km); the geoid computed with this viscosity profile fits the observed geoid around $l = 26$. (b) and (c) Geoid and dynamic-topography kernels, respectively, calculated for $l = 26$, using the viscosity structure in Figure C.2a. (d) Light lines and heavy solid line are the harmonic coefficient of the calculated geoid, $\tilde{N}^l$ for $l = 26$, as a function of η_{LVC} and h_{LVC} defined in Figure C.2a; heavy dashed line is the observed value, $\overline{N}^l$, derived from the harmonic analysis described in the text; shaded zone represents the 50% uncertainty of the observed value. The intersection between the heavy

solid line ($\eta_{LVC} = 0.32$) and the dashed line (heavy dot) is the viscosity model shown in Figure C.2a.

Figure C.3. Effect of a LVC with gradational bottom on the geoid. (a) A viscosity profile, which mimics PA5 (Figure 4.2), with a low-viscosity asthenospheric channel below the seismic G discontinuity, bottomed by a linear increase in the logarithms of the viscosity that extends along the seismic high-gradient zone of PA5; the geoid computed with this viscosity profile fits the observed geoid around $l = 26$. (b) and (c) Geoid and dynamic-topography kernels, respectively, calculated for $l = 26$, using the viscosity structure in Figure C.3a. (d) Light lines and heavy solid line are the harmonic coefficient of the calculated geoid, $\tilde{N}^l$, for $l = 26$ as a function of η_{LVC} and h_{LVC} defined in Figure C.3a; heavy dashed line is the observed value, $\overline{N}^l$, derived from the harmonic analysis described in the text; shaded zone represents the 50% uncertainty of the observed value. The intersection between the heavy solid line ($\eta_{LVC} = 0.02$) and the dashed line (heavy dot) is the viscosity model shown in Figure C.3a.

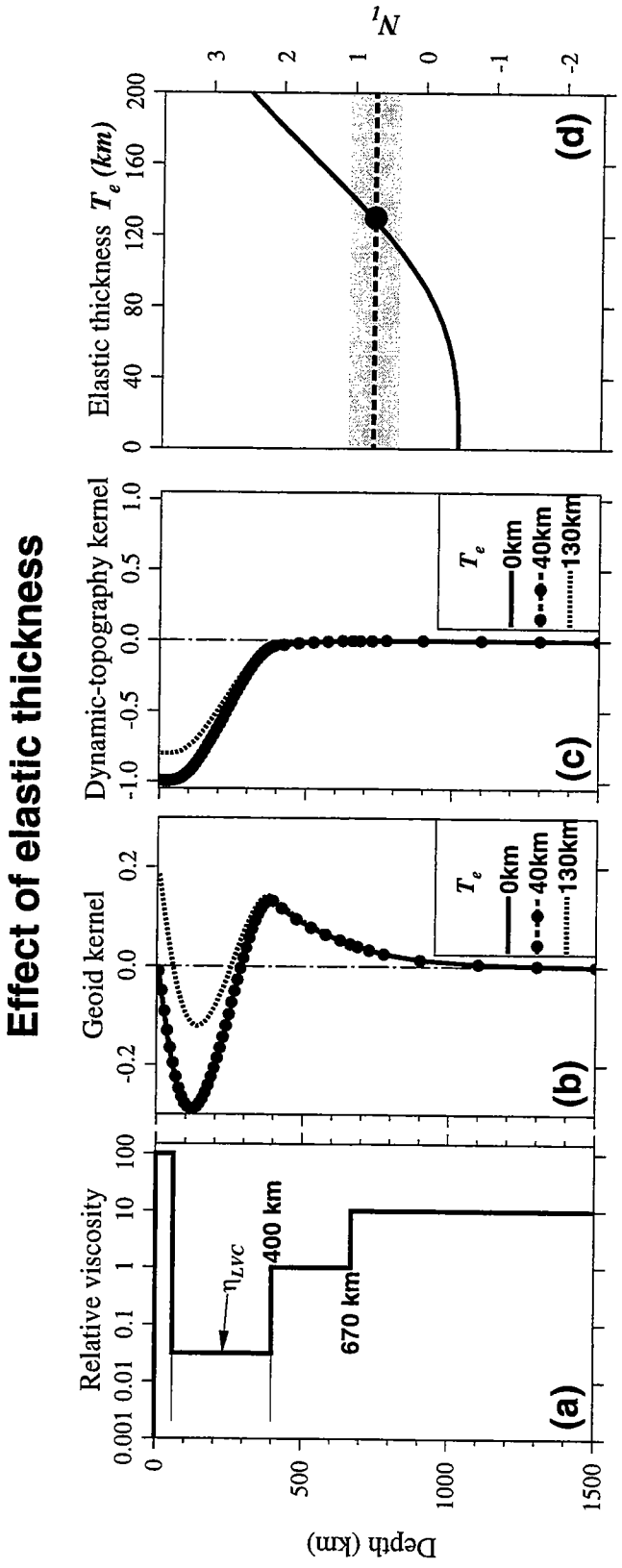
Effect of elastic thickness
Relative viscosity
0.001 0.01 0.1 1 10 100
η_{LVC}
400 km
670 km
(a)
Geoid kernel
-0.2 0.0 0.2
T_e
0km
40km
130km
(b)
Dynamic-topography kernel
-1.0 -0.5 0.0 0.5 1.0
T_e
0km
40km
130km
(c)
Elastic thickness T_e (km)
0 40 80 120 160 200
^1N
3 2 1 0 -1 -2
(d)
0 500 1000 1500
Depth (km)

Figure C.1

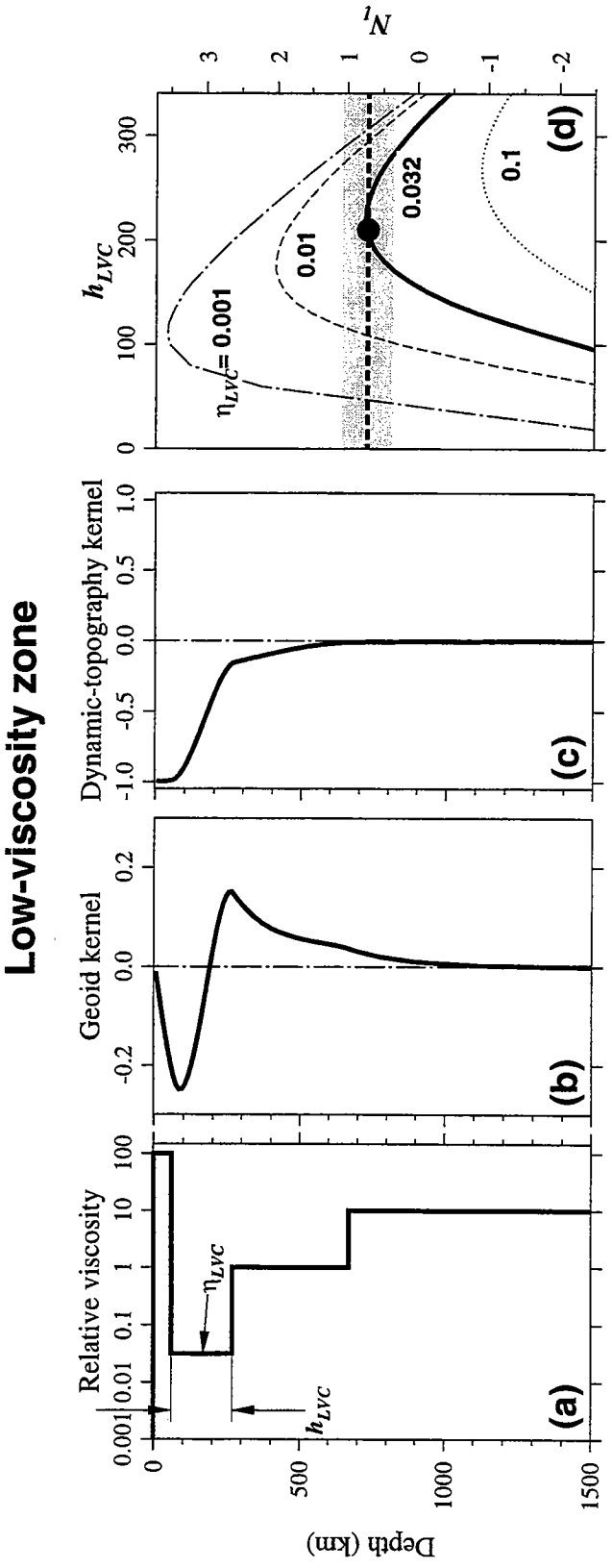
Low-viscosity zone
Relative viscosity
0.001
0.01
0.1
1
10
100
η_{LVC}
h_{LVC}
(a)
Geoid kernel
-0.2
0.0
0.2
(b)
Dynamic-topography kernel
-1.0
-0.5
0.0
0.5
1.0
(c)
h_{LVC}
0
100
200
300
η_{LVC}= 0.001
0.01
0.032
0.1
(d)
^1N
3
2
1
0
-1
-2
0
500
1000
1500
Depth (km)

Figure C.2

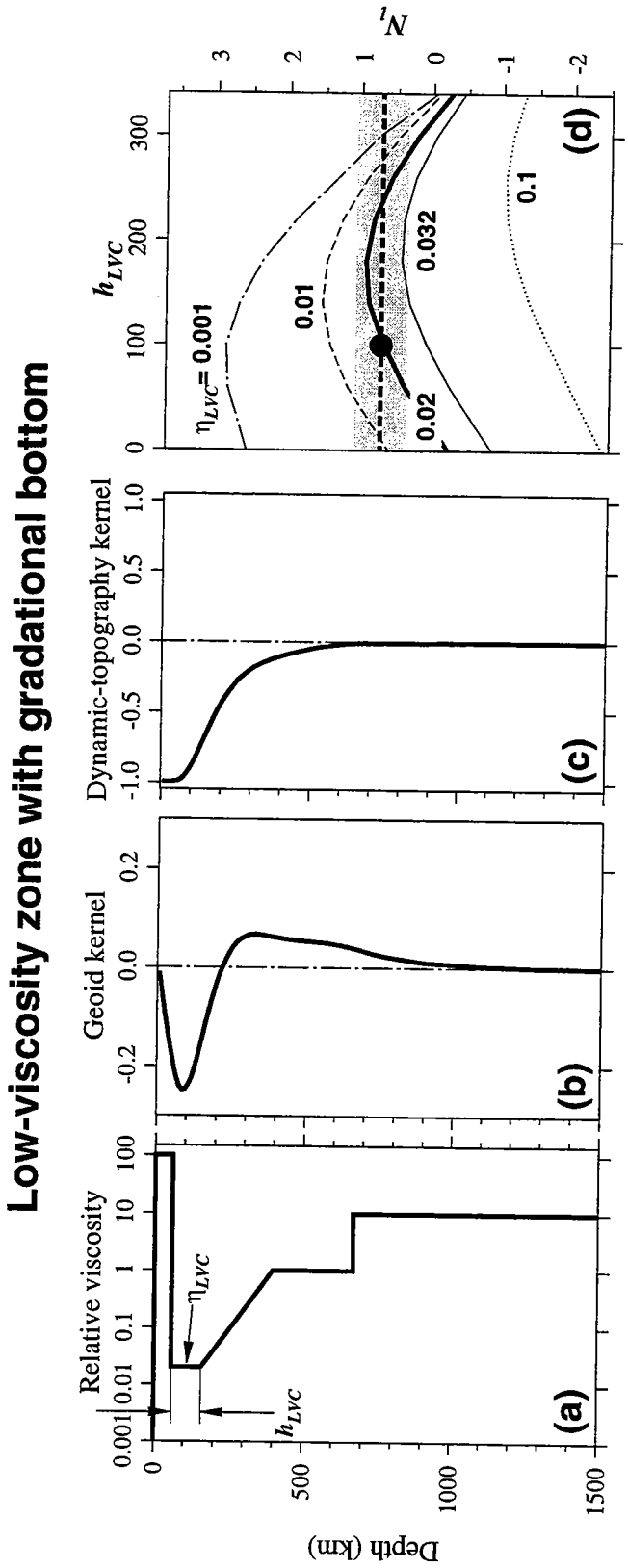
Low-viscosity zone with gradational bottom
Relative viscosity
0.001
0.01
0.1
1
10
100
η_{LVC}
h_{LVC}
(a)
Geoid kernel
-0.2
0.0
0.2
(b)
Dynamic-topography kernel
-1.0
-0.5
0.0
0.5
1.0
(c)
h_{LVC}
0
100
200
300
η_{LVC}= 0.001
0.01
0.02
0.032
0.1
N_1
3
2
1
0
-1
-2
(d)
Depth (km)
0
500
1000
1500

Figure C.3

REFERENCES

Baag, C.-E., and C. A. Langston, Shear-coupled *PL*, *Geophys. J. R. astr Soc.*, *80*, 363–385, 1985.

Backus, G. E., and F. Gilbert, Numerical application of a formalism for geophysical inverse problems, Geophys. J. R. Astron. Soc., 13, 247–276, 1967.

Baudry, N., and L. Kroenke, Intermediate-wavelength (400-600 km), south Pacific geoidal undulations: Their relationship to linear volcanic chains, *Earth Planet. Sci. Lett.*, *102*, 430–443, 1991.

Bhattacharyya, J., G. Masters, and P. Shearer, A global lateral variation of shear-wave attenuation in the upper mantle, *J. Geophys. Res.*, *101*, 22,272–22,289, 1996.

Bina, C., and G. Helffrich, Phase transition Clapeyron slopes and transition zone seismic discontinuity topography, *J. Geophys. Res.*, *99*, 15,853–15860, 1994.

Bock, G., Long-period *S* to *P* converted waves and the onset of partial melting beneath Oahu, Hawaii, *Geophys. Res. Lett.*, *18*, 869–872, 1991.

Burchfiel, B. C., and L. H. Royden, Tectonics of Asia 50 years after the death of Emile Argand, *Eclogae geol. Helv.*, *84*, 599–629, 1991.

Butler, R., The 1973 Hawaii earthquake: a double earthquake beneath the volcano Mauna Kea, *Geophys. J. R. astr. Soc.*, *69*, 173–186, 1982.

Calmant, S., The elastic thickness of the lithosphere in the Pacific Ocean, *Earth Planet. Sci. Lett.*, *85*, 277–288, 1987.

Cara, M., and J. J. Lévêque, Anisotropy of the asthenosphere: the higher mode data of the Pacific revisited, *Geophys. Res. Lett.*, *15*, 205–208, 1988.

Cazenave, A., S. Houry, and K. Dominh, Geosat-derived geoid anomalies at medium wavelengths, *J. Geophys. Res.*, *97*, 7081–7095, 1992.

Cazenave, A., B. Parsons, and P. Calcagno, Geoid lineations of 1000 km wavelength over the central Pacific, *Geophys. Res. Lett.*, *22*, 97–100, 1995.

Cazenave, A., P. Schaeffer, M. Berge, C. Brossier, K. Dominh, and M. C. Gennero, High-resolution mean sea surface computed with data of ERS-1 (geodetic mission) and the Topex-Poseidon, *Geophys. J. Int.*, *125*, 696–704, 1996.

Červený, V., and J. E. P. Soares, Fresnel volume ray tracing, *Geophysics*, *57*, 902–915, 1992.

Chamot-Rooke, N., V. Renard, and X. Le Pichon, Magnetic anomalies in the Shikoku Basin: a new interpretation, *Earth Planet. Sci. Lett.*, *83*, 214–228, 1987.

Clague, D. A., W. S. Weber, and J. E. Dixon, Picritic glasses from Hawaii, *Nature*, *353*, 553–556, 1991.

Clarke, T., P. G. Silver, Y.-L. Yeh, D. E. James, T. C. Wallace, and S. L. Beck, Close in ScS and sScS reverberations from the 9 June 1994 Bolivian earthquake, *Geophys. Res. Lett.*, *22*, 2313–2316, 1995.

Creager, K. C., and T. H. Jordan, Slab penetration into the lower mantle beneath the Mariana and other island arcs of the northwest Pacific, *J. Geophys. Res.*, *91*, 3573–3589, 1986.

Crough, S. T., Hotspot swells, *Ann. Rev. Earth Planet. Sci*, *11*, 165–193, 1983.

Crough, T. S., and R. D. Jarrard, The Marquesas-Line swell, *J. Geophys. Res.*, *86*, 11,763–11,771, 1981.

Davies, G. F., Ocean bathymetry and mantle convection 1. large-scale flow and hotspots, *J. Geophys. Res.*, *93*, 10,467–10,480, 1988.

Davies, G. F., Temporal variation of the Hawaiian plum flux, *Earth Plant. Sci. Lett.*, *113*, 277–286, 1992.

Davies, G. F., and F. Pribac, Mesozoic seafloor subsidence and the Darwin Rise, past and present, in *Geophysical Monograph*, edited by M. S. Pringle, W. W. Sager, W. V. Sliter, and S. Stein, *77*, pp. 39–52, American Geophysical Union, Washington, 1993.

Detrick, R. S., and S. T. Crough, Island subsidence, hot spots, and lithospheric thinning, *J. Geophys. Res.*, *83*, 1236–1244, 1978.

Dziewonski, A. M., and D. L. Anderson, Preliminary reference earth model, *Phys. Earth Plant. Int.*, *25*, 297-356, 1981.

Dziewonski, A. M., G. A. Ekström, and X.-F. Liu, Structure at the top and bottom of the mantle, in *Monitoring a Comprehensive Test Ban Treaty*, edited by E. S. Husebye, and A. M. Dainty, pp. 521–550, Kluwer Academic Publishers, Dordrecht, 1996.

Ekström, G. A., and A. M. Dziewonski, The unique anisotropy of the Pacific upper mantle, *Nature, Submitted*, 1997.

Fischer, K. M., K. C. Creager, and T. H. Jordan, Mapping the Tonga slab, *J. Geophys. Res.*, *96*, 14,403–14,427, 1991.

Flanagan, M. P., and P. M. Shearer, Global mapping of topography on transition zone velocity discontinuities by stacking SS precursors, *J. Geophys. Res.*, *Submitted*, 1997.

Forsyth, D. W., The early structural evolution and anisotropy of the oceanic upper mantle, *Geophys. J. R. Astron. Soc.*, *43*, 103–162, 1975.

Forte, A. M., A. M. Dziewonski, and R. L. Woodward, Aspherical structure of the mantle, tectonic plate motions, nonhydrostatic geoid, and topography of the core-mantle boundary, in *Dynamics of Earth's deep interior and Earth rotation, Geophys. Monogr. Ser*, edited by J.-L. Le Mouel, D. E. Smylie, and T. Herring, *72*, pp. 135–166, 1993.

Fukao, Y., M. Obayashi, H. Inoue, and M. Nenbai, Subducting slabs stagnant in the mantle transition zone, *J. Geophys. Res.*, *97*, 4809–4822, 1992.

Gaherty, J. B., and T. H. Jordan, Lehmann discontinuity as the base of an anisotropic layer beneath continents, *Science*, *268*, 1468–1471, 1995.

Gaherty, J. B., T. H. Jordan, and L. S. Gee, Seismic structure of the upper mantle in a western Pacific Corridor, *J. Geophys. Res.*, *101*, 22,291–22,309, 1996.

Gaherty, J. B., M. Kato, and T. H. Jordan, Seismic structure of the upper mantle: A regional comparison of seismic layering, *Phys. Earth Planet. Inter., submitted*, 1997.

Garnero, E. J., and D. V. Helmberger, Seismic detection of a thin laterally varying layer at the base of the mantle beneath the central-Pacific, *Geophys. Res. Lett.*, *23*, 977–980, 1996.

Gee, L. S., and T. H. Jordan, Generalized seismological data functionals, *Geophys. J. Int.*, *111*, 363-390, 1992.

Gee, L. S., and B. Romanowicz, Attenuation and differential travel times in the western Pacific, *EOS, Trans. AGU*, *73*, 384, 1992.

Gilbert, F., and D. V. Helmberger, Generalized ray theory for a layered sphere, *Philos. Trans. R. Soc. London*, *A278*, 187–269, 1972.

Grand, S. P., Tomographic inversion for shear velocity beneath the North American plate, *J. Geophys. Res.*, *92*, 14,065–14,090, 1987.

Grand, S. P., Mantle shear structure beneath the Americas and surrounding oceans, *J. Geophys. Res.*, *99*, 11,591–11,621, 1994.

Grand, S. P., and D. V. Helmberger, Upper mantle shear structure of North America, *Geophys. J. R. astr. Soc.*, *76*, 399–438, 1984.

Grand, S. P., R. van der Hilst, and S. Widiyantoro, Global seismic tomography: A snapshot of convection in the Earth, *GSA today*, *7*, 1–7, 1997.

Green, D. H., and R. C. Liberman, Phase equilibria and elastic properties of a pyrolite model for the oceanic upper mantle, *Tectonophysics*, *32*, 61–92, 1976.

Gripp, A. E., and R. G. Gordan, Current plate velocities relative to the hotspots incorporating the NUVEL-1 global plate motion model, *Geophys. Res. Lett.*, *17*, 1109–1112, 1990.

Hager, B. H., Subducted slabs and the geoid: Constrains on mantle rheology and flow, *J. Geophys. Res.*, *89*, 6003–6015, 1984.

Hager, B. H., Mantle Viscosity: A comparison of models from postglacial rebound and from geoid, plate driving forces, and advected heat flux, in *Glacial Isostasy, Sea Level and Mantle Rheology*, edited by R. Sabadini, K. Lambeck, and E. Boschi, pp. 493–513, Kluwer Academic Publishers, Dordrecht, 1991.

Hager, B. H., and R. W. Clayton, Constraints on the structure of mantle convection using seismic observations, flow models, and the geoid, in *Mantle Convection: Plate Tectonics and Global dynamics*, edited by W. R. Peltier, pp. 658–763, Gordon And Bench, New York, 1989.

Hager, B. H., and M. A. Richards, Long-wavelength variations in Earth's geoid: physical models and dynamical implications, *Phil. Trans. R. Soc. Lond. A.*, *328*, 309–327, 1989.

Haxby, W. F., and J. K. Weissel, Evidence for small-scale mantle convection from Seasat altimeter data, *J. Geophys. Res.*, *91*, 3507–3520, 1986.

Helmberger, D. V., Theory and application of synthetic seismograms, in *Earthquakes: Observation, Theory, and Interpretation*, edited by H. Kanamori, and E. Boschi, pp. 174–217, North-Holland, New York, 1983.

Helmberger, D. V., and R. A. Wiggins, Upper-mantle structure of midwestern united states, *J. Geophys. Res.*, *76*, 3229–3245, 1971.

Hilde, T. W. C., and C.-S. Lee, Origin and evolution of the West Philippine Basin: a new interpretation, *Tectonophysics*, *102*, 85–104, 1984.

Hirahara, K., and A. Hasemi, Tomography of subduction zones using local and regional earthquake and teleseisms, in *Seismic Tomography: Theory and Practice*, edited by H. M. Iyer, and K. Hirahara, pp. 519–562, Chapman & Hall, London, 1993.

Hirth, G., and D. L. Kohlstedt, Water in the oceanic upper mantle: implications for the rheology, melt extraction and the evolution of the lithosphere, *Earth Planet. Sci. Lett.*, *144*, 93–108, 1996.

Honda, S., D. A. Yuen, S. Balachandar, and D. Reuteler, Three-dimensional instabilities of mantle convection with multiple phase transition, *Science*, *259*, 1308–1311, 1993.

Hong, T.-L., and D. V. Helmberger, Glorified optics and wave propagation in nonplanar structure, *Bull. Seismol. Soc. Am.*, *68*, 1313–1358, 1978.

Houseman, G., and D. P. McKenzie, Numerical experiments on the onset of convective instabilities in the Earth's mantle, *Geophys. J. R. astr. Soc.*, *68*, 133–164, 1982.

Hron, F., Criteria for selection of phases in synthetic seismograms for layered media, *Bull. Seism. Soc. Am.*, *1971*, 765–779, 1971.

Hron, F., Numerical method for ray generation in multilayered media, in *Methods in Computational Physics*, edited by B. A. Bolt, *12*, pp. 1-34, Academic press, New York, 1972.

Jordan, T. H., Mineralogies, densities and seismic velocities of garnet lherzolites and their geophysical implications, in *Mantle Sample: Inclusions in Kimberlites and other volcanics*, edited by F. R. Boyd, and H. O. A. Meyer, pp. 1-13, American Geophysical Union, Washington, D.C., 1979.

Jordan, T. H., and S. A. Sipkin, Estimation of the attenuation operator for multiple *ScS* waves, *Geophys. Res. Lett.*, *4*, 167–170, 1977.

Karato, S., Importance of anelasticity in the interpretation of seismic tomography, *Geophys. Res. Lett.*, *20*, 1623–1626, 1993.

Karato, S.-I., Effects of water on seismic wave velocities in the upper mantle, *Proc. Japan. Acad.*, *71*, 61–66, 1995.

Karato, S.-I., S. Zhang, and H.-R. Wenk, Superplasticity in Earth's lower mantle: evidence from seismic anisotropy and rock physics, *Science*, *270*, 458–461, 1995.

Kato, M., An analysis of the temperature derivative of shear-wave velocity in the oceanic lithosphere of the Pacific Basin, *J. Phys. Earth.*, *45*, 67–71, 1997.

Kato, M., and T. H. Jordan, Seismic structure of the upper mantle beneath the western Philippine Sea, *Phys. Earth Planet. Inter., submitted*, 1997.

Katzman, R., L. Zhao, and T. H. Jordan, Image of small-scale convection in the Pacific upper mantle: implications for the Hawaii, Marquesas and Society hotspots, *EOS Trans. AGU*, *78*, S322, 1997a.

Katzman, R., L. Zhao, and T. H. Jordan, High-resolution, 2D vertical tomography of the central Pacific mantle using ScS reverberations and frequency-dependent travel times, *J. Geophys. Res, submitted*, 1997b.

Kawasaki, I., and F. Kon'no, Azimuthal anisotropy of surface waves and the possible type of the seismic anisotropy due to preferred orientation of olivine in the uppermost mantle beneath the Pacific Ocean,, *J. Phys. Earth*, *32*, 229–244, 1984.

Lay, T., and T. C. Wallace, Multiple *ScS* travel times and attenuation beneath Mexico and Central America, *Geophys. Res. Lett.*, *10*, 301–304, 1983.

Lebedev, S., G. Nolet, and R. v. d. Hilst, The upper mantle beneath the Philippine Sea region from waveform inversion, *Geophys. Res. Lett.*, *24*, 1851–1854, 1997.

Lemoine, F. G., et al., The NASA and DMA Joint Geopotential Model, *Eos Trans. Am. Geophys. Un.*, *77*, F136, 1996.

Lerner-Lam, A., and T. H. Jordan, Earth structure from fundamental and higher-mode waveform analysis, *Geophys. J. R. astr. Soc.*, *75*, 759-797, 1983.

Li, X.-D., and B. Romanowicz, Comparison of global waveform inversions with and without considering cross-branch model coupling, *Geophys. J. Int.*, *121*, 695–709, 1995.

Li, X.-D., and B. Romanowicz, Global mantle shear velocity model developed using nonlinear asymptotic coupling theory, *J. Geophys. Res.*, *101*, 22,245–22,272, 1996.

Li, X.-D., and T. Tanimoto, Waveforms of long-period waves in a slightly aspherical earth model, *Geophys. J. Int.*, *112*, 92–102, 1993.

Liu, M., and C. G. Chase, Evolution of Hawaiian basalts: a hotspot melting model, *Earth Planet. Sci. Lett.*, *104*, 151–165, 1991.

Machetel, P., and P. Weber, Intermittent layered convection in a model mantle with an endothermic phase change at 670 km, *Nature*, *350*, 55-57, 1991.

Maia, M., and M. Diament, An analysis of the altimetric geoid in various wavebands in the central Pacific Ocean: constraints on the origin of intraplate features, *Tectonophysics*, *190*, 133–153, 1991.

Marquering, H., and R. Snieder, Surface-wave mode coupling for efficient forward modeling and inversion of body-wave phases, *Geophys. J. Int.*, *120*, 186–208, 1995.

Marquering, H., R. Snieder, and G. Nolet, Waveform inversions and the significance of surface-wave mode coupling, *Geophys. J. Int.*, *124*, 258–278, 1996.

Masters, G., S. Johnson, G. Laske, and H. Bolton, A shear velocity model of the mantle, *Philos. Trans. R. Soc. London, Ser. A*, *354*, 1996.

Maupin, V., Partial derivatives of surface-wave phase velocities for flat anisotropic models, *Geophys. J. R. Astron. Soc.*, *83*, 379–398, 1985.

Maupin, V., Modeling of laterally trapped surface wave with application to Rayleigh waves in the Hawaiian swell, *Geophys. J. Int.*, *110*, 553–570, 1992.

McKenzie, D., and M. J. Bickle, The volume and composition of melt generated by extension of lithosphere, *J. Petrol.*, *29*, 625–679, 1988.

Menard, H. W., Darwin Reprise, *J. Geophys. Res.*, *89*, 9960–9968, 1984.

Montagner, J.-P., and B. L. N. Kennett, How to reconcile body-wave and normal mode reference Earth models, *Geophys. J. Int.*, *125*, 229–248, 1996.

Montagner, J.-P., and T. Tanimoto, Global upper-mantle tomography of seismic velocities and anisotropy, *J. Geophys. Res.*, *96*, 20,337–20,351, 1991.

Morgan, W. J., Deep mantle convection plumes and plate motion, *Amer. Assoc. Pertol. Geol. Bull.*, *56*, 203–213, 1972.

Mueller, R. D., W. R. Roest, J.-Y. Royer, L. M. gahagan, and J. G. Sclater, A digital age map of the ocean floor, *SIO reference series 93-30*, 1993.

Nakanishi, I., Attenuation of multiple *ScS* beneath the Japanese arc, *Phys. Earth. Planet. Inter.*, *19*, 337–347, 1979.

Nicolas, A., and N. I. Christensen, Formation of anisotropy in upper mantle peridotites: A review, in *Composition, Structure, and Dynamics of Lithosphere-Asthenosphere System, Geodyn. Ser.*, edited by K. F. a. C. Froidevaux, *16*, pp. 111–123, AGU, Washington, D.C., 1987.

Nishimura, C. E., and D. W. Forsyth, The anisotropic structure of the upper mantle in the Pacific, *Geophys. J. Int.*, *96*, 203, 1989.

Nolet, G., Partitioned waveform inversion and two-dimensional structure under the network of autonomously recording seismographs, *J. Geophys. Res.*, *95*, 8499–8512, 1990.

Nolet, G., S. P. Grand, and B. L. N. Kennett, Seismic heterogeneity in the upper mantle, *J. Geophys. Res.*, *99*, 23,753–23,766, 1994.

O'Hara, M. J., Is there an Icelandic mantle plume?, *Nature*, *253*, 708–710, 1975.

Oxburgh, E. R., and E. M. Parmentier, Compositional and density stratification in oceanic lithosphere—causes and consequences, *J. Geol. Soc. Lond.*, *133*, 343–355, 1977.

Palvis, G. L., and J. R. Brooker, The mixed discrete-continuous inverse problem: application to the simultaneous determination of earthquake hypocenters and velocity structure, *J. Geophys. Res.*, *85*, 4801–4810, 1980.

Panasyuk, S. V., B. H. Hager, and A. M. Forte, Understanding the effects of mantle compressibility on geoid kernels, *Geophys. J. Int.*, *124*, 121–133, 1996.

Park, C.-H., K. Tamaki, and K. Kobayashi, Age-depth correlation of the Philippine Sea back-arc basins and other marginal basins in the world, *Tectonophysics*, *181*, 351–371, 1990.

Parsons, B., and D. McKenzie, Mantle convection and the thermal structure of the plates, *J. Geophys. Res.*, *83*, 4485-4496, 1978.

Phipps Morgan, J., W. J. Morgan, and E. Price, Hotspots melting generates both hotspot volcanism and hotspot swell, *J. Geophys. Res.*, *100*, 8045–8062, 1995.

Phipps Morgan, J., and P. Shearer, Seismic constraints on mantle flow and topography of the 660-km discontinuity: Evidence for whole mantle convection, *Nature*, *365*, 506–511, 1993.

Puster, P., J. B. Gaherty, T. H. Jordan, and D. J. Weidner, Fine-scale structure of the 660-km discontinuity region, *EOS Trans. AGU*, *77*, F472, 1996.

Puster, P., and T. H. Jordan, How stratified is mantle convection?, *J. Geophys. Res.*, *102*, 7625–7646, 1997.

Regan, J., and D. L. Anderson, Anisotropy models of the upper mantle, *Phys. Earth Plant. Inter.*, *35*, 227–263, 1984.

Revenaugh, J., and T. H. Jordan, Observations of first-order mantle reverberations, *Bull. Seism. Soc. Am.*, *77*, 1704-1717, 1987.

Revenaugh, J., and T. H. Jordan, A study of mantle layering beneath the western Pacific, *J. Geophys. Res.*, *94*, 5787-5813, 1989.

Revenaugh, J., and T. H. Jordan, Mantle layering from ScS reverberations 1. Waveform inversion of zeroth-order reverberations, *J. Geophys. Res.*, *96*, 19749-19762, 1991a.

Revenaugh, J., and T. H. Jordan, Mantle layering from ScS reverberations 2. The transition zone, *J. Geophys. Res.*, *96*, 19763-19780, 1991b.

Revenaugh, J., and T. H. Jordan, Mantle layering from ScS reverberations 3. The upper mantle, *J. Geophys. Res.*, *96*, 19781-19810, 1991c.

Revenaugh, J., and T. H. Jordan, Mantle layering from ScS reverberations 4. The lower mantle and core-mantle boundary, *J. Geophys. Res.*, *96*, 19781-19810, 1991d.

Revenaugh, J., and S. A. Sipkin, Mantle discontinuity structure beneath China, *J. Geophys. Res.*, *99*, 21,911-21,927, 1994a.

Revenaugh, J., and S. A. Sipkin, Seismic evidence for silicate melt atop the 410-km mantle discontinuity, *Nature*, *369*, 474–476, 1994b.

Ribe, M. N., Seismic anisotropy and mantle flow, *J. Geophys. Res.*, *94*, 4213–4223, 1989.

Richards, M. A., B. H. Hager, and N. H. Sleep, Dynamically supported geoid highs over hotspots: observation and Theory, *J. Geophys. Res.*, *93*, 7690–7708, 1988.

Richter, F., Convection and large-scale circulation of the mantle, *J. Geophys. Res.*, *78*, 8735–8745, 1973.

Richter, F., Focal mechanism and seismic energy release of deep and intermediate earthquakes in the Tonga-Kermadec region and their bearing on the depth extent of mantle flow, *J. Geophys. Res.*, *84*, 6783–6795, 1979.

Richter, F., and B. Parsons, On the interaction of two scales of convection in the mantle, *J. Geophys. Res.*, *80*, 2529–2541, 1975.

Ringwood, A. E., *Composition and Petrology of the Earth's Mantle*, 604 pp., McGraw-Hill, New York, 1975.

Robinson, E. M., B. Parsons, and S. F. Daly, The effect of a shallow low viscosity zone on the apparent compensation of mid-plate swells, *Earth Planet. Sci. Lett.*, *82*, 335–348, 1987.

Rutland, R. W. R., Structural framework of the Australian Precambrian, in *Precambrian of the southern Hemisphere*, edited by D. R. Hunter, pp. 1–32, Elsevier, Amsterdam, 1981.

Saltzer, R. L., and E. D. Humphreys, Upper mantle *P* wave velocity structure of the eastern Snake River Plain and its relationship to geodynamic models of the region, *J. Geophys. Res.*, *102*, 11,829–11,841, 1997.

Sammis, C. G., J. C. Smith, G. Schubert, and D. A. Yuen, Viscosity-depth profile of the Earth's mantle: effects of polymorphic phase transition, *J. Geophys. Res.*, *82*, 3747–3761, 1977.

Sandwell, D. T., and M. Renkin, Compensation of swells and plateaus in the North Pacific: No direct evidence for mantle convection, *J. Geophys. Res.*, *93*, 2775–2783, 1988.

Sato, H., I. S. Sacks, and T. Murase, The use of laboratory velocity for estimating temperature and partial melt fraction in the low-velocity zone: comparison with heat flow and electrical conductivity studies, *J. Geophys. Res.*, *94*, 5689–5704, 1989.

Shearer, P. M., Constraints on upper mantle discontinuities from observations of long period reflected and converted phases, *J. Geophys. Res.*, *96*, 20,353–20,364, 1991.

Shearer, P. M., Global mapping of upper mantle reflectors from long-period SS precursors, *Geophys. J. Int.*, *115*, 878–904, 1993.

Silver, P. G., Seismic anisotropy beneath continents: Probing the depths of geology, *Annu. Rev. Earth Planet. Sci.*, *24*, 385–432, 1996.

Sipkin, S. A., and T. H. Jordan, Lateral heterogeneity of upper mantle determined from the travel times of multiple *ScS*, *J. Geophys. Res.*, *81*, 6307–6320, 1976.

Sipkin, S. A., and T. H. Jordan, Frequency dependence of Q_{ScS}, *Bull. Seismol. Soc. Am.*, *69*, 1055–1079, 1979.

Sipkin, S. A., and T. H. Jordan, Multiple *ScS* travel times in the western Pacific: implications for mantle heterogeneity, *J. Geophys. Res.*, *85*, 853-861, 1980a.

Sipkin, S. A., and T. H. Jordan, Regional variation of Q_{ScS}, *Bull. Seismol. Soc. Am.*, *70*, 1071–1102, 1980b.

Sleep, N. H., Hotspots and mantle plumes: Some Phenomenology, *J. Geophys. Res.*, *95*, 6715–6736, 1990.

Solheim, L. P., and W. R. Peltier, Avalanche effects in phase transition modulated thermal convection: A model of earth's mantle, *J. Geophys. Res.*, *99*, 6997-7018, 1994.

Spencer, C., and D. Gubbins, Travel-time inversion for simultaneous earthquake location and velocity structure determination in laterally varying media, *Geophys. J. R. Astron. Soc.*, *63*, 95–116, 1980.

Stein, C. A., and S. Stein, A model for the global variation in oceanic depth and heat flow with lithospheric age, *Nature*, *359*, 123–129, 1992.

Su, W.-J., R. L. Woodward, and A. M. Dziewonski, Degree 12 model of shear velocity heterogeneity in the mantle, *J. Geophys. Res.*, *99*, 6945–6980, 1994.

Tackely, P. J., D. J. Stevenson, G. A. Glatzmair, and G. Schubert, Effect of an endothermic phase transition at 670 km depth in spherical model of convection in the earth mantle, *Nature*, *361*, 699-703, 1993.

Tamaki, K., and E. Honza, Global tectonics and formation of marginal basins: Role of the western Pacific, *Episodes*, *14*, 224–230, 1991.

Tanimoto, T., and D. L. Anderson, Lateral heterogeneity and azimuthal anisotropy in the upper mantle: Love and Rayleigh waves 100-250 s, *J. Geophys. Res.*, *90*, 1842–1858, 1985.

Tarantola, A., *Inverse Problems Theory*, 613 pp., Elsevier, New York, 1987.

Tarantola, A., and A. Nercessian, Three-dimensional inversion without blocks, *Geophys. J. R. astr. Soc.*, *76*, 299–306, 1984.

Tarantola, A., and B. Valette, Generalized nonlinear inverse problem solved using the least squares criterion, *Rev. Geophys. Space Phys.*, *20*, 219–232, 1982.

Thatcher, W., and J. N. Brune, Higher mode interference and observed anomalous apparent Love wave phase velocities, *J. Geophys. Res.*, *74*, 6603–6611, 1969.

Turcotte, D. L., and G. Schubert, *Geodynamics, Applications of Continental Physics to Geological Problems*, 450 pp., John Wiley, New York, 1982.

VanDecar, J. C., D. James, and M. Assumcao, Seismic evidence for fossil mantle plume beneath South America and implications for plate driving forces, *Nature*, *378*, 25–31, 1995.

van der Hilst, R., Complex morphology of subducted lithosphere in the mantle beneath the Tonga trench, *Nature*, *374*, 154–157, 1995.

van der Hilst, R., R. Engdahl, W. Spakman, and G. Nolet, Tomographic imaging of subducted lithosphere below northwest Pacific island arcs, *Nature*, *353*, 37-43, 1991.

van der Hilst, R., S. Widiyantoro, and E. R. Engdahl, Evidence for deep mantle circulation from global tomography, *Nature*, *386*, 578–584, 1997.

van der Lee, S., and G. Nolet, The upper-mantle *S* velocity structure of North America, *J. Geophys. Res.*, *102*, 22,815–22,838, 1997.

Vasco, D. W., J. John E. Peterson, and E. L. Majer, Beyond ray tomography: Wavepath and Fresnel volumes, *Geophysics*, *60*, 1790–1804, 1995.

Von Herzen, R. P., M. J. Cordery, R. S. Detrick, and C. Fang, Heat flow and thermal origin of hotspot swells: The Hawaiian swell revisited, *J. Geophys. Res.*, *94*, 13,783–13,799, 1989.

Watts, A. B., Gravity and bathymetry in the central Pacific Ocean, *J. Geophys. Res.*, *81*, 1533–1553, 1976.

Watts, A. B., J. H. Bodine, and N. M. Ribe, Observations of flexure and the geological evolution of the Pacific ocean, *Nature*, *283*, 532–537, 1980.

Watts, A. B., and U. S. ten Brink, Crustal structure, flexure, and subsidence history of the Hawaiian swell, *J. Geophys. Res.*, *94*, 10,473–10,500, 1989.

Weidner, D. J., and Y. Wang, Chemical and induced buoyancy at the 660 km discontinuity, *J. Geophys. Res., Submitted*, 1997.

Wessel, P., Observational constraints on model of the Hawaiian hot spots swell, *J. Geophys. Res.*, *98*, 16,095–16,104, 1993.

Wessel, P., D. Bercovici, and L. W. Kroenke, The possible reflection of mantle discontinuities in Pacific geoid and bathymetry, *Geophys. Res. Lett.*, *21*, 1943–1946, 1994.

Wessel, P., L. W. Kroenke, and D. Bercovici, Pacific plate motion and undulation in geoid and bathymetry, *Earth Planet. Sci. Lett.*, *140*, 53–66, 1996.

Wessel, P., and W. H. F. Smith, Free software helps map and display data, *EOS Trans. AGU*, *72*, 441, 445–446, 1991.

Woodhouse, J. H., The coupling and attenuation of nearly resonant multiplets in the earth's free oscillation spectrum, *Geophys. J. R. astr. Soc.*, *61*, 261-283, 1980.

Woodhouse, J. H., The joint inversion of seismic waveforms for lateral variations in Earth structure and earthquake source parameters, *Proc. Int. School Phys. Enrico Fermi, 85*, 366-397, 1983.

Woodhouse, J. H., and A. M. Dziewonski, Mapping the upper mantle: Three dimensional modeling of earth structure by inversion of seismic waves, *J. Geophys. Res.*, *89*, 5953–5986, 1984.

Woods, M. T., and E. A. Okal, Rayleigh-wave dispersion along the Hawaiian swell: a test of lithospheric thinning by thermal rejuvenation, *Geophys. J. Int.*, *125*, 325–339, 1996.

Woods, M. T., E. A. Okal, and M. Cara, Two-station measurements of Rayleigh wave group velocity along the Hawaiian swell, *Geophys. Res. Lett.*, *18*, 105–108, 1991.

Wysession, M. E., Large-scale structure at the core-mantle boundary from diffracted waves, *Nature*, *382*, 244–248, 1996.

Zhang, S., and S.-I. Karato, Lattice preferred orientation of olivine aggregates deformed in simple shear, *Nature*, *375*, 774–777, 1995.

Zhang, Y.-S., and T. Tanimoto, Three-dimensional modeling of upper mantle structure under the Pacific ocean and surrounding area, *Geophys. Res. J. R. Astron. Soc.*, *98*, 255–269, 1989.

Zhang, Y.-S., and T. Tanimoto, Global Love wave phase velocity variation and its significance to plate tectonics, *Phys. Earth. Plant. Inter.*, *66*, 160–202, 1991.

Zhang, Y.-S., and T. Tanimoto, High-resolution global upper mantle structure and plate tectonics, *J. Geophys. Res.*, *98*, 9793–9823, 1993.

Zhao, L., and T. H. Jordan, Sensitivity of frequency-dependent travel times to laterally-heterogeneous, anisotropic earth structure, *Geophys. J. Int., submitted*, 1997.

Zhou, H.-w., and R. W. Clayton, *P* and *S* wave travel time inversions for subduction slab under the island arcs of the northwest pacific, *J. Geophys. Res.*, *95*, 6829–6851, 1990.

Zielhuis, A., and G. Nolet, Shear-wave velocity variations in the upper mantle beneath central Europe, *Geophys. J. Int.*, *117*, 695–715, 1994.

Zielhuis, A., and R. van der Hilst, Upper-mantle shear velocity beneath eastern Australia from inversion of waveform SKIPPY portable arrays, *Geophys. J. Int.*, *127*, 1–16, 1996.

ACKNOWLEDGMENTS

During my long graduate career at MIT and WHOI, I have had the opportunity to work in several groups and with quite a few outstanding people to whom I would like to express my deepest gratitude.

Steve Holbrook, who has been my primary advisor during the first two years in the program, enabled me to collect and analyze exciting wide-angle, marine data for a gas-hydrate study. While working on this paper, which is not included in the thesis, I have benefited tremendously from the interaction with Steve, and with Dan Lizarralde, John Collins, and the other fellows in the Ocean-Bottom Seismology group at WHOI.

The collaboration with Uri ten Brink during the second stage of my work at WHOI has been very productive. Working together with Jian Lin, our study on crustal deformation has resulted in papers which are also not documented here. Uri also allowed me to join his scientific expedition to the Antarctic polar plateau which became one of the highlights of my life. His friendship and support have been deeply rewarding.

Tom Jordan was willing to accept me into his seismology group at MIT towards the end of my third year. Tom is a real scientific leader and a remarkable advisor; with him, every problem seemed to be much easier to tackle. Despite his hectic schedule as a department head, he was always available to dig me out of "dead ends". Margaret's and Tom's parties were always happy gatherings and provided a great deal of gastronomical joy.

I am particularly indebted to Jim Gaherty and Li Zhao. Jim introduced me to some of the secrets of the GSDF analysis and made my first months in the group much easier. Li developed the 2D sensitivity kernels, which became essential to this thesis. Over the years, both of them have been great partners for numerous seismological discussions.

I thank Rob van der Hilst, Jeroen Tromp, Brad Hager, Stan Hart, and Uri ten Brink for reading my thesis and providing stimulating discussion and useful suggestions.

Much of my understanding of Earth Sciences has come from classes and discussions with Brad Hager, Rob van der Hilst, Jeroen Tromp, Bill Rodi, Chris Marone, Greg Hirth, Marcia McNutt, Sam Bowring, Alberto Saal, Garrett Ito, Mark Simons, Peter Puster, Olav Van Genabeer, Sri Widiyantoro, and Jun Korenaga.

The friendships with my fellow students made my time at WHOI and MIT most enjoyable through frequent parties, dinners, barbecues, and hiking trips. For that I am particularly grateful to Garrett Ito, Alberto Saal, Dan Lizarralde, Gary Jaraslow, Javier Escartín, Einat Aharnonov, Danny Sigman, Emilie Hooft, Jim Gaherty, Mark Simons, and Jeff McGuire. In addition, I have enjoyed the interaction with Pierre Ihmlé, Mamoru Kato, Mosumi Roy, Cecily Wolfe, Yu Jin, Shijie Zhong, Frederik Simons, Hrafnkell Karason, Rebecca Saltzer, and Eliza Richardson.

The technical support of Jim Dolan and Dave DuBois at WHOI and of Linda Meinke at MIT was irreplaceable. Beverly Kozel-Tattlebaum, Deb Sykes, Darla Smutka, and Amanda Bourque smoothed out the administrative part.

I am grateful to my parents who have always encouraged me to pursue my education even if it meant that I would be about 8800 km away from home for many years.

Most of all, I am thankful to my wife, Niva, who spent her first Bostonian winter of 1993-94 alone, while I was enjoying the Antarctic polar plateau which, at that time, was not much colder than New England. It is not easy to be married to an MIT student who spends about 70 hours a week at work. Niva has turned the last 4 years of my studentship into a pleasant memory by supporting me through the hard times and giving me all the freedom I could have possibly asked for. I am looking forward to spending the next six months with her (and away from work) in our upcoming trip to South America.

This research was supported by the National Science Foundation under grant EAR-9628351 and by the Defense Special Weapons Agency under grant DSWA-F49620-95-1-0051. The ray-tracing code for the ScS reverberations was initiated from Justin Revenaugh's code. Lana Panasyuk and Brad Hager provided the software for the dynamic-compensation calculations used in Appendix C. The seismic data were acquired from the IRIS-Data Management System, and some of the figures were generated using the GMT software freely distributed by *Wessel and Smith* [1991].